Research Topics

# Using high energy density plasmas for nuclear experiments relevant to nuclear astrophysics

**Edited by**
Maria Gatu Johnson, Michael Wiescher, Mark Paris, Alex Zylstra and Gerald Hale

**Published in**
Frontiers in Physics

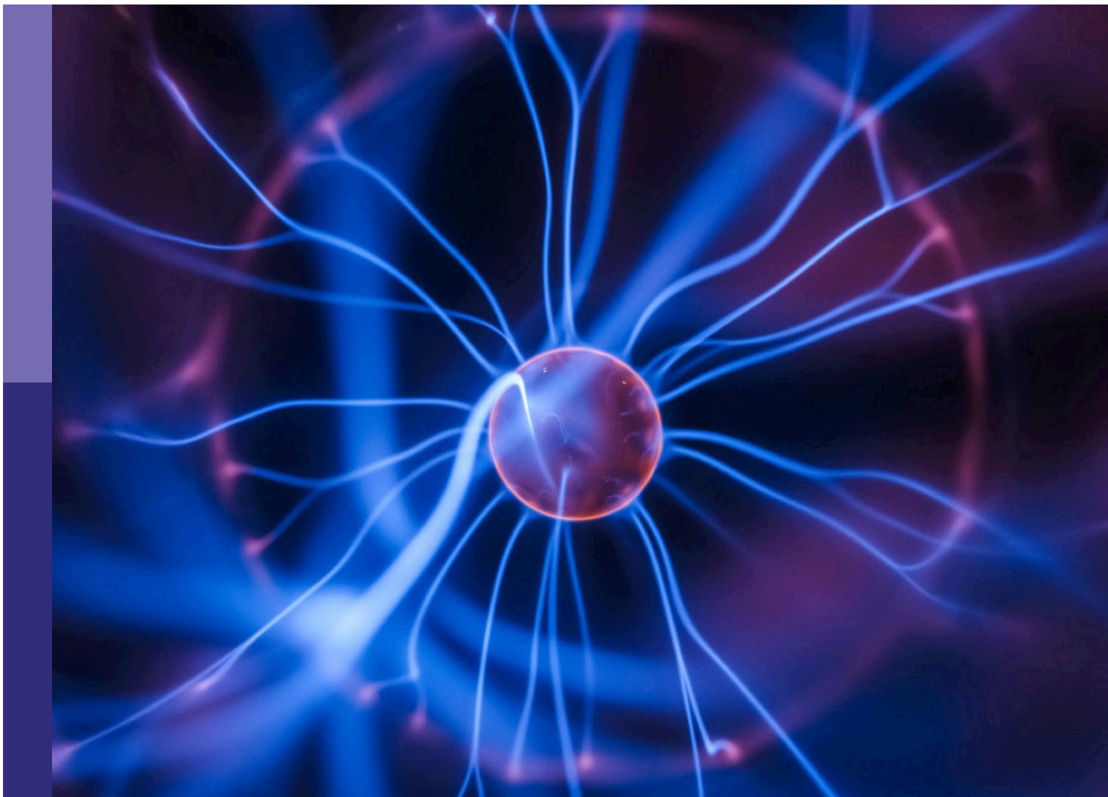

ISSN 1664-8714
ISBN 978-2-83252-082-6
DOI 10.3389/978-2-83252-082-6

## About Frontiers

Frontiers is more than just an open access publisher of scholarly articles: it is a pioneering approach to the world of academia, radically improving the way scholarly research is managed. The grand vision of Frontiers is a world where all people have an equal opportunity to seek, share and generate knowledge. Frontiers provides immediate and permanent online open access to all its publications, but this alone is not enough to realize our grand goals.

## Frontiers journal series

The Frontiers journal series is a multi-tier and interdisciplinary set of open-access, online journals, promising a paradigm shift from the current review, selection and dissemination processes in academic publishing. All Frontiers journals are driven by researchers for researchers; therefore, they constitute a service to the scholarly community. At the same time, the *Frontiers journal series* operates on a revolutionary invention, the tiered publishing system, initially addressing specific communities of scholars, and gradually climbing up to broader public understanding, thus serving the interests of the lay society, too.

## Dedication to quality

Each Frontiers article is a landmark of the highest quality, thanks to genuinely collaborative interactions between authors and review editors, who include some of the world's best academicians. Research must be certified by peers before entering a stream of knowledge that may eventually reach the public - and shape society; therefore, Frontiers only applies the most rigorous and unbiased reviews. Frontiers revolutionizes research publishing by freely delivering the most outstanding research, evaluated with no bias from both the academic and social point of view. By applying the most advanced information technologies, Frontiers is catapulting scholarly publishing into a new generation.

## What are Frontiers Research Topics?

Frontiers Research Topics are very popular trademarks of the *Frontiers journals series*: they are collections of at least ten articles, all centered on a particular subject. With their unique mix of varied contributions from Original Research to Review Articles, Frontiers Research Topics unify the most influential researchers, the latest key findings and historical advances in a hot research area.

Find out more on how to host your own Frontiers Research Topic or contribute to one as an author by contacting the Frontiers editorial office: frontiersin.org/about/contact

# Using high energy density plasmas for nuclear experiments relevant to nuclear astrophysics

**Topic editors**
Maria Gatu Johnson — Massachusetts Institute of Technology, United States
Michael Wiescher — University of Notre Dame, United States
Mark Paris — Theoretical Division, Los Alamos National Laboratory (DOE), United States
Alex Zylstra — Lawrence Livermore National Laboratory (DOE), United States
Gerald Hale — Los Alamos National Laboratory (DOE), United States

**Citation**
Johnson, M. G., Wiescher, M., Paris, M., Zylstra, A., Hale, G., eds. (2023). *Using high energy density plasmas for nuclear experiments relevant to nuclear astrophysics*. Lausanne: Frontiers Media SA. doi: 10.3389/978-2-83252-082-6

# Table of contents

frontiers | Frontiers in Physics

TYPE Editorial
PUBLISHED 20 March 2023
DOI 10.3389/fphy.2023.1180821

# Editorial: Using high energy density plasmas for nuclear experiments relevant to nuclear astrophysics

Maria Gatu Johnson[1]*, Gerald Hale[2], Mark Paris[2], Michael Wiescher[3] and Alex Zylstra[4]

[1]Massachusetts Institute of Technology, Cambridge, MA, United States, [2]Los Alamos National Laboratory (DOE), Los Alamos, NM, United States, [3]Department of Physics and Astronomy, University of Notre Dame, Notre Dame, IN, United States, [4]Lawrence Livermore National Laboratory (DOE), Livermore, CA, United States

OPEN ACCESS

EDITED AND REVIEWED BY
Jie Meng,
Peking University, China

*CORRESPONDENCE
Maria Gatu Johnson,
✉ gatu@psfc.mit.edu

SPECIALTY SECTION
This article was submitted to Nuclear Physics, a section of the journal Frontiers in Physics

RECEIVED 06 March 2023
ACCEPTED 13 March 2023
PUBLISHED 20 March 2023

CITATION
Gatu Johnson M, Hale G, Paris M, Wiescher M and Zylstra A (2023), Editorial: Using high energy density plasmas for nuclear experiments relevant to nuclear astrophysics.
*Front. Phys.* 11:1180821.
doi: 10.3389/fphy.2023.1180821

KEYWORDS

**nuclear astrophysics, nucleosynthesis, plasma screening, high energy density physics (HEDP), national ignition facility (NIF), omega laser facility, short-pulse laser experiments, charged-particle-induced reactions**

Editorial on the Research Topic
Using high energy density plasmas for nuclear experiments relevant to nuclear astrophysics

Thermonuclear reaction rates and nuclear processes have traditionally been explored by means of accelerator experiments, which are difficult to execute at conditions relevant to nucleosynthesis. High energy density (HED) plasmas generated using lasers, such as the inertial confinement fusion (ICF) platform, more closely mimic astrophysical environments in several ways, including with thermal distributions of reacting ions as opposed to mono-energetic ions impinging on a cold target; stellar-relevant plasma temperatures and densities; and neutron flux densities not found anywhere else on earth [1]. The most extreme conditions can currently be achieved at the National Ignition Facility (NIF) laser in the US, where densities of $10^3$ g/cm$^3$ and neutron fluxes up to $5{\cdot}10^{27}$ neutrons/cm/s [2, 3] have been demonstrated over a time period of a few tens of picoseconds. The HED platform is emerging as an interesting complement to accelerator experiments.

This Research Topic explores the potential of this new platform for helping address questions including nuclear rates in plasmas, plasma effects on nuclear reactions, electron screening, and neutron reactions on excited states, with emphasis placed on how accelerator and HED experiments can complement each other to generate answers. For example, Aliotta and Langanke summarize the current understanding of screening effects in stellar environments. They identify an open question in that accelerator measurements suggest a higher screening potential than expected in the adiabatic limit, and discuss how laser facilities hold promise for solving this problem. In particular, accelerator measurements of charged particle-induced reactions are handicapped by the rapidly declining cross section and the uncertainties in the screening. Thomson describes how the high neutron flux environment in ICF plasmas opens up possibilities for second neutron scattering or reactions on excited states at much higher energies than previously possible. To study these unique reaction paths, the lifetimes of the newly accessible excited states must be understood; he uses statistical Hauser-Feshbach decay models to calculate relevant lifetimes.

At large laser facilities such as the NIF and OMEGA [4], stellar-like conditions are achieved by symmetrically illuminating a target using a large number of high-energy laser beams. This leads to compression of the target materials, which subsequently generates a high-density, high-temperature plasma environment. Using deuterium and tritium as fuel in the target, this process can also produce high neutron yields (up to $1{\cdot}10^{18}$ at the NIF) over a short (~100 ps) time window through fusion reactions. The platform has been successfully used for studying rates of low-Z reactions, using the reactants as fuel in the target, as reported in [5–7] and in Mohamed et al. Future directions for this path of research are explored by Casey et al., who lay the foundations for using this platform to study plasma screening including discussion of practical constraints, and Wiescher et al., who examine feasibility of studying three charged-particle-induced reactions involving mid-Z reactants using this platform. Despotopulos et al. review available techniques for adding small amounts of seed nuclei of interest for stellar nucleosynthesis into or in close proximity to the target for exposure to stellar-like conditions or nucleosynthesis-relevant neutron fluxes.

High neutron fluxes in short time periods can also be achieved using high-power, short-pulse lasers based on chirped pulse amplification [8]. This path to stellar-relevant experiments is the subject of two of the papers in this Research Topic, Jiao et al. and Burggraf and Zylstra.

The HED platform comes with its own challenges. Rapid gradients in space and time must be considered. In some cases, thermalization rates may be lower than plasma confinement times, which means standard hydrodynamic and Maxwellian assumptions must be examined. Crilly et al. address these challenges by theoretically investigating impact of hydrodynamic and kinetic effects on S-factors inferred from ICF-type experiments.

The new platform cannot be exploited without state-of-the-art diagnostics [1, 9, 10]. Despotopulos et al. review the radiochemistry diagnostic suite available at the NIF. Mohamed et al. review gamma detection capabilities available at OMEGA and the NIF, and identify a gamma spectrometer as an additional tool that would enable many more experiments. Additional nuclear diagnostics are also available at the various facilities, and should be exploited as research continues (see, e.g., Refs. [11, 12]).

Broad interdisciplinary nuclear, plasma and astrophysical expertise will be required to tap the potential of this new line of research. The intent with this Research Topic is to advertise the platform's capabilities to attract the necessary expertise to this emerging field, and to gather momentum behind the efforts to utilize these new capabilities to answer questions previously impossible to address in terrestrial experiments.

## Author contributions

MGJ, GH, MP, MW, and AZ co-edited the Research Topic. MGJ wrote the editorial text with feedback and input from MW, GH, MP, and AZ.

## Conflict of interest

The authors declare that the research was conducted in the absence of any commercial or financial relationships that could be construed as a potential conflict of interest.

## Publisher's note

## References

1. Cerjan CJ, Bernstein L, Berzak Hopkins L, Bionta RM, Bleuel DL, Caggiano JA, et al. Dynamic high energy density plasma environments at the National Ignition Facility for nuclear science research. *J Phys G: Nucl Part Phys* (2018) 45:033003. doi:10.1088/1361-6471/aa8693

2. Abu-Shawareb H, Acree R, Adams P, Adams J, Addis B, Aden R, et al. Lawson criterion for ignition exceeded in an inertial fusion experiment. *Phys Rev Lett* (2022) 129:075001. doi:10.1103/PhysRevLett.129.075001

3. Zylstra AB, Kritcher AL, Hurricane OA, Callahan DA, Ralph JE, Casey DT, et al. Experimental achievement and signatures of ignition at the national ignition facility. *Phys Rev E* (2022) 106:025202. doi:10.1103/PhysRevE.106.025202

4. Boehly TR, Brown DL, Craxton RS, Keck RL, Knauer JP, Kelly JH, et al. Initial performance results of the OMEGA laser system. *Opt Commun* (1997) 133:495. doi:10.1016/s0030-4018(96)00325-2

5. Casey DT, Sayre DB, Brune CR, Smalyuk VA, Weber CR, Tipton RE, et al. Thermonuclear reactions probed at stellar-core conditions with laser-based inertial-confinement fusion. *Nat Phys* (2017) 13(12):1227. doi:10.1038/nphys4220

6. Zylstra AB, Herrmann HW, Gatu Johnson M, Kim YH, Frenje JA, Hale G, et al. Using inertial fusion implosions to measure the T + 3He fusion cross section at nucleosynthesis-relevant energies. *Phys Rev Lett* (2016) 117:035002. doi:10.1103/PhysRevLett.117.035002

7. Zylstra AB, Herrmann HW, Kim YH, McEvoy A, Frenje JA, Johnson MG, et al. 2H(ρ,γ)3He cross section measurement using high-energy-density plasmas. *Phys Rev C* (2020) 101:042802(R). doi:10.1103/physrevc.101.042802

8. Strickland D, Mourou G. Compression of amplified chirped optical pulses. *Opt Commun* (1985) 56:219. doi:10.1016/0030-4018(85)90120-8

9. Gatu Johnson M, Zylstra AB, Bacher A, Brune CR, Casey DT, Forrest C, et al. Development of an inertial confinement fusion platform to study charged-particle-producing nuclear reactions relevant to nuclear astrophysics. *Phys Plasmas* (2017) 24:041407. doi:10.1063/1.4979186

10. Gatu Johnson M, Casey DT, Hohenberger M, Zylstra AB, Bacher A, Brune CR, et al. Optimization of a high-yield, low-areal-density fusion product source at the National Ignition Facility with applications in nucleosynthesis experiments. *Phys Plasmas* (2018) 25:056303. doi:10.1063/1.5017746

11. Moore AS, Schlossberg DJ, Appelbe BD, Chandler GA, Crilly AJ, Eckart MJ, et al. Neutron time of flight (nToF) detectors for inertial fusion experiments. *Rev Sci Instrum* (2023).

12. Gatu Johnson M. Charged particle diagnostics for inertial confinement fusion and high-energy-density physics experiments. *Rev Sci Instrum* (2023) 94:021104. doi:10.1063/5.0127438

frontiers | Frontiers in Physics

MINI REVIEW
published: 06 July 2022
doi: 10.3389/fphy.2022.942726

# Screening Effects in Stars and in the Laboratory

*Marialuisa Aliotta*[1]* *and Karlheinz Langanke*[2,3]

[1]*School of Physics and Astronomy, University of Edinburgh, Edinburgh, United Kingdom,* [2]*GSI Helmholtzzentrum für Schwerionenforschung, Darmstadt, Germany,* [3]*Theoriezentrum, Institut für Kernphysik, TU Darmstadt, Darmstadt, Germany*

Nuclear reactions are the driver of the evolution of many astrophysical objects. In the astrophysical environment their respective reaction rates are, however, modified due to the presence of other charges. The effects depend on the relative importance of Coulomb energy versus thermal energy and are distinguished between weak and strong screening. In the extreme case of pycnonuclear reactions, fusion reactions can be induced by the zero-point motion of nuclei in a Coulomb crystal. This paper reviews the various screening situations and discusses important applications. We also briefly review laboratory approaches to study screening effects.

**Keywords: electron screening, stellar plasma, stellar burning, nucleosynthesis, pycno-nuclear reactions**

***Edited by:***
*Maria Gatu Johnson,*
*Massachusetts Institute of Technology, United States*

***Reviewed by:***
*Carlos Bertulani,*
*Texas A&M University-Commerce, United States*
*Carl Brune,*
*Ohio University, United States*

***Correspondence:**
*Marialuisa Aliotta*
*m.aliotta@ed.ac.uk*

***Specialty section:***
*This article was submitted to Nuclear Physics, a section of the journal Frontiers in Physics*

***Received:*** *12 May 2022*
***Accepted:*** *06 June 2022*
***Published:*** *06 July 2022*

***Citation:***
*Aliotta M and Langanke K (2022) Screening Effects in Stars and in the Laboratory.*
*Front. Phys. 10:942726.*
*doi: 10.3389/fphy.2022.942726*

## 1 INTRODUCTION

Willy Fowler liked to tease his colleagues by calling astrophysics and astronomy applied nuclear physics. With this witty remark he pointed to the fact that the dynamics, and hence the evolution, of many astrophysical objects is driven by nuclear reactions of charged nuclei, in this way also producing the elements in the Universe. During their long lives in hydrostatic equilibrium stars generate the necessary energy by fusing nuclei in their interior. When the nuclear energy source finally ceases, massive stars collapse under their own gravity resulting in a supernova explosion which finally liberates the produced elements to make them available for the next generation of stars or as the building blocks of life on Earth-like planets. During the collapse, it is nuclear reactions mediated by the weak interaction which fight against gravity [1]. Nuclear reactions are also essential to trigger thermonuclear supernovae where carbon burning is ignited as a runaway in a White Dwarf in a binary system [2].

In astrophysical environments, nuclear reactions take place in the presence of other charges that impact the rates at which such reactions occur. The conditions of density and temperature defining the stellar environment are usually such that atoms are fully ionized and hence the surrounding exists as a plasma made of nuclei of different kinds and charges, and of electrons. However, there are also important situations where atoms are only partially ionized, as is the case for heavier nuclei in the solar interior.

The effect of the surrounding charges on the reactions depend on the competition between Coulomb and thermal energies, which for a one-component plasma is defined by the parameter

$$\Gamma = \frac{(Ze)^2}{akT} \tag{1}$$

where $k$ is the Boltzmann constant, $T$ the temperature, $Ze$ the charge of the nucleus and $a$ an appropriate distance between the interacting nuclei. If $\Gamma \ll 1$, one speaks of a "weak screening regime" which is realized at high temperatures and/or low densities. In contrast, for high densities, i.e., $\Gamma \gg 1$, one encounters the "strong screening regime", if the most effective energy for nuclear

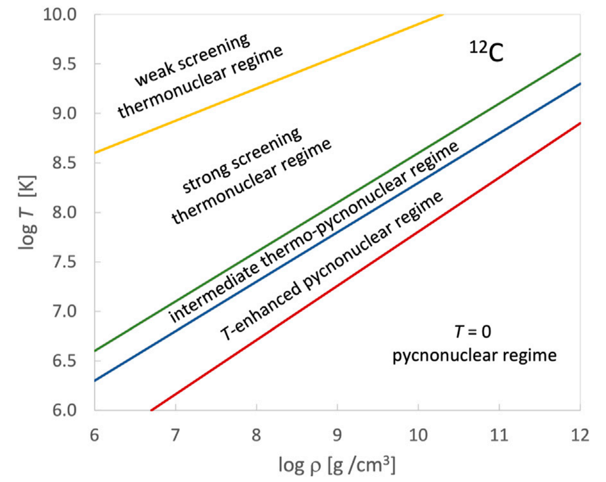

**FIGURE 1 |** Temperature-density diagram covering the various screening regimes for $^{12}$C matter. The diagram follows the definition by Salpeter [4] and subsequent work by Gasques et al. [5] (for the definition and treatment of screening in the intermediate thermo-pycnonuclear and *T*-enhanced pycnonuclear regimes the reader is referred to [5]).

reactions (Gamow peak energy) is sufficiently larger than the thermal energy, or the "pycnonuclear regime", where, even at $T = 0$ K, fusion reactions are induced by density fluctuations. In between weak and strong regimes, one has a plasma with intermediate screening ($\Gamma \approx 1$). The weak screening limit applies during stellar hydrostatic burning, while the ignition of the nuclear runaway in a type Ia supernova falls into the strong screening regime. Pyconuclear reactions, instead, are mainly important for the crust evolution of neutron stars [3]. While screening regimes are not strictly defined, **Figure 1** sketches, as an example, the ranges of temperature and densities relevant to different screening in $^{12}$C matter.

Here, we review screening effects of nuclear reactions in these interesting and important astrophysical scenarios, and briefly discuss the extreme case where reactions are initiated by density fluctuations rather than by the thermal motion of the reaction partners. While we mainly focus on nuclear fusion reactions, screening is also relevant for processes mediated by the weak interaction, such as beta decay and electron capture. Important examples are the electron captures on $^7$Be during solar hydrogen burning and generally on nuclei during core-collapse of massive stars leading to a type II supernova. While most of the work related to screening has been based on progress in modelling, recent years witnessed also advances in experimental approaches to study screening effects in laboratory plasmas made possible by laser facilities, and in measurements of low-energy nuclear reactions. In the latter case the experimentally observed effects are somewhat larger than theoretically predicted.

## 2 STELLAR FUSION REACTIONS

Nuclear fusion reactions in stars occur at thermal energies *E* well below the Coulomb barrier between interacting nuclei. Thus the energy dependence of the fusion cross section $\sigma(E)$ is dominated by the tunnel probability and is usually written as [6]:

$$\sigma(E) = \frac{S(E)}{E} \exp\left[-2\pi\eta(E)\right] \tag{2}$$

Here, $\eta = Z_1 Z_2 e^2/\hbar v$ is the Sommerfeld parameter and v the relative velocity. The astrophysical S-factor $S(E)$ accounts for nuclear effects and is a function usually mildly varying with energy. The astrophysical fusion rate is then given by folding the energy- (i.e. velocity-) dependent cross section with the stellar velocity distribution of the reaction partners, which is usually given by a Boltzmann distribution [6]. The product of the Boltzmann distribution and the tunnel probability has a pronounced peak at an energy (the Gamow peak energy) where the reaction occurs most effectively. The Gamow peak energy is noticeably larger than the thermal energy, but significantly smaller than the Coulomb barrier [6].

However, in the astrophysical environment the fusion reactions occur in the presence of other charges which modify the Coulomb barrier and hence have an impact on the astrophysical fusion rates. Starting with the pioneering work of Salpeter [4, 7], it has been customary and often possible to describe these screening effects by an enhancement factor $F_{sc}$ which multiplies the bare nuclear reaction rate, yielding a screened rate:

$$R_{sc} = F_{sc} R_{bare} \tag{3}$$

While $R_{bare}$ depends on the temperature via the Boltzmann distribution, the enhancement factor is also a function of plasma properties such as density, temperature, degeneracy and composition. The factorization of **Eq. (3)** allows to treat the problem as two distinct parts and is a very efficient way to incorporate the screening effects into astrophysical simulations. The screening factor $F_{sc}$ is customarily given in the form of an exponential function for weak and strong screening as discussed below.

In the weak screening case, in which the average interaction energy between the reaction partners is much smaller than their kinetic energy, the nuclei are surrounded by a screening cloud, such that they are attracted by the electrons and repelled by the nuclei in the partner's cloud. Due to the effect of the screening clouds, the reaction partners with charges $Z_1$, $Z_2$ feel a screened Coulomb potential

$$U_{sc}(r) = \frac{Z_1 Z_2 e^2}{r} \exp\left(-r/R_D\right) \tag{4}$$

rather than the Coulomb repulsion of bare nuclei, $U_b(r) = Z_1 Z_2 e^2/r$, where the parameter $R_D$ (Debye length) is given by $\zeta R_D = (\frac{kT}{4\pi\alpha\rho})^{1/2}$ with the fine-structure constant $\alpha$ and the number density of nucleons $\rho$ [8]. The parameter $\zeta$ depends on the composition of the plasma and its degree of degeneracy [4, 8]. Salpeter's model of weak screening is equivalent to the Debye-Hückel theory of dilute solutions of electrolytes [9].

The tunnel process occurs at radii which are significantly smaller than the Debye radius. Thus, the exponential in the screened Coulomb potential (**Eq. (4)**) can be expanded to first order, $\exp(-r/R_D) \approx 1 - r/R_D \ldots$. Hence, the effect of screening is a reduction of the Coulomb barrier by a constant screening energy $U_{sc} = (Z_1 Z_2 e^2)/R_D$. Equivalently, the partners in the plasma fuse with a slightly increased energy $(E + U_{sc})$ and the enhancement factor in **Eq. (3)** reduces to $F_{sc} = \exp(-U_{sc}/kT)$.

The screening enhancement factors are incorporated in the stellar evolution codes. For the solar plasma, the Debye radius is of the order $10^{-11}$ m and the screening enhancement of nuclear reactions at the relevant solar energies is relatively small, about 5% for the important proton-proton reaction [10]. Special care has to be taken for resonances as the modification of the Coulomb potential lowers the resonance energy compared to the reaction threshold. Hence, the resonance lifetime is increased due to screening. If screening is sufficiently strong, the resonance might get bound in the astrophysical environment; we will mention an example below. The theory for resonant screening has been discussed for example in Ref. [11].

The Debye-Hückel theory of screening, as adopted by Salpeter, is based on a mean-field approach. Hence, it depends on the distance between the reaction partners, but not on their velocity. It has been argued that such a static approach would not be appropriate for the solar plasma [12]. In fact, studies of dynamical screening performed within the molecular dynamics approach for a proton plasma [13–15] indicate that fast moving protons which might not be accompanied by their full screening cloud [15] experience less screening than slow moving ones. These studies suggest that the static screening overestimates the enhancement of nuclear reactions in stellar plasmas, as fast moving particles with energies around the Gamow peak dominate the reaction rates. This view has, however, been disputed by Bahcall and collaborators who argued that Salpeter's screening approach is valid also at the Gamow peak energy due to the nearly perfect thermodynamic equilibrium present in the solar plasma [16].

At high densities, where $\Gamma \gg 1$, the bulk of the nuclei form a lattice (or quantum fluid). If the Gamow peak energy is significantly larger than the thermal energy, the main contribution to the reaction rate will come from fusing nuclei with energies around the Gamow peak. Again, Salpeter laid out the basis for the treatment of this situation of "strong screening" [4]. He showed that electrons can be treated as a uniform background and derived an enhancement factor assuming that the fusing nuclei move while being surrounded by a uniform cloud of electrons that neutralise the nuclear charge. In this approximation, the enhancement factor can again be written as $F_{sc} = \exp(-U_{sc}/kT)$ and the screening energy $U_{sc}$ is given by the difference of electrostatic energies between the fused system with combined $(Z_1 + Z_2)$ charge and that of the two individual nuclei with charges $Z_1$ and $Z_2$.

An improved treatment of strong screening is obtained by determining the pair correlation function $g(r)$ which is a measure for the probability for a given nucleus to find a reaction partner at distance $r$ in the plasma. (In multicomponent plasmas $g$ carries indices defining the partners.) The calculation of $g(r)$ is identical to determining the mean potential of the plasma $w(r)$, with $g(r) = \exp(-w(r)/kT)$.

Defining $g$ and $g_0$ as the pair correlation functions with and without screening, the enhancement factor can be approximated as $F_{sc} = g(0)/g_0(0)$, where one considers that the ratio is quite insensitive to $r$ at nuclear distances. The enhancement factor is usually split into a "classical" and a "quantum" part [17, 18], $F_{sc} = \exp(h_0 + h_1)$. The classical part is approximately related to the difference of free energies $\Delta F$ for the many-body system before and after the fusion reaction [19], leading to $\exp(h_0) = \exp(\Delta F/kT)$. The parameter $h_0$ can also be calculated using Monte Carlo techniques. A parametrized form of $h_0$ as a function of the Coulomb coupling parameter $\Gamma$ and valid for $1 < \Gamma < 170$ is given in [20]. The quantum contribution $\exp(h_1)$ considers that the potential is not constant during the tunnel process. It has been calculated in different approximate ways (by path integrals [21], within the WKB approach [22, 23], and directly by Monte Carlo techniques [24, 25]) and found to be small compared to the classical contribution.

An important astrophysical application of strong screening occurs for carbon fusion reactions which are believed to trigger type Ia supernovae in degenerate White Dwarfs in the so-called single-degenerate scenario [2]. Under these degenerate conditions carbon burning occurs as a thermonuclear runaway where the reaction rate is enhanced by many orders of magnitude due to screening effects. The different approximations to the quantum effects lead to noticeable differences in the enhancement factors, which, however, are small compared to the total enhancement. Hence the differences are not expected to be too relevant [5]. A convenient parametrization for the screening of the carbon fusion rate can be found in [5].

At high densities and sufficiently low temperatures the nuclei settle into a Coulombic lattice, for which usually a body-centred-cubic (*bcc*) structure is assumed [26]. At very high densities the lattice is destroyed due to the zero-point motion of the nuclei and the system rather becomes a quantum fluid. However, due to its strong dependence on charge, this transition occurs at such high densities that it is usually irrelevant for astrophysical purposes [27]. An exception is $^4$He, as we will see below. The energy scale of the zero-point motion can be estimated by the ion plasma frequency [7] and allows to tunnel the Coulomb barrier, which is significantly modified due to the interaction with other ions and the neutralising electron background. Such density-induced reactions are called pycnonuclear reactions [7] and they are the reason why no Coulomb crystal exists at arbitrarily large densities.

The pyconuclear reaction rate $R_{pyc}$ for a one-component crystal can be expressed (in $s^{-1}cm^{-3}$) as [5]:

$$R_{pyc} = \rho X_i A Z^4 S(E_{pk}) C_{pyc} 10^{46} \lambda^{3-C_{pl}} \exp\left(-C_{exp} \big/ \sqrt{\lambda}\right) \quad (5)$$

where $\rho$ is the density in g/cm$^3$, $X_i$, $A$, $Z$ are the mass fraction, mass number and charge of the fusing nuclei and the astrophysical S-factor $S$ is evaluated at the energy $E_{pk}$ of the plasma frequency (see [5] for details). Above (below) the neutron drip density at $4 \times 10^{11}$ g/cm$^3$, $X_i < 1$ $(X_i = 1)$ due to the presence of free neutrons. The parameter $\lambda$ is defined as $\lambda = \frac{\hbar^2}{mZ^2e^2}(n_i/2)^{1/3}$ with nucleon mass $m$ and number density $n_i$. The three parameters ($C_{pyc}$, $C_{pl}$, $C_{exp}$) in **Eq. (5)** have to be calculated using a model for the tunnel process. Various values are presented in [7, 24, 27].

Beyond the static approximation to the rate given in **Eq. (5)**, effects related to the polarization of the surrounding Coulomb lattice were discussed by Schramm and Koonin [27]. They found that these dynamical effects, which are non-negligible per se, cancel each other. It is estimated that pycnonuclear reaction rates can be uncertain by a few orders of magnitude [26].

Pycnonuclear reactions play a role in the structure of isolated neutron stars which accrete matter from the interstellar medium [28]. Due to the accretion, the original matter of the neutron star crust is successively pushed to higher densities and hence undergoes a series of double electron captures which make the matter more neutron-rich. These captures produce free neutrons above the neutron drip density, until the system finally reaches densities at which nuclei become able to fuse by pycnonuclear reactions. In the pioneering work of [3, 29], where the original composition of the crust was assumed to consist purely of $^{56}$Fe, pycnonuclear fusion is expected to occur for $^{34}$Ne nuclei at densities slightly exceeding $10^{12}$ g/cm$^3$. Dynamical studies of the neutron star crust evolution encompassing a large reaction network are presented in [30]. These authors also find that the uncertainty in the pyconuclear reaction rates have only a modest effect on the crust evolution.

Special care has to be taken for $^4$He matter at high densities. Of particular interest is the triple-alpha rate, by which $^4$He is transformed into $^{12}$C. During helium burning in normal stars, temperatures are sufficiently high that the process occurs in two steps via the formation of an intermediate $^8$Be resonance (the ground state) at 92.2 keV above the $\alpha + \alpha$ threshold [31]. In Wolf-Rayet stars, temperatures are lower and the triple-alpha reaction is enabled via the low-energy wing of the $^8$Be resonance [32, 33]. Finally, in accreting neutron stars, temperatures might be so low that the triple-alpha process occurs via pycnonuclear fusion [34]. At the relevant densities ($\rho > 3 \times 10^8$ g/cm$^3$), zero-point motion transforms $^4$He matter into a quantum fluid. Under these conditions, the triple-alpha fusion rate was calculated in [35]. However, because of the low energy of the $^8$Be resonance, the nuclear $\alpha$-$\alpha$ potential must also be included in addition to the Coulomb interaction. As it was pointed out in [36], screening in $^4$He matter becomes strong enough around $3 \times 10^9$ g/cm$^3$ to transform it to bound $^8$Be matter. This phase transition was confirmed in a study which described the $^4$He quantum fluid within the hypernetted chain approach taking higher-order correlations into account [37]. The study also showed that these correlations are strong enough to transform $^4$He matter into $^{12}$C at densities lower than the critical density for the phase transition to $^8$Be matter. The latter is then probably not realised in nature.

For screening effects of very strong magnetic fields on thermonuclear reactions the reader is referred to Refs. [38, 39] and references therein.

## 3 REACTION MEDIATED BY THE WEAK INTERACTION

Although reactions mediated by the weak force are usually slower than competing time scales, they can be significantly altered by their astrophysical surroundings often with interesting consequences. For example, temperature can change the effective half lives of nuclei due to thermal population of excited nuclear states. In s-process nucleosynthesis this occurs at certain branching points making the rates for beta decays and neutron captures competitive. As a consequence, the matter flow branches at these nuclei allowing to determine the neutron density or the temperature of the astrophysical environment from the observed abundances [40, 41]. An extreme change in half life occurs for $^{180}$Ta where a long-lived excited state with half live comparable to the age of the Universe is thermally mixed with the ground state which lives only a few hours [42, 43]. Other than by s-process nucleosynthesis [44, 45], $^{180}$Ta can also be made by neutrino nucleosynthesis [46–48]. Finite-temperature effects also modify inelastic neutrino-nucleus cross sections, in particular at low and modest neutrino energies [49]. Inelastic neutrino scattering off nuclei had been discussed as a potential source for thermalization of neutrinos with matter during the collapse of massive stars [50, 51], but turns out to be rather unimportant [52].

The plasma density has important effects also on beta decays, as the presence of electrons blocks final states for the decay. This Pauli blocking effect at finite density reduces the rate and has to be accounted for in the derivation of stellar beta decay rates [53, 54]. As a consequence of this reduction, beta decays are basically prohibited during final collapse of a massive star, but play an interesting role during silicon burning where beta decay and

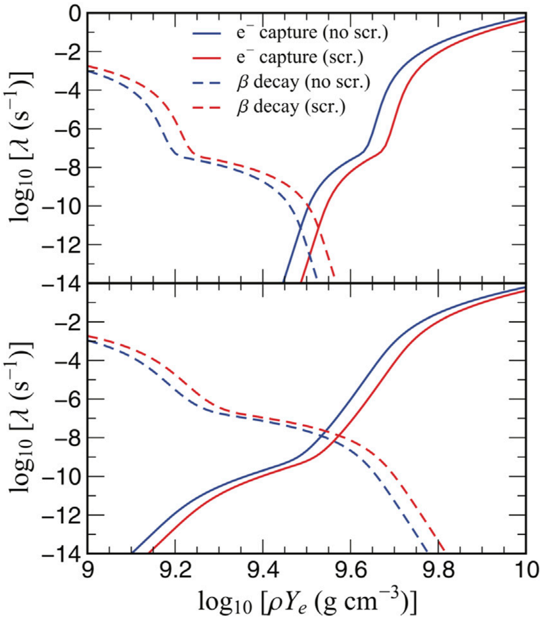

**FIGURE 2 |** Rates for electron capture on $^{20}$Ne (solid) and beta decay (dashed) of $^{20}$F for densities typical for a collapsing NeMg core of an intermediate mass star and two relevant temperatures ($T = 4 \times 10^8$ K (top) and $10^9$ K (bottom)). The rates have been calculated with and without screening corrections (red and blue lines, respectively). Due to screening, the densities at which both rates become identical are shifted to higher values. Figure reprinted with permission from [61].

electron capture rates are comparable and contribute significantly to the cooling of the stellar core without changing the electron-to-nucleon ratio [55]. The blocking of beta decays allows the collapsing core to get successively more neutron-rich by continuous electron captures on nuclei [1, 56, 57]. These electron captures accelerate the collapse as they reduce both the pressure of the relativistic electron gas and the entropy of the core matter. The latter effect is responsible for the fact that nuclei survive the collapse. Coulomb corrections are important for the thermodynamic properties of the high density plasma [58], but they also modify the weak interaction rates [59]. Screening contributes to these rates in two different ways. First, it changes the threshold energy between initial and final states. Second, the electron energy is reduced by the presence of the background compared to the unscreened case. Refs. [60, 61] present a formalism on how screening corrections can be incorporated into the stellar electron capture and beta decay rates. In general, electron capture rates are slightly reduced due to screening, while beta decay rates are enhanced [61], as shown in **Figure 2**.

This result has important consequences for the URCA process which is essential for the cooling of NeMg cores in the final evolutionary stages of intermediate mass stars as it shifts the operation of the URCA process to higher densities [61–63]. Significant experimental and theoretical progress in determining stellar weak interaction rates has recently been reviewed in [64].

Electron captures on selected nuclei occur also during hydrostatic stellar burning. At such conditions screening cannot be treated as caused by a degenerate relativistic electron gas like during core collapse, but rather as due to an ideal electromagnetic plasma. A particularly interesting and important case is the electron capture on $^7$Be which, in competition with proton capture, determines the rate of high-energy neutrinos produced in the Sun. In the laboratory the half life of $^7$Be is about 53 days. As the electron density at the nucleus in the solar plasma is reduced compared to the atomic case, the half life is longer in the Sun. Under solar conditions, $^7$Be has a non-negligible probability, which also depends on screening effects, of having a bound K-shell electron. Therefore, a consistent treatment of $^7$Be ions embedded in the solar surroundings is required. Such studies have been performed on the basis of two quite distinct methods, a mean-field approach [65] and a density matrix formalism [66], yielding, however, nearly identical results for the solar $^7$Be half life (about 81 days).

## 4 EXPERIMENTAL APPROACHES TO STUDY SCREENING EFFECTS

The strategy to determine nuclear reaction rates for astrophysical applications is a two-step process: at first one derives the cross section (astrophysical S-factor) for bare nuclei, which is then modified to account for environmental effects. The measurement of the bare cross section is, however, an experimental challenge, as the astrophysically most important energy region (around the Gamow peak energy) lies far below the Coulomb barrier, where the cross sections are extremely small and their direct measurement in the laboratory is difficult with presently available techniques. Therefore, one measures the cross sections down to energies as low as possible and then extrapolates the data to the relevant energy region. It was generally believed that the uncertainty in the extrapolation procedure could be reduced by steadily lowering the energies at which data are taken in the laboratory. This approach, however, might be problematic as at very low energies the experimentally measured cross section does not represent the required case for bare nuclei: the cross section is enhanced due to screening effects connected with the electrons present in the target (and possibly in the projectile) [67].

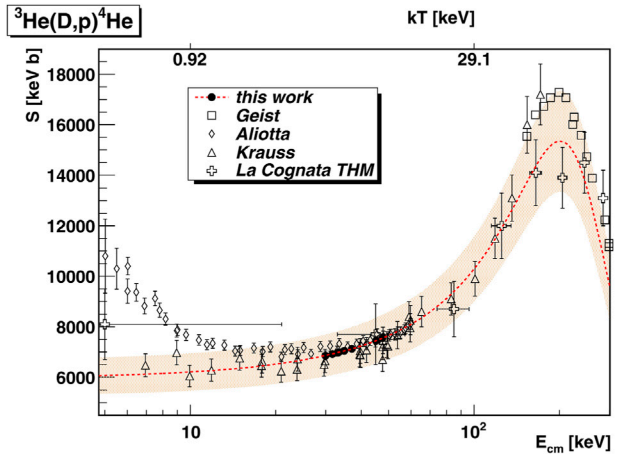

**FIGURE 3 |** Low-energy S-factor for the d ($^3$He,p)$^4$He reaction, obtained by accelerator experiments [68, 70, 71] and high-power laser measurements ("this work" from [72]). The crosses represent results obtained with the Trojan-Horse Method (THM) [73]. The dashed curve shows the bare nuclear S-factor obtained from a fit to the data at higher energies. The exponential enhancement in the S-factor at low energies, observed in the data by Aliotta et al. [70], is attributed to screening effects. Figure reprinted with permission from [72].

The $^3$He (d,p)$^4$He reaction is probably the best studied case for the experimental observation of laboratory screening, as the available low-energy data [68–71, 73] are the most definitive in this case.

In the laboratory the cross section was measured by shooting an ion beam of (bare) deuterons onto an atomic $^3$He gas (with two electrons per atom). At the lowest accessible energies, the separation of target and projectile during tunnelling is much smaller than the atomic radius; thus, the two electrons, originally bound to $^3$He, are now attracted by the joint charge of projectile and target, corresponding to $^5$Li. The gain in electronic binding energy (about $\Delta E \simeq 120$ eV) between the fused $^5$Li and the well-separated (d+$^3$He) systems should be transferred to the relative motion so that the fusion process occurs with a slightly enhanced energy compared to the case of bare nuclei. Analogue to **Eq. (3)** the measured cross section should be increased by an exponential factor which can be expresses as $f_{sc} \approx \exp\,(\pi\eta(E)\Delta E/E)$, considering that $\Delta E$ is much smaller than the relative energy $E$

of the fusing nuclei [67]. Such an exponential enhancement is indeed experimentally observed [69, 70], as shown in **Figure 3**. However, the screening energy $U_{\mathrm{sc}}$ obtained by fitting the data to the exponential parametrization for $f_{\mathrm{sc}}$ is larger than the adiabatic limit $\Delta E$, i.e. the difference in binding energies. Yet, the applicability of the adiabatic limit was confirmed within a Time Dependent Hartree-Fock (TDHF) calculation of the electron dynamics in the fusion reaction [74]. In addition, a noticeably smaller experimental screening energy was observed in an experiment performed in inverse kinematics using a molecular deuteron target [75]. A TDHF study of screening effects for proton scattering on a molecular hydrogen target shows a strong sensitivity of the enhancement factor to the orientation of the molecule [76]. It is smaller if the proton has to pass the spectator nucleus before the fusion process occurs. No isotopic dependence of the screening effect has been found, as expected [77, 78]. The use of possibly incorrect stopping powers, which the fusion energies have to be corrected for, has also been suggested in [79] as a possible solution of the difference between experimental results and adiabatic limit. Indeed, theoretical calculations [80, 81] of stopping power for the same systems mentioned above using dynamic calculations do not agree with extrapolations to lower energies, thus corroborating the findings in [79].

Differences between experimental and adiabatic screening energies have been found also for other nuclear reactions [82]. In some cases, clustering configurations (e.g., $d \oplus \alpha$ in $^6$Li) in the interacting nuclei could potentially explain the large screening potentials observed experimentally, as suggested in [83].

In general, an obvious source of uncertainty are the bare nuclear cross sections required to determine the experimental screening value. To eliminate this uncertainty experimental approaches like the Trojan Horse Method (THM) [84, 85] have been developed, which allow for an indirect determination of the bare nuclear cross sections also at very low energies. **Figure 3** includes bare nuclear cross sections obtained via the THM [73] that are consistent with the extrapolation of the cross sections from higher energies. The S-factor has also been determined by an experiment where a molecular deuteron target was bombarded with intense and ultrafast laser pulses [72]. The discrepancy between observed and expected screening enhancement for gaseous targets is still not explained.

Large screening enhancements were also found for the low-energy d + d fusion reaction in deuterated metals [86–88]. Here the low-energy S-factor shows an exponential enhancement, but the deduced screening energy for metals can exceed the value obtained for a gas-target experiment by more than an order of magnitude [88, 89]. Importantly, if the deuterons are implanted into semiconductor or insulator materials, the screening energy is consistent with the gas-target result. This observation led to the proposal that the classical Debye theory might be applicable to describe the screening enhancement in metals [90]. The Debye model predicts a characteristic temperature dependence of the screening proportional to $T^{1/2}$ which was tentatively observed in [91]. Considering the ion-momentum distribution and inhomogeneous screening effects beyond the Debye model reduced the gap between prediction and observation [92, 93]. The Debye model was, however, questioned in [89]. These authors argued that the screening in deuterated metals requires a dynamical treatment of the deuteron density which indeed reproduced the dependence of the screening energy on the charge of the host material. But also this improved model predicts screening energies which are about a factor of 2 smaller than the observed values [89, 94]. A quantum-mechanical model for the screening effects was presented in [95], but has not yet been fully applied due to computer limitations.

The unresolved discrepancy between theoretical and experimental screening energies for atomic or molecular targets is an obstacle to reducing existing uncertainties for nuclear reactions with light ions. The problem would, of course, become obsolete if it was possible to measure the relevant cross sections directly for the appropriate astrophysical plasmas. At least for interactions between light ions in the Sun, in early stellar burning stages, or in Big Bang nucleosynthesis, this perspective becomes possible using high-intensity lasers. For example, a measurement of the low-energy d($^3$He,p)$^4$He S-factor is included in **Figure 3** [72]. Other laser-induced measurements of astrophysical S-factors dealt with the d(p,$\gamma$)$^3$He [96] and the t+$^3$He [97] reactions, both of interest for Big Bang nucleosynthesis. These pioneering works were, however, performed under plasma conditions at which screening is expected to be negligible. Such dedicated studies of plasma screening effects are envisioned for future laser facilities, including the Extreme Light Infrastructure ELI-NP under construction in Bucharest [98] making use of two laser-induced colliding plasmas [99]. An alternative approach, i.e. to measure directly the bare reaction cross section, exploits a unique combination of experimental devices at the CRYRING storage ring at GSI. Here, a stored beam of ions can be made to collide with a transverse beam and the reaction products be detected with a newly developed detection array [100]. If successful, such measurements have the potential for significant breakthroughs in our understanding of the electron screening effect.

## 5 CONCLUSION

In astrophysical environments nuclear reactions are affected by the presence of other charges in the stellar plasma. Starting with the pioneering work of Salpeter [4, 7] such effects have been included in astrophysical simulations taking also into account that the relative importance of Coulomb versus thermal energy, defined by the Coulomb plasma parameter $\Gamma$, requires different screening treatments under different physical conditions. The progress of these treatments is mainly theoretical. In the case of weak screening, as it applies for example to the solar plasma, the enhancement of the fusion reactions is quite small (typically, a few percent) and appears not to be a considerable source of uncertainty [8]. Similar conclusions also apply to the electron capture reaction on $^7$Be, which has drawn specific attention in [101]. The uncertainty in the enhancement factors for the strong screening case and in particular in the pyconuclear regime remains noticeably larger.

Experimental approaches to screening are so far restricted to studies of light-ion fusion reactions where (at the lowest energies reachable in accelerator experiments) the presence of electrons in the nuclear target (and possibly also in the projectile) screens the Coulomb barrier, effectively enhancing the relative energy of the collision partners during the tunnel process. The energy shift obtained from experimental data is often larger than the value expected if the collision proceeds adiabatically. This discrepancy is not yet fully understood and introduces some uncertainty into the determination of astrophysical cross sections for light ion reactions. For heavier nuclei the energies reachable in accelerator experiments are too high for screening effects to be relevant. In the future it might be possible to circumvent this uncertainty source by measuring the relevant cross sections directly in a laser-induced plasma.

## AUTHOR CONTRIBUTIONS

MA and KL have contributed, respectively, to some of the experimental and theoretical results presented in this review and have co-written the manuscript.

## FUNDING

MA acknowledges funding from the UK Science and Technology Facilities Council (Grant ST/V001051/1).

## ACKNOWLEDGMENTS

The authors have benefited from the collaborations and discussions with many colleagues. In particular, they like to thank Claus Rolfs with whom they had the pleasure to collaborate and to learn from for many years. For the purpose of open access, the authors have applied a Creative Commons Attribution (CC BY) licence to any Author Accepted Manuscript version arising from this submission.

## REFERENCES

1. Bethe HA. Supernova Mechanisms. *Rev Mod Phys* (1990) 62:801–66. doi:10.1103/revmodphys.62.801
2. Hillebrandt W, Kromer M, Röpke FK, Ruiter AJ. Towards an Understanding of Type Ia Supernovae from a Synthesis of Theory and Observations. *Front Phys* (2013) 8:116–43. doi:10.1007/s11467-013-0303-2
3. Haensel P, Zdunik JL. Equation of State and Structure of the Crust of an Accreting Neutron star. *Astron Astrophys* (1990) 229:117.
4. Salpeter E. Electron Screening and Thermonuclear Reactions. *Aust J Phys* (1954) 7:373. doi:10.1071/ph540373
5. Gasques LR. Nuclear Fusion in Dense Matter: Reaction Rate and Carbon Burning. *Phys Rev* (2005) C72:025806.
6. Burbidge EM, Burbidge GR, Fowler WA, Hoyle F. Synthesis of the Elements in Stars. *Rev Mod Phys* (1957) 29:547–650. doi:10.1103/revmodphys.29.547
7. Salpeter EE, Van Horn HM. Nuclear Reaction Rates at High Densities. *Astrophysical J* (1969) 155:183. doi:10.1086/149858
8. Adelberger EG, García A, Robertson RGH, Snover KA, Balantekin AB, Heeger K, et al. Solar fusion cross sections. II. The *pp* chain and CNO cycles. *Rev Mod Phys* (2011) 83:195. doi:10.1103/RevModPhys.83.195
9. Debye P, Hückel E. *Z Phys* (1923) 24:305.
10. Ichimaru S. Nuclear fusion in dense plasmas. *Rev Mod Phys* (1993) 65:255. doi:10.1103/RevModPhys.65.255
11. Zinner NT. Alpha decay rate enhancement in metals: An unlikely scenario. *Nucl Phys A* (2007) 781:81–7. doi:10.1016/j.nuclphysa.2006.10.071
12. Carraro C, Schäfer A, Koonin SE. Dynamic screening of thermonuclear reactions. *Astrophysical J* (1988) 331:565. doi:10.1086/166582
13. Shaviv NJ, Shaviv G. The Electrostatic Screening of Thermonuclear Reactions in Astrophysical Plasmas. I. *Astrophysical J* (1996) 468:433. doi:10.1086/177702
14. Shaviv NJ, Shaviv G. The Electrostatic Screening of Nuclear Reactions in the Sun. *Astrophysical J* (2001) 558:925–42. doi:10.1086/322273
15. Mao D, Mussack K, Däppen W. Dynamic Screening in Solar Plasma. *Astrophysical J* (2009) 701:1204–8. doi:10.1088/0004-637x/701/2/1204
16. Bahcall JN, Brown LS, Gruzinov A, Sawyer RF. The Salpeter plasma corrections for solar fusion reactions. *A&A* (2002) 388:660. doi:10.1051/0004-6361:20020462
17. Jancovici B. Pair correlation function in a dense plasma and pycnonuclear reactions in stars. *J Stat Phys* (1977) 17:357–70. doi:10.1007/bf01014403
18. Schatzman E. On the Rate of Pycno-nuclear Reactions. *Astron Astrophys* (1978) 65:L17.
19. DeWitt HE, Graboske HC, Cooper MS. Screening Factors for Nuclear Reactions. General Theory. *Astrophysical J* (1973) 181:439. doi:10.1086/152061
20. DeWitt HE, Slattery W. *Contrib Plasma Phys* (1999) 43:279.
21. Alastuey A, Jancovici B. Nuclear reaction rate enhancement in dense stellar matter. *Astrophysical J* (1978) 226:1034. doi:10.1086/156681
22. Itoh N, Totsuji H, Ichimaru S. Enhancement of thermonuclear reaction rate due to strong screening. *Astrophysical J* (1977) 218:477. doi:10.1086/155701
23. Itoh N, Totsuji H, Ichimaru S, DeWitt HE. Enhancement of thermonuclear reaction rate due to strong screening. II - Ionic mixtures. *Astrophysical J* (1979) 234:1079. doi:10.1086/157590
24. Ogata S, Iyetomi H, Ichimaru S. Nuclear reaction rates in dense carbon-oxygen mixtures. *Astrophysical J* (1991) 372:259. doi:10.1086/169971
25. Ogata S. Enhancement of Nuclear Reaction Rates in Dense Stellar Matter: A Path-Integral Monte Carlo Simulation Study. *Astrophysical J* (1997) 481:883–97. doi:10.1086/304086
26. Yakovlev DG. *Phys Rev* (2006) C74:035803.
27. Schramm S, Koonin SE. Pycnonuclear fusion rates. *Astrophysical J* (1990) 365:296. doi:10.1086/169482
28. Blaes O, Blandford R, Madau P, Koonin S. Slowly accreting neutron stars and the origin of gamma-ray bursts. *Astrophysical J* (1990) 363:612. doi:10.1086/169371
29. Bisnovatyi-Kogan G, Chethetkin V. *Soviet Phys Uspekhi* (1979) 22:89.
30. Lau R, Beard M, Gupta SS, Schatz H, Afanasjev AV, Brown EF, et al. Nuclear Reactions in the Crusts of Accreting Neutron Stars. *Astr J* (2018) 859:62. doi:10.3847/1538-4357
31. Salpeter EE. Nuclear Reactions in Stars Without Hydrogen. *Astrophysical J* (1952) 115:326. doi:10.1086/145546
32. Nomoto K, Thielemann KK, Miyayi S. *Astr Astrophys* (1985) 149:239.
33. Langanke K, Wiescher M, Thielemann F-K. The triple-alpha-reaction at low temperatures. *Z Physik A - At Nuclei* (1986) 324:147–52. doi:10.1007/bf01325126
34. Fushiki I, Lamb DQ. S-matrix calculation of the triple-alpha reaction. *Astrophysical J* (1987) 317:368. doi:10.1086/165284
35. Schramm S, Koonin KSE, Langanke K. Pycnonuclear triple-alpha fusion rates. *Astrophysical J* (1992) 397:579. doi:10.1086/171815
36. Langanke K, Lukas D, Müller HM, Schramm S, Koonin SE. Phase transition from a4He plasma to stable8Be matter. *Z Physik A - Hadrons Nuclei* (1991) 339:419–20. doi:10.1007/bf01560646
37. Müller H-M, Langanke K. Study of dense helium plasma in the optimal hypernetted chain approximation. *Phys Rev C* (1994) 49:524–32. doi:10.1103/physrevc.49.524
38. Luo ZQ, Peng QH. *Chin Astron Astrophys* (1997) 21:28.
39. Famiano M, Balantekin AB, Kajino T, Kusakabe M, Mori K, Luo Y. Nuclear Reaction Screening, Weak Interactions, and r-process Nucleosynthesis in High Magnetic Fields. *Astrophysical J* (2020) 898:163. doi:10.3847/1538-4357/aba04d
40. Käppeler F, Gallino R, Bisterzo S, Aoki W. Thesprocess: Nuclear physics, stellar models, and observations. *Rev Mod Phys* (2011) 83:157–93. doi:10.1103/revmodphys.83.157
41. Wiescher M, Käppeler F, Langanke K. Critical Reactions in Contemporary Nuclear Astrophysics. *Annu Rev Astron Astrophys* (2012) 50:165–210. doi:10.1146/annurev-astro-081811-125543

42. Mohr P, Käppeler F, Gallino R. Survival of nature's rarest isotope $^{180}$Ta under stellar conditions. *Phys Rev* (2007) C75:012802. doi:10.1103/PhysRevC.75.012802
43. Hayakawa T, Mohr P, Kajino T, Chiba S, Mathews GJ. Reanalysis of the $(J=5)$ state at 592 keV in $^{180}$Ta and its role in the ν-process nucleosynthesis of $^{180}$Ta in supernovae. *Phys Rev* (2010) C82:058801. doi:10.1103/PhysRevC.82.058801
44. Belic D, Arlandini C, Besserer J, de Boer J, Carroll JJ, Enders J, et al. Photo-induced depopulation of the $^{180}$Ta$^m$ isomer via low-lying intermediate states: Structure and astrophysical implications. *Phys Rev* (2002) C65:035801. doi:10.1103/PhysRevC.65.035801
45. Käppeler F, Arlandini C, Heil M, Voss F, Wisshak K, Reifarth R, et al. Stellar neutron capture on $^{180}$Ta$^m$. II. Defining the s-process contribution to nature's rarest isotope. *Phys Rev* (2004) C69:055802. doi:10.1103/PhysRevC.69.055802
46. Woosley SE, Hartmann DH, Hoffman RD, Haxton WC. The nu-process. *Astrophysical J* (1990) 356:272. doi:10.1086/168839
47. Heger A, Kolbe E, Haxton WC, Langanke K, Martínez-Pinedo G, Woosley SE. Neutrino nucleosynthesis. *Phys Lett B* (2005) 606:258–64. doi:10.1016/j.physletb.2004.12.017
48. Sieverding A, Langanke K, Martínez-Pinedo G, Bollig R, Janka H-T, Heger A. The ν-process with Fully Time-dependent Supernova Neutrino Emission Spectra. *Astrophysical J* (2019) 876:151. doi:10.3847/1538-4357/ab17e2
49. Langanke K, Martínez-Pinedo G, Richter PA, von Neumann-Cosel P. Supernova Inelastic Neutrino-Nucleus Cross Sections from High-Resolution Electron Scattering Experiments and Shell-Model Calculations. *Phys Rev Lett* (2004) 93:202501. doi:10.1103/physrevlett.93.202501
50. Haxton WC. Neutrino Heating in Supernovae. *Phys Rev Lett* (1988) 60:1999–2002. doi:10.1103/physrevlett.60.1999
51. Bruenn SW, Haxton WC. Neutrino-nucleus interactions in core-collapse supernovae. *Astrophysical J* (1991) 376:678. doi:10.1086/170316
52. Langanke K, Martínez-Pinedo G, Müller B, Janka HT, Marek A, Hix WR, et al. Effects of Inelastic Neutrino-Nucleus Scattering on Supernova Dynamics and Radiated Neutrino Spectra. *Phys Rev Lett* (2008) 100:011101. doi:10.1103/physrevlett.100.011101
53. Fuller GM, Fowler WA, Newman MJ. *Astr J* (1982) 42:447.
54. Langanke K, Martı´nez-Pinedo G. Shell-model calculations of stellar weak interaction rates: II. Weak rates for nuclei in the mass range in supernovae environments. *Nucl Phys A* (2000) 673:481–508. doi:10.1016/s0375-9474(00)00131-7
55. Heger A, Woosley SE, Martinez-Pinedo G, Langanke K. Presupernova Evolution with Improved Rates for Weak Interactions. *Astrophysical J* (2001) 560:307–25. doi:10.1086/324092
56. Langanke K, Martínez-Pinedo G. Nuclear weak-interaction processes in stars. *Rev Mod Phys* (2003) 75:819–62. doi:10.1103/revmodphys.75.819
57. Janka H, Langanke K, Marek A, Martinezpinedo G, Muller B. Theory of core-collapse supernovae. *Phys Rep* (2007) 442:38–74. doi:10.1016/j.physrep.2007.02.002
58. Yakovlev DG, Shalybkov DA. *Sov Sci Rev E Astrophys Space Phys* (1989) 7:311.
59. Bravo E, García-Senz D. Coulomb corrections to the equation of state of nuclear statistical equilibrium matter: implications for SNIa nucleosynthesis and the accretion-induced collapse of white dwarfs. *Mon Not R Astron Soc* (1999) 307:984–92. doi:10.1046/j.1365-8711.1999.02694.x
60. Juodagalvis A, Langanke K, Hix WR, Martínez-Pinedo G, Sampaio JM. Improved estimate of electron capture rates on nuclei during stellar core collapse. *Nucl Phys A* (2010) 848:454–78. doi:10.1016/j.nuclphysa.2010.09.012
61. Martinez-Pinedo G. *Phys Rev* (2014) C89:045806.
62. Kirsebom OS, Hukkanen M, Kankainen A. Measurement of the $2^+ \to 0^+$ ground-state transition in the $\beta$ decay of $^{20}$F. *Phys Rev* (2019) C100:065805. doi:10.1103/PhysRevC.100.065805
63. Zha S, Leung S-C, Suzuki T, Nomoto Ki.. Evolution of ONeMg Core in Super-AGB Stars toward Electron-capture Supernovae: Effects of Updated Electron-capture Rate. *Astrophysical J* (2019) 886:22. doi:10.3847/1538-4357/ab4b4b
64. Langanke K, Martínez-Pinedo G, Zegers RGT. Electron capture in stars. *Rep Prog Phys* (2021) 84:066301. doi:10.1088/1361-6633/abf207
65. Johnson CW, Kolbe E, Koonin SE, Langanke K. The fate of Be-7 in the sun. *Astrophysical J* (1992) 392:320. doi:10.1086/171431
66. Gruzinov AV, Bahcall JN. The7Be Electron Capture Rate in the Sun. *Astrophysical J* (1997) 490:437–41. doi:10.1086/304854
67. Assenbaum HJ, Langanke K, Rolfs C. Effects of electron screening on low-energy fusion cross sections. *Z Physik A - At Nuclei* (1987) 327:461–8. doi:10.1007/bf01289572
68. Krauss A, Becker HW, Trautvetter HP, Rolfs C, Brand K. Low-energy fusion cross sections of D + D and D + 3He reactions. *Nucl Phys A* (1987) 465:150–72. doi:10.1016/0375-9474(87)90302-2
69. Engstler S, Krauss A, Neldner K, Rolfs C, Schröder U, Langanke K. Effects of electron screening on the 3He(d, p)4He low-energy cross sections. *Phys Lett B* (1988) 202:179–84. doi:10.1016/0370-2693(88)90003-2
70. Aliotta M, Raiola F, Gyurky G, Formicola A, Bonetti R, Broggini C, et al. Electron screening effect in the reactions $^3$He(d, p)$^4$He and d($^3$He, p)$^4$He. *Nucl Phys* (2001) A690:790. doi:10.1016/S0375-9474(01)00366-9
71. Geist WH, Brune CR, Karwowski HJ, Ludwig EJ, Veal KD, Hale GM. *Phys Rev* (2003) C60:054003. doi:10.1103/PhysRevC.60.054003
72. Barbui M, Bang W, Bonasera A, Hagel K, Schmidt K, Natowitz JB, et al. Measurement of the Plasma Astrophysical *S* Factor for the $^3$He(d,p)$^4$He Reaction in Exploding Molecular Clusters. *Phys Rev Lett* (2013) 111:082502. doi:10.1103/PhysRevLett.111.082502
73. La Cognata M. *Phys Rev* (2005) C72:065802.
74. Shoppa TD, Koonin SE, Langanke K, Seki R. One- and two-electron atomic screening in fusion reactions. *Phys Rev C* (1993) 48:837–40. doi:10.1103/physrevc.48.837
75. Schröder U, Engstler S, Krauss A, Neldner K, Rolfs C, Somorjai E, et al. Search for electron screening of nuclear reactions at sub-coulomb energies. *Nucl Instr Meth* (1989) 40/41:466. doi:10.1016/0168-583X(89)91022-7
76. Shoppa TD, Jeng M, Koonin SE, Langanke K, Seki R. Electron screening in molecular fusion reactions. *Nucl Phys A* (1996) 605:387–402. doi:10.1016/0375-9474(96)00183-2
77. Engstler S, Raimann G, Angulo C, Greife U, Rolfs C, Schröder U, et al. Test for isotopic dependence of electron screening in fusion reactions. *Phys Lett* (1992) B279:20. doi:10.1016/0370-2693(92)91833-U
78. Engstler S, Raimann G, Angulo C, Greife U, Rolfs C, Schröder U, et al. Isotopic dependence of electron screening in fusion reactions. *Z Physik A - Hadrons Nuclei* (1992) 342:471–82. doi:10.1007/bf01294958
79. Langanke K, Shoppa TD, Barnes CA, Rolfs C. Energy loss, electron screening and the astrophysical 3He(d, p)4He cross section. *Phys Lett B* (1996) 369:211–4. doi:10.1016/0370-2693(96)00066-4
80. Bertulani CA. Electronic stopping in astrophysical fusion reactions. *Phys Lett B* (2004) 585:35–41. doi:10.1016/j.physletb.2004.01.082
81. Bertulani CA, de Paula DT. Stopping of swift protons in matter and its implication for astrophysical fusion reactions. *Phys Rev C* (2000) 62:045802. doi:10.1103/physrevc.62.045802
82. Strieder F, Rolfs C, Spitaleri C, Corvisiero P. Electron-screening effects on fusion reactions. *Naturwissenschaften* (2001) 88:461–7. doi:10.1007/s001140100267
83. Spitaleri C, Bertulani CA, Fortunato L, Vitturi A. The electron screening puzzle and nuclear clustering. *Phys Lett B* (2016) 755:275–8. doi:10.1016/j.physletb.2016.02.019
84. Baur G, Bertulani CA, Rebel H. Coulomb dissociation as a source of information on radiative capture processes of astrophysical interest. *Nucl Phys A* (1986) 458:188–204. doi:10.1016/0375-9474(86)90290-3
85. Typel S, Baur G. Theory of the Trojan-Horse method. *Ann Phys* (2003) 305:228–65. doi:10.1016/s0003-4916(03)00060-5
86. Czerski K, Huke A, Biller A, Heide P, Hoeft M, Ruprecht G. Enhancement of the electron screening effect for d + d fusion reactions in metallic environments. *Europhys Lett* (2001) 54:449–55. doi:10.1209/epl/i2001-00265-7
87. Kasagi J, Yuki H, Baba T, Noda T, Ohtsuki T, G. Lipson A. Strongly Enhanced DD Fusion Reaction in Metals Observed for keV D+Bombardment. *J Phys Soc Jpn* (2002) 71:2881–5. doi:10.1143/jpsj.71.2881
88. Raiola F, Migliardi P, Gangak L, Bonomo C, Gyürky G, Bonetti R, et al. Electron screening in d(d, p)t for deuterated metals and the periodic table. *Phys Lett* (2002) B547:193. doi:10.1016/S0370-2693(02)02774-0

89. Huke A, Czerski K, Heide P, Ruprecht G, Targosz N, Żebrowski W. Enhancement of deuteron-fusion reactions in metals and experimental implications. *Phys Rev* (2008) C78:015803. doi:10.1103/PhysRevC.78.015803
90. Bonomo C, Fiorentini G, Fulop Z, Gang L, Gyurky G, Langanke K, et al. Enhanced electron screening in $d(d, p)t$ for deuterated metals: a possible classical explanation. *Nucl Phys* (2003) A719:37c. doi:10.1016/S0375-9474(03)00955-2
91. Raiola F. *Eur Phys Journ* (2006) A27:79.
92. Coraddu M, Lissia M, Quarati P. Anomalous enhancements of low-energy fusion rates in plasmas: the role of ion momentum distributions and inhomogeneous screening. *Cent Eur J Phys* (2009) 7:527. doi:10.2478/s11534-009-0068-y
93. Coraddu M, Lissia M, Quarati P, Scarfone AM. Nuclear problems in astrophysical q-plasmas and environments. *Braz J Phys* (2009) 39:380. doi:10.1590/s0103-97332009000400006
94. Targosz-Sleczka N, Czerski K, Huke A, Ruprecht G, Weissbach D, Martin L, et al. Experiments on screening effect in deuteron fusion reactions at extremely low energies. *Eur Phys Journ Spec Top* (2013) 222:2353. doi:10.1140/epjst/e2013-02016-9
95. Huke A, Czerski K, Chun SM, Biller A, Heide P. Quantum mechanical Ab Initio simulation of the electron screening effect in metal deuteride crystals. *Eur Phys J A* (2008) 35:243–52. doi:10.1140/epja/i2007-10532-1
96. Zylstra AB, Herrmann HW, Kim YH, McEvoy A, Frenje JA, Gatu Johnson M, et al. $^2$H($p$,$\gamma$)$^3$He cross section measurement using high-energy-density plasmas. *Phys Rev* (2020) C101:042802(R). doi:10.1103/PhysRevC.101.042802
97. Zylstra AB, Herrmann HW, Gatu Johnson M, Kim YH, Frenje JA, Hale G, et al. Using Inertial Fusion Implosions to Measure the T+3He Fusion Cross Section at Nucleosynthesis-Relevant Energies. *Phys Rev Lett* (2016) 117:035002. doi:10.1103/PhysRevLett.117.035002
98. Wu Y, Pálffy A. Determination of Plasma Screening Effects for Thermonuclear Reactions in Laser-generated Plasmas. *Astrophysical J* (2017) 838:55. doi:10.3847/1538-4357/aa6252
99. M Roth P Thirolf, editors. *Laser Driven Nuclear Physics at ELI-NP* (2016). Technical Design Report (ELI-NP RA3-TDR, version 5.1).
100. Bruno CG. *Letter of Intent (E155) Submitted at the 2020 GSI G-PAC* (2022). Private Communication.
101. Adelberger EG. Solar fusion cross sections. *Rev Mod Phys* (1998) 70:1265. doi:10.1103/RevModPhys.70.1265

**Conflict of Interest:** The authors declare that the research was conducted in the absence of any commercial or financial relationships that could be construed as a potential conflict of interest.

frontiers | Frontiers in Physics

ORIGINAL RESEARCH
published: 19 August 2022
doi: 10.3389/fphy.2022.917229

# Prospects for Neutron Reactions on Excited States in High-Density Plasmas

*Ian J. Thompson* *

*Livermore Laboratory, Livermore, CA, United States*

With the reactions of high flux neutrons, such as in a DT plasma, there is a prospect of seeing new kinds of neutron-nucleus reactions for the first time. If neutrons excite a heavy nucleus, for example, there is possibility of a second neutron reacting on excited states of the residual nucleus before that nucleus has de-excited to its ground state. The possibility of such reactions on excited states has rarely been considered. The cross section for neutron induced fission on the isomeric state of $^{235}$U has been measured (D'Eer et al., Phys. Rev. C, 1988, 38: 1270–1276) and calculated (Younes et al., 2003, Maslov, 2007), and reactions on rotationally excited nuclear states has been calculated (Kawano et al., Phys. Rev. C, 2009, 80: 024611). In high flux plasmas, however, a much wider range of reactions is possible. We therefore need to consider excited states at much higher-energies than previously modeled, and then estimate whether second neutrons are likely to rescatter on those excited states. To determine the likelihood of such rescattering events, we first need to know the probable time series of nuclear decays of those excited states. The lifetimes of many low-lying states have been measured experimentally, but now we need to know the lifetimes of the many higher excited states that could be produced from incident 14 MeV neutrons. These are too numerous to be measured and also too numerous to be calculated individually, so statistical Hauser-Feshbach decay models are used. I show some lifetime calculations for $^{89}$Y, $^{169}$Tm, and $^{197}$Au targets, and predictions for the number of rescattering events in plausible plasma scenarios.

**Keywords: nuclear reactions, excited states, high-density plasma, nuclear lifetimes, rescattering**

**Edited by:**
*Gerald Hale,*
*Los Alamos National Laboratory (DOE), United States*

**Reviewed by:**
*Mrutunjaya Bhuyan,*
*University of Malaya, Malaysia*
*Marco La Cognata,*
*Laboratori Nazionali del Sud (INFN), Italy*

***Correspondence:**
*Ian J. Thompson*
*thompson97@llnl.gov*

**Specialty section:**
*This article was submitted to Nuclear Physics, a section of the journal Frontiers in Physics*

**Received:** *10 April 2022*
**Accepted:** *21 June 2022*
**Published:** *19 August 2022*

**Citation:**
*Thompson IJ (2022) Prospects for Neutron Reactions on Excited States in High-Density Plasmas. Front. Phys. 10:917229. doi: 10.3389/fphy.2022.917229*

## INTRODUCTION

Traditionally nuclear reactions are measured and modeled with both the projectile and the target starting in their ground states. At high temperatures in the interior of stars, the thermal energy will keep a statistical fraction of the nuclides in excited states, but that is difficult to reproduce in the laboratory. The closest we come to this so far is inside the imploding capsules during inertial confinement experiments such as those in the National Ignition Facility NIF [1]. In such locations with a high flux of neutrons, a nuclide may receive enough energy from incident neutrons that a second incident neutron could react with it before it stops emitting particles or gamma rays. There can then be two successive energy transfers, and the increased amount of excitation energy may enable reactions not possible before. To date the cross sections for neutron induced fission on the isomeric state of $^{235}$U has been measured [2] and calculated [3, 4], and reactions on rotationally excited nuclear states has been calculated [5]. If incident 14 MeV neutrons are used that result from DT fusion, then a great many more inelastic states will have been excited and maybe subject to a second neutron reaction.

The first step in seeing whether this could occur is to calculate the lifetimes of the excited states that could arise in reactions induced by 14 MeV neutrons. The low-lying levels in nuclei will have had their lifetimes measured in experiments, but now we will need to calculate the lifetimes of the higher-lying states that are predicted to be produced by statistical decay models following the Hauser-Feshbach (HF) method. The HF methods work by calculating the decay rate of excited states by summing the rates of possible decay paths for different kinds of decays such as by neutron, proton, alpha or gamma emissions. This is a statistical method that ignores the quantum interferences possible when multiple decay paths end at the same final state, and assumes that collections of states are well characterized by their average properties and so may be gathered into energy groups of similar spins and parities. It needs an optical potential for each incoming and exiting particle, as well as an equivalent 'strength function', as defined below, for gamma transitions. The HF methods include higher-lying compound-nucleus states which will have longer lifetimes than collective rotational levels, though still with shorter lifetimes than many known isomeric levels.

## NUCLEAR LIFETIMES

The average decay rate of an excited state $\lambda$ is related to the width $\Gamma$ of that state by $\Gamma = \hbar\lambda$, and to its lifetime by $\tau = 1/\lambda$. These determine the survival probabilities $P(t) = \exp(-t/\tau)$, so the *half life* (the time for an initial population to decay by a half) is $T_{1/2} = \tau \ln(2) = 0.693\tau$. We denote the averages of these properties over similar states by $\langle\lambda\rangle$ and $\langle\Gamma\rangle$. If there are multiple exit channels $c$ from a given state then each route will have its own partial width $\Gamma_c$, and the total width will be $\Gamma_T = \sum_c \Gamma_c$. The decay rates $\lambda$ will add similarly, and the result will be shorter lifetime for that state. The decays of excited states thus depend on the branching ratios $B_c = \Gamma_c/\Gamma_T$ which, summing up to unity, give the probability of a decay proceeding via channel $c$.

The Hauser-Feshbach method requires knowledge of the *level density* $\rho(E)$ of levels per unit energy. These are connected to the average partial widths by physical principles that depend on the type of channel $c$. If these are particle decay channels, then information from the scattering optical potential is used to give a *transmission coefficient* $T_c$, which is the probability that such an incoming particle will be absorbed by typical compound-nucleus resonances and so leave the elastic channel. By time reversal, the same transmission coefficients apply to the emission probabilities of those particles. From R-matrix scattering theory [6, ch. 11], the transmission coefficients are related to the average partial widths of levels by $T_c = 2\pi\langle\Gamma_c\rangle\rho(E)$. The decay branching ratios calculated in the Hauser-Feshbach method are $B_c = T_c/\sum_c T_c$. If a level decays by gamma (photon) emission, then the partial gamma widths are typically described as $\Gamma_\gamma = E_\gamma^{2L+1} f_L(E_\gamma)/\rho(E)$ in terms of a *gamma strength function* $f_L(E_\gamma)$. The $E_\gamma$ is the energy of the gamma-ray emitted, and $L$ is its multipolarity (sentence removed).

The other parameters of Hauser-Feshbach calculations have been estimated by nuclear evaluators as they use these reaction and decay models to fit the known reaction data for a 14 MeV neutron incident on the targets $^{89}$Y, $^{169}$Tm, and $^{197}$Au we are considering. These three materials are chosen because they have only one stable isotope each, and so any products of neutron capture or removal will produce experimentally distinctive decay products. Hauser-Feshbach codes TALYS [7], EMPIRE [8] and YAHFC [9] are all widely available to use, and include good collections of default parameter sets. YAHFC takes discrete levels from [10], gamma strength parameters from [7] using the functional form of [11], and neutron optical potentials from [12]. I am thus able to use the default parameter sets that give a reasonably good description of how these targets are excited and subsequently decay.

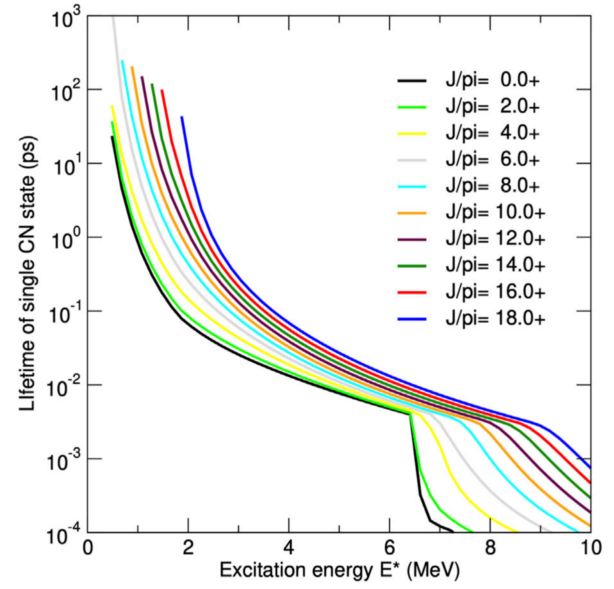

**FIGURE 1** | Calculated level lifetimes in pico-seconds ($10^{-12}$ s) from a Hauser-Feshbach model of $^{197}$Au decay mechanisms for positive parity compound-nucleus levels with a selection of spins. The lines end on the left at known discrete levels, or when the level density drops below 1 level per MeV.

I use an instrumented version of YAHFC, wherein the Hauser-Feshbach denominators $D = \sum_c T_c$ are saved separately for each level, as well as specifications of the chain of intermediate states appearing in each Monte Carlo instance of a decay path. These denominators $D = \sum_c 2\pi\langle\Gamma_c\rangle\rho(E)$ may be used to calculate the average total width of each state by $\Gamma_T = \sum_c T_c/2\pi\rho(E) = D/2\pi\rho(E)$, and they give us its average lifetime $\tau = 2\pi\hbar\,\rho(E)/D$. **Figure 1** shows the lifetimes of some positive-parity levels in $^{197}$Au. Above the neutron emission threshold at 6.3 MeV the lifetimes become much shorter because neutrons are emitted more quickly than gamma rays. The lifetimes are longer for higher spin states because the wave functions for both gammas and neutrons behave as $(kr)^{L+1}$ at short distances $r$ with wave number $k$ well within the range $kr \ll 1$, so larger multipolarities $L$ will give weaker transitions and hence longer lifetimes.

For each saved instance of a decay path, we can determine how long on average each decay process took. Each step in a Monte Carlo instance of a decay chain generates a random time interval of a level before it decays by sampling an exponential decay time

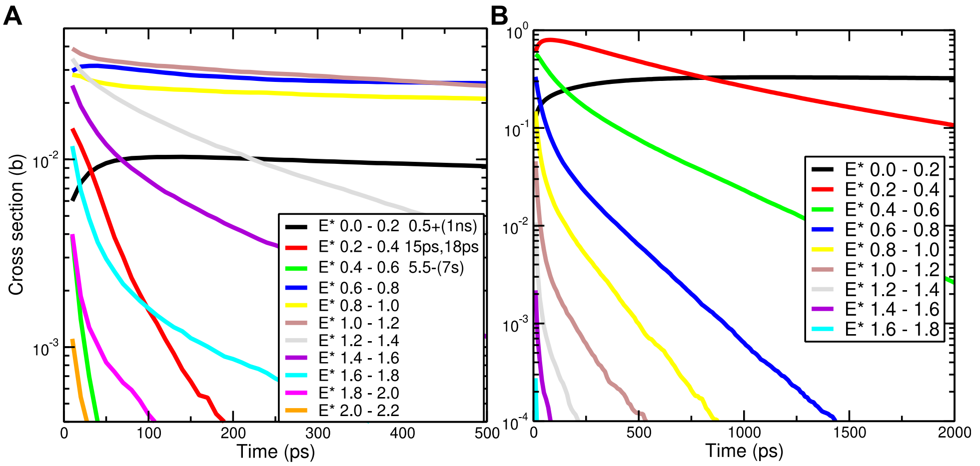

**FIGURE 2 |** Persistence cross sections $\sigma_{01}$ ($t$, $E^*$) for the population of excited states for a range of times $t$ in pico-seconds from Hauser-Feshbach models of 14 MeV incident neutrons on $^{197}$Au nuclei. Levels are shown after (n,n′) in **(A)**, and after (n, 2n) in **(B)**. The decay levels at excitation energies $E^*$ are grouped in bins 0.2 MeV wide.

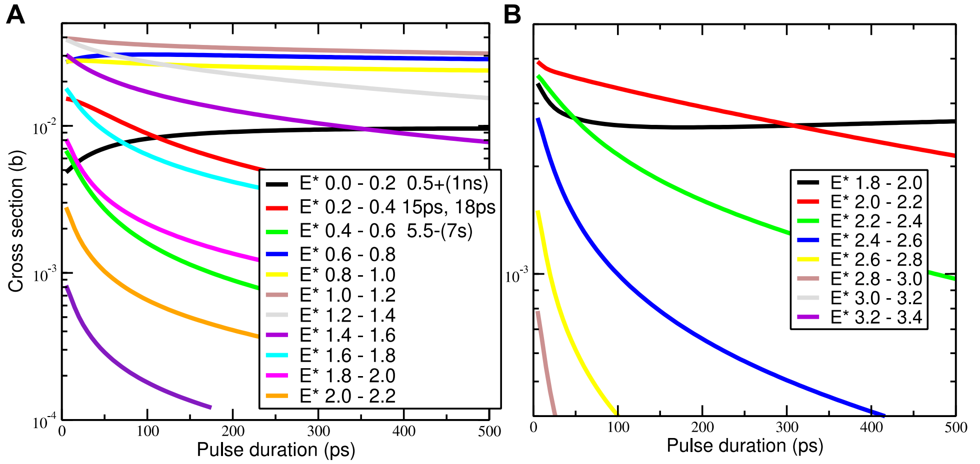

**FIGURE 3 |** Effective production cross sections $\sigma_{\mathrm{eff}}$ ($T$, $E^*$) for the population of excited states for a range of pulse durations $T$ in pico-seconds from 14 MeV incident neutrons on $^{197}$Au nuclei after (n,n′) reactions **(A)**, and on $^{169}$Tm nuclei after (n, 2n) reactions **(B)**.

probability distribution $P(t) = \tau^{-1} \exp(-t/\tau)$. The cumulative persistence time $t_p$ for a level is the sum of all the previous individual level durations $t$ in that path. Using this information, we can determine the persistence cross sections $\sigma_{01}$ ($t_p$, $E^*$) for the population of excited states at $E^*$ for a range of times after the initial neutron reaction.

**Figure 2** show the persistence cross sections $\sigma_{01}$ ($t_p$, $E^*$) on the left 1) for levels in $^{197}$Au* after (n,n′) reactions, and on the right 2) for levels in after (n, 2n) reactions for times up to 500 ps. The legend of plot 1) shows at least four isomeric states in $^{197}$Au but in the plot these do not give long-lived levels: they must have been rarely produced in this reaction. Some energy groups at low energies increase with time rather than decaying since they are fed by the incoming decays from states at higher excitation energies.

## CALCULATING REACTIONS ON EXCITED STATES

During neutron pulses, the produced excited states may undergo *second* reactions if there are enough neutrons incident on them during the persistence times shown in **Figure 2**. High fluxes of neutrons (many neutrons per second per unit area) will make this more likely to occur. The number of such reactions per second is the product of the incident flux, the above production cross section, and the number of targets.

Let $n_0$ be the number of incident neutrons of energy $E_0$ in a pulse of duration $T$ passing through an area $A$ at a constant rate, giving an incident neutron flux of $j_0 = n_0/AT$. Suppose

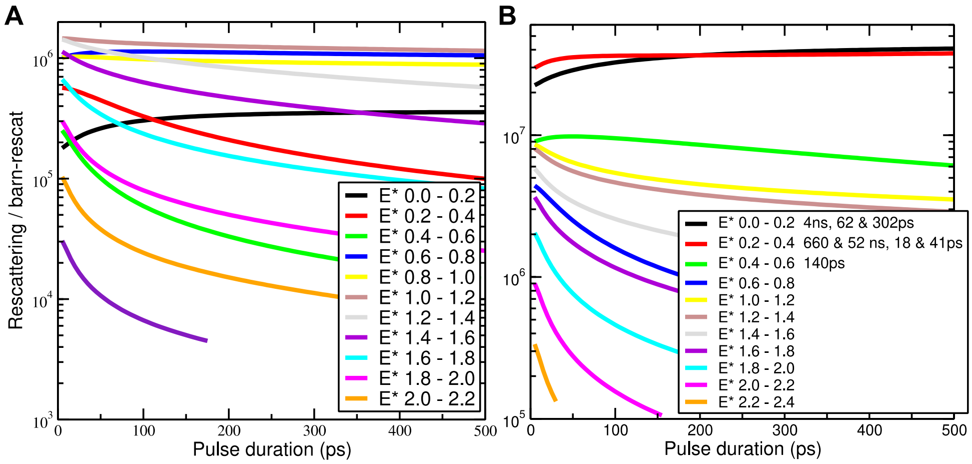

**FIGURE 4 |** Numbers of neutron rescattering events per barn of rescattering cross section for a range of pulse durations *T* in pico-seconds from 14 MeV incident neutrons on $^{197}$Au nuclei **(A)** and $^{169}$Tm nuclei **(B)** after (n,n′) reactions.

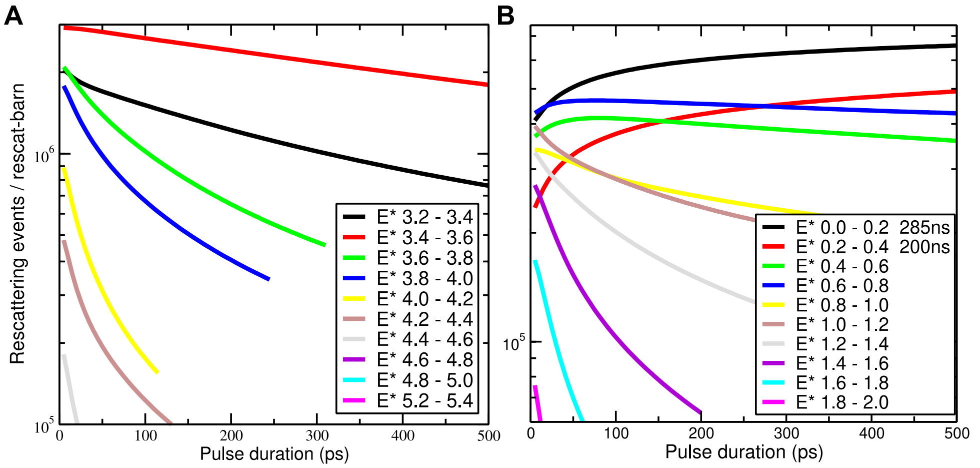

**FIGURE 5 |** Numbers of neutron rescattering events per barn of rescattering cross section for a range of pulse durations *T* in pico-seconds from 14 MeV incident neutrons after (n,n′) reactions on $^{89}$Y nuclei **(A)**, and after (n,p) reactions on $^{169}$Tm nuclei **(B)**.

there are $n_1$ heavy target nuclei in the area $A$ such as the surface of a sphere inside which the neutrons are generated. The excited states (called particle 2) are then produced at a rate $dn_2(t)/dt = j_0 n_1 \sigma_{01}$, which when integrated gives $n_2(t)$ as their produced population. After being produced, they persist or decay according to curves shown in **Figure 2**. The needed effective persistence cross section is the average of $\sigma_{01}$ ($t_2 - t_0$, $E^*$) for both first-scattering time $t_0$ and second-scattering time $t_2$ within the pulse duration. If the flow of neutrons is constant during the pulse duration, then the second scattering rate depends on the direct average cross section

$$\sigma_{\text{eff}}(T, E^*) = \frac{2}{T^2}\int_0^T dt_2 \int_0^{t_2} dt_0\ \sigma_{01}(t_2 - t_0, E^*). \tag{1}$$

**Figure 3** shows these effective averaged cross sections for producing excited states for a range of pulse durations from 14 MeV incident neutrons on $^{197}$Au nuclei after (n,n′) reactions (a), and on $^{169}$Tm nuclei after (n, 2n) reactions (b). **Figure 3A** takes for its input the data in **Figure 2A**, and is similar only in general terms because of the averaging. If the flow rate of neutrons varies significantly over the pulse duration then an experimentally-specific calculation will be needed.

When a second neutron rescatters on the $n_2(t)$ excited-state targets, the products of that reaction (called particle 3) in the pulse of duration $T$ will be counted by

$$n_3(T, E^*) = \frac{1}{2}\sigma_{02}(E_0 + E^*)\ \frac{n_0^2}{A^2}\ n_1\ \sigma_{\text{eff}}(T, E^*). \tag{2}$$

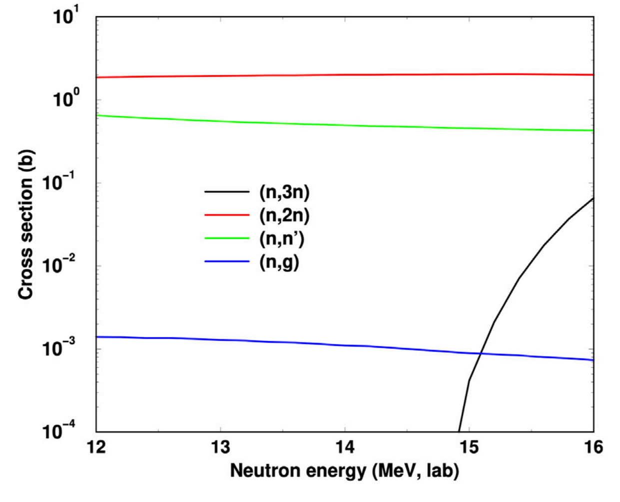

**FIGURE 6 |** Cross sections for neutrons incident on $^{197}$Au in the range 12–16 MeV, from default TALYS Hauser-Feshbach calculations [7].

This depends quadratically in the incident neutron areal density $n_0/A$ because the first and second scatterings are both linear in that density. The factor of 1/2 is because of the averaging the linear time production of excited states during the neutron pulse. The cross section to produce particle three from particle two is written as $\sigma_{02}$ $(E_0 + E^*)$ because the incident neutron energy and the excitation energy are added together to give that combined energy of the compound system after the second reaction. That would be the incident energy of a single neutron to produce the same intermediate state.

## RESPONSES IN SHORT NEUTRON PULSES

For a numerical example, consider from the experiment [13] the number $n_0 = 1.73 \times 10^{16}$ of neutrons passing at 14 MeV energy through the surface of a sphere of radius 25 $\mu$m taken from the measured radius of implosion hotspot [13, **Figure 5C**]. We now consider a trial calculation for these neutrons incident on $10^{16}$ heavy target nuclei implanted in that surface. If the effective production $\sigma_{\mathrm{eff}}$ and rescattering cross sections $\sigma_{02}$ are given in barns, then

$$n_3 = \frac{1}{2}\sigma_{02}\ \frac{n_0^2}{A^2}\ n_1\ \sigma_{\mathrm{eff}} = 4.44 \times 10^8\ \sigma_{02}\ \sigma_{\mathrm{eff}}. \tag{3}$$

Since we know $\sigma_{\mathrm{eff}}$ from above, but not $\sigma_{02}$, I will in **Figures 4**, **5** show plots of $n_3/\sigma_{02}$ as the number of neutron rescattering events per barn of rescattering cross section for targets of $^{89}$Y, $^{169}$Tm, and $^{197}$Au. Because I am assuming constant neutron flux during the incident pulse, **Figure 4A** is simply a scaled **Figure 3A**. **Figures 4B**, **5** show further reaction varieties with shapes different from $^{197}$Au. **Figures 4B**, **5B** are dominated by known isomer states at low energies. Apart from such isomer states, the most likely excited states to be subject to rescattering events are between 1 and 3 MeV: much larger the 50–150 keV considered in any of the earlier models [2–4]. Furthermore, it is encouraging that the 2020 NIF experiment [13] has high enough flux that rescattering cross sections even in the millibarn range ought to produce 100 or 1,000 rescattering events.

## DETECTING RESCATTERING EVENTS

To detect these rescattering events on excited states in a distinctive manner, we would ideally want their cross sections $\sigma_{02}$ $(E_0 + E^*)$ to be rather sensitive to the additional compound-state energy $E^*$. Then there might be new reactions such as (n, 3n) that would likely not occur with only an energy of $E_0$ from a single incident neutron. The threshold for the $^{197}$Au (n, 3n)$^{195}$Au reaction is just above 14 MeV, as shown in **Figure 6**. In principle, the detection of specific gamma decay peaks in the decay spectrum of $^{195}$Au would be indicative of higher-order reactions of the kinds described in this paper. We note, however, that the (n, 3n) cross sections are themselves small near threshold, and these small values are those needed to convert the quantities in **Figures 4**, **5** in scattering events. It will also be necessary to allow for an energy spread in the initial neutrons around 14 MeV. A more detailed transport calculation, however, is beyond the scope of this paper.

## CONCLUSION

New experimental facilities with high-fluence neutron pulses may allow new measurements of neutron reactions on excited states. We have the theory and modeling methods needed to calculate the lifetimes of excited states during decay cascades. This is possible not only for the known discrete levels at low excitation energies, but also at the higher energies where particle emission can compete with gamma production mechanisms. At the higher energies it is necessary to use statistical Hauser-Feshbach models of the decay processes, since the denominators of the branching ratios in those models may be directly converted to average decay widths and hence also average lifetimes. With that lifetime information we can model the time progress of excitation energies, and in this preliminary study calculate the rescattering rates on excited states during the neutron pulses. These rescattering events would show themselves in experiments by the decays of residual nuclei that would not otherwise be produced.

## DATA AVAILABILITY STATEMENT

The raw data supporting the conclusion of this article will be made available by the authors, without undue reservation.

## AUTHOR CONTRIBUTIONS

IT is the sole contributor.

## FUNDING

This work was performed under the auspices of the U.S. Department of Energy by Lawrence Livermore National Laboratory under Contract DE-AC52-07NA27344.

## REFERENCES

1. D'Eer A, Wagemans C, Nève de Mévergnies M, Gönnenwein F, Geltenbort P, Moore MS, et al. Neutron-induced Fission of the 26 minU235isomer. *Phys Rev C* (1988) 38:1270–6. doi:10.1103/PhysRevC.38.1270
2. Younes W, Britt HC, Becker JA. *Simulated (N,f) Cross Section of Isomeric* $^{235m}$*U. Tech. Rep. UCRL-CONF-201697*. Lawrence Livermore National Laboratory (2003).
3. Maslov VM. $^{235m}$*U and* $^{235}$*U Neutron-Induced Fission*. Les Ulis Cedex, France: EDP Sciences: ND2007 proceedings (2007). doi:10.1051/ndata:07242
4. Kawano T, Talou P, Lynn JE, Chadwick MB, Madland DG. Calculation of Nuclear Reaction Cross Sections on Excited Nuclei with the Coupled-Channels Method. *Phys Rev C* (2009) 80:024611. doi:10.1103/PhysRevC.80.024611
5. Moses EI, Atherton J, Lagin L, Larson D, Keane C, MacGowan B, et al. The National Ignition Facility: Transition to a User Facility. *J Phys Conf Ser* (2016) 688:012073. doi:10.1088/1742-6596/688/1/012073
6. Thompson I, Nunes F. *Nuclear Reactions for Astrophysics: Principles, Calculation and Applications of Low-Energy Reactions*. Cambridge, UK: Cambridge University Press (2009).
7. Koning AJ, Rochman D. Modern Nuclear Data Evaluation with the Talys Code System. *Nucl Data Sheets* (2012) 113:2841–934. doi:10.1016/j.nds.2012.11.002
8. Herman M, Capote R, Carlson BV, Obložinský P, Sin M, Trkov A, et al. Empire: Nuclear Reaction Model Code System for Data Evaluation. *Nucl Data SheetsSpecial Issue Evaluations Neutron Cross Sections* (2007) 108:2655–715. doi:10.1016/j.nds.2007.11.003
9. Ormand WE. *Monte Carlo Hauser-Feshbach Computer Code System to Model Nuclear Reactions: YAHFC. Tech. Rep. LLNL-TR-824700*. Lawrence Livermore National Laboratory (2021). doi:10.2172/1808762
10. [Dataset] Capote R, Herman M, Young P, Goriely S, Belgya T. Reference Input Parameter Library (RIPL-3) (2009). Available at: https://www-nds.iaea.org/RIPL-3/(accessed 10 25, 2020).
11. Kopecky J, Uhl M. Test of Gamma-ray Strength Functions in Nuclear Reaction Model Calculations. *Phys Rev C* (1990) 41:1941–55. doi:10.1103/PhysRevC.41.1941
12. Koning AJ, Delaroche JP. Local and Global Nucleon Optical Models from 1 keV to 200 MeV. *Nucl Phys A* (2003) 713:310. doi:10.1016/s0375-9474(02)01321-0
13. Baker KL, Thomas CA, Casey DT, Hohenberger M, Khan S, Spears BK, et al. Hotspot Parameter Scaling with Velocity and Yield for High-Adiabat Layered Implosions at the National Ignition Facility. *Phys Rev E* (2020) 102:023210. doi:10.1103/PhysRevE.102.023210

**Conflict of Interest:** The author declares that the research was conducted in the absence of any commercial or financial relationships that could be construed as a potential conflict of interest.

frontiers | Frontiers in Physics

TYPE Review
PUBLISHED 02 September 2022
DOI 10.3389/fphy.2022.944400

OPEN ACCESS

EDITED BY
Maria Gatu Johnson,
Massachusetts Institute of Technology,
United States

REVIEWED BY
Craig Sangster,
Laboratory for Laser Energetics,
University of Rochester, United States
Aidan Crilly,
Imperial College London,
United Kingdom

*CORRESPONDENCE
John D. Despotopulos,
despotopulos1@llnl.gov

SPECIALTY SECTION
This article was submitted to Nuclear Physics,
a section of the journal
Frontiers in Physics

RECEIVED 15 May 2022
ACCEPTED 29 July 2022
PUBLISHED 02 September 2022

CITATION
Despotopulos JD, Gharibyan N, Moody KJ, Yeamans C, Velsko C and Shaughnessy DA (2022), Radiochemical capabilities for astrophysics experiments at the national ignition facility.
*Front. Phys.* 10:944400.
doi: 10.3389/fphy.2022.944400

# Radiochemical capabilities for astrophysics experiments at the national ignition facility

John D. Despotopulos*, Narek Gharibyan, Kenton J. Moody, Charles Yeamans, Carol Velsko and Dawn A. Shaughnessy

Lawrence Livermore National Laboratory, Nuclear and Chemical Sciences Division, Physical and Life Sciences Directorate, Livermore, CA, United States

The Nuclear and Radiochemistry Group at Lawrence Livermore National Laboratory (LLNL) has developed a suite of diagnostics and techniques that can be used for astrophysics experiments at the National Ignition Facility (NIF). Capabilities have been developed to add material to the outside of NIF hohlraum assemblies as well as to the interior of NIF target capsules or the fill gas. The ability to place very small amounts of material close to the NIF target enables activation with very large, short-pulse neutron fluxes. The Solid Radiochemistry Diagnostic can be used to collect solid debris from a NIF shot within 2 h of the execution of a shot, and this can be analyzed for radioactive signatures with or without post-shot chemical processing. The Radiochemical Analysis of Gaseous Samples diagnostic system can be used to collect gaseous products produced during a NIF shot. Capsule doping and radiochemical analysis capabilities at NIF will be discussed. The application of these techniques to astrophysical measurements will be discussed as well as some preliminary results.

KEYWORDS

**radiochemistry, NIf, diagnostics, astrophysics, targets**

## Introduction

The National Ignition Facility at LLNL uses an indirect drive configuration of 192 laser beams with high energy (>MJ), ns-long pulses to heat the interior of a cylindrical hohlraum to extremely high temperatures (3.5 million K) [1–3]. This results in a flux of x-ray photons that ablates the surface of a 2-mm outer diameter (~1800 μm inner diameter) spherical target at the center of the hohlraum (indirect drive). Target capsules can be manufactured out of plastic (CH), high density carbon (HDC, diamond), or beryllium. The interior of the target is filled with a mixture of deuterium-tritium (DT) either as a gas (in indirect drive exploding pusher capsules) or as an ice layer with a central, lower-density gaseous zone (ignition capsules). Ablation of the ignition capsule causes the remainder of the capsule and DT fuel to compress by a factor of 20–40, which heats the central hot spot to 10–100 million K (~1–10 keV) with Gbar pressures. At peak compression, a part of the fuel undergoes the D (T,n) thermonuclear reaction, producing upwards of ~$10^{17}$ neutrons (14.1 MeV) in a time span of ~100 ps [3]. For the

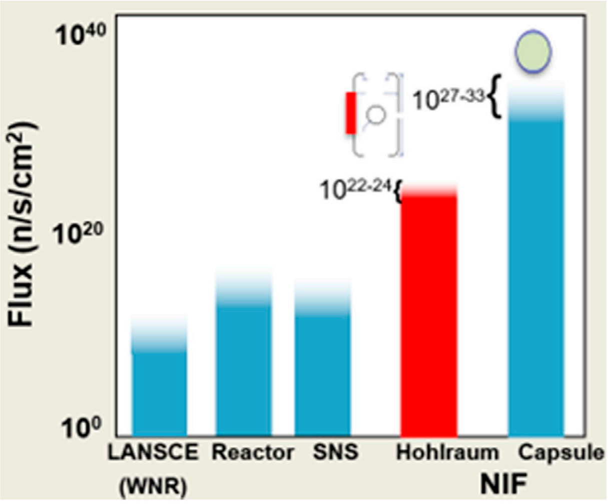

FIGURE 1
Neutron flux at various neutron sources, demonstrating the extremely high fluxes possible for material placed on the hohlraum or in the capsule at NIF. Capsule fluxes have a larger range due to both varying neutron yields as well as capsule compressions, whereas the hohlraum does not compress and has a range simply based on neutron yield differences.

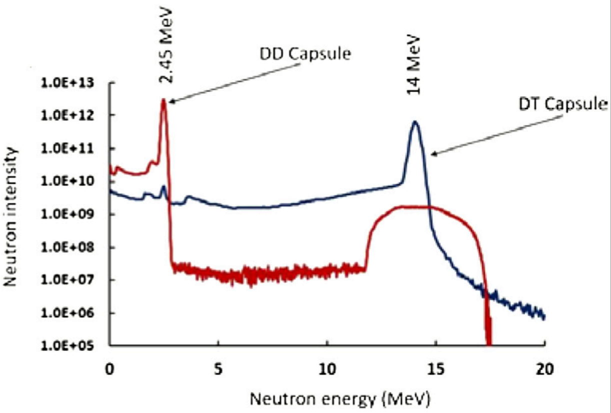

FIGURE 2
Neutron spectrum resulting from DD and DT NIF shots.

exploding pusher capsules, well-characterized plasmas at even hotter temperatures (10–20 keV) and lower densities are possible with yields of $10^{12-14}$ neutrons [1]. The fusion burn phase of a NIF capsule create the most intense neutron flux in the world (Figure 1).

It is also possible to fill a capsule with deuterium-deuterium (DD) only, which will result in a peak neutron energy at 2.45 MeV (Figure 2).

The extremely high neutron flux and short timescale of the neutron pulse in a NIF shot allows for nuclear reactions to be measured on radioactive species that would be impossible at traditional accelerator facilities. Limited real-world data exists for reactions on short-lived, excited nuclear states or multi-reaction pathways that are important to the high energy density (HED) plasma environment. In the absence of measured nuclear data, the models currently used to calculate these neutron-capture cross sections under stellar and thermonuclear reaction conditions have large uncertainties, on the order of 100–300% [4].

No other facilities exist with the ability to study, in stellar-like plasma conditions, charged particle- and neutron-induced nuclear reactions, which are integral to stellar nucleosynthesis and solar neutrino production. Decreasing reaction cross sections as a function of energy make measurements at the energy ranges that are found in the core of stars (<100 keV) inaccessible with accelerator-based experiments. Due to these very low reaction rates, it is exceedingly difficult to perform appropriate measurements as extremely long irradiation times would be required. Furthermore, an accelerator cannot create the plasma environment found within a stellar interior. While some neutron-induced and thermonuclear reaction rates of interest to stellar nucleosynthesis and big-bang nucleosynthesis have been studied at accelerators, these conditions are very different from those found in stars. In accelerator experiments, target nuclei are surrounded by bound electrons; in stars, electrons occupy mainly degenerate states. Therefore, results from accelerator experiments must be corrected for the differences in electron screening between the dense, stellar interior and beam-target experiments [5, 6].

Due to the convergence of conditions present in a NIF capsule, performing high-fidelity measurements of stellar reactions is possible as reaction rates are dramatically higher, and the temperature and density conditions are closer to those in a stellar interior. A NIF shot creates plasma conditions that are closer to those in stars; therefore, NIF-based experiments require less extrapolation from experimental parameters to determine actual stellar screening conditions [5]. The high compression of a NIF capsule dramatically increases the effective target areal density, and the electron-free cloud in the plasma contained within a NIF capsule is a unique condition that cannot be created at an accelerator and contains some aspects of a stellar interior. This unique environment makes NIF experiments excellent opportunities for resolving gaps in theoretical calculations of nuclear reactions in plasmas with real-world data. The Nuclear and Radiochemistry Group at LLNL has developed several techniques and diagnostics for measuring such nuclear reactions at NIF. By employing radiochemical techniques coupled with solid and gaseous debris collection systems, nuclear reaction measurements on very small quantities of radioactive material are now possible at NIF.

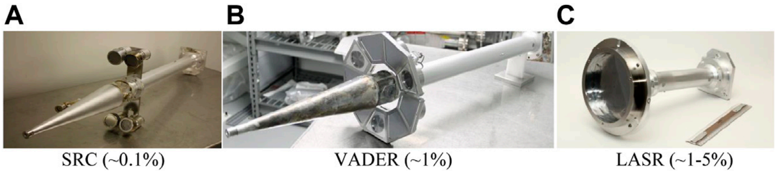

FIGURE 3
Solid radiochemical collection capabilities at NIF. The SRC **(A)** and VADER **(B)** are shown mounted on snout tubes that are subsequently mounted to DIMs; LASR **(C)** is attached directly to the end of the DIM snout. The percent solid angle of the NIF chamber subtended by the collector face is given for each collector.

# Radiochemistry capabilities

## Solid debris collection

Several solid debris collectors have been developed to capture post shot debris containing the nuclear reaction products of interest. The Solid Radiochemistry Diagnostic (SRC) consists of 2-inch diameter, 0.5–1 mm thick metal discs (typically Ta, W or C but other materials are possible) that are contained in a cap, which is attached to the snout of a Diagnostic Insertion Module (DIM) with a quick release bracket (Figure 3A) [7]. A maximum of four SRC collectors can be fielded at three different DIM locations (0,0) (90,78) and (90,375). With the collectors positioned 50 cm from the Target Chamber Center (TCC), each of the SRC discs has a surface area that covers $4 \times 10^{-4}$ of the 4π solid angle of the NIF chamber [7]. The Vast Area Detector for Experimental Radiochemistry (VADER, Figure 3B) is another solid debris collector that can be attached to a DIM 50 cm from TCC. This collector can field up to nine collectors simultaneously as either trapezoidal foils or standard SRC 2-inch discs mounted within a trapezoidal holder. The VADER collector covers roughly 1% of the 4π solid angle [8]. The final solid debris collector in use at NIF is the Large Area Solid Radiochemistry (LASR, Figure 3C) collector. LASR consists of a 20-cm diameter V or Ta foil and Al side foils with a 4π solid angle of ~1% when it is fielded 50 cm from TCC. This collector may be installed on DIMs at (90,75) or (90,315) and it is possible to position the LASR collector closer to TCC, which increases its solid angle coverage to roughly 5% [9].

For all solid debris collectors, the DIMs are retracted from the NIF chamber following a NIF shot, the collectors are disassembled from their housings, then delivered to the LLNL Nuclear Counting Facility (NCF) for gamma-ray spectroscopy. It is possible to have these samples arrive at the NCF within 2 h post-shot depending on the neutron yield. The collectors can be chemically leached or dissolved for further radiochemical processing, if needed, to isolate the reaction products of interest from the background activity produced via neutron activation of the collector materials, which can enable more accurate measurements [10].

FIGURE 4
The Radiochemical Analysis of Gaseous Samples (RAGS) system installed at NIF. The system consists of two carts (center of image). The first is to remove water vapors, particulates and reactive gasses, while the second cart is a gas collection cart where gasses collect on a cryogenic cold head.

## Gaseous debris collection

The Radiochemical Analysis of Gaseous Samples (RAGS, Figure 4) diagnostic is used for the isolation and purification of gases produced in a NIF shot [11]. RAGS uses the NIF target chamber (TC) turbopumps to remove gas from the NIF chamber after a shot. The NIF TC cryopumps are closed just before the shot to prevent the loss of gases that would freeze on their 20 K stages. The gas is first sent through a filter cart that removes water vapor and particulates, as well as an reactive gases such as nitrogen and oxygen if necessary, and then to a gas collection cart where gases collect on a cryogenic cold head that can reach 44 K. Gases that do not freeze at 44 K are held in a tank at the end of the sampling train. The RAGS system has several advantages including high collection efficiency (~90%) and the ability to release known amounts of stable or radioactive tracer gases into the TC on a shot to determine the RAGS fraction of gas

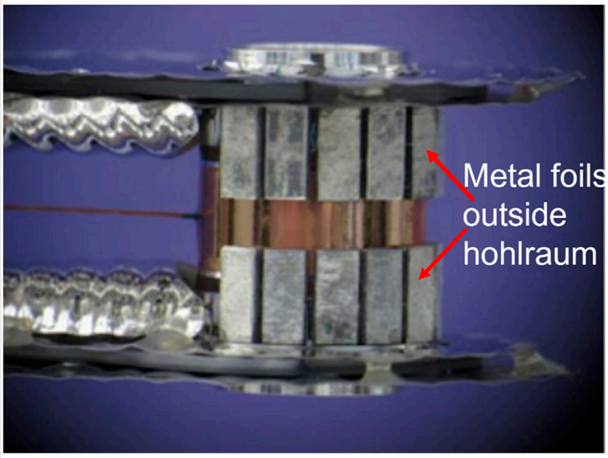

FIGURE 5
NIF target assembly showing materials added to the outside of the hohlraum.

recovered. Samples can be released into sample bottles for measurements with mass spectrometry or High Purity Germanium (HPGe) gamma-spectroscopy at the NCF [9]. There are also *in situ* HPGe and $LaBr_3$ radiation detectors for measuring activity at various locations within the system. The RAGS system can also be used to collect gases other than noble gases. It is routinely used to collect $^{13}N$ [12], krypton and xenon fission products, and neutron activation products, such as $^{41}Ar$, either of gases added to the DT fill gas at concentrations less than one atom percent, or of gases trapped in capsules during fabrication.

## Modification of NIF hohlraum

In the NIF chamber, the hohlraum is surrounded by a thermal-mechanical package (TMP), which positions the hohlraum and manages the thermal environment of the hohlraum and capsule. Materials with masses on the milligram scale (0.5 mm thick) can be added to the outside of the TMP and undergo neutron reactions during a NIF shot which can be used for measuring reaction cross sections (Figure 5) [10].

These materials can be positioned toward one of the solid radiochemistry collectors, which enables directed collection with a higher efficiency than can be obtained based solely on the solid angle. The addition of extra mass to the TMP may also help increase the collection of capsule debris as well, but the reasons for this are unclear (see Ref. [10]). A similar method is used for gases-aluminum foil may be ion-implanted with the gas of interest and glued to the outside of the hohlraum. Gaseous reaction products are collected in RAGS.

## NIF capsule doping

Doping the inner surface of a NIF capsule with target atoms is required to take full advantage of the large neutron flux and plasma environment at NIF. Two novel systems have been developed at LLNL to add dopants to the inner surface of NIF capsules: Apparatus for NIF-Doping Automated Robotic Injection System for Targets (ANDARIST) and Vacuum Optimized Radionuclide-to-Capsule Administer for NIF (VORCAN). Both systems use pre-made NIF capsules with a pre-drilled fill hole and have been used successfully to dope capsules that were subsequently fired in a NIF shot. Dopants have included single isotopes ($^{7}Be$, $^{152}Eu$, and $^{238}U$) as well as mixed species ($^{7,10}Be$, $^{91}Y/^{171}Tm$, stable Y/stable Tm). In particular, the dopant cocktail of stable Y/stable Tm was used in the measurement of $^{89}Y$ (n, 2n)$^{88}Y$ reaction. A variety of capsules can be used with both systems including standard CH capsules, and HDC capsules. The doping systems could also be used with Be capsules, but this has not been performed yet.

ANDARIST (Figure 6) is based on *in vitro* fertilization technology. A miniature hexapod (Figure 6B) is used to hold and position the NIF capsule such that the pre-drilled fill hole is facing vertically, which is determined by two digital microscopes directed at the hexapod (Figure 6B). Once the capsule is in the correct position, a microcapillary filled with the desired dopant(s) is lowered through the fill hole by a three-axis manipulator (Figure 6C), and the dopants are injected into the capsule (Figures 6C,D small solution bubble, after 1 µL of solution injected). After injection the fill solution, typically a weakly acidic solution containing the target material of interest, pools to one side due to surface tension. The capsule is centrifuged and then dried on a hotplate, at 200°C, which causes the solution to coat the inner surface during drying. Finally the dried capsule is analyzed by HPGe gamma-spectroscopy to verify the contents. The advantage of this system is the ability to manipulate very small volumes, <1 µl, with extremely high efficiency. This is the highest-fidelity NIF capsule doping system and allows for rare radionuclides that cannot be obtained in large quantities to be added to a NIF capsule for cross section measurements. The main drawback of this system is that the injection cocktail must be extremely clean of all contaminates (salts, etc.) as any mass can clog the injection capillary. Figure 6 shows the injection of dopants into a pre-drilled 2 mm NIF capsule as well as a finished, injected capsule.

The VORCAN system (Figure 7) is used for radionuclides that can be produced with sufficient activity in larger solution volumes (~10 µl). This system was designed based on the vacuum system used to fill NIF capsules with foam layers [13]. VORCAN consists of a three-axis manipulator inside a small vacuum chamber. A NIF capsule is suspended above a sample holder containing 3–10 µl of a solution containing the dopants of interest with the pre-drilled fill hole pointing toward the solution. The chamber is evacuated with a vacuum pump and

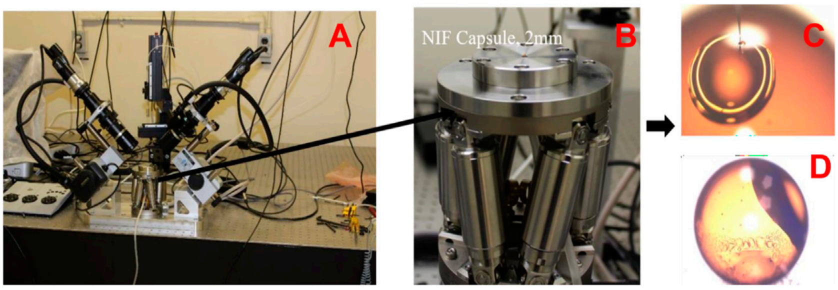

FIGURE 6
**(A)** ANDARIST; **(B)** miniature hexapod holding NIF capsule from center of system depicted in A; **(C)** NIF capsule being injected; **(D)** Filled NIF capsule.

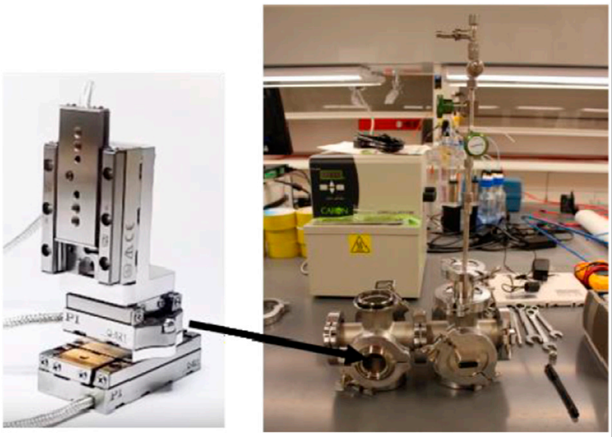

FIGURE 7
VORCAN system.

the manipulator is used to submerge the NIF capsule in the solution. The chamber is returned to atmospheric pressure and a known amount of solution (based on the pressure difference) is pulled into the NIF capsule. The capsule is dried and analyzed the same way as with ANDARIST. Unlike ANDARIST, VORCAN is simple to use and does not have stringent requirements on solution cleanliness due to its operational mechanism. However, it cannot be used to manipulate few microlitervolumes and has a lower efficiency (~10–30% of the total solution is doped into the capsule) meaning more target material is needed.

Capsules may also be doped with gases either through the capsule production method or by ion implantation with isotopically enriched gases at specific thicknesses during capsule growth. Quantification of neutron and charged particle reaction products helps to constrain ablator mix and areal density (ρr). Beryllium capsules are made by sputtering beryllium onto a mandrel in an argon atmosphere. Some of the argon is captured during the process. The argon remaining in the residual capsule wall when neutrons are produced will undergo neutron reactions. In addition, $^{10}$B can be added during the initial sputtering to create an ablator layer with about 10 atomic % that reacts with DT fusion alpha particles (α,n) to make $^{13}$N [12]. Plastic (CH) and HDC capsules have the $^{12}$C isotope that may be mixed into the plasma and react with upscattered deuterons (d*,n) to make $^{13}$N.

## Astrophysics experiments with radiochemistry diagnostics and capsule doping

As described above, radiochemistry diagnostics and capsule doping capabilities enable the measurement of nuclear reactions with exceedingly small amounts of material at NIF. Therefore, work is being performed to develop experimental platforms for stellar reaction rate measurements at NIF. To perform cross section measurements using doped NIF capsules a tracer is required to yield the collection efficiency for the reaction product of interest. If possible, a known flux monitor should also be added to the capsule along with the target material to avoid relying on calculated neutron fluxes.

An initial investigation into developing a platform for stellar reaction rates at NIF was performed with the goal of measuring the $^{13}$C (n,α)$^{10}$Be reaction cross-section, using $^{7}$Be as the reaction tracer. As the use of a collection tracer is vital to interpret the data from a NIF experiment, the first step was to determine if Be isotopes would fractionate during the NIF shot, either after implosion or during transit to the radiochemistry collectors. Three CH capsules provided by General Atomics (GA) were doped with $^{7,10}$Be using the ANDARIST system and fired in a series of three NIF shots (N180514-001, −002, −003). The results demonstrated that a collection tracer ($^{7}$Be) would collect with the same efficiency as the reaction product of interest ($^{10}$Be). For the cross-section measurement, GA created CH capsules with a layer enriched in $^{13}$C (10 μm from the inner surface), which would serve as the target. The capsules were shipped to LLNL, and ANDARIST was used to inject the $^{7}$Be tracer into the capsule through a pre-drilled fill hole. Two shots, N18104-001 and N190519-001, were completed successfully with these capsules and data analysis is ongoing.

## Conclusion

The Nuclear and Radiochemistry Group at LLNL has developed a suite of diagnostics and capabilities that are well suited to perform astrophysics measurements at NIF. Many reaction rates in stellar systems are impossible to measure at traditional accelerator facilities or require large extrapolations if measurements are possible. The HED plasma environment at NIF is far more similar to a stellar interior, and considerably less extrapolation to stellar energies is necessary, which enables a greater fundamental understanding of stellar reactions. Through radiochemical techniques developed to dope capsules as well as to collect and analyze debris from a NIF shot, measurements are feasible on samples with $10^{13}$ atoms (ng) of material ($10^{6}$ atoms on SRC collectors) enabling a broader range of measurements than is feasible at any other facility, which would require targets with micrograms to milligrams of target material (not always feasible for radioactive species). The unique environment and radiochemistry diagnostics at NIF will enable a wide variety of astrophysical measurements that opens a new avenue for exploring stellar reaction rates and improving our understanding of the Universe.

Future experiments will take advantage of the unique environment created by a NIF shot and the extensive suite of diagnostic capabilities to measure reactions that are extremely important to our understanding of astrophysical processes like the hydrogen burning cycle and s-process nucleosynthesis. There is interest in measuring (n,γ) reaction cross sections for radioactive s-process branching isotopes, such as $^{171}$Tm or $^{134}$Cs, which would increase our understanding of the s-process and the formation of elements [2, 14, 15]. Other experiments made possible by the development of a NIF platform for measuring stellar reaction rates include reactions important to the hydrogen burning cycle, including the $^{14}$N (p,γ) $^{15}$O reaction which is used for stellar dating [2].

## Author contributions

This manuscript was written by JD with contributions and inputs from the other authors.

## Funding

This work was performed under the auspices of the (U.S.) Department of Energy by Lawrence Livermore National Laboratory under Contract Nos. DE-AC52-07NA27344. This word was funded by the Laboratory Directed Research and Development Program at LLNL under project tracking code 16-SI-001.

## Conflict of interest

The authors declare that the research was conducted in the absence of any commercial or financial relationships that could be construed as a potential conflict of interest.

## Publisher’s note

## References

1. Cerjan CJ, Bernstein L, Hopkins LB, Bionta RM, Bleuel DL, Caggiano JA, et al. *Dynamic high energy density plasma Environments at the national ignition Facility for nuclear science research. J Phys G: Nucl Part Phys* (2018) 45:(033003). doi:10.1088/1361-6471/aa8693

2. Moses EI, Boyd RN, Remington BA, Keane CJ, Al-Ayat R. The National Ignition Facility: Ushering in a new age for high energy density science. *Phys Plasmas* (2009) 16:(041006). doi:10.1063/1.3116505

3. Zylstra AB, Kritcher AL, Hurricane OA, Callahan DA, Baker K, Braun T, et al. *Record Energetics for an inertial fusion Implosion at NIF. Phys. Rev. Lett. 126* (2021) 025001. doi:10.1103/PhysRevLett.126.025001

4. Kaeppeler F, Gallino R, Bisterzo S, Wako A. The s process: Nuclear Physics, stellar models, and observations. *Rev Mod Phys* (2011) 83:157. doi:10.48550/arXiv.1012.5218

5. Boyd RN, Bernstein LA, Brune C. Studying Nuclear Astrophysics at NIF. *Phys Today* (2009) 62:60–1. doi:10.1063/1.3206102

6. Assenbaum HJ, Langanke K, Rolfs C. Effects of electron screening on low-energy fusion cross sections. *Z Physik A - At Nuclei* (1987) 327:461–8. doi:10.1007/bf01289572

7. Shaughnessy DA, Moody KJ, Gharibyan N, Grant PM, Gostic JM, Torretto PC, et al. *Radiochemical Determination of Inertial Confinement Fusion Capsule Compression at the National Ignition Facility*. 85 (2014) 063508. doi:10.1063/1.4883186

8. Galbraith J, Bettencourt R, Shaughnessy D, Gharibyan N, Talison B, Morris K, et al. Vast area detection for experimental radiochemistry (VADER) at the national ignition facility. Proc. *SPIE* (2015) 9591:95910G. doi:10.1117/12.2189310

9. Waltz C, Jedlovec DR, Hardy MC, Shaughnessy DA, Gharibyan N. Large area solid radiochemistry (LASR) collector at the national ignition facility. *Proc SPIE* (2017), 10390. 103900H. doi:10.1117/12.2272640

10. Shaughnessy DA, Gharibyan N, Moody KJ, Despotopulos JD, Grant PM, Yeamans CB, et al. Nuclear science research with dynamic high energy density

plasmas at NIF. *J Phys : Conf Ser* (2016) 717:(012080). doi:10.1088/1742-6596/717/1/012080

11. Shaughnessy DA, Velsko CA, Jedlovec DR, Yeamans CB, Moody KJ, Tereshatov E, et al. The radiochemical analysis of gaseous samples (RAGS) apparatus for nuclear diagnostics at the national ignition facility (invited). *Rev Sci Instrum* (2012) 83:10D917. doi:10.1063/1.4742145

12. Lonardoni D, Sauppe JP, Batha SH, Birge N, Bredeweg T, Freeman M, et al. First measurement of the 10B(α, n)13N reaction in an inertial confinement fusion implosion at the national ignition facility: Initial steps toward the development of a radiochemistry mix diagnostic. *Plasma Phys* (2022). published online 5/13/2022. doi:10.1063/5.0079676

13. Biener J, Dawedeit C, Kim SH, Braun T, Worsley MA, Chernov AA, et al. *A new Approach to foam-lined indirect-drive NIF ignition targets. Nucl Fusion* 52, (2012) 062001. doi:10.1088/0029-5515/52/6/062001

14. Bernstein LA, Bleuel DL, Caggiano JA, Cerjan C, Fortner RJ, Gostic J, et al. Low energy neutron measurements in high energy density plasmas using the national ignition facility. *Plasma Fusion Res* (2014) 9:4404101. doi:10.1585/pfr.9.4404101

15. Li K-A, Qi C, Kugaro M, Lopez AY, Karakas AI, Hartogh J, et al. The stellar β-decay rate of $^{134}$Cs and its impact on the barium nucleosynthesis in the s-process. *Astrophys J Lett* (2021) 919:L19. doi:10.3847/2041-8213/ac260f

frontiers | Frontiers in Physics

TYPE Original Research
PUBLISHED 20 September 2022
DOI 10.3389/fphy.2022.937972

OPEN ACCESS

EDITED BY
Mark Paris,
Los Alamos National Laboratory (DOE),
United States

REVIEWED BY
Daniel Odell,
Ohio University, United States
Carlo G. Bruno,
University of Edinburgh,
United Kingdom

*CORRESPONDENCE
A. J. Crilly,
ac116@ic.ac.uk

SPECIALTY SECTION
This article was submitted to Nuclear Physics,
a section of the journal
Frontiers in Physics

RECEIVED 06 May 2022
ACCEPTED 25 August 2022
PUBLISHED 20 September 2022

CITATION
Crilly AJ, Garin-Fernandez I, Appelbe BD and Chittenden JP (2022), Efficacy of inertial confinement fusion experiments in light ion fusion cross section measurement at nucleosynthesis relevant energies.
*Front. Phys.* 10:937972.
doi: 10.3389/fphy.2022.937972

# Efficacy of inertial confinement fusion experiments in light ion fusion cross section measurement at nucleosynthesis relevant energies

A. J. Crilly*, I. Garin-Fernandez, B. D. Appelbe and J. P. Chittenden

Centre for Inertial Fusion Studies, The Blackett Laboratory, Imperial College, London, United Kingdom

Inertial confinement fusion (ICF) experiments create a unique laboratory environment in which thermonuclear fusion reactions occur within a plasma, with conditions comparable to stellar cores and the early universe. In contrast, accelerator-based measurements must compete with bound electron screening effects and beam stopping when measuring fusion cross sections at nucleosynthesis-relevant energies. Therefore, ICF experiments are a natural place to study nuclear reactions relevant to nuclear astrophysics. However, analysis of ICF-based measurements must address its own set of complicating factors. These include: the inherent range of reaction energies, spatial and temporal thermal temperature variation, and kinetic effects such as species separation. In this work we examine these phenomena and develop an analysis to quantify and, when possible, compensate for their effects on our inference. Error propagation in the analyses are studied using synthetic data combined with Markov Chain Monte Carlo (MCMC) machine learning. The novel inference techniques will aid in the extraction of valuable and accurate data from ICF-based nuclear astrophysics experiments.

KEYWORDS

**inertial confinement fusion (ICF), nuclear astrophysics, Bayesian inference, S factor, bare nuclear cross section, thermal reactivity, ion kinetic effects**

## 1 Introduction

Inertial confinement fusion (ICF) experiments use implosions to reach thermonuclear conditions with high temperatures ($T \gtrsim 1$ keV) and densities ($\rho \gtrsim 1$ g/cc). The short-lived plasma is sufficiently hot that thermal ions can undergo fusion reactions, at typical densities plasma screening effects are currently modelled to be at the $<1\%$ level [1]. Recent ICF experiments [1–3] have utilised this unique environment to perform measurements of fusion cross sections at low reaction energies. The results of these experiments compared favourably to previous accelerator-based measurements [4, 5] and theoretical models [6–8] (within 1-2 standard deviations), without requiring corrections for electron screening and beam stopping. However, ICF experiments possess their own set of complicating factors including the inherent range of reaction energies, spatial and temporal thermal temperature variation, and ion kinetic effects. We must examine how these factors affect fusion yields to better understand both the experiments and the effect on cross section inference.

The fusion cross section is canonically written in the following form:

$$\sigma(K) = \frac{S(K)}{K}\exp\left[-\sqrt{\frac{K_B}{K}}\right], \tag{1}$$

where $K$ is the reactants relative kinetic energy, $S$ is the S-factor, and $K_B$ is the Coulomb barrier energy. By splitting terms in this form, the S-factor gives the nuclear physics dependent contribution to the cross section. As the Coulombic part is already known, cross section measurements aim to extract the value of the S-factor as a function of reaction energy.

The probability of a reaction is proportional to the product of the cross section and relative velocity, $\sigma v$. The reactant species in a thermonuclear plasma have a range of velocities and thus the probability of reaction and number of fusion reactions depends on the average $\sigma v$ value. Mathematically, the volumetric reaction rate and yield of a reaction involving reactants labelled 1 and 2 are given by:

$$R_{12} = \frac{1}{1+\delta_{12}} n_1 n_2 \langle\sigma v\rangle_{12}, \tag{2}$$

$$Y_{12} = \frac{1}{1+\delta_{12}} \cdot \int dV \int dt \; n_1 n_2 \langle\sigma v\rangle_{12}, \tag{3}$$

where $n_1$ and $n_2$ are the reactant number densities, $\langle\sigma v\rangle_{12}$ is the reactivity and $\delta_{12}$ is a Kronecker delta to account for double counting in homonuclear reactions. Extracting reactivity information from a yield requires knowledge of the number densities of the reactants and their burn time and volume. Instead, it is preferable to perform a differential measurement through a yield ratio. The yield ratio between reactions involving reactants 1,2 and 3,4 is given by:

$$\mathcal{R}_Y = \frac{Y_{12}}{Y_{34}} = \frac{1+\delta_{34}}{1+\delta_{12}} \cdot \frac{\int dV \int dt \; n_1 n_2 \langle\sigma v\rangle_{12}}{\int dV \int dt \; n_3 n_4 \langle\sigma v\rangle_{34}}. \tag{4}$$

Generally, one of the reactions considered has a well-known S-factor and acts as a reference from which the other target reaction S-factor can be measured. A temperature must also be measured to evaluate the reference reaction reactivity. The ion temperature is typically measured using fusion product spectroscopy [9–13]. However, in order to relate the yield ratio and temperature measurements to the underlying fusion cross section a number of approximations must be made. Listed below are the set of approximations commonly used to infer cross-sections from yield ratio measurements in ICF experiments:

1. Maxwellian reactant ion velocity distributions
2. No species separation, $n_i/n_{\mathrm{tot}}$ = constant
3. Uniform static temperature, $T$ = constant
4. Narrow Gamow peak, $S(K) \simeq$ constant

Approximations (1) and (2) can only be violated if ion kinetic effects are present, while approximation (3) is violated by spatial and/or temporal hydrodynamic temperature gradients. Finally, approximation (4) introduces errors even for a single temperature plasma–the Gamow peak is the range of relative kinetic energies over which the majority of fusion reactions occur, a more detailed description will be given in Section 2.

In this work we will examine the yield ratio measurement and the error associated with the common approximations made. This will provide both quantitative estimates of the error but also analysis techniques to reduce or remove the errors.

## 2 Gamow peak approximations

Within a local description of a plasma, ions have a range of velocities as determined by the distribution function. Therefore, there is an inherent range of relative velocities in the reactants. The number density of reactions at a given relative kinetic energy is given by:

$$dN = n_1 n_2 v_r \sigma(K) g(K) dK, \tag{5}$$

$$v_r = \sqrt{\frac{2K}{m_{12}}}, \tag{6}$$

where $g(K)$ is the distribution of relative kinetic energy in the reactants, $v_r$ is the relative velocity and $m_{12}$ is the reactants' reduced mass. The cross section more than exponentially suppresses reactions a low $K$, while typical ion velocity distributions are decreasing functions of $K$. Therefore, the product of the cross section and $v_r g(K)$ define a peaked window of probable reaction energies known as the Gamow peak. For Maxwellian reactants at temperature $T$:

$$v_r g(K) \propto K \exp\left[-\frac{K}{T}\right]. \tag{7}$$

Integrating Eq. 5 over all energies gives rise to the following reactivity:

$$\langle\sigma v\rangle \propto \int K\sigma(K)\exp\left[-\frac{K}{T}\right] dK. \tag{8}$$

Yield ratios depend on these reactivities and we wish to relate them to the form of the cross section. Using the canonical form of cross section, we can separate the fast Coulomb barrier penetrability from the slow S-factor dependence. The product of the Coulomb barrier penetrability and the reactant $K$ distribution is the primary determinant in the form of the Gamow peak. Now, the S-factor is sampled across the narrow

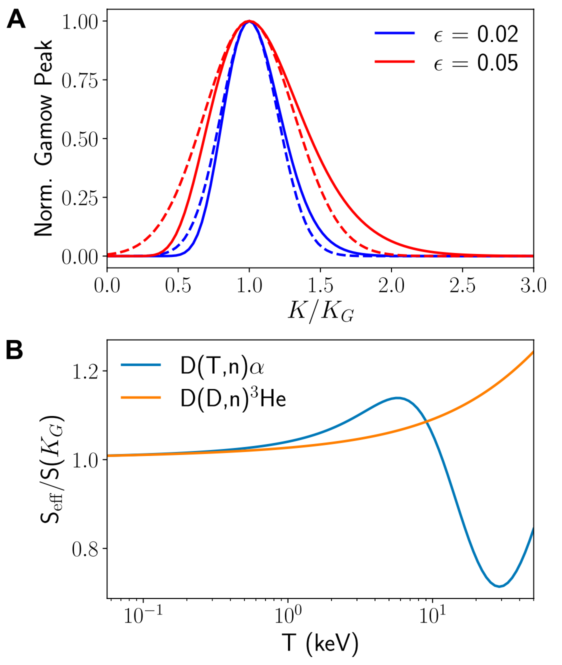

**FIGURE 1**
**(A)** The normalised Gamow peak for $\epsilon$ values of 0.02 and 0.05. The solid lines use the exact form and the dashed lines show the saddlepoint approximation, which is valid for $\epsilon \ll 1$. **(B)** The ratio of $S_{\mathrm{eff}}$ (as defined in Eq. 13) to $S(K_G)$ for the resonant D (T,n)$\alpha$ and non-resonant D (D,n)$^3$He reactions. These are evaluated using the Bosch-Hale cross section fit [8].

Gamow peak giving an opportunity for an energy-resolved measurement. The problem is greatly simplified by working in the natural energy unit of the Gamow peak energy [14, 15], $K_G$. At a given temperature, this is the most probable (modal) reaction energy.

$$K_G = \left(\frac{K_B T^2}{4}\right)^{1/3}, \tag{9}$$

$$\epsilon = \frac{T}{3K_G}\left(=\frac{1}{\tau}\right), \tag{10}$$

where we include the definition of Clayton's large dimensionless parameter [15], $\tau$. Using this canonical variable transformation leads to a reactivity formula of the form:

$$\langle\sigma v\rangle = \frac{4}{\sqrt{2\pi m_{12}}T^{\frac{3}{2}}}\int_0^\infty S(K)\exp\left[-\frac{f(K)}{\epsilon}\right]dK, \tag{11}$$

$$f(K) = \frac{1}{3}\left(2\sqrt{\frac{K_G}{K}} + \frac{K}{K_G}\right) \tag{12}$$

If $\epsilon \ll 1$, then this reactivity formula is a Laplace-type integral and the saddlepoint method will give a good approximation [9]. A temperature-dependent effective S-factor can then be constructed which takes into account the finite width of the Gamow peak, the energy dependence of the S-factor and the innate skew of the Gamow peak [14].

$$S_{\mathrm{eff}} = \frac{1}{\sqrt{4\pi\epsilon}}\frac{1}{K_G}\int_0^\infty S(K)\exp\left[-\frac{f(K)-1}{\epsilon}\right]dK, \tag{13}$$

$$\langle\sigma v\rangle = S_{\mathrm{eff}}(T)\cdot\frac{4}{3}\sqrt{\frac{2}{3}}\frac{\exp[-1/\epsilon]}{\epsilon\sqrt{m_{12}K_G}}. \tag{14}$$

Figure 1 shows the saddlepoint approximation for the Gamow peak and the ratio of effective S-factor to the S-factor evaluated at the Gamow peak energy for a resonant and non-resonant reaction. It is the effective S-factor which governs the reactivity beyond that given by the Coulomb barrier penetrability. Solar fusion reactivities are often calculated using the effective S-factor form of reactivity [7]. Any plasma screening effects can also be absorbed into the effective S-factor, in this work we will assume weak plasma coupling which is valid for typical ICF conditions [1] and therefore neglect screening effects. Experimental yield ratio measurements are direct measures of effective S-factors. Any microscopic cross section measurement at a single energy must be inferred from a measured effective S-factor. The level of approximation determines the accuracy of this inference.

Similar to the saddlepoint approximation to the Gamow peak, the small parameter $\epsilon$ can be used as an expansion coefficient for the effective S-factor. This expansion will give a formula relating the effective S-factor to the nuclear S-factor [16]:

$$S^{(N)}_{\mathrm{eff},\epsilon} = \sum_{n=0}^{N} S_n K_G^n \delta_{A,n}(\epsilon), \tag{15}$$

$$S_n = \left.\frac{d^{(n)}S}{dK^{(n)}}\right|_{K=K_G}. \tag{16}$$

Full expressions for $\delta_{A,n}$ are given in Supplementary Appendix SA, these terms can be used to evaluate the accuracy of the Gamow peak approximation. As long as $\epsilon$ is sufficiently small to validate the expansion, these equations provide the relationship between effective and nuclear S-factors. As shown by Eq. 15, the value of the effective S-factor is sensitive to local behaviour of S(K) around the Gamow peak energy, beyond just the value of S($K_G$). For non-resonant reactions a linear or quadratic order expansion of S(K) will likely be sufficient. As shown in Figure 1, the deviation between effective and nuclear S-factors is larger for resonant reactions and therefore more expansion terms would be required to maintain accuracy; it is therefore preferable to use resonant reactions as reference reactions. At higher temperatures or $\epsilon$, the Gamow peak will be broader and thus sample the S-factor over a larger range of energies. Consequently, more terms may be required for accuracy at higher $\epsilon$.

As discussed in Section 1, yield ratio measurements are used to infer target reaction S-factors relative to a well-known reference reaction. If we permit ourselves to utilise approximations (1)–(3), this inference uses the following equation:

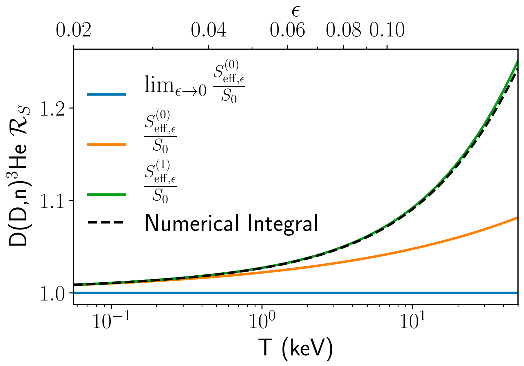

FIGURE 2
Plot showing the ratio of effective to nuclear S-factor, $\mathcal{R}_S = S_{\mathrm{eff}}(T)/S(K_G)$, for D (D,n)$^3$He at varying levels of approximation given by $S^{(N)}_{\mathrm{eff},\epsilon}$ as defined in Eq. 15. The black dashed line shows a numerical evaluation of $\mathcal{R}_S$ using the Bosch-Hale cross section fit [8]. Literature results [1] have utilised the $N$ = 0 approximation to $\mathcal{R}_S$.

$$S_{\mathrm{eff,\,tar}} = S_{\mathrm{eff,\,ref}}\mathcal{R}_f\mathcal{R}_G\mathcal{R}_Y, \tag{17}$$

where:

$$\mathcal{R}_G(T) = C_0 \exp[\chi(T)], \tag{18a}$$

$$\chi = \frac{3}{4^{1/3}}\left(K^{1/3}_{B,\mathrm{tar}} - K^{1/3}_{B,\mathrm{ref}}\right)T^{-1/3}, \tag{18b}$$

$$C_0 = \left(\frac{m_{12}Z_3Z_4}{m_{34}Z_1Z_2}\right)^{\frac{1}{3}}, \tag{18c}$$

$$\mathcal{R}_f = \frac{1+\delta_{12}}{1+\delta_{34}}\cdot\frac{f_3f_4}{f_1f_2}, \tag{18d}$$

where the target reaction involves species 1 and 2, and reference reaction species 3 and 4. The particle charges are $Z_i$ and the concentration fractions are $f_i$. The exponent function $\chi(T)$ is set by the difference in the two reactions' Coulomb barriers. These equations can be used to evaluate the target reaction $S_{\mathrm{eff}}$ from knowledge of the reference reaction effective S-factor. For non-resonant reactions, we expect the effective S-factor to be closely related to the nuclear S-factor evaluated at the Gamow peak energy. More formally, we can define a ratio of these terms, $\mathcal{R}_S$, such that:

$$S_{\mathrm{eff}} = S_0\mathcal{R}_S, \tag{19}$$

Accurately computing $\mathcal{R}_S$ requires *a-priori* knowledge of the S-factors' behaviour about $K_G$. This is unsurprising as a range of reaction energies is sampled in a thermal plasma. Without this *a-priori* knowledge, low order approximations to $\mathcal{R}_S$ must be made. It is worth noting that all errors associated with approximating $\mathcal{R}_S$ can be avoided if the effective S-factors are used. The effective S-factor is a more natural quantity to work with when considering fusion reactions in thermal plasmas, both in terrestrial fusion and astrophysics. In thermal plasmas temperature, reactivity and hence the effective S-factor have well-defined relationships between them and thus bypass the need to reference energy-dependent nuclear S-factors. Comparison between accelerator S-factor data in the energy domain and $S_{\mathrm{eff}}$ in the temperature domain is non-trivial. With sufficient accelerator data, Eq. 13 can be used to convert from the energy to temperature domain and allow direct comparison of accelerator and ICF inferred effective S-factors.

Within the literature, a commonly studied non-resonant reference is D (D,n)$^3$He—we will use this as a case study for errors introduced by approximations to $\mathcal{R}_s$. Figure 2 compares a precise numerical evaluation and various orders of the $\epsilon$-series. We see that an accurate approximation to $\mathcal{R}_S$ can be found with the $N$ = 1 $\epsilon$-series over the temperature range relevant to fusion plasmas. This presents an alternative method for relating the effective and nuclear S-factor. If we assume the nuclear S-factor is linear over the whole Gamow peak then [15]:

$$S(K) \to S_0 + S_1(K - K_G), \tag{20a}$$

$$\begin{aligned} S_{\mathrm{eff}} &= \delta_{A,0}\left[S_0 + S_1\frac{\delta_{A,1}}{\delta_{A,0}}K_G\right] \\ &= \delta_{A,0}S\left(K_G + \frac{\delta_{A,1}}{\delta_{A,0}}K_G\right) \end{aligned} \tag{20b}$$

It is simple to show that the argument of S(K) above is the mean energy for the Gamow peak [17], $\bar{K}_G$. Due to the positive skew of the Gamow peak (c.f. Figure 1), the mean is greater than the modal energy i.e., $\bar{K}_G > K_G$ for all temperatures. Rearranging the above gives a equation for the nuclear S-factor at $\bar{K}_G$:

$$S(\bar{K}_G) = \frac{S_{\mathrm{eff}}}{\delta_{A,0}}, \tag{20c}$$

$$\bar{K}_G = K_G + \frac{5}{6}T + \mathcal{O}(\epsilon). \tag{20d}$$

It is important to make a distinction here between $K_G$, $\bar{K}_G$ and the mean reaction energy, $\langle K\rangle$. As discussed above, $K_G$ and $\bar{K}_G$ are the mode and mean energies of the Gamow peak where we exclude the nuclear contribution to the cross section. Including the full cross section gives the true reaction rate averaged reaction energy, $\langle K\rangle$. This will be close in value to $\bar{K}_G$ for non-resonant reactions. It is worth noting that $\langle K\rangle$ can be measured from the first and second moment of the fusion product spectra [10].

In summary, the nuclear S-factor can be inferred from a measured effective S-factor for non-resonant reactions with low error. This does require additional correction factors to be evaluated which will depend on the local behaviour of the nuclear S-factor about the Gamow peak. This complicates the inference as *a-priori* information on the S-factor is required. Avoiding this complication by assuming $S(K)$ is linear or constant over the whole Gamow peak can introduce errors from a few percent to tens of percent depending on the temperature and reactions. It is therefore vitally important to consider the acceptable level of approximation and when necessary introduce *a-priori* information on the nuclear S-factor to improve the accuracy of the inference.

## 3 Hydrodynamic plasmas

### 3.1 Temperature variance

In the previous section we consider reactions from an isothermal fusion plasma. In ICF experiments the temperature rapidly varies in space and time. Therefore, there is an inherent range of temperatures in which fusion reactions are occurring. The reaction-weighted temperature distribution will have a mean temperature ($T$) and variance ($\sigma_T^2$) which we must now include in our analysis. The reaction-weighted (or burn-average) temperature can be inferred through primary fusion product spectroscopy (for appropriate reactions). The temperature variance can be inferred from multiple reactions' burn-average temperatures [18] or remain a free parameter with constraints on its magnitude obtained from hydrodynamics simulations. For reference, hydrodynamic simulation results from Casey et al. [1] give a range of 10%–50% for the ratio of burn-weighted standard deviation to mean temperatures. In this section we will quantify the effect of these temperature variances on yield ratios.

Previous work by Kabadi et al. [18] derived a second order yield-temperature relation which included the effect of temperature variance. We can extend this work to the effective S-factor reactivity formalism by including a correction factor, $\mathcal{R}_T$, to the yield ratio formula to account for temperature variance:

$$S_{\text{eff, tar}} = S_{\text{eff, ref}} \mathcal{R}_f \mathcal{R}_G \mathcal{R}_T \mathcal{R}_Y, \tag{21a}$$

The second-order correction factor is then given by:

$$\mathcal{R}_T = \frac{1}{1 + \left(\frac{\sigma_T}{T}\right)^2 \Gamma_T}, \tag{21b}$$

$$\begin{aligned} \Gamma_T &= \frac{T^2}{2} \frac{\langle \sigma v \rangle_{\text{ref}}}{\langle \sigma v \rangle_{\text{tar}}} \frac{d^2}{dT^2} \left( \frac{\langle \sigma v \rangle_{\text{tar}}}{\langle \sigma v \rangle_{\text{ref}}} \right) \\ &= \left[ \frac{\chi^2}{18} + \frac{\chi}{9} (3s_1 - 2) + \frac{1}{2} s_2 \right], \end{aligned} \tag{21c}$$

where $s_1$ and $s_2$ are functions of the target and reference reaction effective S-factors:

$$s_1 = \frac{S_{\text{eff, ref}}}{S_{\text{eff, tar}}} \cdot T \frac{d}{dT} \left( \frac{S_{\text{eff, tar}}}{S_{\text{eff, ref}}} \right), \tag{21d}$$

$$s_2 = \frac{S_{\text{eff, ref}}}{S_{\text{eff, tar}}} \cdot T^2 \frac{d^2}{dT^2} \left( \frac{S_{\text{eff, tar}}}{S_{\text{eff, ref}}} \right). \tag{21e}$$

The temperature-dependent function $\Gamma_T$ can be used to explore fusion reactions' sensitivity to temperature variance. As one might expect, yield ratios are sensitive to the local behaviour of the effective S-factor when there is a range of temperatures. As in the previous section, we must evaluate whether this sensitivity precludes an accurate inference of the target reaction S-factor. Separate to S-factor gradients, it is clear that a significant correction will arise from reaction pairs with large differences in Coulomb barrier penetrability. Figure 3 explores the temperature dependence of $\Gamma_T$ for the reaction pair $^3$He (D,p)$\alpha$ and D (D,n)$^3$He. We find that a temperature variance correction including only the Coulomb barrier terms, i.e., $s_1 = s_2 = 0$, provides a good estimate of the effect on yield ratio for the reaction pair $^3$He (D,p)$\alpha$ and D (D,n)$^3$He, for T < 30 keV. However, the effect of temperature variance on yield ratio can be large and therefore it is vital to include it in the analysis.

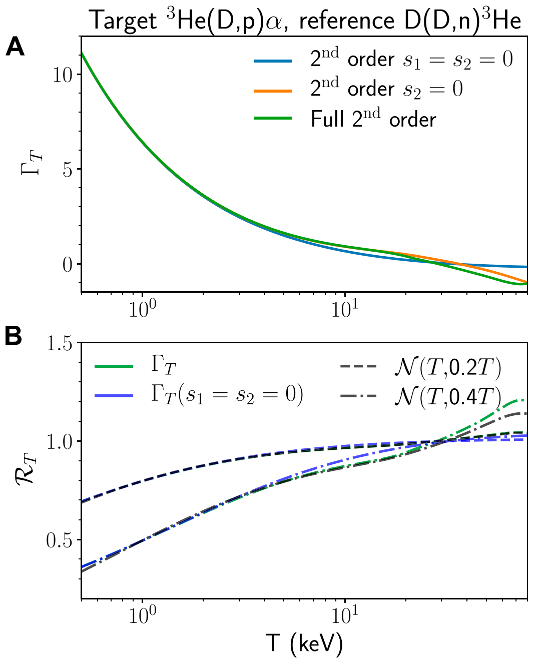

**FIGURE 3**
**(A)** Plot showing the temperature dependence of the second-order yield ratio temperature variance correction, $\Gamma_T$. Including the effect of the effective S-factor temperature is shown. **(B)** Plot showing the $\mathcal{R}_T$ value for Gaussian distributions of burn-averaged temperatures, denoted $\mathcal{N}(\mu, \sigma)$ where $\mu$ and $\sigma$ are the mean and standard deviation, respectively. Numerical evaluations are shown as black lines. Green lines show the second-order expressions for $\mathcal{R}_T$ using $\Gamma_T$, while the blue lines set $s_1 = s_2 = 0$.

### 3.2 Synthetic data study

We will use synthetic data to illustrate the propagation of errors involved with both our assumptions and typical measurement uncertainties. We will use the non-resonant reactions p (D,$\gamma$)$^3$He and D (D,n)$^3$He as our first target/reference pair. This will allow a comparison to recent ICF-based measurements by Zylstra et al. [3].

**TABLE 1** A table summarising the Bayesian model and MCMC sampling statistics for the two synthetic data studies in this work.

| Synthetic data study: target/References | Input Parameters (p) | Log Likelihood | Priors | Autocorrelation time, $\tau_{AC}$ |
|---|---|---|---|---|
| Hydrodynamic p (D,$\gamma$) $^3$He/D (D,n)$^3$He | $S_{\mathrm{eff},pD}$, $S_{\mathrm{eff},DD}$, $f_D$, $T$, $\sigma_T^2$, $\sigma_v^2$ | $-\frac{1}{2}\,(\frac{\mathcal{R}_Y^* - \mathcal{R}_Y\,(\mathbf{p})}{\sigma_{\mathcal{R}_Y}})^2$<br>$-\frac{1}{2}\,(\frac{T_s' - T_s\,(\mathbf{p})}{\sigma_{T_s}})^2_{DD}$ | $S_{\mathrm{eff},DD}/S^{\mathrm{BH}}_{\mathrm{eff},DD} \sim \mathcal{N}\,(1, 0.05)$, $f_D \sim \mathcal{N}\,(0.5, 0.01)$,<br>$\sigma_T \sim \mathcal{N}_{1/2}(1.62\ \mathrm{keV})$, $2m_D\sigma_v^2 \sim \mathcal{N}_{1/2}(1.08\ \mathrm{keV})$ | 100 |
| Kinetic D (D,n)$^3$He/ D (T,n)$\alpha$ | $S_{\mathrm{eff},DD}$, $S_{\mathrm{eff},DT}$, $\langle T_D \rangle_{DD}$, $\theta$, $\sigma_{T_D}^2$, $\sigma_v^2$ | $-\frac{1}{2}\,(\frac{\mathcal{R}_Y^* - \mathcal{R}_Y\,(\mathbf{p})}{\sigma_{\mathcal{R}_Y}})^2$<br>$-\frac{1}{2}\sum_{DT,DD}[\,(\frac{T_s' - T_s\,(\mathbf{p})}{\sigma_{T_s}})^2]$ | $S_{\mathrm{eff},DT}/S^{\mathrm{BH}}_{\mathrm{eff},DT} \sim \mathcal{N}\,(1, 0.05)$, $\sigma_{T_D} \sim \mathcal{N}_{1/2}(3\ \mathrm{keV})$,<br>$2m_D\sigma_v^2 \sim \mathcal{N}_{1/2}(2\ \mathrm{keV})$ | 105 |

A $\chi^2$ log likelihood function is used for the observables of yield ratio and spectral temperatures which have 10% and 0.2 keV errors, respectively. The starred values denote the exact calculated values (the synthetic observable) and model values are given as functions of the input parameters, **p**–full details of the synthetic observable models are given in Supplementary Appendix SB. Priors are defined with either Gaussian, $\mathcal{N}\,(\mu, \sigma)$, or half-normal, $\mathcal{N}_{1/2}\,(\sigma)$ distribution, where $\mu$ and $\sigma$ denote the mean and standard deviation. The superscript BH denotes the Bosch-Hale evaluation [8] of the respective S-factor. For the kinetic synthetic data study, the presence of species separation precludes prior distribution estimation of fuel fractions (instead a fixed value was used to illustrate potential error). The MCMC was performed with the Python library *emcee* [19] which implements Goodman and Weare's ensemble sampler [20]. In both studies, 32 walkers each taking 50,000 steps were used for sampling for a total chain length of 1.6 million ($\gg \tau_{AC}$). For parameter estimation from the chain, the first $2\tau_{AC}$ samples were removed, and the remaining samples are down-sampled by $\tau_{AC}/5$ giving ~80,000 random samples.

We will use the Bosch-Hale [8] fit for D (D,n)$^3$He and the Adelberger et al. [7] fit for p (D,$\gamma$)$^3$He to create the synthetic data. These fits use accelerator-based data down to nucleo-synthesis relevant energies, additional modern data is available for these reactions [21–23]. For measurement uncertainties we assume: a 10% uncertainty in the yield ratio, 0.2 keV error in the spectral temperature [9], 1% uncertainty in the fuel fill fractions and 5% uncertainty in the D (D,n)$^3$He S-factor. There are additional known unknowns which increase the uncertainty in our inference. The spectral temperature ($T_s$) is inflated above the burn-averaged temperature by fluid velocity effects [11–13], for D (D,n)$^3$He this is given by $2m_D\sigma_v^2$ where $\sigma_v^2$ is the fluid velocity variance. In addition, there is an unknown amount of temperature variance ($\sigma_T^2$) in the fusing plasma. For the chosen reference and target reactions it is not possible to use spectroscopic measurements to approximately account for these effects [18]. Instead, in this analysis, we will introduce these hydrodynamic effects as "nuisance" parameters with known half-normal ($> 0$) priors. These are chosen such that there was a 5% probability of $\sigma_T > 0.6T$ and $2m_D\sigma_v^2 > 0.4T$. To rigorously capture the propagation of errors, we utilise Markov Chain Monte Carlo (MCMC) to extract the posterior distribution of $S_{\mathrm{eff,\ pD}}$ which is consistent with the yield ratio measurement using the model given by Eq. 21a. MCMC methods [24] create samples from the product of likelihood and prior distributions i.e. the posterior distribution. This is done by using an ensemble of Markov chains which perform random walks where the probability of accepting a given step depends on the posterior probability.

For the synthetic data study, we will also assume no *a-priori* information on the target reaction effective S-factor and thus we will drop the $s_1$ and $s_2$ terms in $\Gamma_T$. The second part of the analysis is to extract the nuclear S-factor from the effective S-factor to allow comparison with accelerator data. This can be done using a 0th or 1st order approximation for $\mathcal{R}_S$ as defined in Section 2. The detailed summary of input parameters, likelihood, priors, number of steps and autocorrelation time is given in Table 1.

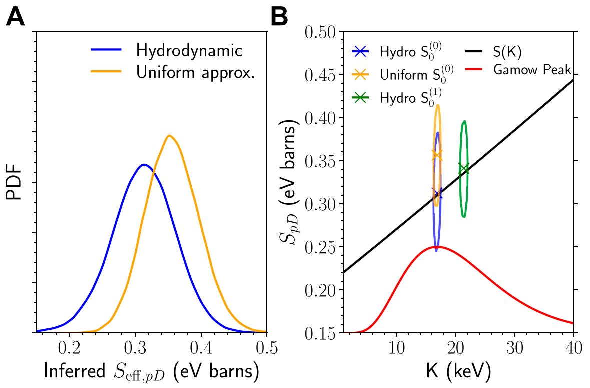

**FIGURE 4**
**(A)** Plot showing the probability distribution function (PDF) of the inferred p (D,$\gamma$)$^3$He effective S-factor for two different sets of assumptions on plasma conditions. For the study: the burn-averaged and spectrally inferred temperatures were 5.40 and 5.65 keV, respectively, the temperature standard deviation was 1.62 keV and the p/D fuel fractions were 50/50. The associated uncertainties are given at the beginning of Section 3.2. **(B)** Plot showing the inferred and "true" [7] nuclear S-factors from the synthetic data study. The crosses denote the centroid of the PDF and they are surrounded by the 1$\sigma$ contour, all inferences exhibit ~ 18% error. The zeroth order estimates ($S_0^{(0)}$) assume $S_{\mathrm{eff}} \approx S(K_G)$, while the first order estimate ($S_0^{(1)}$) uses Eqs 20a–20d. For reference, the Gamow peak is shown in red. The MCMC was performed with the Python library *emcee* [19], PDFs shown here use ~80,000 samples, see Table 1 for more detail.

Figure 4 shows the results of this synthetic data study. It is seen that the effects of fluid velocity and temperature variance introduce a systematic error of a similar order to the local behaviour of the S-factor around the Gamow peak. This systematic error will be increased for implosions with larger deviations from uniform conditions or for reactions with stronger sensitivity to temperature variance. It is also clear that the local behaviour of the S-factor around the Gamow peak is of equal importance. When these effects are properly accounted for, this synthetic data study suggests the analysis presented above can be highly accurate and remove much of the systematic error. This synthetic data study is directly comparable to the p (D,$\gamma$)$^3$He measurement by Zylstra et al. [3]. Using a uniform model, Zylstra et al. found a S-factor above model values [7] and recent accelerator data [25]. Using the hydrodynamic model described here would improve agreement between the ICF and accelerator measurements. Improvements in experimental uncertainties, particularly for the yield ratio measurement, will be necessary to reduce the remaining random error in the inference. Simulation studies could also be used to improve our priors on temperature variance and spectral broadening by isotropic flows. Alternatively, experiments with multiple reference reactions could be used to measure these effects independently.

# 4 Kinetic plasmas

Shock-driven ICF implosions can operate in a regime where the ion mean free path is large compared to gradient length scales. This gives rise to ion kinetic effects which violate many of the approximations of hydrodynamics. In the following we will consider the effect of species separation, thermal decoupling and non-Maxwellian velocity distributions on fusion product based diagnostics.

## 4.1 Species separation

Ion kinetic effects can cause the concentration of reactants to spatially and temporally vary. This will have an effect on the yields by modifying the reactant number densities and therefore the yield ratio and subsequent S-factor measurements.

It is considerably easier to consider plasmas with only two reactants which have both hetero- and homo-nuclear fusion reactions, for example a DT mixture. The concentration fractions, denoted $f_i$ for species $i$, then satisfy

$$f_2 = 1 - f_1, \tag{22}$$

simplifying the dependence down to just a single variable, $f_1$, for which we define:

$$\hat{f}_1 \equiv \frac{\iint f_1 n^2 \langle \sigma v \rangle dV dt}{\iint n^2 \langle \sigma v \rangle dV dt}, \tag{23}$$

$$\alpha_1 \equiv \frac{\mathrm{Var}(f_1)}{\hat{f}_1 \left(1 - \hat{f}_1\right)}, \tag{24}$$

where both $\hat{f}_1$ and $\alpha_1$ have values between 0 and 1 by definition and Var($x$) is the variance in variable $x$. The normalised variance, $\alpha_1$, makes use of the Bhatia-Davis inequality to ensure it is bounded between 0 and 1. In addition, the mean squared concentration can be related to $\hat{f}_1$ and $\alpha_1$ as follows:

$$\widehat{f_1^2} = \mathrm{Var}(f_1) + \hat{f}_1^2 = \hat{f}_1 \left(1 - \hat{f}_1\right) \alpha_1 + \hat{f}_1^2 \tag{25}$$

From Eqs 22–25, one can find the lowest order effect of fuel fractions on the associated yield ratios:

$$\frac{Y_{11}}{Y_{12}} \sim \mathcal{R}_f' \approx \frac{1}{2} \frac{\widehat{f_1^2}}{\hat{f}_1 - \widehat{f_1^2}} = \frac{1}{2} \left( \frac{\frac{\alpha_1}{1-\alpha_1} + \hat{f}_1}{1 - \hat{f}_1} \right), \tag{26}$$

$$\frac{Y_{11}}{Y_{22}} \sim \mathcal{R}_f' \approx \frac{\widehat{f_1^2}}{1 - 2\hat{f}_1 + \widehat{f_1^2}} = \left( \frac{\frac{\hat{f}_1}{1-\hat{f}_1} + \alpha_1}{\frac{1-\hat{f}_1}{\hat{f}_1} + \alpha_1} \right). \tag{27}$$

It is clear that even if the mean concentration remains fixed, increased variance in the concentration acts to increase the yield ratio of homo-to hetero-nuclear reactions ($Y_{11}/Y_{12}$). For the ratio of homo-nuclear reactions ($Y_{22}/Y_{11}$), if $\hat{f}_1 < 0.5$ then variance acts to decrease this yield ratio. Conversely, for $\hat{f}_1 > 0.5$ variance acts to increase this yield ratio. If all other contributions to the yield ratios are known, these two yield ratios can be used to find $\hat{f}_1$ and $\alpha_1$. Without full information of the other contributions, species separation can create large uncertainties if $\hat{f}_1$ and $\alpha_1$ are unconstrained. Species separation also modifies the spatial and temporal dependence of the reaction rate, this has an indirect effect on spectral measurements by altering the burn-averaging. A quantitative study of these terms will be given later in this section.

## 4.2 Thermal decoupling

The second ion kinetic effect we will consider is thermal decoupling between the reactant species. This is where the different ion species have different temperatures but still maintain a Maxwellian distribution of velocities. Thermal decoupling is expected to occur as strong shocks deliver different amounts of energy to different ion species depending on their ion mass and charge [26, 27]. If inter-species equilibration times are longer than the fusion burn period then the separate species temperatures will affect fusion reactivity and spectra.

As shown in Eq. 5, the reaction rate and reactivity is determined by the distribution of relative kinetic energies. First we will consider a locally uniform thermally decoupled plasma. It can be shown [9, 28] that the reactivity for Maxwellians with separate temperatures is equal to the single temperature Maxwellian reactivity evaluated at a mass weighted temperature:

$$T_{r12} = \frac{m_2 T_1 + m_1 T_2}{m_1 + m_2}. \tag{28}$$

Separately, the spectral temperature, which determines the width of the fusion product spectra, depends on the average centre of mass kinetic energy [10]. When reactants have separate temperatures, this introduces correlation between the relative and centre of mass velocity. This modifies the relationship between thermal and spectral temperature due to the cross section weighting. The spectral temperature from a thermally decoupled plasma is then given by:

$$T_{s12}^{th} = \frac{m_1 T_1 + m_2 T_2}{m_1 + m_2} + \frac{2}{3}\left(\frac{T_2 - T_1}{m_1 T_2 + m_2 T_1}\right)^2 m_1 m_2 \left(\langle K \rangle_{12} - \frac{3}{2} T_{r12}\right). \tag{29}$$

The second term in Eq. 29 is often neglected [29], it can however cause a significant increase in spectral temperature for large temperature separations. The superscript *th* is included to show that this is the spectral temperature without the effect of fluid velocity Doppler broadening. The average reaction energy, $\langle K \rangle$, can be calculated from the formula of Brysk [9] and Eq. 14:

$$\langle K \rangle = T^2 \frac{d}{dT} \ln\left(T^{\frac{3}{2}} \langle \sigma v \rangle\right) = K_G + \frac{5}{6} T + \frac{T^2}{S_{\text{eff}}} \frac{dS_{\text{eff}}}{dT}, \tag{30}$$

where for thermally decoupled plasmas the above formula is evaluated at the reactivity temperature, $T_{r12}$.

Thermally decoupled ICF plasmas will also have spatial and temporally changes in temperature; potentially with species separation as well. Therefore, the effect of burn-averaging must also be considered. For the hetero-nuclear reactions, the spectral width will depend on the burn-averaged value of Eq. 29, making it non-trivial to extract reactivity temperatures from spectral measurements. It is more straightforward for the homo-nuclear reaction as the spectral temperature, $\langle T_{s11} \rangle$, is simply the burn-averaged temperature, $\langle T_1 \rangle_{11}$, plus a fluid velocity variance term. Kabadi et al. [18] provided a methodology to extract an averaged temperature ratio $T_2/T_1$ using yield and spectral measurements from both hetero- and homo-nuclear reactions in the absence of species separation and fluid velocity. Note this methodology requires knowledge of the reactivities for both reactions i.e., known S-factors. We will follow from this methodology while maintaining the species separation terms from the previous section. First, the yield ratio can be manipulated to the following form:

$$\frac{Y_{12}}{Y_{11}} = 2\left(\frac{1 - \hat{f}_1}{\frac{\alpha_1}{1-\alpha_1} + \hat{f}_1}\right) \frac{\iint n_1^2 \langle \sigma v \rangle_{11} R dV dt}{Y_{11}}, \tag{31}$$

$$R(T_1, \theta) = \frac{\langle \sigma v \rangle_{12}(\theta\, T_1)}{\langle \sigma v \rangle_{11}(T_1)}, \tag{32}$$

$$\theta = \frac{T_{r12}}{T_1} = \frac{m_1 \cdot \frac{T_2}{T_1} + m_2}{m_1 + m_2}. \tag{33}$$

We will assume the thermal decoupling parameter, $\theta$, is approximately constant over the burn volume and time. This allows us to use the same model as used for single temperature plasma with $T_1$ expanded about homo-nuclear burn-averaged temperature, $\langle T_1 \rangle_{11}$, and the species separation fuel fraction term, $\mathcal{R}_f'$:

$$S_{\text{eff},12}(\theta \langle T_1 \rangle_{11}) = S_{\text{eff},11}(\langle T_1 \rangle_{11}) \mathcal{R}_f' \mathcal{R}_G' \mathcal{R}_T' \mathcal{R}_Y, \tag{34a}$$

$$\mathcal{R}_G' = \left(\frac{m_{12} Z_1 \theta^2}{m_{11} Z_2}\right)^{\frac{1}{3}} \exp[\chi'], \tag{34b}$$

$$\chi' = \frac{3}{4^{1/3}} \left[\left(\frac{K_{B,12}}{\theta}\right)^{1/3} - K_{B,11}^{1/3}\right] \langle T_1 \rangle_{11}^{-1/3} \tag{34c}$$

$$\mathcal{R}_T' = \frac{1}{1 + \left(\frac{\sigma_{T_1}}{\langle T_1 \rangle_{11}}\right)^2 \Gamma_T'}, \tag{34d}$$

$$\Gamma_T' = \frac{\chi'^2}{18} + \frac{\chi'}{9}(3s_1' - 2) + \frac{1}{2} s_2' \tag{34e}$$

To proceed we need estimates of $\theta$, $\langle T_1 \rangle_{11}$, $\sigma_{T_1}^2$ and $\mathcal{R}_f'$. If available, information from spectroscopic measurements can be used to constrain these parameters. However, this is non-trivial. The measured spectral temperature for the homo-nuclear reaction will be inflated above $\langle T_1 \rangle_{11}$ by fluid velocity variance [11–13], $\sigma_v^2$. The measured spectral temperatures are given by:

$$\langle T_{s11} \rangle = \langle T_1 \rangle_{11} + 2m_1 \sigma_v^2, \tag{35}$$

$$\langle T_{s12} \rangle = \frac{\iint \frac{1-f_1}{f_1} n_1^2 \langle \sigma v \rangle_{11} T_1 P dV dt}{Y_{12}} + (m_1 + m_2)\sigma_v^2, \tag{36}$$

$$P(T_1, \theta) = \frac{T_{s12}^{th}(T_1, \theta)}{T_1} R(T_1, \theta) \tag{37}$$

It is clear from the form of $\langle T_{s12} \rangle$ that it will be sensitive to correlations of reactant concentration and temperature. Quantifying this correlation will introduce additional parameters. Instead, we consider the zeroth order effect of reactant concentration on the burn-averaging i.e., a multiplicative factor of $\mathcal{R}_f'$ on the yield integrals. Then, expanding $P$ in $T_1$ about $\langle T_1 \rangle_{11}$ at constant $\theta$ yields:

$$\langle T_{s12} \rangle \approx \frac{T_{s12}^{th}(\langle T_1 \rangle_{11}, \theta)}{\mathcal{R}_T'} \left(1 + \Gamma_{T_{s12}} \left(\frac{\sigma_{T_1}}{\langle T_1 \rangle_{11}}\right)^2\right) + (m_1 + m_2)\sigma_v^2 \tag{38}$$

$$\Gamma_{T_{s12}} = \left[s_1' + \frac{\chi'}{3}\right] + \frac{\langle T_1 \rangle_{11}^2}{T_{s12}^{th}(\langle T_1 \rangle_{11}, \theta)} \frac{d}{dT_1}\left(\frac{T_{s12}^{th}}{T_1}\right)_{T_1 = \langle T_1 \rangle_{11}}, \tag{39}$$

With the approximations applied above, the derived system is both under-determined and non-linear, with 6 unknowns ($\theta$, $\langle T_1 \rangle_{11}$, $\sigma_{T_1}^2$, $\mathcal{R}_f'$, $\sigma_v^2$ and the target effective S-factor) and up to 3 measurables (yield ratio and two spectral temperatures). An additional issue is the potential degeneracy of thermal decoupling and fluid velocity variance. If $m_2 > m_1$, then increased $T_2$ over $T_1$ has the same effect on the spectral temperatures as increased $\sigma_v^2$. One approach to tackle this would be to further expand the system and constrain the problem by introducing additional spectral information such as the isotropic mean shift [13, 30, 31].

However, very small errors ($< 5$ keV) are required on these measurements to isolate the fluid velocity variance effect from the spectral temperatures—for DT neutrons this corresponds to a $< 9$ km/s error on the isotropic velocity which is outside the current capabilities [30, 31]. Alternatively, priors on the magnitude of fluid velocity and temperature variance are necessary—this is the approach which was used in Section 3.2. Separate to these effects, it is worth noting that the species separation term only affects the yield ratio measurement i.e., it is not constrained by additional spectral measurements. Therefore, an external estimate on $\mathcal{R}_f'$ is required to infer the target S-factor value.

A synthetic data study can be used to explore S-factor inference in the presence of species separation and thermal decoupling. The reference reaction is taken as D (T,n)$\alpha$ and target D (D,n)$^3$He such that neutron spectral measurements can be included in the analysis. While both of these reactions are well known, this study serves to test the efficacy of the model when complete spectral information is available. To provide a suitably generic set of test conditions, we consider a multivariate normal distribution of reaction rate weighted temperatures and concentrations:

$$n^2 \langle \sigma v \rangle_{DD} dV dt = A \mathcal{N}\left(\underline{\mu}, \underline{\Sigma}\right) dT_D dT_T df_D, \tag{40}$$

$$\underline{\mu} = \begin{bmatrix} T_D - \langle T_D \rangle \\ T_T - \langle T_T \rangle \\ f_D - \langle f_D \rangle \end{bmatrix}, \tag{41}$$

$$\underline{\Sigma} = \begin{bmatrix} \varsigma_{T_D}^2 & C_{T_D,T_T} \varsigma_{T_D} \varsigma_{T_T} & C_{T_D,f_D} \varsigma_{T_D} \varsigma_{f_D} \\ C_{T_D,T_T} \varsigma_{T_D} \varsigma_{T_T} & \varsigma_{T_T}^2 & C_{T_T,f_d} \varsigma_{T_T} \varsigma_{f_D} \\ C_{T_D,f_D} \varsigma_{T_D} \varsigma_{f_D} & C_{T_T,f_d} \varsigma_{T_T} \varsigma_{f_D} & \varsigma_{f_D}^2 \end{bmatrix}, \tag{42}$$

$$A = \iint n^2 \langle \sigma v \rangle_{DD} dV dt \tag{43}$$

on the domain $T_D, T_T \in [T_{\mathrm{min}}, \infty]$ and $f_D \in [0, 1]$, where $T_{\mathrm{min}}$ is chosen to be 0.5 keV. We expect strong positive correlation between $T_D$ and $T_T$ as the ion species are heated by the same processes and exchange energy through collisions. Correlations between species concentration and temperature are more difficult to predict. Thermo-diffusion models [32] suggest a negative correlation between the lighter species concentration and temperature in a "saturated" state. It is worth noting that the above model does not have constant value of $\theta$. Given these physical insights, in this study the following fixed parameters are chosen for the model defined in Eqs 40–42:

$$\langle T_D \rangle = 10\mathrm{keV}, \quad \langle T_T \rangle = 15\mathrm{keV}, \varsigma_{T_D} = 2\mathrm{keV}, \quad \varsigma_{T_T} = 3keV, C_{T_D,T_T} = 0.9, \quad C_{T_D,f_D} = C_{T_T,f_D} = -0.2,$$

while $\langle f_D \rangle$ and $\varsigma_{f_D}$ are varied to investigate the effect of species separation. Given a yield ratio and two spectral temperature measurements, we can infer the product $\mathcal{R}_f' S_{\mathrm{eff,DD}}$, c. f. Equation 34a. Without further information, these terms cannot be separated. For the purpose of inferring a nuclear S-factor we will assume the "hydrodynamic" value $\mathcal{R}_f' = 2$ i.e., one that is set by the initial fuel fractions of 50/50 DT. This assumption will cause a systematic error in the presence of species separation. As in Section 3.2, MCMC will be used to find the distribution of inferred S-factors given the model outlined in this section. The same prior distributions for fluid velocity and temperature variance as given in Section 3.2 will be used in this analysis, although scaled to the D (D,n)$^3$He spectral temperature. Figure 5 shows the results of the synthetic data study and details of the Bayesian model are given in Table 1. It is shown that the spectral measurements can infer accurate temperature information when both species separation and thermal decoupling are in effect. However, species separation creates a large systematic uncertainty in the S-factor measurement. This is especially true when the mean concentration of reactants is altered. A possible resolution to this would be to have use two reference reactions. In the most straightforward application, this would utilise both of the homo-nuclear reactions to avoid the need for additional reactants with their own species separation effects. With known

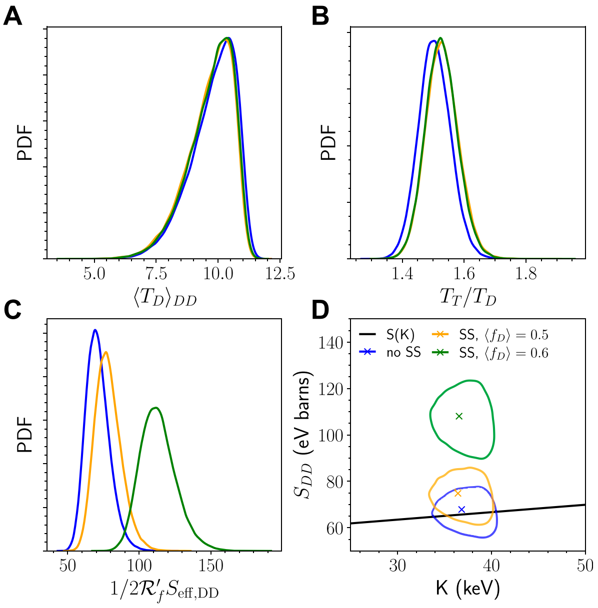

**FIGURE 5**
For all subplots: blue data includes no species separation (SS), orange data includes species separation with $\langle f_D \rangle = 0.5$ and $\varsigma_{f_D} = 0.1$ and green data includes species separation with $\langle f_D \rangle = 0.6$ and $\varsigma_{f_D} = 0.1$. **(A)** Plot showing the probability distribution functions (PDFs) for the inferred D (D,n)$^3$He burn averaged deuteron temperature. The long tail arises from the unknown fluid velocity variance contribution to the spectral temperatures. **(B)** Plot showing the inferred ratio of triton to deuteron temperatures. **(C)** Plot showing the PDFs of the inferred product of effective S-factor and species separation term. **(D)** Plot showing the inferred and "true" [8] nuclear S-factors from the synthetic data study. The crosses denote the centroid of the PDF and they are surrounded by the 1$\sigma$ contour. In inferring the nuclear S-factor from $\mathcal{R}_f' S_{\mathrm{eff}}$, we use the "hydrodynamic" value $\mathcal{R}_f' = 2$ which is set by the initial 50/50 DT fill. The MCMC was performed with the Python library *emcee* [19], PDFs shown use ~80,000 samples, see Table 1 for more detail.

S-factors, the above analysis can be used to infer a value of $\mathcal{R}_f^\prime$ and thus the magnitude of the species separation effect. As an example, in a DT mixture one could use D (T,n)$\alpha$ and D (D,n)$^3$He to measure species separation and thermal decoupling effects, this could then aid in the inference of the T (T,2n)$\alpha$ cross section.

### 4.3 Non-Maxwellian velocity distributions

Once the reactant velocity distributions are non-Maxwellian we must revisit the definition of reactivity and the Gamow peak. Without *a-priori* knowledge of the form the velocity distributions, we have no known relationships between the yields, spectral measurements, effective S-factor and Gamow peak energy. This makes it difficult to relate the cross section to yield ratios. One possible approach is to introduce a model which can predict the kinetic ion velocity distributions in the experiment [33, 34]. Synthetic diagnostics of yield and spectra could be compared to experimental values [33] and sensitivity to varying model S-factors can be studied in this way. However, this cannot be used to infer an S-factor without making the assumption that the ion kinetic model had very accurately reproduced the reactant velocity distributions present in the experiment. In absence of a model, one can determine if the reactant velocity distributions have become non-Maxwellian via spectroscopy methods by comparison of the first two spectral moments to the Maxwellian prediction [35]. This suggests a future avenue of investigation into the relationship between reactivity and spectral moments to improve understanding of yields in highly kinetic experiments. This future work would be key in understanding cross section measurements in the presence of non-Maxwellian velocity distributions.

## 5 Discussion

Inertial confinement fusion (ICF) experiments create a unique laboratory environment in which thermonuclear fusion reactions occur within a plasma. Previous experiments have leveraged this environment to perform measurements of light ion fusion S-factors without the need for screening corrections [1–3]. However, to further increase the accuracy of ICF-based measurements requires an examination of the physical mechanisms affecting fusion yields and spectra. In this work we have discussed and analysed the effects of the inherent range of reaction energies, spatial and temporal thermal temperature variation, and kinetic effects such as species separation.

We showed that yield ratio measurements in an uniform Maxwellian plasma are directly related to the effective S-factors of the reactions. By considering expansions about the Gamow peak we were able to relate the effective and nuclear S-factors as well as provide the commonly used saddlepoint approximation to the reactivity ratio. It was seen that the local behaviour of the nuclear S-factor at the Gamow peak can affect its inference. In a hydrodynamic plasma, spatial and temporal temperature variation was seen to effect yield ratio measurements. The temperature variation has the largest effect on the yield ratio when the reactants have large differences in $K_B$ due to charge and/or mass. A synthetic data study was used to illustrate the propagation of errors in S-factor inference in hydrodynamic ICF plasmas. The results showed that using a more detailed model can remove systematic uncertainty present in previous, more approximate, analyses.

Finally, we considered the effect of notable ion kinetic behaviours, particularly species separation and thermal decoupling. To simplify the problem, only two species plasmas were considered. Then, the model developed for hydrodynamic plasmas was extended to include the ion kinetic effects. In order to constrain thermal decoupling, additional spectroscopic data was included *via* both hetero- and homo-nuclear spectral temperatures. The dominant effect of species separation was to alter the yield ratios. Again, a synthetic data study was used to investigate the efficacy of these models in handling these novel kinetic factors. It was found that thermal decoupling is well constrained by the spectral measurements but species separation can cause large changes in the yield ratios and hence large systematic uncertainty in the S-factor inference.

The synthetic data studies in this work give single examples of the inference process with chosen physical parameters and priors subject to bias. Future work should provide a more systematic approach to this data study. The proposed models of distributions of temperatures, velocities and concentrations should be compared to integrated hydrodynamic and kinetic simulations. This will ensure confidence in the conclusions drawn from these case studies.

## Data availability statement

The raw data supporting the conclusion of this article will be made available by the authors, without undue reservation.

## Author contributions

AC is the main author and contributed the main body of the work. IG-F performed the initial work on S-factor inference in hydrodynamic plasmas. BA provided knowledge and insights particularly in respect to ion kinetic effects in ICF implosions. JC supervised the work and provided an expert perspective on the hydrodynamics of ICF implosions.

## Acknowledgments

The authors would like to thank G. Kagan for useful discussions.

## Conflict of interest

## Publisher's note

## Supplementary material

The Supplementary Material for this article can be found online at: https://www.frontiersin.org/articles/10.3389/fphy.2022.937972/full#supplementary-material

## References

1. Casey DT, Sayre DB, Brune CR, Smalyuk VA, Weber CR, Tipton RE, et al. Thermonuclear reactions probed at stellar-core conditions with laser-based inertial-confinement fusion. *Nat Phys* (2017) 13(12):1227–31. doi:10.1038/nphys4220

2. Zylstra AB, Herrmann HW, Gatu Johnson M, Kim YH, Frenje JA, Hale G, et al. Using inertial fusion implosions to measure the T +$^{3}$He fusion cross section at nucleosynthesis-relevant energies. *Phys Rev Lett* (2016) 117:035002. doi:10.1103/physrevlett.117.035002

3. Zylstra AB, Herrmann HW, Kim YH, McEvoy A, Frenje JA, Gatu Johnson M, et al. $^{2}$H($p$, $\gamma$)$^{3}$He cross section measurement using high-energy-density plasmas. *Phys Rev C* (2020) 101:042802. doi:10.1103/physrevc.101.042802

4. Otuka N, Dupont E, Semkova V, Pritychenko B, Blokhin AI, Aikawa M, et al. Towards a more complete and accurate experimental nuclear reaction data library (exfor): International collaboration between nuclear reaction data centres (nrdc). *Nucl Data Sheets* (2014) 120:272–6. doi:10.1016/j.nds.2014.07.065

5. Spitaleri C, Cognata ML, Lamia L, Pizzone RG, Tumino A. Astrophysics studies with the trojan horse method. *Eur Phys J A* (2019) 55(9):161–29. doi:10.1140/epja/i2019-12833-0

6. Chadwick MB, Obložinský P, Herman M, Greene NM, McKnight RD, Smith DL, et al. ENDF/B-VII.0: Next generation evaluated nuclear data library for nuclear science and technology. *Nucl Data Sheets* (2006) 107(12):2931–3060. Evaluated Nuclear Data File ENDF/B-VII.0. doi:10.1016/j.nds.2006.11.001

7. Adelberger EG, García A, Hamish Robertson RG, Snover KA, Balantekin AB, Heeger K, et al. Solar fusion cross sections. II. Theppchain and CNO cycles. *Rev Mod Phys* (2011) 83:195–245. doi:10.1103/revmodphys.83.195

8. Bosch H-S, Hale GM. Improved formulas for fusion cross-sections and thermal reactivities. *Nucl Fusion* (1992) 32(4):611–31. doi:10.1088/0029-5515/32/4/i07

9. Brysk H. Fusion neutron energies and spectra. *Plasma Phys* (1973) 15(7):611. doi:10.1088/0032-1028/15/7/001

10. Ballabio L, Allne JK, Gorini G. Relativistic calculation of fusion product spectra for thermonuclear plasmas. *Nucl Fusion* (1998) 38(11):1723–35. doi:10.1088/0029-5515/38/11/310

11. Appelbe B, Chittenden J. The production spectrum in fusion plasmas. *Plasma Phys Control Fusion* (2011) 53(4):045002. doi:10.1088/0741-3335/53/4/045002

12. Murphy TJ. The effect of turbulent kinetic energy on inferred ion temperature from neutron spectra. *Phys Plasmas* (2014) 21(7):072701. doi:10.1063/1.4885342

13. Munro DH. Interpreting inertial fusion neutron spectra. *Nucl Fusion* (2016) 56(3):036001. doi:10.1088/0029-5515/56/3/036001

14. John N. Bahcall. Non-resonant nuclear reactions at stellar temperatures. *Astrophysical J* (1966) 143:259–61.

15. Clayton DD. *Principles of stellar evolution and nucleosynthesis*. University of Chicago press (1983).

16. Bahcall JN. *Neutrino astrophysics*. Cambridge University Press (1989).

17. Williams MMR. A generalized energy exchange kernel for inelastic neutron scattering and thermonuclear reactions. *J Nucl Energ* (1971) 25(10):489–501. doi:10.1016/0022-3107(71)90029-3

18. Kabadi NV, Adrian PJ, Bose A, Casey DT, Frenje JA, Johnson MG, et al. A second order yield-temperature relation for accurate inference of burn-averaged quantities in multi-species plasmas. *Phys Plasmas* (2021) 28(2):022701. doi:10.1063/5.0032139

19. Foreman-Mackey D, Hogg DW, Lang D, Goodman J. emcee: The mcmc hammer. *Publications Astronomical Soc Pac* (2013) 125(925):306–12. doi:10.1086/670067

20. Goodman J, Weare J. Ensemble samplers with affine invariance. *Comm App Math Comp Sci* (2010) 5(1):65–80. doi:10.2140/camcos.2010.5.65

21. Mossa V, Stöckel K, Cavanna F, Ferraro F, Aliotta M, Barile F, et al. The baryon density of the universe from an improved rate of deuterium burning. *Nature* (2020) 587(7833):210–3. doi:10.1038/s41586-020-2878-4

22. Turkat S, Hammer S, Masha E, Akhmadaliev S, Bemmerer D, Grieger M, et al. Measurement of the $^{2}$H($p$, $\gamma$)$^{3}$He $s$ factor at 265–1094 kev. *Phys Rev C* (2021) 103: 045805. doi:10.1103/physrevc.103.045805

23. Leonard DS, Karwowski HJ, Brune CR, Fisher BM, Ludwig EJ. Precision measurements of $^{2}$H($d$, $p$)$^{3}$H and $^{2}$H($d$, $n$)$^{3}$He total cross sections at big bang nucleosynthesis energies. *Phys Rev C* (2006) 73:045801. doi:10.1103/PhysRevC.73.045801

24. Van Ravenzwaaij D, Cassey P, Brown SD. A simple introduction to Markov chain monte–carlo sampling. *Psychon Bull Rev* (2018) 25(1):143–54. doi:10.3758/s13423-016-1015-8

25. Casella C, Costantini H, Lemut A, Limata B, Bonetti R, Broggini C, et al. First measurement of the d(p, $\gamma$ )3he cross section down to the solar gamow peak. *Nucl Phys A* (2002) 706(1):203–16. doi:10.1016/s0375-9474(02)00749-2

26. Rinderknecht HG, Rosenberg MJ, Li CK, Hoffman NM, Kagan G, Zylstra AB, et al. Ion thermal decoupling and species separation in shock-driven implosions. *Phys Rev Lett* (2015) 114:025001. doi:10.1103/physrevlett.114.025001

27. Kabadi NV, Simpson R, Adrian PJ, Bose A, Frenje JA, Gatu Johnson M, et al. Thermal decoupling of deuterium and tritium during the inertial confinement fusion shock-convergence phase. *Phys Rev E* (2021) 104:L013201. doi:10.1103/physreve.104.l013201

28. Bellei C, Rinderknecht H, Zylstra A, Rosenberg M, Sio H, Li CK, et al. Species separation and kinetic effects in collisional plasma shocks. *Phys Plasmas* (2014) 21(5):056310. doi:10.1063/1.4876614

29. Inglebert A, Canaud B, Larroche O. Species separation and modification of neutron diagnostics in inertial-confinement fusion. *EPL (Europhysics Letters)* (2014) 107(6):65003. doi:10.1209/0295-5075/107/65003

30. Hatarik R, Nora RC, Spears BK, Eckart MJ, Grim GP, Hartouni EP, et al. Using multiple neutron time of flight detectors to determine the hot spot velocity. *Rev Scientific Instr* (2018) 89(10):10I138. doi:10.1063/1.5039372

31. Mannion OM, Knauer JP, Glebov VY, Forrest CJ, Liu A, Mohamed ZL, et al. A suite of neutron time-of-flight detectors to measure hot-spot motion in direct-drive inertial confinement fusion experiments on omega. *Nucl Instr Methods Phys Res Section A: Acc Spectrometers, Detectors Associated Equipment* (2020) 964:163774. doi:10.1016/j.nima.2020.163774

32. Kagan G, Tang X-Z. Thermo-diffusion in inertially confined plasmas. *Phys Lett A* (2014) 378(21):1531–5. doi:10.1016/j.physleta.2014.04.005

33. Higginson DP, Ross JS, Ryutov DD, Fiuza F, Wilks SC, Hartouni EP, et al. Kinetic effects on neutron generation in moderately collisional interpenetrating plasma flows. *Phys Plasmas* (2019) 26(1):012113. doi:10.1063/1.5048386

34. Appelbe BD. *Primary neutron spectra in ion vlasov-fokker-planck simulations* (2022). in prep.

35. Mannion OM, Taitano WT, Appelbe BD, Crilly AJ, Forrest CJ, Glebov VY, et al. *Evidence of non-maxwellian ion velocity distributions in spherical shock driven implosions* (2022). in preparation.

frontiers | Frontiers in Physics

TYPE Original Research
PUBLISHED 05 October 2022
DOI 10.3389/fphy.2022.1009489

EDITED BY
Pierre Descouvemont,
Université libre de Bruxelles, Belgium

REVIEWED BY
Petr Navratil,
TRIUMF, Canada
Andres Arazi,
Comisión Nacional de Energía Atómica,
Argentina

*CORRESPONDENCE
Michael Wiescher,
mwiesche@nd.edu

SPECIALTY SECTION
This article was submitted to Nuclear Physics,
a section of the journal
Frontiers in Physics

RECEIVED 02 August 2022
ACCEPTED 14 September 2022
PUBLISHED 05 October 2022

CITATION
Wiescher M, deBoer RJ and Görres J (2022), Threshold effects in the $^{10}$B($p$,$\alpha$)$^{7}$Be, $^{12}$C($p$,$\gamma$)$^{13}$N and $^{14}$N($p$,$\gamma$)$^{15}$O reactions.
*Front. Phys.* 10:1009489.
doi: 10.3389/fphy.2022.1009489

# Threshold effects in the $^{10}$B($p$,$\alpha$)$^{7}$Be, $^{12}$C($p$,$\gamma$)$^{13}$N and $^{14}$N($p$,$\gamma$)$^{15}$O reactions

Michael Wiescher*, Richard James deBoer and Joachim Görres

Department of Physics and Astronomy, University of Notre Dame, Notre Dame, IN, United States

The typical energy range for charge particle interactions in stellar plasmas corresponds to a few 10s or 100s of keV. At these low energies, the cross sections are so vanishingly small that they cannot be measured directly with accelerator based experimental techniques. Thus, indirect studies of the compound structure near the threshold are used in the framework of reaction models to complement the direct data in order to extrapolate the cross section into the low energy regime. However, at the extremely small cross sections of interest, there maybe other quantum effects that modify the such extracted cross section. These may result from additional nuclear interactions associated with the threshold itself or could be due to other processes, such as electron screening. Measurements in plasma environments like at the OMEGA or National Ignition Facility facilities offer an entirely new set of experimental conditions for studying these types of reactions, often directly at the energies of interest. In this paper, we examine three reaction, $^{10}$B($p$,$\alpha$)$^{7}$Be, $^{12}$C($p$,$\gamma$)$^{13}$N and $^{14}$N($p$,$\gamma$)$^{15}$O, which have all been measured at very low energies using accelerator based methods. All three reactions produce relatively long-lived radioactive nuclei, which can be collected and analyzed at plasma facilities using a variety of collection and identification techniques.

KEYWORDS

**nuclear plasmas, nuclear reactions, R-matrix, electron screening, nuclear astrophysics**

## 1 Introduction

Nuclear reactions in high density plasma environments in the interior of stars are the engine for the chemical evolution of our universe. The nuclear reaction rates used for simulating the associated nucleosynthesis patterns rely mostly on accelerator based reaction cross section measurements folded with the Maxwell Boltzmann energy distribution of the interacting particles. However, the laboratory cross section data are typically obtained at much higher energies than those that occur in a stellar environment and in most cases the reaction rates rely on theoretical extrapolation into the stellar energy range, the so-called Gamow window. While such extrapolations require a reliable understanding of the nuclear structure near the particle threshold as well of the contributing nuclear reaction components and mechanisms, they also require a reliable understanding of the environmental conditions in the stellar plasma. The latter is not yet available and relies entirely on model predictions [1], which do not seem to match the available experimental data very well. This requires the development of an experimental program in nuclear reaction studies in a hot plasma environment. The production of a stellar plasma at sufficiently high temperature and density conditions in the laboratory is a unique challenge, but the development of high power laser induced inertial plasma environments seems to provide a path in that direction. First experiments on the study of fusion reactions between different hydrogen and helium isotopes have revealed promising results, but they have focused so far on fusion reactions between low $Z$ isotopes, such as $^3$H ($^2$H, $n$)$^4$He [2] or $^3$H ($^3$H, $2n$)$^4$He [3], and $^3$He ($^3$H, $p$)$^5$Li and $^3$He ($^3$He, $2p$)$^4$He fusion branches [4] where the cross section study is less handicapped by the Coulomb barrier and supported by the strong interaction based fusion mechanism.

Inertial confinement fusion (ICF) [5] facilities like the National Ignition Facility (NIF) [6] and OMEGA [7] endeavour to create an environment similar to that found in a nuclear detonation or in the core of a star, but under highly spatially confined and controlled conditions. This is accomplished by focusing an array of high powered laser beams onto a tiny pellet or capsule of fusion fuel. The radiation pressure causes its rapid implosion achieving for short nano-second time periods temperature and density conditions comparable to stellar plasma conditions [8]. So far nuclear reaction studies at both OMEGA and NIF have not gone beyond the fusion of very light hydrogen and helium isotopes. To explore the value of these facilities for a broader nuclear astrophysics program, it might be appropriate to investigate possible measurements for higher $Z$ isotopes. A first attempt has been made recently to study the $^{10}$B($\alpha$, $n$)$^{13}$N reaction [9] at NIF providing a first glimpse at the challenges such measurements will have to be overcome, both in the collection and in identification of the reactions products [10].

While the cross section of the aforementioned fusion reactions between hydrogen isotopes is rather large, many, if not most, of the reactions of interest to astrophysics are radiative capture processes. They typically have a substantially lower cross section since the Hamiltonian is determined by the electromagnetic and not the strong interaction force. Nevertheless the production and measurement of long-lived reaction products might provide a sufficiently efficient way to directly determine the reaction rate for the temperature and density condition of an inertial fusion plasma.

In the following sections, we will discuss three suggested reactions $^{10}$B($p$,$\alpha$)$^7$Be, $^{12}$C($p$,$\gamma$)$^{13}$N and $^{14}$N($p$,$\gamma$)$^{15}$O and their role in different stellar environments. We will also present the cross sections anticipated for conditions that can be reached at laser plasma facilities such as OMEGA and NIF. These cross sections are based on extrapolations of accelerator based data using phenomenological $R$-matrix theory [17, 11]. The $R$-matrix calculations presented here were performed with the AZURE2 code [13] and are extensions of those described in detail in the works of [13,14], and [15] for the $^{10}$B($p$,$\alpha$)$^7$Be, $^{12}$C($p$,$\gamma$)$^{13}$N and $^{14}$N($p$,$\gamma$)$^{15}$O reactions, respectively. Therefore, only the details relevant to this work are discussed here. The anticipated reaction yield in the laser driven plasma environment will be presented and the feasibility of radiative capture experiments at laser plasma facilities will be estimated and discussed.

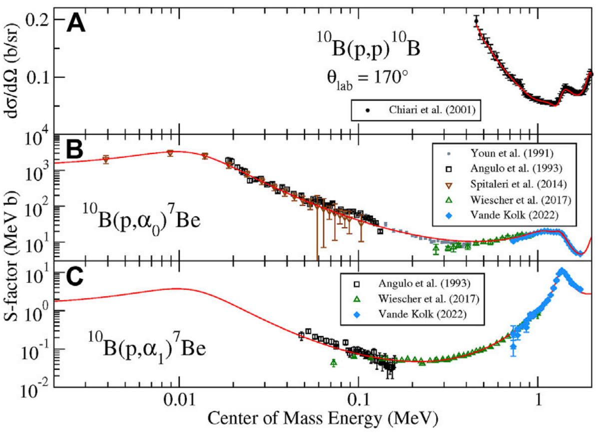

**FIGURE 1**
Simultaneous $R$-matrix fits to **(A)** the scattering data of Chiari et al. [20], **(B)** the $^{10}$B($p$, $\alpha_0$)$^7$Be (transition to the ground state of $^7$Be) data of Youn et al. [21], Angulo et al. [22], Wiescher et al. [18], Spitaleri et al. [23], and Vande Kolk et al. [14] and **(C)** the $^{10}$B($p$, $\alpha_1$)$^7$Be (transition to the first excited state of $^7$Be) data of Angulo et al. [24], Wiescher et al. [18], and Vande Kolk et al. [14].

## 2 The $^{10}$B($p$,$\alpha$)$^7$Be reaction

The $^{10}$B($p$,$\alpha$)$^7$Be reaction plays an important role in the nucleosynthesis of first stars. It effectively reduces the flow of the competing $^{10}$B($\alpha$,$d$)$^{12}$C reaction by which the primordial He and Li can be converted into C, N, and O [16]. On the other hand, it feeds two alternative branches of the hot $pp$-chains [17], $^7$Be($e^-$,$\nu$)$^7$Li($\alpha$,$\gamma$)$^{11}$B($\alpha$,$n$)$^{14}$N and at higher temperatures $^7$Be($\alpha$,$\gamma$)$^{11}$C($p$,$\gamma$)$^{12}$N($\beta^+$)$^{12}$C. Both branches facilitate alternative break-out possibilities, however without the production of the important deuterons as fuel for the hot $pp$-chains.

The $^{10}$B($p$,$\alpha$)$^7$Be reaction has been extensively studied over a wide energy range between 20 keV and 2 MeV using a number of different accelerator facilities (see Wiescher et al. [18] and references therein). The reaction cross section is considerably larger than the competing $^{10}$B($p$,$\gamma$)$^{11}$C radiative capture reaction [19]. Figure 1 shows the $S$-factor for the transitions to the ground state and the first excited state in $^7$Be. The astrophysical $S$-factor, $S(E)$, represents the energy dependent cross section $\sigma(E)$ of the reaction corrected in first order for the Coulomb penetrability. $S(E)$ therefore represents the nuclear transition probability as well as the tunneling probability through the orbital momentum barrier as a function of the energy $E$.

$$S(E) = \sigma(E) \cdot E \cdot e^{2\pi\eta}, \tag{1}$$

with $\eta$ being the classical Sommerfeld parameter.

The $S$-factor curve for the $^{10}\text{B}(p,\alpha)^{7}\text{Be}$ reaction towards lower energies is characterized by the tail of a strong resonance at 10 keV [7, 22] and by the contribution of several broad and interfering resonances in the higher energy range [18]. The cross section determination is based on a comprehensive $R$-matrix analysis including representative sets of $^{10}\text{B}(p,\alpha)^{7}\text{Be}$ data and also includes data for complementary reaction channels such as radiative capture $^{10}\text{B}(p,\gamma)^{11}\text{C}$ and elastic scattering $^{10}\text{B}(p,p)^{10}\text{B}$ as described by [14]. Through this self-consistent application of the phenomenological $R$-matrix theory [13], a reliable extrapolation over the entire energy range with relative small uncertainty has been achieved [43, 25].

## 2.1 *R*-matrix analysis of the $^{10}\text{B}(p,\alpha)^{7}\text{Be}$

As discussed above, the low energy cross section of the $^{10}\text{B}(p,\alpha)^{7}\text{Be}$ reaction is dominated by a strong $s$-wave, near threshold, resonance at ≈10 keV. The corresponding level has a total width of ≈15 keV and has $J^{\pi} = 5/2^{+}$. There is a single direct experimental study that measures down to the very low energy of $E_{\text{c. m.}} = 17$ keV [22]. A more recent Trojan Horse measurement has also studied the very low cross section, reporting data down to 5 keV that maps the near threshold resonance [23]. Despite these low energy measurements, the cross section at the energies of inertial confinement fusion facilities still is rather uncertain. For example, Spitaleri et al. [25] quotes a low energy uncertainty of between 10 and 20%. While the data of Angulo et al. [22] have rather small error bars, the data also show a significant amount of scatter, indicating the presence of significant non-statistical uncertainties.

In addition, the near threshold $5/2^{+}$ resonance can interfere strongly with other higher energy resonances, which strongly motivates an $R$-matrix analysis that covers a broader energy range. The recent work of Vande Kolk et al. [14] provided a consistent set of $^{10}\text{B}(p,\alpha)^{7}\text{Be}$ angular distribution data that resulted in a much improved characterization of the next highest energy $5/2^{+}$ resonance at ≈1.3 MeV, which has a total width of ≈740 keV and interferes strongly with the near threshold state.

It should be noted that the TUNL evaluation lists another $5/2^{+}$ state at $E_x = 9.200$ (50) keV, but in Vande Kolk et al. [14] no evidence for this state was found, so it has not been considered. Additionally, the large widths of the resonances in this region tend to obfuscate level identification. Microscopic calculations near the proton separation energy in $^{11}\text{C}$ would be very helpful in producing firmer level assignments.

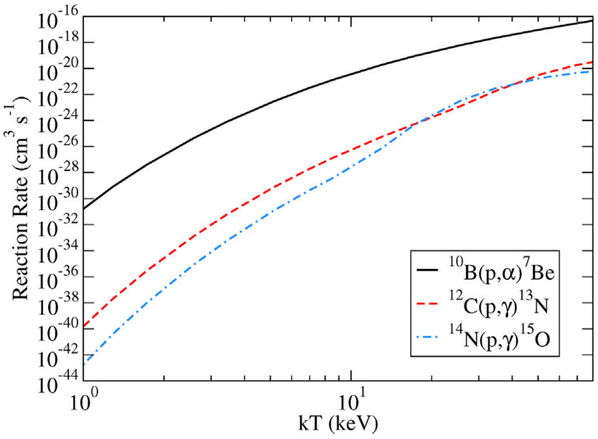

FIGURE 2
Reaction rates for the $^{10}\text{B}(p,\alpha)^{7}\text{Be}$ (sold black line), $^{12}\text{C}(p,\gamma)^{13}\text{N}$ (dashed red line) and $^{14}\text{N}(p,\gamma)^{15}\text{O}$ (dashed-dotted blue line) reactions calculated from the $R$-matrix fits described throughout the remainder of the text.

## 2.2 The reaction rate of $^{10}\text{B}(p,\alpha)^{7}\text{Be}$

The reaction rate for a nuclear reaction process characterized by broad overlapping and interfering resonances is determined by numerical integration over the reaction cross section and Maxwell Boltzmann distribution of the interacting particles, with the factors $f(\rho)$, which corrects for electron screening, and the partition function $G(T)$, which takes into account the contribution of thermally excited states in a plasma environment

$$N_A\langle\sigma v\rangle = \left(\frac{8}{\pi\mu}\right)^{1/2} \frac{N_A}{(k_B T)^{3/2}} \int_0^\infty f(\rho) \cdot G(T) \cdot \sigma(E) \cdot E \cdot e^{-E/k_B T} dE. \tag{2}$$

Here $N_A$ is Avogadro's number, $k_B$ is the Boltzmann constant, $T$ is the temperature, $\rho$ is the density, and $\mu$ is the reduced mass. The reaction rate as a function of temperature is shown in Figure 2. The electron screening factor $f(\rho)$ depends on the density of the stellar environment [26] and is typically based on theoretical estimates based on assumptions on an additional screening potential term in the nuclear potential [27], while the partition function $G(T)$ is calculated as the probability for thermally populating excited states in a hot plasma [28], respectively. These two model dependent terms carry a substantial uncertainty, depending on the assumptions about the screening potential in the laboratory experiment and the plasma as well on the knowledge or assumptions on the excitation energies and level density of the target nucleus. The rate declines rapidly with temperature with the contributions of the broad resonance structures observed in the cross section (see Figure 1) determining the absolute value of the rate at each temperature. The reaction rate measured directly at a laser plasma facility will differ from the reaction rate based on low energy accelerator experiments, which does not provide information about the screening factor and the partition function. A direct measurement of a reaction rate in a quasi-stellar plasma such as provided by Omega and NIF in comparison with accelerator based reaction rate estimates offers a unique way for experimentally determining these parameters.

The production of $^7$Be in a laser driven hot plasma environment can be calculated from the reaction rate and the abundances of $^{10}$B boron and $^1$H hydrogen fuel. The difference between observed and predicted number of reaction products will provide the necessary information about the environmental parameters in a plasma environment.

The production rate of $^7$Be is determined by

$$\frac{dN_{^7Be}}{dt} = N_{^{10}B} \cdot N_{^1H} \cdot \rho \cdot N_A \langle \sigma v \rangle_{^{10}B(p,\alpha)^7Be}. \tag{3}$$

This equation does not include any possible depletion reaction of $^7Be$ by either electron capture or radiative proton capture, since these processes are anticipated to have a much smaller reaction rate than the $^{10}$B($p$,$\alpha$)$^7$Be production rate.

## 2.3 The $^7$Be production in a laser driven plasma environment

The production of $^7$Be can be obtained by integrating the production rate over the temperature and density development in the laser driven plasma. The yield $Y_{^7Be}$ of $^7$Be produced in a high temperature shot environment can be easily estimated in the framework of a simplified 1D hot spot model from the reaction rate per particle pair, the number densities $N_{^{10}B}$ and $N_{^1H}$ for the reaction partners in the plasma, boron and hydrogen, respectively, the hot spot volume $V_{HS}$, and the actual burn width $\Delta t$:

$$Y_{^7Be} = N_{^{10}B} \cdot N_{^1H} \cdot \langle \sigma v \rangle_{^{10}B(p,\alpha)^7Be} \cdot V_{HS} \cdot \Delta t. \tag{4}$$

For a NIF like laser driven plasma study of the reaction, the optimum gas filling of the capsule would be a$^{10}B_2H_6$ Di-Borane fill gas with number densities of $N_{^{10}B} \approx 10^{20}$ cm$^{-3}$ and $N_{^1H} \approx 3 \cdot 10^{20}$ cm$^{-3}$, respectively. This would correspond to a rather high density after compression to a hot spot volume of about $V_{HS} \approx 10^{-6}$ cm$^3$ for the burn width period of $\Delta t \approx 10^{-10}$ s. From Figure 2, the reaction rate can be estimated to be $\langle \sigma v \rangle_{^{10}B(p,\alpha)^7Be} \approx 10^{-20}$ cm$^3$s$^{-1}$ at a temperature of about $kt \approx 30$ keV. It should be noted that these temperature levels have so far only be reached in direct drive implosions, with the laser beams directly incident on the target [29]. Adopting these conditions results in a production yield of $Y_{^7Be} \approx 10^4$ to $10^{5}$$^7$Be nuclei per shot. This number depends linearly on the amount of gas in the shot capsule, but exponentially on the temperature reached in the plasma during the shot since the reaction rate varies exponentially with temperature. Higher shot temperatures would certainly translate into a substantially higher $^7$Be production.

This material must be collected either by catcher foils or by the cryogenic Radiochemical Analysis of Gaseous Samples (RAGS) system [30] to be analyzed and counted by high sensitivity mass separation or Accelerator Mass Spectrometry (AMS) techniques. The RAGS system so far has been only applied to the analysis of indirect drive implosions with a Hohlraum system and new developments are required for its application in direct drive implosions. Considering the low number of $^7$Be isotopes produced during a single shot, their identification by measuring the characteristic 10% $\gamma$ decay at 478 keV would not provide sufficient sensitivity for a successful counting experiment.

This is of course only a rather crude estimate of the production of $^7$Be, a more reliable simulation would also require taking other reaction channels, such as $^7$Be($p$,$\gamma$)$^8$B, into account, which would reduce the production number. However, as this reaction cross section is orders of magnitude smaller, it can be neglected in the present calculations.

# 3 The $^{12}$C($p$,$\gamma$)$^{13}$N reaction

The $^{12}$C($p$,$\gamma$)$^{13}$N reaction is an important link in the so-called CNO cycle, which facilitates stellar hydrogen burning in massive stars. The CNO cycle is a catalytic process that is based on the capture of four protons on the existing abundance of carbon, nitrogen, and also oxygen isotopes in a stellar environment with the subsequent emission of one alpha particle as well as two positrons $^{12}$C($p$,$\gamma$)$^{13}$N($\beta^+\nu$)$^{13}$C($p$,$\gamma$)$^{14}$N($p$,$\gamma$)$^{15}$O($\beta^+\nu$)$^{15}$N($p$,$\alpha$)$^{12}$C [31]. The CNO cycle is not only important as an energy source for massive stars but it also contributes to the production of CNO neutrinos in our sun [32].

In the CNO reaction sequence, the $^{12}$C($p$,$\gamma$)$^{13}$N reaction plays an important role in determining the fate of the $^{12}$C isotope in an hydrogen burning environment as well for the production of $^{13}$N. The $\beta^+$ decay of $^{13}$N is one of the predicted CNO neutrino sources, whose strength is defined by the $^{12}$C($p$,$\gamma$)$^{13}$N capture rate since the production and the $^{13}$N decay are in equilibrium. This shows that the respective neutrino emission rate $A_\gamma(^{13}N)$ depends directly on the $^{12}$C($p$,$\gamma$)$^{13}$N reaction rate $N_A \langle \sigma v \rangle_{^{12}C(p,\gamma)^{13}N}$ and the abundances of $^{12}$C and $^1$H in the solar core:

$$A_\gamma(^{13}N) = \frac{dN_{^{13}N}}{dt} = N_{^{12}C} \cdot N_{^1H} \cdot \rho \cdot N_A \langle \sigma v \rangle_{^{12}C(p,\gamma)^{13}N}. \tag{5}$$

To reliably evaluate the $^{13}$N component in the solar CNO neutrino flux a reliable reaction rate for the $^{12}$C($p$,$\gamma$)$^{13}$N reaction in a plasma environment is necessary. This however presents a major challenge because of the low reaction cross section.

The $^{12}$C($p$,$\gamma$)$^{13}$N reaction is a radiative capture process, which is based on the electromagnetic interaction, rather than the

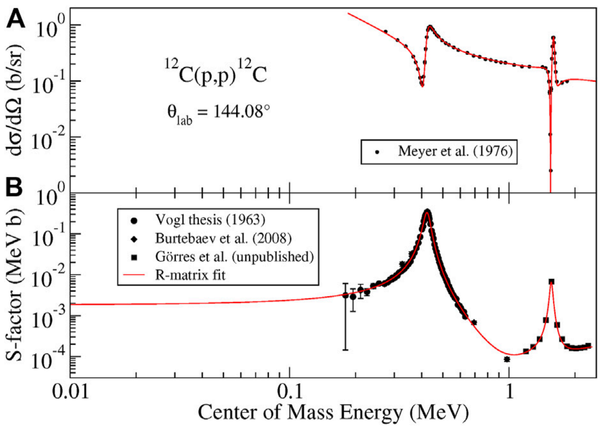

FIGURE 3
Simultaneous *R*-matrix fit to **(A)** the differential cross section data of Meyer et al. [34], **(B)** the $^{12}C(p,\gamma)^{13}N$ angle integrated data of Vogl [35] and Burtebaev et al. [36] as well as the differential cross section data of Rolfs and Azuma [33], with adjustments for energy calibration.

strong interaction, in contrast to our previous example. For this reason, the cross section is expected to be substantially weaker. However, at low energies, the $^{12}C(p,\gamma)^{13}N$ reaction is characterized by the contributions from two pronounced resonances and a non-resonant direct capture mechanism as well as possible interference between these reaction components [33]. The strength of these components define the low energy cross section of the reaction and therefore also the reaction rate. Figure 3 shows the *S*-factor of the $^{12}C(p,\gamma)^{13}N$ reaction at low energies characterized by the contributions of the two broad low energy resonances including new and as yet unpublished data in the energy range above 1 MeV to obtain a better handle on the upper resonance. The solid line presents a new *R*-matrix analysis of the reaction cross section as described in the following.

### 3.1 *R*-matrix analysis of $^{12}C(p,\gamma)^{13}N$

The $^{12}C(p,\gamma)^{13}N$ reaction is ideally suited for an *R*-matrix description. Only a single, broad, *s*-wave resonance contributes to the low energy cross section at $E_{c.\,m.} = 461$ keV. As shown in Azuma et al. [13], the low energy cross section can be described very well by the interference of this broad resonance with *E*1 direct capture, modeled with external capture [5, 11, 37]. The exceptional data of Vogl [35] carefully map this low energy resonance. These data have been found to be consistent with the recent measurements of Burtebaev et al. [36]. The reaction was also studied by Rolfs and Azuma [33], but was found to have issues with its energy calibration [40]. The *R*-matrix fit is found to give an excellent reproduction of the data and the extrapolation of the low energy cross section is quoted as having an uncertainty of ≈18% [13], which is largely dominated by the overall normalization uncertainty.

### 3.2 The $^{13}$N production in a laser driven plasma environment

The measurement of $^{12}C(p,\gamma)^{13}N$ in a laser driven plasma environment is a considerable challenge because of the overall low reaction rate at the characteristic conditions of a NIF shot where

$$Y_{^{13}N} = N_{^{12}C}\cdot N_{^{1}H}\cdot\langle\sigma v\rangle_{^{12}C(p,\gamma)^{13}N}\cdot V_{HS}\cdot\Delta t. \tag{6}$$

For a gas filled capsule, methane $^{12}CH_4$ seems to be a suitable choice with a particle densities of $N_{^{12}C}\approx 10^{20}$ cm$^{-3}$ and $N_{^{1}H}\approx 4\cdot 10^{20}$ cm$^{-3}$, respectively. The reaction rate at $kT\approx 30$ keV is $\langle\sigma v\rangle_{^{12}C(p,\gamma)^{13}N}\approx 2\cdot 10^{-24}$ cm$^3$s$^{-1}$, approximately four orders of magnitude weaker than the rate of the $^{10}B(p,\alpha)^7Be$ strong interaction process. This translates, at comparable shot conditions, into six orders of magnitude lower yield, $Y_{^{13}N}\approx 10$ $^{13}$N nuclei per shot. Considering the presently available shot rate of less than 10 shots per day, these are obviously insufficient conditions for a laser plasma experiment. This yield can be enhanced by some factor by increasing the concentration of the reaction components either by using higher filling pressure or exchanging methane $CH_4$ by butane $C_4H_{10}$ gas. The Significantly higher shot temperatures need to be reached to obtain a measurable $^{13}$N yield.

The relatively short half-life of $^{13}$N, $t_{1/2} = 9.97$ min, provides another obstacle since it requires a speedy removal of the reaction products from the NIF environment. Identification and analysis of an on-line AMS or PET microlensing system, as developed for mapping microdoses of radioactivity in pharmaceutical studies [42, 41], could be used. Yet, it remains doubtful if such spurious amounts of characteristic $^{13}$N can be collected and filtered out of the relatively dirty vacuum environment of present generation plasma facilities.

## 4 The $^{14}N(p,\gamma)^{15}O$ reaction

The $^{14}N(p,\gamma)^{15}O$ reaction has been identified as the slowest reaction in the CNO cycles [31]. The reaction includes several sizable transitions to both the ground state and higher excited states and is characterized by non-resonant direct capture contributions as well as contributions from the tails of higher energy resonances [31, 43] interfering with the high energy tails of different subthreshold states [45]. The reaction rate is determined by the sum of all of these transitions at the temperature of the stellar or laboratory hydrogen burning environment. The $^{14}N(p,\gamma)^{15}O$ reaction results in the production of $^{15}$O, which $\beta^+$ decays, also emitting a neutrino at fairly high energies. Recent measurements of the BOREXINO detector showed signatures of the neutrino flux associated with the $^{15}$O decay [46]. The observed neutrino rate $A_\nu(^{15}O)$ seems to be slightly higher than suggested by the reaction rate $N_A\langle\sigma v\rangle_{^{14}N(p,\gamma)^{15}O}$ based on accelerator data

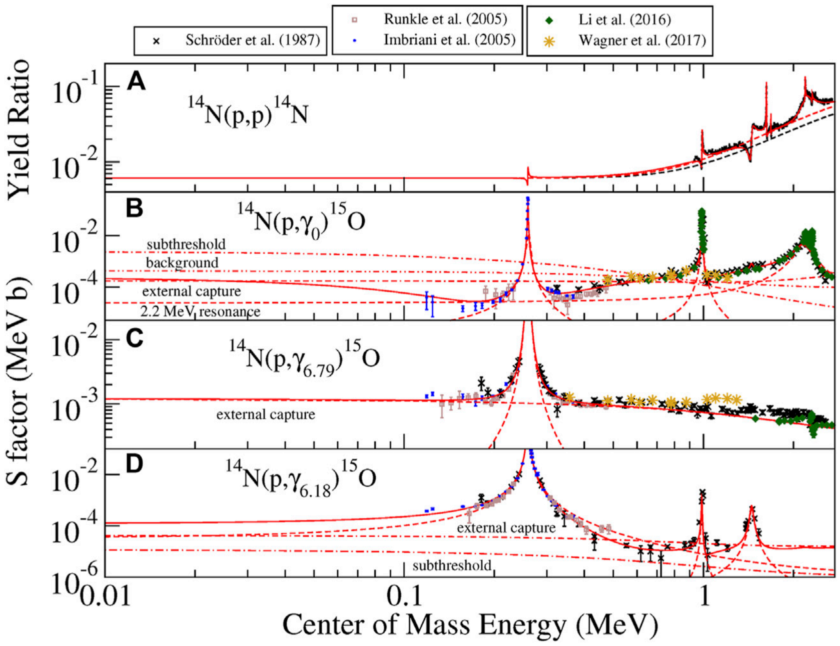

FIGURE 4
Simultaneous *R*-matrix fit to **(A)** the $^{14}$N($p,p$)$^{14}$N data of deBoer et al. [48] and the $^{14}$N($p,\gamma$)$^{15}$O data of Schröder et al. [49], Runkle et al. [50], Imbriani et al. [43], Li et al. [44], Wagner et al. [51] for the ground state **(B)**, 6.79 MeV **(C)**, and 6.18 MeV **(D)** excited states.

$$A_\gamma(^{15}O) = \frac{dN_{^{15}O}}{dt} = N_{^{14}N}\cdot N_{^1H}\cdot\rho\cdot N_A\langle\sigma v\rangle_{^{14}N(p,\gamma)^{15}O}. \quad (7)$$

This might either suggest a higher abundance of $N_{^{14}N}$ or a change in the reaction rate. The latter, however, was confirmed by a new reaction study [15]. The following section provides a short summary of the nuclear physics of the reaction as reflected in the *R*-matrix analysis of the reaction channels.

## 4.1 *R*-matrix analysis of $^{14}$N($p,\gamma$)$^{15}$O

There are three transitions that dominate the total capture cross section for the $^{14}$N($p,\gamma$)$^{15}$O reaction: the 6.79 MeV, ground state, and 6.17 MeV [47] (as shown in Figure 4). The 6.79 MeV transition is described well by pure hard sphere external capture [44]. The 6.17 MeV transition is instead dominated by the tail of the 278 keV resonance at low energies. In constrast, the ground state transition data, especially the very low energy measurements of Imbriani et al. [43], have proven to be very challenging to describe, especially when analyzed simultaneously with higher energy data [21, 16, 44]. The low energy cross section for this transition is made up of contributions from the 278 keV resonance, external capture, at least one subthreshold state, and the low energy tail of broad higher energy resonances [48]. The complications of obtaining a satisfactory *R*-matrix description of this transition are summarized in Frentz et al. [15] and Gyürky et al. [52]. Despite the difficulties in describing the ground state transition, the low energy cross section is thought to have a relatively small uncertainty of ≈7% [47].

## 4.2 The $^{15}$O production in a laser driven plasma environment

A measurement of the reaction in a plasma would be extremely interesting to investigate the possibility of plasma related changes in the reaction rate. The reaction rate at $kT \approx$ 30 keV is $\langle\sigma v\rangle_{^{14}N(p,\gamma)^{15}O} \approx 3.5\cdot 10^{-24}$ cm$^3$s$^{-1}$, which is comparable to the reaction rate of $^{12}$C(p,$\gamma$)$^{13}$N. The best target gas might be an ammonia gas NH$_3$ or a mixture of N$_2$ and H$_2$. Adopting an ammonium gas, particle densities of $N_{^{14}N} \approx 10^{20}$ cm$^{-3}$ and $N_{^1H} \approx 3\cdot 10^{20}$ cm$^{-3}$ are obtained, respectively. This translates, for comparable shot conditions as described above, into a yield of $Y_{^{15}O} \approx 10$ $^{15}$O nuclei per shot, comparable to the anticipated count rate for the $^{12}$C($p,\gamma$) $^{13}$N reaction.

Again, the low production rate of the adopted shot conditions makes an experimental study of radiative capture reactions challenging. Higher densities would be desirable to improve the conditions for a direct study of such a reaction in a laser plasma experiment. An additional technical challenge is the half life of $^{15}$O, $t_{1/2}$ = 2.01 min, considerably shorter than that of $^{13}$N; this requires the development of speedy high efficiency extraction methods.

## 5 Conclusion

Three reactions have been analyzed on their suitability for study at laser confined plasma facilities such as NIF or Omega. These studies would be important as a direct way to explore the screening of the deflecting Coulomb barrier in a charged particle fusion or capture process at the conditions of a stellar plasma. While a number of reactions have been studied for fusion between light hydrogen and helium isotopes [52, 23, 2], no studies exist for these kind of reactions for higher $Z$ nuclei. The more recent measurement of $^{10}$B($\alpha$,$n$)$^{13}$N was a promising first step [10], however, the technique was not quite suitable for the study of reactions at stellar burning conditions. The boron content was part of the outer beryllium ablator containing a 65/35 % deuterium–tritium (DT) gas fill. The $\alpha$ particles were produced by D+T fusion reactions and therefore had a much higher energy than $\alpha$ particles in a thermal plasma. The successful analysis of the $^{13}$N reaction products using RAGS, however, demonstrated that such measurements remain feasible.

The $^{10}$B($p$,$\alpha$)$^{7}$Be, $^{12}$C($p$,$\gamma$)$^{13}$N, and the $^{14}$N($p$,$\gamma$)$^{15}$O reactions are suitable because the radioactive decay of the reaction products provide a unique signature. In addition, these reactions play an important role in astrophysics, from the nucleosynthesis in first stars to the interpretation of the CNO neutrino flux from our sun. The cross section data derived from accelerator based reaction data have been extrapolated into the energy range of the plasma environment by a extensive $R$-matrix analyses, taking into account many reaction channels. The reaction yield produced in a generic NIF shot has been estimated on the basis of these reaction cross sections. The results indicate that the production rate is limited by the low cross sections compared to the fusion reactions with lower $Z$ nuclei. The strong interaction $^{10}$B($p$,$\alpha$)$^{7}$Be process is the most promising, not only is the reaction cross section much higher than the typical one for radiative capture reactions such as $^{12}$C($p$,$\gamma$)$^{13}$N and the $^{14}$N($p$,$\gamma$)$^{15}$O, but also because of the lower $Z$ of the isotopes involved. Without significant improvement in the experimental arrangements, the chances for measuring reactions with higher $Z$ isotopes are limited.

## Data availability statement

Publicly available datasets were analyzed in this study. This data can be found here: https://www-nds.iaea.org/exfor/.

## Author contributions

MW, RD, and JG contributed to the conception of this research. MW and JG made the NIF yield calculations and RD provided the cross sections and reaction rates. MW wrote the first draft of the manuscipt and RD and JG edited and contributed to sections of the manuscipt. All authors contributed to the final editting and revision of the manuscipt and approved it for submission.

## Funding

This research utilized resources from the Notre Dame Center for Research Computing and was funded by the National Science Foundation through Grant No. PHY-2011890 (University of Notre Dame Nuclear Science Laboratory), Grant No. PHY-1430152 (the Joint Institute for Nuclear Astrophysics—Center for the Evolution of the Elements).

## Conflict of interest

The authors declare that the research was conducted in the absence of any commercial or financial relationships that could be construed as a potential conflict of interest.

## Publisher's note

## References

1. Assenbaum HJ, Langanke K, Rolfs C. Low-energy $^{2}$H(d, $\gamma$)$^{4}$He reaction and the d-state admixture in the $^{4}$He ground state. *Phys Rev C* (1987) 36:17–20. doi:10.1103/PhysRevC.36.17

2. Sayre DB, Brune CR, Caggiano JA, Glebov VY, Hatarik R, Bacher AD, et al. Measurement of the $T$ + $T$ neutron spectrum using the national ignition facility. *Phys Rev Lett* (2013) 111:052501. doi:10.1103/PhysRevLett.111.052501

3. Gatu Johnson M, Forrest CJ, Sayre DB, Bacher A, Bourgade J-L, Brune CR, et al. Experimental evidence of a variant neutron spectrum from the $T(t, 2n)\alpha$ reaction at center-of-mass energies in the range of 16–50 keV. *Phys Rev Lett* (2018) 121:042501. doi:10.1103/PhysRevLett.121.042501

4. Zylstra AB, Frenje JA, Gatu Johnson M, Hale GM, Brune CR, Bacher A, et al. Proton spectra from $^{3}$He + T and $^{3}$He +$^{3}$He fusion at low center-of-mass energy, with potential implications for solar fusion cross sections. *Phys Rev Lett* (2017) 119: 222701. doi:10.1103/PhysRevLett.119.222701

5. Nuckolls J, Wood L, Thiessen A, Zimmerman G. Laser compression of matter to super-high densities: Thermonuclear (CTR) applications. *Nature* (1972) 239:139–42. doi:10.1038/239139a0

6. Edwards MJ, Patel PK, Lindl JD, Atherton LJ, Glenzer SH, Haan SW, et al. Progress towards ignition on the national ignition facility. *Phys Plasmas* (2013) 20: 070501. doi:10.1063/1.4816115

7. Boehly T, Brown D, Craxton R, Keck R, Knauer J, Kelly J, et al. Initial performance results of the omega laser system. *Opt Commun* (1997) 133:495–506. doi:10.1016/S0030-4018(96)00325-2

8. Cerjan CJ, Bernstein L, Hopkins LB, Bionta RM, Bleuel DL, Caggiano JA, et al. Dynamic high energy density plasma environments at the National Ignition Facility for nuclear science research. *J Phys G: Nucl Part Phys* (2018) 45:033003. doi:10.1088/1361-6471/aa8693

9. Liu Q, Febbraro M, deBoer RJ, Aguilar S, Boeltzig A, Chen Y, et al. Low-energy cross-section measurement of the $^{10}\text{B}(\alpha,n)^{13}\text{N}$ reaction and its impact on neutron production in first-generation stars. *Phys Rev C* (2020) 101:025808. doi:10.1103/PhysRevC.101.025808

10. Lonardoni D, Sauppe JP, Batha SH, Birge N, Bredeweg T, Freeman M, et al. First measurement of the $^{10}\text{B}(\alpha,n)^{13}\text{N}$ reaction in an inertial confinement fusion implosion at the National Ignition Facility: Initial steps toward the development of a radiochemistry mix diagnostic. *Phys Plasmas* (2022) 29:052709. doi:10.1063/5.0079676

11. Lane AM, Thomas RG. R-matrix theory of nuclear reactions. *Rev Mod Phys* (1958) 30:257–353. doi:10.1103/RevModPhys.30.257

12. Descouvemont P, Baye D. The *R*-matrix theory. *Rep Prog Phys* (2010) 73:036301. doi:10.1088/0034-4885/73/3/036301

13. Azuma RE, Uberseder E, Simpson EC, Brune CR, Costantini H, de Boer RJ, et al. Azure: An *R*-matrix code for nuclear astrophysics. *Phys Rev C* (2010) 81:045805. doi:10.1103/PhysRevC.81.045805

14. Vande Kolk B, Macon KT, deBoer RJ, Anderson T, Boeltzig A, Brandenburg K, et al. Investigation of the $^{10}\text{B}(p,\alpha)^{7}\text{Be}$ reaction from 0.8 to 2 0 MeV. *Phys Rev C* (2022) 105:055802. doi:10.1103/PhysRevC.105.055802

15. Frentz B, Aprahamian A, Boeltzig A, Clark A, deBoer R, Gilardy G, et al. (2022). Investigation of the $^{14}\text{N}(p,\gamma)^{15}\text{O}$ reaction for the CNO cycle (PRC in print).

16. Wiescher M, Clarkson O, deBoer RJ, Denisenkov P. Nuclear clusters as the first stepping stones for the chemical evolution of the universe. *Eur Phys J A* (2021) 57:24. doi:10.1140/epja/s10050-020-00339-x

17. Wiescher M, Gorres J, Graff S, Buchmann L, Thielemann FK. The hot proton-proton chains in low-metallicity objects. *ApJ* (1989) 343:352. doi:10.1086/167709

18. Wiescher M, deBoer RJ, Görres J, Azuma RE. Low energy measurements of the $^{10}\text{B}(p,\alpha)^{7}\text{Be}$ reaction. *Phys Rev C* (2017) 95:044617. doi:10.1103/PhysRevC.95.044617

19. Wiescher M, Boyd RN, Blatt SL, Rybarcyk LJ, Spizuoco JA, Azuma RE, et al. $^{11}$C level structure via the $^{10}\text{B}(p,\gamma)$ reaction. *Phys Rev C* (1983) 28:1431–42. doi:10.1103/PhysRevC.28.1431

20. Chiari M, Giuntini L, Mandò P, Taccetti N. Proton elastic scattering cross-section on boron from 0.5 to 3.3 MeV. *Nucl Instr Methods Phys Res Section B: Beam Interactions Mater Atoms* (2001) 184:309–18. doi:10.1016/S0168-583X(01)00787-X

21. Youn M, Chung H, Kim J, Bhang H, Chung K-H. The $^{10}\text{B}(p,\alpha_0)^{7}\text{Be}$ reaction in the thermonuclear energy region. *Nucl Phys A* (1991) 533:321–32. doi:10.1016/0375-9474(91)90493-P

22. Angulo C, Engstler S, Raimann G, Rolfs C, Schulte WH, Somorjai E. The effects of electron screening and resonances in $(p,\alpha)$ reactions on $^{10}$B and $^{11}$B at thermal energies. *Z Physik A - Hadrons Nuclei* (1993) 345:231–42. doi:10.1007/BF01293350

23. Spitaleri C, Lamia L, Puglia SMR, Romano S, La Cognata M, Crucillà V, et al. Measurement of the 10 keV resonance in the $^{10}\text{B}(p,\alpha_0)^{7}\text{Be}$ reaction via the Trojan Horse method. *Phys Rev C* (2014) 90:035801. doi:10.1103/PhysRevC.90.035801

24. Angulo C, Schulte WH, Zahnow D, Raimann G, Rolfs C. Astrophysical *S(E)* factor of $^{10}\text{B}(p,\alpha_1)^{7}\text{Be}$ at low energies. *Z Physik A - Hadrons Nuclei* (1993) 345:333–4. doi:10.1007/BF01280844

25. Spitaleri C, Puglia SMR, La Cognata M, Lamia L, Cherubini S, Cvetinović A, et al. Measurement of the $^{10}\text{B}(p,\alpha_0)^{7}\text{Be}$ cross section from 5 keV to 1.5 MeV in a single experiment using the Trojan horse method. *Phys Rev C* (2017) 95:035801. doi:10.1103/PhysRevC.95.035801

26. Gasques LR, Afanasjev AV, Aguilera EF, Beard M, Chamon LC, Ring P, et al. Nuclear fusion in dense matter: Reaction rate and carbon burning. *Phys Rev C* (2005) 72:025806. doi:10.1103/PhysRevC.72.025806

27. Assenbaum HJ, Langanke K, Rolfs C. Effects of electron screening on low-energy fusion cross sections. *Z Physik A - At Nuclei* (1987) 327:461–8. doi:10.1007/BF01289572

28. Fowler WA, Caughlan GR, Zimmerman BA. Thermonuclear reaction rates, ii. *Annu Rev Astron Astrophys* (1975) 13:69–112. doi:10.1146/annurev.aa.13.090175.000441

29. Jeet J, Zylstra AB, Gatu-Johnson M, Kabadi NV, Adrian P, Forrest C, et al. (2022). Development of a platform for studying solar CNO reactions in an ICF plasma.

30. Shaughnessy DA, Velsko CA, Jedlovec DR, Yeamans CB, Moody KJ, Tereshatov E, et al. The radiochemical analysis of gaseous Samples (RAGS) apparatus for nuclear diagnostics at the national ignition facility (invited). *Rev Scientific Instr* (2012) 83:10D917. doi:10.1063/1.4742145

31. Wiescher M, Görres J, Uberseder E, Imbriani G, Pignatari M. The cold and hot i404. doi:10.1146/annurev.nucl.012809.104505

32. Haxton W, Hamish Robertson R, Serenelli AM. Solar neutrinos: Status and prospects. *Annu Rev Astron Astrophys* (2013) 51:21–61. doi:10.1146/annurev-astro-081811-125539

33. Rolfs C, Azuma R. Interference effects in $^{12}\text{C}(p,\gamma)^{13}\text{N}$ and direct capture to unbound states. *Nucl Phys A* (1974) 227:291–308. doi:10.1016/0375-9474(74)90798-2

34. Meyer H, Plattner G, Sick I. Elastic $p+^{12}\text{C}$ scattering between 0.3 and 2 MeV. *Z Physik A* (1976) 279:41–5. doi:10.1007/BF01409090

35. Vogl JL. Radiative capture of protons by 12C and 13C below 700 keV. Ph.D. thesis. Pasadena, CA, United States: California Institute of Technology (1963).

36. Burtebaev N, Igamov SB, Peterson RJ, Yarmukhamedov R, Zazulin DM. New measurements of the astrophysical *S* factor for $^{12}\text{C}(p,\gamma)^{13}\text{N}$ reaction at low energies and the asymptotic normalization coefficient (nuclear vertex constant) for the $p + {}^{12}\text{C} \rightarrow {}^{13}\text{N}$ reaction. *Phys Rev C* (2008) 78:035802. doi:10.1103/PhysRevC.78.035802

37. Holt RJ, Jackson HE, Laszewski RM, Monahan JE, Specht JR. Effects of channel and potential radiative transitions in the $^{17}\text{O}(\gamma,n_0)^{16}\text{O}$ reaction. *Phys Rev C* (1978) 18:1962–72. doi:10.1103/PhysRevC.18.1962

38. Barker FC, Kajino T. The $^{12}\text{C}(\alpha,\gamma)^{16}\text{O}$ cross section at low energies. *Aust J Phys* (1991) 44:369–96. doi:10.1071/PH910369

39. Angulo C, Descouvemont P. The $^{14}\text{N}(p,\gamma)^{15}\text{O}$ low-energy *S*-factor. *Nucl Phys A* (2001) 690:755–68. doi:10.1016/S0375-9474(00)00696-5

40. Angulo C, Arnould M, Rayet M, Descouvemont P, Baye D, Leclercq-Willain C, et al. A compilation of charged-particle induced thermonuclear reaction rates. *Nucl Phys A* (1999) 656:3–183. doi:10.1016/S0375-9474(99)00030-5

41. Lappin G, Garner R. Big physics, small doses: The use of ams and pet in human microdosing of development drugs. *Nat Rev Drug Discov* (2003) 2:233–40. doi:10.1038/nrd1037

42. Turteltaub K, Vogel J. Bioanalytical applications of accelerator mass spectrometry for pharmaceutical research. *Curr Pharm Des* (2000) 6:991–1007. doi:10.2174/1381612003400047

43. Imbriani G, Costantini H, Formicola A, Bemmerer D, Bonetti R, Broggini C, et al. The bottleneck of CNO burning and the age of Globular Clusters. *Astron Astrophys* (2004) 420:625–9. doi:10.1051/0004-6361:20040981

44. Li Q, Görres J, deBoer RJ, Imbriani G, Best A, Kontos A, et al. Cross section measurement of $^{14}\text{N}(p,\gamma)^{15}\text{O}$ in the CNO cycle. *Phys Rev C* (2016) 93:055806. doi:10.1103/PhysRevC.93.055806

45. Frentz B, Aprahamian A, Clark AM, Deboer RJ, Dulal C, Enright JD, et al. Lifetime measurements of excited states in $^{15}$O. *Phys Rev C* (2021) 103:045802–10. doi:10.1103/PhysRevC.103.045802

46. Agostini M, Altenmüller K, Appel S, Atroshchenko V, Bagdasarian Z, Basilico D, et al. Experimental evidence of neutrinos produced in the CNO fusion cycle in the Sun. *Nature* (2020) 587:577–82. doi:10.1038/s41586-020-2934-0

47. Adelberger E, García A, Hamish Robertson R, Snover K, Balantekin A, Heeger KM, et al. Solar fusion cross sections. II. Theppchain and CNO cycles. *Rev Mod Phys* (2011) 83:195–245. doi:10.1103/RevModPhys.83.195

48. deBoer RJ, Bardayan DW, Görres J, LeBlanc PJ, Manukyan KV, Moran MT, et al. Low energy scattering cross section ratios of $^{14}\text{N}(p,p)^{14}\text{N}$. *Phys Rev C* (2015) 91:045804. doi:10.1103/PhysRevC.91.045804

49. Schröder U, Becker H, Bogaert G, Görres J, Rolfs C, Trautvetter HP, et al. Stellar reaction rate of $^{14}\text{N}(p,\gamma)^{15}\text{O}$ and hydrogen burning in massive stars. *Nucl Phys A* (1987) 467:240–60. doi:10.1016/0375-9474(87)90528-8

50. Runkle RC, Champagne AE, Angulo C, Fox C, Iliadis C, Longland R, et al. Direct measurement of the $^{14}\text{N}(p,\gamma)^{15}\text{O}$ *S* factor. *Phys Rev Lett* (2005) 94:082503. doi:10.1103/PhysRevLett.94.082503

51. Wagner L, Akhmadaliev S, Anders M, Bemmerer D, Caciolli A, Gohl S, et al. Astrophysical *S* factor of the $^{14}\text{N}(p,\gamma)^{15}\text{O}$ reaction at 0.4-1.3 MeV. *Phys Rev C* (2018) 97:015801–15. doi:10.1103/PhysRevC.97.015801

52. Gyürky G, Halász Z, Kiss GG, Szücs T, Fülöp Z. Activation cross section measurement of the $^{14}\text{N}(p,\gamma)^{15}\text{O}$ astrophysical key reaction. *Phys Rev C* (2022) 105:L022801. doi:10.1103/PhysRevC.105.L022801

frontiers | Frontiers in Physics

TYPE Review
PUBLISHED 06 October 2022
DOI 10.3389/fphy.2022.993632

OPEN ACCESS

EDITED BY
Giuseppe Verde,
National Institute of Nuclear Physics,
Italy

REVIEWED BY
Tommaso Marchi,
Legnaro National Laboratories (INFN),
Italy
Theocharis S. Kosmas,
University of Ioannina, Greece

*CORRESPONDENCE
Jeffrey Burggraf,
burggraf1@llnl.gov

SPECIALTY SECTION
This article was submitted to Nuclear
Physics,
a section of the journal
Frontiers in Physics

RECEIVED 13 July 2022
ACCEPTED 16 September 2022
PUBLISHED 06 October 2022

CITATION
Burggraf J and Zylstra A (2022), Lasers
for the observation of multiple order
nuclear reactions.
*Front. Phys.* 10:993632.
doi: 10.3389/fphy.2022.993632

# Lasers for the observation of multiple order nuclear reactions

Jeffrey Burggraf* and Alex Zylstra

Lawrence Livermore National Laboratory, Livermore, CA, United States

Nuclear reaction rates become nonlinear with respect to flux ($cm^{-2}s^{-1}$) in extreme environments such as those found during stellar nucleosynthesis and terrestrial nuclear detonations. To observe these effects directly in the laboratory, extremely high particle fluences ($cm^{-2}$) are necessary but not sufficient. Reactor-based neutron sources, such as the Institut Laue-Langevin's high-flux neutron reactor, were previously the closest to meeting this challenge, albeit over ~hour time scales. In ultra-high flux environments, where multiple reactions occur on picosecond time scales, nuclei are unable to return to their ground states between reactions; consequently, reactions take place on excited nuclei. To accurately model high-flux environments, data on the cross-sections of excited nuclear states are required, which differ significantly from those of ground states due to spin/parity effects. In order to replicate these effects in the laboratory, short high-fluence pulses on the order of the lifetime of a typical nuclear excited state (generally $\lesssim$1 ns) are required. Particle beams generated by high-intensity lasers are uniquely positioned to meet this need with the potential to produce fluences of $10^{17}$ protons/$cm^2$ and $10^{22}$ neutrons/$cm^2$ over a few pico-seconds or less. In addition to providing a quantitative analysis of the rates of multiple rapid reactions in general, the present work examines a number of laser-based experiments that could be conducted in the near future to observe multiple rapid reactions for laboratory-based astrophysics and the measurement of exotic cross-sections.

KEYWORDS

**lab-based astrophysics, r-process, national ignition facility (NIF), TNSA, high-intensity laser, fission, isomer, cross-section**

## 1 Introduction

The rates of certain nuclear reactions in extremely hot and dense environments are determined not only by the nuclear cross-sections of the ground state, but also by the nuclear cross-sections of isomeric states since a significant population of them can be maintained by constant bombardment from high particle flux and electromagnetic processes. While the term "isomer" typically refers to nuclear excited states with half-lives greater than 1 ns, an isomer in the present context is a nuclear excited state with a half-life greater than 1 ps. Most nuclear isomers have an energy range of a few keV to a few MeV and a half-life of less than a few hundred nanoseconds, making sample preparation in sufficient quantity for cross-section measurements extremely difficult for traditional experiments. However, due to its exceptionally low excitation energy of 76 eV coupled with a long half-life of 26 min, the first excited state of $^{235}$U is among the few cases where measurement, while very difficult, has been possible up to now. Measurements of cross-sections on $^{235m}$U appear to be up to a factor of 2.5 greater than that of the ground state for thermal neutron induced fission [1]. Deviations of a similar magnitude are expected to exist in the numerous short-lived isomers too and will have a large influence on reaction rates in certain extreme environments.

In plasmas with temperatures less than 10 keV, calculations have suggested that isomeric states are strongly populated by energetic neutrons and/or protons as opposed to other electromagnetic processes [2]. Nevertheless, complex processes such as nuclear excitation by electron capture (NEEC) and nuclear excitation by electron transition (NEET) may also contribute significantly despite the fact that previous observations have ranged from inconclusive to controversial [3–5]. The NEEC and NEET processes require the overlap of an atomic and (extremely narrow) nuclear transition. Thus, accurate predictions require very precise knowledge of atomic transitions in a plasma, which is challenging due to density effects, charge screening, and other phenomena. Definitive observation of NEEC and NEET, especially in the plasma environment, will be of great importance to the question of *how* a population of nuclear isomers is maintained in a plasma.

As the use of high intensity short-pulsed lasers to generate ultra-high flux particle beams has increased in popularity, so has the desire to study isomers and other short-lived nuclei using such beams. It has been proposed that short, high-flux laser-accelerated particle pulses could be used to excite a population of isomers (*via* both nuclear plasma interactions and other nuclear reactions) while also inducing a nuclear reaction in the excited target population [6]. The astrophysical implications of the maintenance of a thermal population of nuclear excited states by various mechanisms in extreme environments is covered elsewhere, for example see [7]. The present work focuses on the generation and probing of short-lived nuclei by rapid repeat nuclear reactions using energetic particles produced by lasers, as well as the potential for novel cross-section measurements relevant to the astrophysics community as higher fluxes become available. Two nuclear reactions occur on the “same” nucleus during this process, with the first reaction producing the nucleus to be studied, which is then subjected to a second nuclear reaction. The term *double reaction* is used herein to refer to such a reaction.

In the past, reactor-based neutron sources have utilized double reactions to make cross-section measurements on nuclei as short-lived as $^{233}$Th ($t_{1/2}$ = 22 min) [8]. In contrast, many more excited states are accessible at high intensity laser facilities with pulse lengths between $10^{-15}$ to $10^{-11}$ s and time integrated particle fluxes that are comparable to those produced by the most powerful reactor-based sources in an hour. Following a nuclear reaction, such as neutron capture or inelastic scattering, the nucleus is nearly always left in a short-lived excited state. Because laser pulse lengths are shorter than the lifetimes of many of these excited states, if two nuclear reactions occur on the same nucleus, the second reaction will sometimes occur on an excited nucleus. Section 2 provides several examples of possible measurements on radioactive nuclei and nuclear isomers that may be of interest to the community, as well as a quantitative analysis of the rates of multiple reactions on a single nucleus. Section 3 provides a quantitative assessment of the prospects for studying double reactions at existing facilities.

## 2 Multiple rapid reactions

### 2.1 Precise definition and significance

During the r-process, many successive nuclear reactions occur on short time scales. Even during terrestrial nuclear detonations, up to 16 rapid neutron captures have been observed [9]. Detailed quantitative analysis of large leaps in nuclear mass up to the neutron drip lines requires the modeling of a large number of reaction channels and is a complex task best left to codes. The observation of more than a few consecutive reactions in sufficient quantities would demand a flux well beyond the capabilities of current facilities. For these reasons, the present work is primarily concerned with double successive reactions of the general form

$$I + n \rightarrow J \tag{1}$$

followed by

$$J + n \rightarrow K \tag{2}$$

where a flux of particle $n$ is incident on a sample of some initial target nucleus, $I$, producing an intermediate residue nucleus, $J$, which undergoes a further reaction to produce the final nucleus, K. For example consider double neutron capture on $^{56}$Fe

$$\begin{gathered} ^{56}\mathrm{Fe} + \mathrm{n} \longrightarrow {}^{57}\mathrm{Fe}^{*} \\ ^{57}\mathrm{Fe}^{*} + \mathrm{n} \longrightarrow {}^{58}\mathrm{Fe} \end{gathered} \tag{3}$$

where * indicates that $^{57}$Fe is in an excited state, which will be the case at the time of the second neutron capture if it occurs on a short time scale due to the presence of several long-lived isomeric levels encountered during the de-excitation of $^{57}$Fe. Thus, double neutron capture on $^{56}$Fe is a candidate for measurements of cross-sections on a short-lived isomer. Another application is cross-sections measurements on nuclei whose preparation in sufficient quantities is prohibitively difficult due to their short half lives. Consider, for instance, double neutron capture on $^{50}$Ti, which, in contrast to double capture on $^{56}$Fe, results in the $^{51}$Ti nucleus returning to its ground state almost instantly after the first capture. At the National Ignition Facility (NIF), the required neutron yields for the observation of such double reactions are already attainable.

Astrophysics is interested in double proton/neutron absorption reactions as a possible pathway to measuring cross-sections on unstable proton/neutron-rich nuclei that are

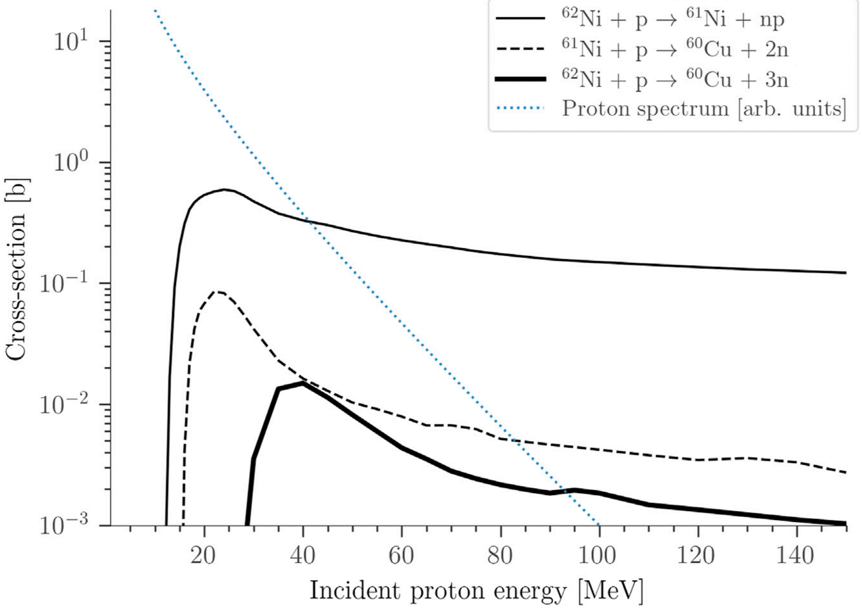

**FIGURE 1**
Cross-sections for the reactions in Eqs 4 and 5. Taken from the ENDF library. For reference, a typical distribution of laser accelerated proton energies is shown.

needed to constrain models. Neutron capture cross-sections on unstable nuclei are important to the rapid neutron capture process (r-process), which produces approximately half of the atomic nuclei heavier than iron. Proton absorption cross-sections on unstable nuclei are important to the rapid-proton process (rp–process), which may explain the abundances of a few nuclei that are bypassed by the other known processes. Double capture/absorption reactions are more straightforward to observe experimentally. To see why, consider the following reaction where the incoming proton is not absorbed,

$$\begin{array}{ll} {}^{62}\mathrm{Ni} + \mathrm{p} \to {}^{61}\mathrm{Ni} + \mathrm{np} & (460\,\mathrm{mb}) \\ {}^{61}\mathrm{Ni} + \mathrm{p} \to {}^{60}\mathrm{Cu} + 2\mathrm{n} & (44\,\mathrm{mb}) \end{array} \tag{4}$$

where the cross-sections are taken from the ENDF library and integrated over a typical laser accelerated proton energy spectrum (see Figure 1). The double reaction pathway for the production of $^{60}$Cu from Eq. (4) is in competition with the following ordinary reaction pathway

$${}^{62}\mathrm{Ni} + \mathrm{p} \to {}^{60}\mathrm{Cu} + 3\mathrm{n} \qquad (2\,\mathrm{mb}). \tag{5}$$

Because the cross-sections of the double reaction pathway are larger than those of the ordinary reaction pathway, it may be tempting to predict that the double reaction pathway will contribute significantly to $^{60}$Cu production in high flux environments. However, due to the statistics of double reactions, the ordinary reaction pathway will continue to predominate over the double reaction pathway even at the highest proton fluence that is currently achievable in the laboratory. The same problem exists for any double reactions involving fission, which is exemplified in section 3.1.2 using neutrons produced at NIF. In contrast, double capture/absorption reactions, in which Z increases by two for incident protons (or A for neutrons), avoid this problem because the final product can only be produced *via* the double reaction pathway.This problem is also avoided in circumstances where the maximum energy of the incident particles is below the cut-off for the competing single-order reaction. For example, consider the following reaction induced using 14 MeV energy of neutrons from D-T fusion

$$\begin{array}{l} {}^{208}\mathrm{Pb} + \mathrm{n} \to {}^{207}\mathrm{Pb} + 2\mathrm{n} \\ {}^{207}\mathrm{Pb} + \mathrm{n} \to {}^{206}\mathrm{Pb} + 2\mathrm{n}. \end{array} \tag{6}$$

The cross-section for the production of $^{206}$Pb from $^{208}$Pb in a single reaction, or $^{208}\mathrm{Pb} + n \to {}^{206}\mathrm{Pb} + 3\mathrm{n}$, is vanishingly small because the two-neutron separation energy of $^{208}$Pb is 14.1 MeV. Therefore, like double absorption reactions, the detection of $^{206}$Pb is unambiguously linked to the double reaction in Eq. (6).

## 2.2 Quantitative analysis of double reaction rates

### 2.2.1 Simplified mathematical forms

The following assumptions are useful in order to analyze double reaction rates in laboratory conditions:

1. All reactions occur virtually instantaneously (zero pulse width), and
2. Multiple order reaction rates are low relative to ordinary reactions.

Assumption (I) is true if nuclides $J$ and $K$ have a long half-life relative to the pulse width; and hence, species decay is irrelevant. This assumption highlights a benefit of short pulsed lasers: shorter pulse widths make more intermediate states available as short-lived isomers that would otherwise decay to the ground state before a second reaction occurs. Assumption (II) is mathematically true if the inverse of the fluence is much less than the relevant cross-sections, which in practice amounts to a fluence of at least ~ $10^{22}$ particles per cm$^2$ in most cases of interest. A consequence of assumption (II) is that "burn-up" of the initial target atoms can be ignored. While the neutron fluence from recent high yield NIF shots approach this limit, none of the other laboratory sources currently available come close. Establishing a differential equation accounting for the rate of production and loss, such as through decay or nuclear reactions (if applicable), of each nucleus is the standard procedure for calculating the amounts of a species of nuclei over time while subject to flux. Other examples of this procedure can be seen in [8–10]. Under the assumptions (I) and (II), the relevant rate equations are

$$\frac{\partial}{\partial_t}\begin{bmatrix} I(t) \\ J(t) \\ K(t) \end{bmatrix} = \begin{bmatrix} 0 & 0 & 0 \\ \phi\sigma_J & 0 & 0 \\ 0 & \phi\sigma_K & 0 \end{bmatrix}\begin{bmatrix} I(t) \\ J(t) \\ K(t) \end{bmatrix}$$
$$\text{such that} \quad \begin{bmatrix} I(0) \\ J(0) \\ K(0) \end{bmatrix} = \begin{bmatrix} N_I \\ 0 \\ 0 \end{bmatrix} \tag{7}$$

where $I(t)$, $J(t)$, and $K(t)$ are the time dependent number of the initial target nucleus, the intermediate residue nucleus, and the final nucleus following the double reaction, respectively. $\phi$ is the flux (cm$^{-2}$s$^{-1}$) and $N_I$ is the number of target nuclei. $\sigma_J$ is the cross-section for the reaction that produces $J$ from $I$ and $\sigma_K$ is the cross-section for the reaction that produces $K$ from $J$. The diagonal terms of the matrix in Eq. (7) vanish due to the simplifying assumptions described above. Otherwise, the solutions become unwieldy but can be handled using mathematical software if needed. Assumption (II) makes a difference of less than 5% for all figures given in the present work. The solutions of interest to Eq. (7) are

$$\begin{aligned} J(t) &= N_I(\phi t)\sigma_J \\ K(t) &= \frac{1}{2}N_I(\phi t)^2\sigma_K\sigma_J \end{aligned} \tag{8}$$

$K(t)$ in Eq. (8) is the total number of double reactions. A lower bound on the fluence ($\phi t$) in order to observe double reactions is then determined by setting $K(t) = 1$, giving

$$(\phi t)_{\min} \sim \sqrt{\frac{2}{N_I\sigma_K\sigma_J}}. \tag{9}$$

### 2.2.2 General mathematical forms

Eq. (8) is easily generalized to higher order reactions (e.g. triple neutron capture) giving

$$\left(\text{yield of } \text{n}^{\text{th}} \text{ order reaction}\right) = \frac{N_I}{n!}(\phi t)^n \prod_{i=1}^{n}\sigma_i \tag{10}$$

where $n$ is the number of successive reactions and $\sigma_i$ is the cross-section for the $i$th reaction.

Relaxing assumption (I) by allowing the intermediate nucleus, J, to undergo decay at a rate of $\lambda_J$ per second, the following multiplicative correction factor can be applied to Eq. (8) to get double reaction yield

$$\left(\text{multiplicative decay correction}\right) = \frac{2\left(t\lambda_j + e^{-t\lambda_j} - 1\right)}{t^2\lambda_j^2}. \tag{11}$$

Since the rate of double-reactions is not linear with respect to the fluence, the following generalization of Eq. (8) must be used in the case of spatially non-uniform fluence

$$K(t) = \frac{1}{2}\int F^2\langle\sigma_K(E)\rangle\langle\sigma_J(E)\rangle\rho\, dV \tag{12}$$

where the angle brackets around $\sigma_K(E)$ and $\sigma_J(E)$ represent flux-weighted average cross-sections, $F$ is the fluence, and $\rho$ is the atom density. Because Eq. (12) depends on the square of the fluence, the rates for diverging sources break from the intuition one may have for ordinary reaction rates. Consider the following example. An isotropic point source is embedded in a spherical vacuum of radius $r_0$ and surrounded by material with atom density $\rho$ extending from $r_0 < r < \infty$. The total double reaction yield is, assuming zero attenuation

$$\begin{aligned} (\text{yield}) &= \frac{1}{2}\sigma_K\sigma_J\rho\int F^2\, dV = \frac{1}{2}\sigma_K\sigma_J\rho\int_{r_0}^{\infty}\left(\frac{s}{4\pi r^2}\right)^2 4\pi r^2\, dr \\ &= \frac{s^2\sigma_K\sigma_J\rho}{8\pi r_0} \end{aligned} \tag{13}$$

where a total of $s$ particles are emitted by the point source. Interestingly, the yield of the double reaction is finite despite particles traversing an infinite amount of material, whereas the yield of single, ordinary reactions diverges to infinity.

## 2.3 Cross-section determination

Because most cross-sections for the population of isomers by inelastic nuclear reactions have not been experimentally measured, the present work uses the TALYS [11] code to estimate cross-sections as needed. The $^{235}U(\text{n},\text{n}')^{235\text{m}}U$ cross-section has been measured experimentally with results agreeing

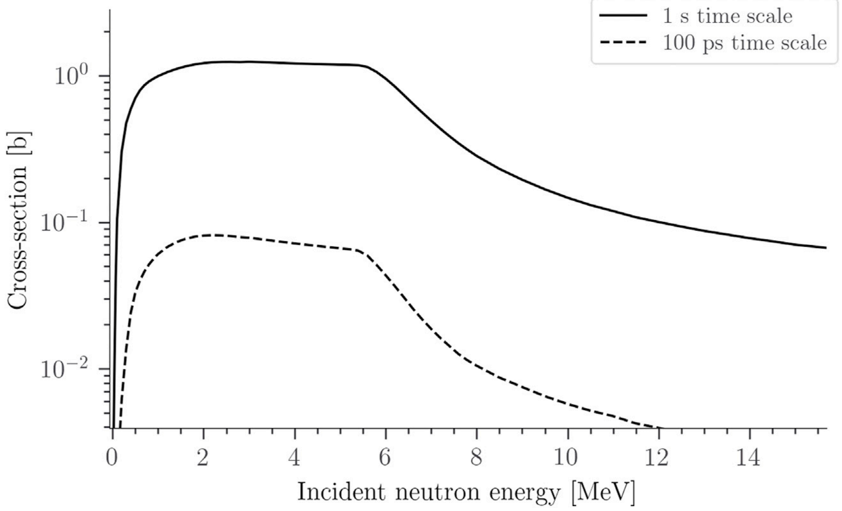

**FIGURE 2**
Two different TALYS calculations of the cross-sections for the production of the first excited state in $^{235}U$ by neutron inelastic scattering. The time-scale can be adjusted by setting the minimum half-life to be treated as an isomer. The effective cross-section for the production of the first excited state is smaller on short time scales because higher excited states do not have enough time to feed the first excited state.

very well with TALYS [12]. While such success is not universal, errors greater than a factor of two are expected to be uncommon. TAYLS can calculate the cross-section for the production of any isomer given that the corresponding discrete nuclear level is documented and assigned a half-life in the Evaluated Nuclear Data Structure File (ENDSF) library. If the discrete state is not assigned a half-life then it cannot be treated as an isomer by TALYS. In TALYS, isomers are produced by both direct inelastic scattering and a time-dependent cascade of decays from higher levels. Fortunately, the code can account for isomer production *via* feeding from decay of higher excited states, which in many cases is the dominant mechanism as opposed to direct inelastic excitation to a given level. This feature is crucial for isomer production calculations in laser environments where isomeric states with lifetimes as short as a few hundred ps may be effectively stable on the time-scale of the laser's pulse width. The algorithm in TALYS will allow an excited nucleus to decay to any available lower lying discrete levels until a level is reached with a half-life greater than or equal to a user-specified threshold, at which point further decays stop. The effects of this setting are demonstrated in Figure 2 where large differences are seen in the calculated cross-sections for the excitation of the 70 eV isomer of $^{235}U$ by neutrons. Setting the minimum half-life threshold to 100 ps results in a lower calculated cross-section because higher, shorter-lived levels are now considered stable by the code and no longer decay to the 70 eV excited state. As a result, perhaps surprisingly, the first excited state of $^{235}U$ is not a great candidate for studying isomers on laser time scales. According to TALYS, the isomer $^{235m}$U is maintained in the largest quantities on ps scales when $^{235}$U target nuclei are irradiated by 14 MeV neutrons, as discussed in greater detail in section 3.1.2.

# 3 Running the numbers

## 3.1 Neutrons at NIF

### 3.1.1 Estimated yields

The National Ignition Facility (NIF) currently holds the record for highest neutron flux produced in a lab. Implosion experiments on the NIF vary in their complexity and the neutron yield, thus fluence, that is achievable. Simple gas-filled capsules can produce DT neutron yields of $10^{14}$–$10^{15}$ and are straightforward to execute. More complex "layered" experiments, in which a layer of DT ice is grown against the inner surface of the capsule, are significantly more complex but enable higher yield. Experiments in the "burning plasma" regime have produced neutron yields up to ~ $5 \times 10^{16}$ [13] and more recent experiments have generated much higher yields, up to ~ $4 \times 10^{17}$ [14]. Based on these results, near-term experiments using yields above $10^{17}$ are possible and even higher yields, for example up to $10^{18}$, may be plausible within the next several years. In these experiments, the neutron flux lasts ~ 100 ps and is contained within a ~ 50 $\mu$m radius. For a neutron yield of $10^{17}$, this corresponds to neutron fluence of $4 \times 10^{21}$ neutrons per cm$^2$. The next most intense neutron source in terms of run-integrated fluence is found in research reactors, which are capable of producing ~ $10^{19}$ thermal neutrons per cm$^2$ per day.

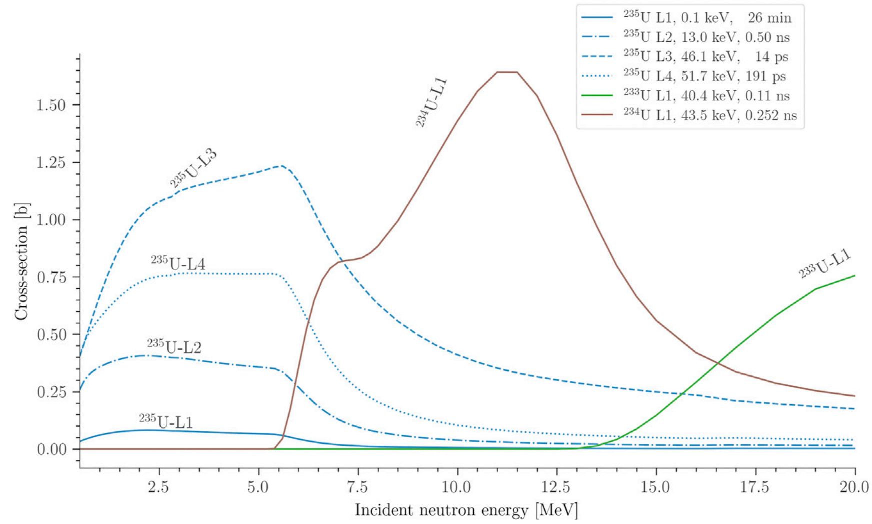

**FIGURE 3**
Cross-sections for the production of several isomers from neutron bombardment of $^{235}$U.

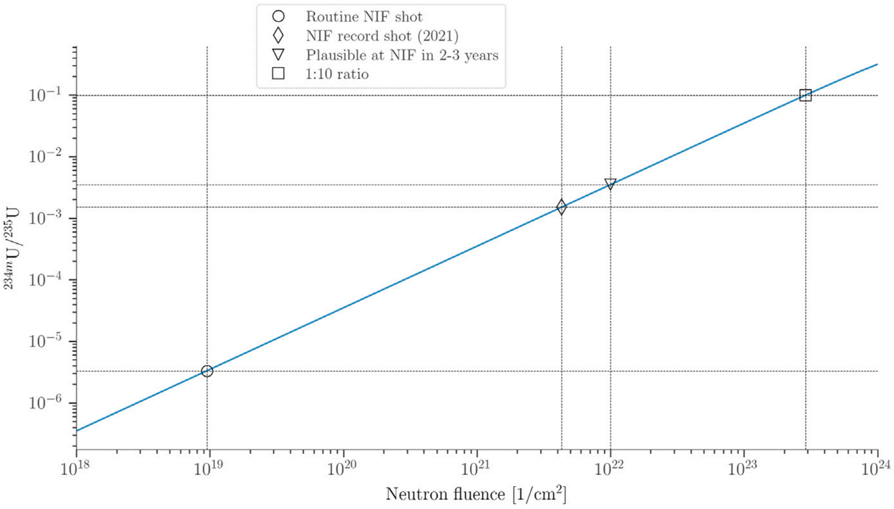

**FIGURE 4**
Time averaged ratio of $^{235m}$U to $^{235}$U maintained by the $^{235}$U(n, 2n)$^{234m}$U reaction during high flux bombardment of $^{235}$U by 14 MeV neutrons. $^{234m}$U refers to the 43.5 keV, 252 ps half-life isomer of $^{234}$U. This isomer of $^{234}$U is chosen here because it has the highest production cross-section from NIF neutrons on $^{235}$U according to TALYS calculations. At a ratio of 1:10, it likely becomes possible to observe changes in fission rates and yields due to multiple reactions.

In the following examples, it is assumed that $10^{15}$ target atoms are seeded in the NIF capsule and exposed to a neutron yield of $10^{17}$ (fluence = $10^{21}$ neutrons/cm$^2$). For a given pair of cross-sections, these conditions give a double reaction yield of

$$(\text{yield of double reaction}) \approx 5 \times 10^{8} \sigma_J \sigma_K \left[b^{-2}\right]. \tag{14}$$

where $\sigma_J$ and $\sigma_K$ are the cross-sections for the first and second reactions in units of barns.

### 3.1.2 Fission on an excited nuclear state $^{235m}U$

According to cross-sections provided by TALYS, the most numerous fissionable isomer created by neutron interactions on

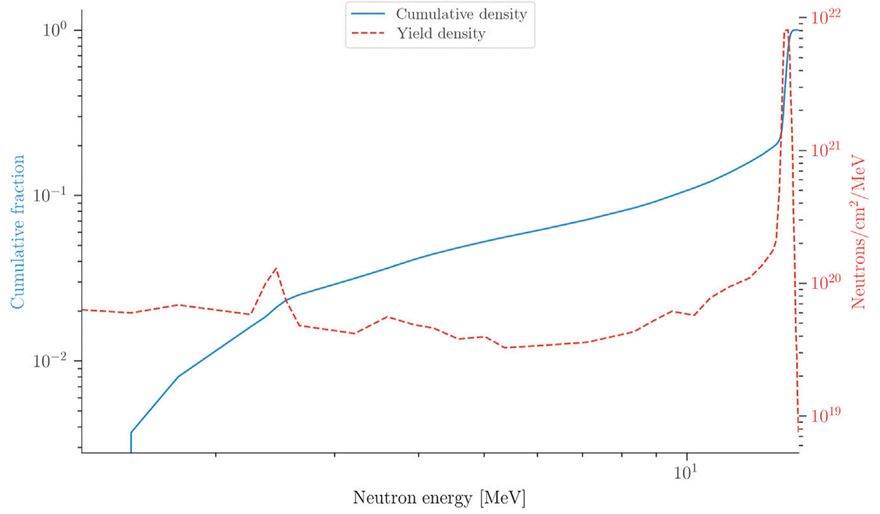

**FIGURE 5**
Energy distribution of neutrons during a NIF implosion. Data taken from [15]; page 7). The cumulative fraction is also given for the reader's convenience so that the fraction of neutrons in a given energy range can be quickly estimated by taking the difference between the values at two energies.

$^{235}$U nuclei under the conditions of a high yield NIF implosion is the 43.5 keV, 252 ps isomer of $^{234}U$ produced by the $^{235}U\,(\mathrm{n, 2n})^{234m}U$ reaction, with a calculated cross-section of about 0.7 b for the relevant neutrons. See Figure 3 for a few other relevent cross-sections output by TALYS. Using this value and a fission cross-section of 2 b, Eq. (14) gives $7 \times 10^8$ fissions on $^{234m}U$. This is small in comparison to the number of ordinary fission on the $^{235}$U target nuclei, which calculated using standard methods gives $2 \times 10^{12}$. Since fission of $^{235}$U dominates over $^{234m}$U by a factor of ~3,000 under these conditions, it is unlikely that there will be a measurable difference in overall fission rate or fission product yields due to the presence of isomers created by neutrons. Figure 4 shows the time averaged ratio between the number of $^{234}U$ isomers and initial $^{235}$U nuclei as a function of neutron fluence. A ratio that would potentially lead to a measurable difference in fission observables is ≈1/10. The flux required to achieve this at NIF, all else equal, would be $\approx 2 \times 10^{23}\ \mathrm{n}/(\mathrm{cm}^2)$, or a factor of ~ 50 increase over current capabilities. Coincidentally, this value is about what is expected for igniting capsules at NIF [15]; page 92). NIF appears to be the most promising high flux source of any particle type currently available for this type of measurement. In the near future, however, completely different approaches, such as using surrogate reactions with reverse kinematics in storage rings are also promising [16].

### 3.1.3 Double neutron capture

In contrast to fission, where the observability of double reaction effects are determined by the ratio of ordinary fission to fission following a secondary reaction, double neutron capture can be observed unambiguously by the detection of (Z, A+ 2) nuclei. While the neutron capture cross-sections for 14 MeV D-T neutrons are quite low, a significant fraction of neutrons at NIF are down scattered to lower energies. Figure 5 depicts the energy spectrum down to 1 MeV; the rates of neutrons with energies less than approximately 1 MeV are poorly understood due to the difficulty of measuring them at NIF [15]; page 76. Even though only a minute fraction of neutron flux is in the thermal energy range, because the cross-sections for neutron capture at thermal energies can be over 100,000 times larger than for MeV neutrons, the low energy neutron component can have a significant effect on capture yields. Note that the calculations below do not include neutron energies below 1 MeV and therefore represent lower bounds on expected yields.

Consider double neutron capture on $^{40}$Ar, yielding $^{42}$Ar. The cross-sections for this reaction, integrated over the NIF spectrum in Figure 5, are $1.2 \times 10^{-4}$ b, and $1.4 \times 10^{-3}$ b for $^{40}\mathrm{Ar} + n \rightarrow {}^{41}\mathrm{Ar}$ and $^{41}\mathrm{Ar} + n \rightarrow {}^{42}\mathrm{Ar}$, respectively, according to the ENDF library. This gives an expected yield according to Eq. (14) of $1.5 \times 10^3$ $^{42}$Ar nuclei given that $10^{15}$ initial $^{40}$Ar nuclei are seeded into the capsule. With a half-life of over 30 years, these rates are not high enough to perform gamma spectroscopy. Efforts are currently underway to test the viability of using the RAGS system to collect and store $^{42}$Ar for transport to Argonne National Laboratory where accelerator mass spectrometry will be performed (per personal communication with Micheal Paul of Argonne National Laboratory). Much higher double neutron capture yields are possible, with the highest achievable at NIF being around $\sim 5 \times 10^6$ if a nucleus with a high neutron capture cross-section like $^{158}$Dy is used. Using a nucleus with a more typical neutron capture cross-section like $^{235}$U gives an estimated yield of ~ 6 × $10^5$ radioactive $^{237}$U nuclei from double neutron capture. As a final example, consider double capture on $^{56}$Fe as denoted in Eq. (3), a possible scheme to measure neutron capture cross-section on excited $^{57}$Fe as compared to the ground state. This reaction gives a calculated yield of ~ $10^4$ $^{58}$Fe nuclei, easily measurable by techniques such as accelerator mass spectroscopy.

### 3.1.4 Other reactions

The production of $^{232}$U from $^{235}$U *via* double reactions cannot occur *via* a single reaction from neutrons at NIF because the threshold for the (n, 4n) reaction is approximately 19 MeV, avoiding the previously described problem of dominance by an ordinary reaction channel. There are two pathways to produce $^{232}$U from $^{235}$U *via* double reactions

$$\begin{aligned} {}^{235}\mathrm{U} + \mathrm{n} &\rightarrow {}^{234}\mathrm{U} + 2\mathrm{n} \qquad (.56\,\mathrm{b}) \\ {}^{234}\mathrm{U} + \mathrm{n} &\rightarrow {}^{232}\mathrm{U} + 3\mathrm{n} \qquad (3.2 \times 10^{-3}\,\mathrm{b}) \end{aligned} \tag{15}$$

and

$$\begin{aligned} {}^{235}\mathrm{U} + \mathrm{n} &\rightarrow {}^{233}\mathrm{U} + 3\mathrm{n} \qquad (3.0 \times 10^{-2}\,\mathrm{b}) \\ {}^{233}\mathrm{U} + \mathrm{n} &\rightarrow {}^{232}\mathrm{U} + 2\mathrm{n} \qquad (0.18\,\mathrm{b}) \end{aligned} \tag{16}$$

where the cross-sections, taken from ENDF, are energy-weighted. The usefulness of this example is the high yields. Compared to the example of double neutron capture reaction on $^{235}$U, the calculated yield of $^{232}$U in this example is 3,000x greater, at 2 × $10^9$, owing to the higher cross-sections.

## 3.2 Protons from TNSA

### 3.2.1 Estimated yields

Irradiating thin foils with short-pulse, ultrahigh intensity lasers to generate energetic protons is emerging as a promising method for achieving fluxes high enough to be relevant for multiple reactions. In particular, the well-known Target Normal Sheath Acceleration (TNSA) method is distinguished from conventional ion accelerators by its ability to send high count particle bunches into very small areas with a very short pulse length. The best set of conditions within reach of current systems is ~ $10^{13}$ protons [17] produced over a 50 $\mu$m radius with a 15° diverging angle. The following yield calculation assumes that the protons traverse through a target material of typical solid densities (5 × $10^{23}$ atoms/cm$^3$) and a thickness of a few mm, beyond which the double reaction rate is virtually zero due to beam divergence (this can be seen by using Eq. (12), following the same pattern of the example of Eq. (13)). Taking into account these (generous) assumptions, the maximum achievable rate of a double proton reaction using protons from TNSA at existing facilities is about

$$(\text{max. tot. yield of double reaction}) \approx 6 \times 10^2 \sigma_J \sigma_K \left[b^{-2}\right] \tag{17}$$

where $\sigma_J$ and $\sigma_K$ and the cross-sections for the two reactions in barns. Thus, to be readily detectable, the product of the cross-sections of the two reactions must be such that $\sigma_J \sigma_K \gtrsim 0.001\ \mathrm{b}^2$.

### 3.2.2 Double proton absorption

For example, consider the following double proton absorption reaction on $^{206}$Pb

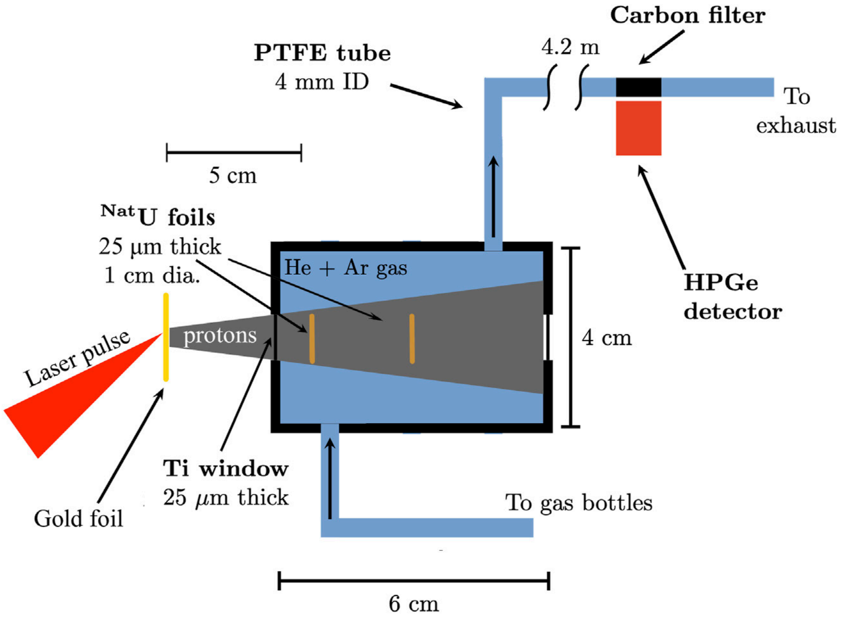

FIGURE 6
Schematic of a gas transport system for the collection of nuclear reaction products that was tested at the PHELIX laser facility.

$$\begin{aligned} ^{206}\mathrm{Pb} + p &\rightarrow {}^{205}\mathrm{Bi} + 2n \\ ^{205}\mathrm{Bi} + p &\rightarrow {}^{204}\mathrm{Po} + 2n. \end{aligned} \tag{18}$$

Using data from ENDF and TALYS for Pb and Bi, respectively, and averaging the cross-sections over a typical TNSA spectrum gives a value of 0.5 b for both reactions. From Eq. (17) this gives a yield of 150 $^{204}$Po per laser shot. Since the conditions leading to Eq. (17) were generous, experimental observation of double reactions using TNSA is possible in the relative near-term with some improvements. Upcoming laser facilities with a higher repetition rate will be particularly useful; newer lasers are expected to shoot once per minute or at Hz to 10 Hz rates, making "rare event" searches feasible with routine proton yields as low as $10^{11}$.

### 3.2.3 Initial steps at PHELIX facility

In the vicinity of high intensity laser interactions with matter, the majority of conventional nuclear measurement techniques will fail due in part to high peak current, strong electromagnetic pulse (colloquially EMP), and the presence of plasmas. This has motivated the development of a gas transport and collection system in which nuclear reactions occur within a small, hermetically sealed chamber through which inert gas flows, carrying reaction products to a filter where gamma spectroscopy is performed (see Figure 6). A successful proof-of-principle demonstration was conducted at the peta-watt PHELIX laser facility in 2020 [18] using 500 fs, ≈ 200 J laser pulses to accelerate bunches of protons *via* TNSA. The maximum proton fluence tested using this method at PHELIX is $2 \times 10^{11}$ protons/cm$^2$, incident on $^{238}$U targets. An optimistic estimate of the rate of double reactions under these circumstances predicts only one occurrence every ~10,000 laser shots, which would require years of daily operation at the maximum repetition rate. The distance between the $^{238}$U target and the gold TNSA foil (5 cm, see Figure 6) was the primary factor limiting the amount of usable fluence in these experiments. This distance, ideally, would be on the order of a few microns, effectively bringing the laser-matter interaction inside the chamber–a significant overhaul over the current design. Nonetheless, this is the initial step toward radchem-type experiments at peta-watt laser facilities, whereas similar capabilities known as RAGS have existed at NIF for about a decade. The development of this platform is ongoing, and additional work by the present authors and collaborators will be published elsewhere in the coming months by the present authors in collaboration with others.

## 4 Summary and outlook

The possibility of inducing multiple nuclear reactions in rapid succession has been considered in order to study nuclear reactions on short-lived isomers and exotic nuclei. A set of practical equations with varying degrees of generality for estimating double reaction rates has been developed. Double neutron-capture reactions have been performed using reactors capable of producing $10^{19}$ neutrons/cm$^2$/day, but the slow accumulation of fluence precludes studies on short-lived nuclear isomers, which are required to conduct studies relevant to ultra high-flux environments such as those that occur during the r-process. High intensity lasers, while posing new measurement challenges, have the potential to outperform the highest fluence achievable with conventional methods by orders of magnitude, and have pulse lengths down to a few ps to ns.

For reactions where an isotopic signature can be uniquely linked to the double reaction, such as double neutron capture, the necessary fluence is currently readily attainable at NIF using D-T fusion neutrons. Upcoming facilities such as ELI-NP will also meet this threshold with sources of neutrons and protons. For double reactions that do not produce an unambiguous isotopic signature, such as neutron capture followed by neutron induced fission, the experimental fluence required to observe them is much higher, generally greater than ~ $10^{23}$ particles per cm$^2$. This is because this class of double reactions will only manifest experimentally if double reaction rates are on the same order as ordinary reaction rates. At this point, nonlinearities in reaction rates with respect to flux become apparent; such an observation in a laboratory would be monumental in the study of extreme environments. NIF is currently the most promising facility for achieving the necessary fluence, but further increases of ~50x are still required.

Owing to their ability to squeeze a large number of particles into a very small area in a very short duration, next-generation lasers will be at the forefront of the study of nuclear reactions in extreme environments. A major challenge in the near term will be the adaptation of current measurement methods and instruments to the hostile environment of the high intensity laser, as well as the development of new measurement methods. The present authors hope that this work will serve as a catalyst for additional research and discussions in this emerging field.

## Author contributions

JB conceived and drafted the document, while AZ contributed insight and editing.

## Funding

This work was performed under the auspices of the U.S. Department of Energy by Lawrence Livermore National Laboratory under Contract DE-AC52-07NA27344 and was supported by the LLNL-LDRD Program under Project No. 20-ERD-031.

## Conflict of interest

The authors declare that the research was conducted in the absence of any commercial or financial relationships that could be construed as a potential conflict of interest.

## Publisher's note

## References

1. D'Eer A, Wagemans C, Nève de Mévergnies M, Gönnenwein F, Geltenbort P, Moore MS, et al.Neutron-induced fission of the 26 min isomer. *Phys Rev C* (1988) 38:1270–6. doi:10.1103/PhysRevC.38.1270

2. Luu TC, Friar JL, Hayes AC. Electromagnetic excitation rates for nuclear isomers in a hot dense plasma. *Nucl Sci Eng* (2006) 152:98–105. doi:10.13182/NSE06-A2567

3. Guo S, Fang Y, Zhou X, Petrache CM. Possible overestimation of isomer depletion due to contamination. *Nature* (2021) 594:E1–2. doi:10.1038/s41586-021-03333-5

4. Chiara CJ, Carroll JJ, Carpenter MP, Greene JP, Hartley DJ, Janssens RVF, et al.Reply to: Possible overestimation of isomer depletion due to contamination. *Nature* (2021) 594:E3–E4. doi:10.1038/s41586-021-03334-4

5. Rzadkiewicz J, Polasik M, Słabkowska K, Syrocki L, Carroll JJ, Chiara CJ. Novel approach to isomer depletion: Nuclear excitation by electron capture in resonant transfer process. *Phys Rev Lett* (2021) 127:042501. doi:10.1103/PhysRevLett.127.042501

6. Chen SN, Negoita F, Spohr K, d'Humières E, Pomerantz I, Fuchs J. Extreme brightness laser-based neutron pulses as a pathway for investigating nucleosynthesis in the laboratory. *Matter Radiat Extremes* (2019) 4:054402. doi:10.1063/1.5081666

7. Rauscher T. Revision of the derivation of stellar rates from experiment and impact on eu s-process contributions. *J Phys : Conf Ser* (2016) 665:012024. doi:10.1088/1742-6596/665/1/012024

8. Chatani H. Measurement of effective cross section of Th-233(n, γ)Th-234 reaction using the KUR. *AIP Conf Proc* (2005) 769. doi:10.1063/1.1945097

9. Lutostansky YS, Lyashuk VI. Production of transuranium nuclides in pulsed neutron fluxes from thermonuclear explosions. *Jetp Lett* (2018) 107:79–85. doi:10.1134/S0021364018020108

10. Zagrebaev VI, Karpov AV, Mishustin IN, Greiner W. Production of heavy and superheavy neutron-rich nuclei in neutron capture processes. *Phys Rev C* (2011) 84:044617. doi:10.1103/PhysRevC.84.044617

11. Koning AJ, Hilaire S, Duijvestijn MC. Talys-1.0. In: *International conference on nuclear data for science and technology*. EDP Sciences (2007). p. 211

12. Bélier G, Bond EM, Vieira DJ, Authier N, Becker JA, Hyneck D, et al.Integral cross section measurement of the reaction in a pulsed reactor. *Phys Rev C* (2015) 91:044605. doi:10.1103/PhysRevC.91.044605

13. Zylstra A, Hurricane O, Callahan D, Kritcher A, Ralph J, Robey H, et al.Burning plasma achieved in inertial fusion. *Nature* (2022) 601:542–8. doi:10.1038/s41586-021-04281-w

14. Herrmann M. Building to a solution: The elements of a fusion breakthrough (2021). Available from: https://lasers.llnl.gov/news/building-to-a-solution-elements-of-a-fusion-breakthrough (accessed July, 2022).

15. Cerjan CJ, Bernstein L, Hopkins LB, Bionta RM, Bleuel DL, Caggiano JA, et al.Dynamic high energy density plasma environments at the national ignition facility for nuclear science research. *J Phys G: Nucl Part Phys* (2018) 45:033003–2. doi:10.1088/1361-6471/aa8693

16. Henriques A, Jurado B, Denis-Petit D, Chiron T, Gaudefroy L, Glorius J, et al.Future perspectives for surrogate-reaction studies at storage rings. In: J Escher, Y Alhassid, LA Bernstein, D Brown, C Fröhlich, P Talou, et al.editors*Compound-nuclear reactions*. Cham: Springer International Publishing (2021). p. 209

17. Borghesi M. Laser-driven ion acceleration: State of the art and emerging mechanisms. In: *Nuclear instruments and methods in Physics research section A: Accelerators, spectrometers, detectors and associated equipment*, 740. Proceedings of the first European Advanced Accelerator Concepts Workshop 2013 (2014). p. 6–9. doi:10.1016/j.nima.2013.11.098

18. Boller P, Zylstra A, Neumayer P, Bernstein L, Brabetz C, Despotopulos J, et al.First on-line detection of radioactive fission isotopes produced by laser-accelerated protons. *Sci Rep* (2020) 10:17183. doi:10.1038/s41598-020-74045-5

frontiers | Frontiers in Physics

TYPE Review
PUBLISHED 18 October 2022
DOI 10.3389/fphy.2022.944339

OPEN ACCESS

EDITED BY
Maria Gatu Johnson,
Massachusetts Institute of Technology,
United States

REVIEWED BY
Massimo Nocente,
University of Milano-Bicocca, Italy
Carl Brune,
Ohio University, United States

*CORRESPONDENCE
Z. L. Mohamed,
zlm@lanl.gov,
zmoh@lle.rochester.edu

SPECIALTY SECTION
This article was submitted to Nuclear Physics,
a section of the journal
Frontiers in Physics

RECEIVED 15 May 2022
ACCEPTED 26 September 2022
PUBLISHED 18 October 2022

CITATION
Mohamed ZL, Kim Y and Knauer JP (2022), Gamma-based nuclear fusion measurements at inertial confinement fusion facilities.
*Front. Phys.* 10:944339.
doi: 10.3389/fphy.2022.944339

# Gamma-based nuclear fusion measurements at inertial confinement fusion facilities

Z. L. Mohamed[1]*, Y. Kim[1] and J. P. Knauer[2]

[1]Los Alamos National Laboratory, Los Alamos, NM, United States, [2]Laboratory for Laser Energetics, University of Rochester, Rochester, NY, United States

Experiments performed on an inertial confinement fusion (ICF) platform offer a unique opportunity to study nuclear reactions, including reaction branches that are useful for diagnostic applications in ICF experiments as well as several that are relevant to nuclear astrophysics. In contrast to beam-accelerator experiments, experiments performed on an ICF platform occur over a short time scale and produce a plasma environment with physical parameters that are directly relevant to big bang and/or stellar nucleosynthesis. Several reactions of interest, such as $D(T,\gamma)^5He$, $H(D,\gamma)^3He$, $H(T,\gamma)^4He$, and $T(^3He,\gamma)^6Li$ produce high-energy gamma rays. S factors or branching ratios for these four reactions have recently been studied using various temporally-resolved Cherenkov detectors at the Omega laser facility. This work describes these detectors as well as the current standard technique for performing these measurements. Recent results for reactions $D(T,\gamma)^5He$, $H(D,\gamma)^3He$, $H(T,\gamma)^4He$, and $T(^3He,\gamma)^6Li$ are reviewed and compared to accelerator-based measurements. Limitations associated with implosion experiments and use of the current standard gamma detectors are discussed. A basic design for a gamma spectrometer for use at ICF facilities is briefly outlined.

KEYWORDS

**inertial confinement fusion, fusion gamma ray, laser-driven fusion, omega laser facility, nuclear astrophysics, big bang nucleosynthesis, gamma-ray emission spectra, S factor**

## 1 Introduction

Inertial confinement fusion (ICF) experiments typically involve laser-driven implosion of a spherical target which produces a high-energy-density (HED) plasma as temperatures and pressures increase to levels at which fusion of ions can occur. “High-performance” ICF experiments generally use cryogenic deuterium-tritium (DT) targets consisting of DT vapor surrounded by DT ice and seek to optimize target and laser parameters so as to promote self-heating of the target through redistribution of energy as $^4He$ or $\alpha$ particles from the $D(T,n)^4He$ reaction slow down in the dense cryogenic DT ice layer. While these types of experiments are of interest from a fusion energy perspective, the ICF experimental platform can also be leveraged for the purpose of nuclear science experiments. This is especially interesting within the context of astrophysically-relevant nuclear reactions. In contrast to the previously mentioned “high performance” fusion energy-focused studies, nuclear experiments performed using an ICF experimental platform typically involve warm (i.e., room-temperature) targets consisting of thin glass or plastic shells filled with a gaseous mixture of reactants.

Nuclear measurements have traditionally been made *via* accelerator experiments. These accelerator experiments typically collect data using ions from a beam which collide with static target nuclei. In contrast, experiments performed on an ICF platform are able to more closely replicate conditions present in astrophysical environments, such as those relevant to big bang or stellar nucleosynthesis. For example, ICF experiments establish a population of moving ions in which reactions occur along with temperature, pressure, and electron screening effects that can come closer to those present when nucleosynthesis occurs in nature. There are, however, also potential disadvantages to use of the ICF platform for cross-section/S-factor measurements. For example, ICF experiments typically generate relatively large particle fluxes per unit time in comparison to accelerator experiments. This can be advantageous for the purpose of limiting backgrounds (e.g., backgrounds from cosmic rays), however, the production of particles in several distinct, pulse-like events instead of one continuous experiment means that particle statistics cannot be improved by a simple increase in the duration of the experiment. This means that certain very low cross-section reactions cannot currently be studied on an ICF platform, as particle statistics would be too poor to produce meaningful results. Furthermore, only certain types of detectors can be successfully used on an ICF platform. Traditional pulse height detectors, for example, cannot be used due to the short time scales of ICF experiments. Time-of-flight detectors are typically used instead, though calibration of these detectors can be challenging.

There are some further restrictions on which reactions can be studied *via* ICF experiments based on the reactants involved. ICF experiments can typically only accommodate nuclear experiments involving gaseous light ions (which are used as the target fill). Implosion of these targets produces primary fusion gammas and neutrons with the energies of the products depending on the reactants present in the gas fill. DT and DD gas fills are the most commonly used in ICF experiments. It is also possible to conduct experiments involving the collision of DT (14-MeV) or DD (2.45-MeV) neutrons on some material situated outside of the target [1]. It is generally not possible to further select the gamma or neutron energies produced by the implosion.

Production of additional reactions besides the reaction of interest to the experiment can also lead to backgrounds on the spectra of interest. For example, implosion of a DT target produces DD and TT neutrons as well as DT neutrons, and DD gammas as well as DT gammas. Considering these many differences from accelerator experiments as well as these unique advantages and disadvantages, it is clear that experiments performed on ICF platforms represent a valuable complement to specific types of accelerator experiments rather than a replacement for accelerator experiments. The properties and particle statistics involved in any given ICF-based experimental campaign that aims to make nuclear cross-section measurements must be closely evaluated before determining whether the ICF platform is suitable for a given study.

This work reviews the current standard procedure for studying gamma-producing nuclear fusion reactions in HED plasmas as produced by ICF experiments. The design and calibration of the standard gamma detectors present at ICF facilities are detailed. The standard procedure for calculating nuclear yields using these detectors is outlined and results of ICF-based studies focusing on the four reactions $D(T,\gamma)^5He$, $H(T,\gamma)^4He$, $H(D,\gamma)^3He$, and $T(^3He,\gamma)^6Li$ are then reviewed. Finally, potential directions for the development of a gamma spectrometer that is practical for use at ICF facilities are discussed.

To date, the fusion gammas from the reactions $D(T,\gamma)^5He$, $H(T,\gamma)^4He$, $H(D,\gamma)^3He$, and $T(^3He,\gamma)^6Li$ have been studied at the Omega laser facility. Due to its relatively large cross section, the reaction $D(T,n)^4He$ is considered to be among the most promising to focus upon for the purposes of fusion energy research. As such, DT implosions constitute the majority of experiments performed at ICF facilities, and neutrons from this reaction are studied intensively. Gamma rays from the branch $D(T,\gamma)^5He$ are produced simultaneously and are also used for complementary diagnostic purposes in fusion energy-focused implosion experiments. In particular, the DT gamma is currently used for measurements of burn width, which is considered a vital parameter in evaluating the performance of these implosions. Gammas from this reaction as well as $H(T,\gamma)^4He$ are additionally used in dedicated experiments that seek to study the mix of ablator material from the target's shell into its hot spot, where most of the fusion occurs, as excessive mixing of ablator material into the hot spot is known to degrade overall implosion performance [2]. In addition to their importance to ICF itself, study of the gammas from these reactions serve as references for the design and execution of experiments that instead seek to perform nuclear measurements using implosions at facilities such as OMEGA or the National Ignition Facility (NIF). The DT gamma is also vital for the absolute calibration that is necessary to make such measurements, which will be further discussed in Section 2.

$H(D,\gamma)^3He$ and $T(^3He,\gamma)^6Li$ are both important reactions within the context of big bang nucleosynthesis (BBN). These reactions are both relevant to the cosmological lithium problem, which describes 1) a factor of ~ 3-4 discrepancy between the observed abundances of primordial $^7Li$ and the primordial $^7Li$ abundance that is expected based on the current standard model of BBN, and 2) a ~3 order of magnitude discrepancy in the amount of $^6Li$ observed in metal-poor stars and the $^6Li$ abundance that is expected according to the standard model of BBN [3–6]. $H(D,\gamma)^3He$ is important to BBN (as well as to the evolution of protostars [7]) due to its consumption of deuterium and production of $^3$He. It is known to be the primary reaction which consumes deuterium and produces the $^3$He needed for the eventual production of heavier nuclei in BBN. It is therefore considered to be a limiting reaction in BBN, as uncertainties or perturbations in the cross section or S factor for this reaction would influence abundances of primordial D, $^3$He, and Li [6, 8]. T($^3$He,$\gamma$)$^6$Li is clearly relevant to the lithium problem as a reaction that directly creates $^6$Li. Furthermore, there is limited experimental data available on the cross section for this reaction, especially at the low energies relevant to BBN [9]. Although there are several reactions that are relevant to BBN, these two reactions have been studied on an ICF platform due to their importance as well as due to the fact that their relatively high cross sections and the energies of their emitted gammas lend themselves towards successful measurements at conditions achievable *via* implosion experiments and with the gamma detectors that are currently available at ICF facilities.

## 2 Detectors and calibration

Due to the relatively short (~100-ps scale burn duration) time scales associated with ICF experiments, the standard gamma detectors available at ICF facilities are all current-mode (i.e., temporally-resolved) detectors. This means that the raw signal from these detectors is a voltage as a function of time. All of the standard gamma detectors currently available at ICF facilities (i.e., NIF and OMEGA) are Cherenkov detectors. These detectors typically involve a glass, plastic, or gas reservoir that serves as a radiator. The radiator is coupled to a photomultiplier tube (PMT). Because all gammas travel at the speed of light and generally are not scattered by materials present in ICF targets, these Cherenkov detectors typically detect all prompt fusion gammas within a relatively short spread of times. Secondary gammas such as neutron-induced inelastic gammas may also be observed at later times in the time-of-flight signal, the exact timing of which can be altered depending on the detector distance and the material's distance from target chamber center (TCC). This configuration can be useful for calibration purposes.

Cherenkov detectors rely on the phenomenon of Cherenkov radiation. Incident gamma rays scatter electrons in the radiator, which produce electromagnetic radiation in the form of photons which are emitted in spherical wavefronts. If the speed of a given electron is greater than the local speed of light within the radiator, constructive interference between the spherical wavefronts produces a conical flux of photons ("Cherenkov radiation") which can be detected by a photo-detector such as a PMT. The local speed of light in a medium is equal to $c/n$ where $c$ represents the speed of light in vacuum while $n$ represents the index of refraction of a material. It is therefore clear that the minimum gamma energy that can be detected by a given Cherenkov detector depends on the index of refraction of its radiator.

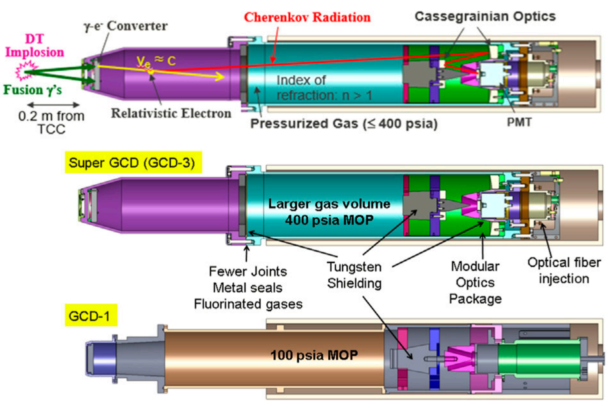

FIGURE 1
Schematic showing design of GCD-1 and GCD-3. The top diagram illustrates the general operation of these similar detectors while the lower two diagrams show the differences in design between GCD-1 and GCD-3. These detectors use Cherenkov radiation in high pressure gases to detect incident gamma rays. The threshold can be adjusted by changing the pressure of the gas. GCD-1 can also use other materials such as fused silica or aerogel radiators. These diagnostics are re-entrant diagnostics on OMEGA and the NIF. They are generally fielded close to TCC to maximize solid angle.

The main detectors that are currently in use at ICF facilities and may be used for nuclear astrophysics experiments such as cross-section or S-factor measurements include the two Gas Cherenkov Detectors (GCD's) GCD-1 [10, 11] and GCD-3 [12] as well as the Diagnostic for Areal Density (DAD) [13]. There are GCD's available at both the NIF and OMEGA, however, the DAD is only available at OMEGA. The three detectors can be run simultaneously at OMEGA, and the two GCD's can be run simultaneously at the NIF.

Both GCD-1 and GCD-3 use pressurized gases as a Cherenkov medium, though the two detectors have somewhat different designs (e.g., maximum operational pressure of GCD-1 is 100 psia while that of GCD-3 is 400 psia). Different gas fills may be used for various purposes. The type of gas and the gas pressure can be adjusted to change the threshold energy for detection *via* changes in the refractive index of the gas. GCD-1 can also use non-gaseous radiators such as fused silica or aerogel. Both GCD's are re-entrant diagnostics. This means that they are fielded by placement in one of OMEGA's ten inch manipulators (TIM's) or one of the NIF's diagnostic instrument manipulators (DIM's). The TIM's or DIM's allow the detectors to enter the vacuum inside of the target chamber to reach close to the implosion for increased solid angle while also providing precise positioning capabilities for diagnostics. GCD-3 is an updated version of GCD-1 which includes additional shielding, improved seals, and a different snout design.

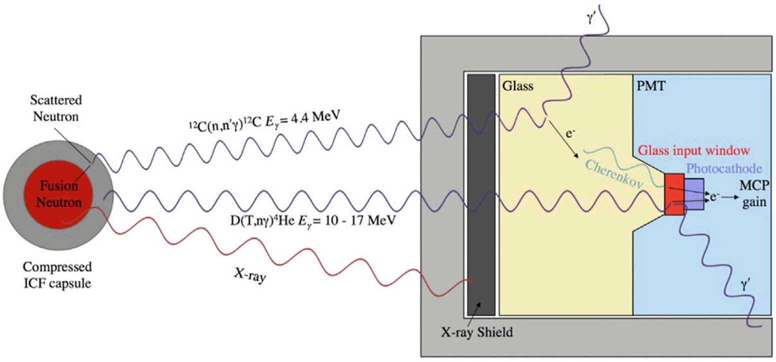

FIGURE 2
Schematic showing design of the DAD and illustrating its response to gamma rays of different energies. This detector uses Cherenkov radiation in fused silica to detect incident gamma rays. It can detect gamma rays above ~ 0.34 MeV. It is a fixed diagnostic that is always located on the OMEGA target chamber wall, about 1.7 m from TCC. Its solid angle is therefore relatively low. Image originally published in Ref. 13 and reproduced with permission from the author and AIP Publishing.

Figure 1 shows a schematic for the two GCD's and points out differences between their designs.

The DAD relies on Cherenkov radiation in fused silica. It is available at OMEGA only. It was originally deployed in 2014 to measure remaining shell areal densities *via* measurement of 4.4-MeV gammas from the first excited state of carbon [13], but is capable of measuring any gammas above ~ 0.34 MeV (assuming the standard index of refraction $n = 1.46$ for fused silica). The DAD consists of 6 mm of tungsten shielding in front of a 6.39-cm diameter, 5-cm thick piece of fused silica, which is directly coupled to a PMT. Figure 2 shows a schematic illustrating the DAD detector design. This setup is situated directly on the wall of the OMEGA target chamber. The face of the detector is located ~172.3 cm from TCC while the PMT and electronics are located outside the target chamber wall. In comparison to the GCD's, the DAD has a smaller solid angle due to its location on the target chamber wall, so its particle statistics on a given experiment are generally poorer than those relevant to either GCD-1 or GCD-3. As a fixed diagnostic, however, it is much simpler to field at OMEGA, as it is always present on the target chamber and does not require any gas fill, leak testing, or precise positioning before a given shot. It is also capable of detecting low energy gammas that cannot be detected by GCD-3 (1.8 MeV minimum threshold with 400 psia $C_2F_6$) or GCD-1 (6.3 MeV minimum threshold with 100 psia $CO_2$) with a gas fill. Its shielding as well as its location also serve to limit the presence of low level backgrounds that may be present in GCD signals. This is known to be a particular concern in the GCD-1 configuration that uses a fused silica radiator [14].

Because they are temporally-resolved detectors and because implosion experiments occur on very short (~ 100-ps scale burn duration) time scales, gamma detectors used at ICF facilities cannot be calibrated using the same methods as traditional pulse height gamma detectors. Temporally-resolved gamma detectors are instead calibrated *in situ* at OMEGA using the relatively well-known cross section for 4.4-MeV gammas produced when DT neutrons impinge upon $^{12}C$ (i.e., C(n,n')γ) [15, 16]. It is preferable to perform the calibration at OMEGA rather than the NIF due to the fact that warm DT implosions occur relatively frequently at OMEGA, so there is ample opportunity to ride along detectors for calibration without the need to secure dedicated shot days for this purpose. The faster shot cycle at OMEGA also allows for collection of much more data than would be possible at the NIF.

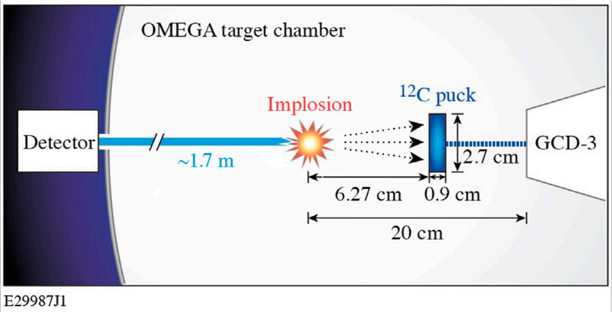

FIGURE 3
Diagram illustrating the setup for the carbon calibration. In this configuration, GCD-1 collects forward-directed gammas while the DAD collects backwards-directed gammas.

The general procedure for calibration involves attaching a carbon puck to the snout of a GCD during warm DT implosions, as shown in Figure 3. When the 14-MeV neutrons impinge upon the carbon puck, some of the carbon nuclei enter an excited state. Upon return to their ground state, 4.4-MeV gammas are emitted at various angles. Forward-directed gammas from the puck are

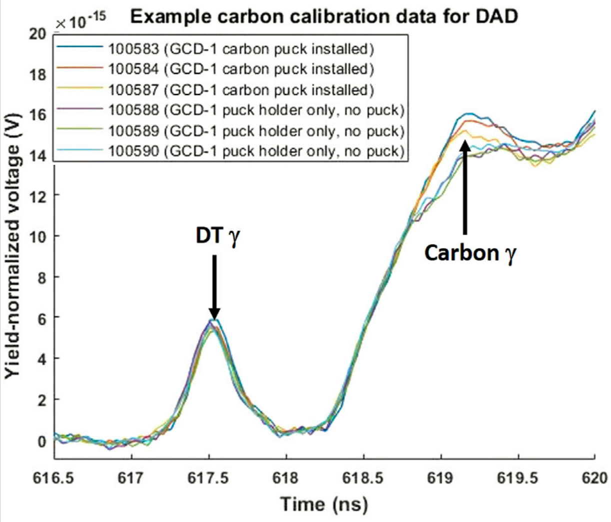

FIGURE 4
Sample of DAD data used for carbon calibration. The 9.92 g carbon puck was placed 6.6 cm away from TCC using the GCD-1 carbon puck holder. Carbon gammas from this puck were detected by DAD at an average scattering angle of 143°. Data was collected with and without the carbon puck in position. Background data without the carbon puck included the presence of the aluminum puck holder. All signals shown here are normalized to the relevant DT neutron yield.

then collected by the GCD holding the puck while the DAD collects backwards-directed gammas. It is also necessary to collect background data without the carbon puck in place but with the puck holder still present in order to obtain background measurements. After several shots, the data with the carbon puck present and the background data can each be averaged separately. Example signals from the DAD are shown in Figures 4, 5. The average signal without the puck present can be subtracted from the average signal with the puck present in order to isolate the signal from the 4.4-MeV carbon gamma. This signal can then be used with the differential (i.e., angularly-resolved) cross section for the C(n,n')$\gamma$ reaction as well as information about the PMT settings and the positions and solid angles of the puck and the detector to calculate a calibration constant ($\chi$) as detailed in Refs. 15 and 16. The major source of uncertainty associated with this calibration procedure generally comes from uncertainties associated with the carbon cross section of interest.

In addition to the GCD's, the Quartz Cherenkov Detectors (QCD's) and the Gamma Reaction History (GRH) diagnostic are also available at the NIF. The GRH is designed to use 4 GCD-like gas cells which are each coupled to a separate PMT. Each of these can be set to a different pressure (i.e., different low-energy threshold) and different PMT settings in order to measure different gamma rays of interest [17]. To date, GRH has only been absolutely calibrated to the D$^3$He gamma, resulting in a calibration with over 30% uncertainty [18, 19]. Statistical uncertainties from the number of incident gammas as well as the number of Cherenkov photons generated in the detector only increase the total uncertainty on any given measurement using these detectors. Further calibration work would therefore be needed in order to make S-factor or cross-section measurements with reasonably low uncertainties. In addition, GRH is located 6 m from TCC, so it would be difficult to use this diagnostic for measurements related to reactions with low cross sections.

The QCD's are similar to the DAD in that they use fused silica radiators, however, the QCD's use a quartz rod paired to a PMT while the DAD at OMEGA uses a disc-shaped volume of quartz located directly in from of a PMT [20]. To date, the QCD's lack absolute calibration and therefore cannot be used for nuclear astrophysics experiments such as cross-section or S-factor measurements. It could, in principle, be possible to build a duplicate QCD that can be calibrated at OMEGA in the same way that the GCD's and DAD were calibrated. This would, however, be unlikely to enable use of the NIF QCD's for cross-section/S-factor measurements of reactions relevant to nuclear astrophysics due to the fact that the NIF detectors are located very far from TCC, causing very low detection statistics for nucleosynthesis-relevant implosions which involve reactions with relatively low cross sections.

## 3 Standard analysis procedure

Once the calibration constant for a given detector is known, it can be used to calculate gamma yield based on a measured signal such that

$$Y_\gamma = \frac{A_\gamma}{\Omega\, R\, e\, QE\, G}\,\frac{1}{C_{ph}(E_\gamma)\,\chi}. \tag{1}$$

where $A_\gamma$ represents the signal area for the gamma of interest, $\Omega$ represents the detector solid angle, $R$ represents digitizer impedance (i.e., 50 $\Omega$), $e$ represents electron charge, $QE$ represents the PMT's quantum efficiency, $G$ represents the PMT's gain, $C_{ph}(E_\gamma)$ represents the detector response to gammas of a given energy (i.e., Cherenkov photons produced per incident gamma), and $\chi$ represents the calibration constant. Note that the detector response $C_{ph}(E_\gamma)$ must be calculated at the relevant gamma energy and that the response as a function of energy is typically calculated using Monte Carlo simulations *via* a particle transport code such as Geant4 or ACCEPT. As Cherenkov detectors utilized at ICF facilities are temporally-resolved, energy-thresholded detectors and not true gamma spectrometers, the relevant gamma energy for a given implosion is generally assumed based on kinematic considerations rather than directly measured.

The gamma yield can then be used to calculate the S factor. As mentioned in the previous section, the S factor for a reaction

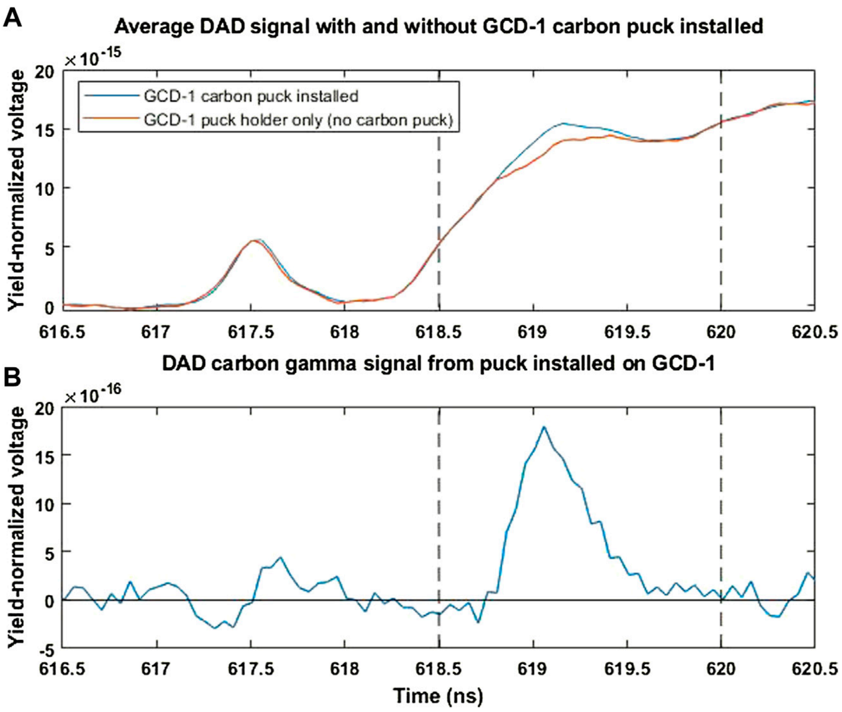

FIGURE 5
Average DAD calibration data with and without the carbon puck in place **(A)** and the carbon gamma data resulting from their subtraction **(B)**. Background data without the carbon puck included the presence of the aluminum puck holder. The area of the subtracted signal is used to calculate the carbon calibration constant χ. The dashed vertical lines in the plot represent the times over which the area was calculated.

of interest can be calculated in reference to the S factor for a reaction that is considered to be well-known such that

$$S_r = S_{ref}\frac{Y_r}{Y_{ref}}\frac{f_{1,ref}f_{2,ref}}{f_{1,r}f_{2,r}}\frac{1+\delta_{12,r}}{1+\delta_{12,ref}}\left[\frac{A_r}{A_{ref}}\frac{\xi_{ref}^2 e^{-3\xi_{ref}}}{\xi_r^2 e^{-3\xi_r}}\right] \quad (2)$$

where the subscript $r$ represents the reaction of interest, the subscript $ref$ represents a reference reaction that produces particles simultaneously, $f_i$ represents fuel fractions for different species involved in a given implosion, and the factor

$$\xi = 6.2696\,(Z_1Z_2)^{2/3}A_{ave}^{1/3}T^{-1/3} \quad (3)$$

is used as shown in Ref. 21.

As previously mentioned, signals measured during implosion experiments may contain backgrounds by virtue of the fact that reactions other than the reaction of interest are occurring simultaneously. For example, in the case of implosion of targets filled with a mixture of $H_2$ and $D_2$ that aim to study the BBN-relevant reaction H(D,$\gamma$)$^3$He, additional gammas are generated *via* the reaction D(D,$\gamma$)$^4$He [14, 21]. Dedicated DD implosions must therefore be included in the experimental campaign in order to isolate the signal contribution from gammas associated with the reaction of interest. Potential backgrounds must therefore be carefully considered during the design phase of any experimental campaign that is to be performed on an ICF platform in order to properly incorporate any additional shots necessary to quantify backgrounds.

Note that any experiments involving tritium in the target fill will necessarily contain some deuterium which is present as an impurity in the tritium part of the fill. As the cross section for DT reactions is known to be relatively large, these reactions will also likely generate DT backgrounds in experiments that aim to study reactions involving tritium [14, 22].

## 4 Recent results and discussion

The following is a review of gamma-branch fusion reactions that are relevant to nuclear astrophysics and have recently been studied at the Omega laser facility. Note that all of these experiments have so far been performed at the OMEGA. Although protons and neutrons from astrophysically-relevant reactions have been performed at the NIF [23], no studies of gamma-branch fusion reactions have yet occurred at this particular facility. It would be possible to perform such studies at the NIF, which has GCD's available as outlined in the previous section, though the length of the NIF shot cycle would make it considerably more difficult to perform duplicate

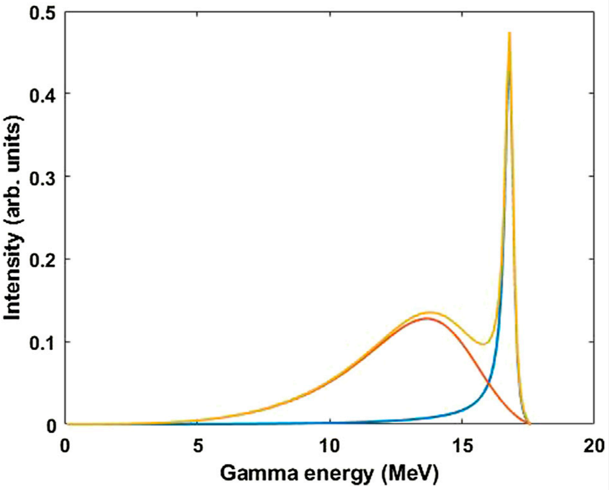

FIGURE 6
DT gamma spectrum used for weighting the DAD response function to determine a DT gamma-to-neutron branching ratio. Data from Ref. 24 has been reproduced with the permission of the corresponding author.

shots as well as to incorporate the shots that are necessary to examine backgrounds for these experiments. It may, however, be advantageous to design campaigns to study these reactions on the NIF at some point, as the NIF is able to reach laser energies (and therefore particle fluxes) that cannot be reached at OMEGA.

## A. D(T,$\gamma$)$^5$He (distributed spectrum, $\gamma_0$ = 16.7 MeV)

The DT gamma from the reaction D(T,$\gamma$)$^5$He has primarily been studied within the context of the DT gamma-to-neutron branching ratio (i.e, the ratio between this gamma-producing reaction and the neutron-producing reaction D(T,n)$^4$He). It is mainly of interest within the context of the endeavor to create a fusion-based source of sustainable energy, as the neutron branch DT reaction has a relatively high cross section and is therefore the focus of most NIF and OMEGA experiments that seek to reach ignition and/or determine improved approaches towards reaching ignition. While the gamma branch reaction is known to be several orders of magnitude lower in cross section than the neutron branch reaction, these gammas can be useful for diagnostic purposes because gammas generally do not scatter within remaining target material and do not experience Doppler broadening in transit (whereas neutrons do). As DT implosions are the most common type of experiments performed on ICF platforms, the DT reaction serves an important role in the calibration of gamma detectors that are to be used in subsequent experiments (as discussed in Section 2). The gamma and neutron branches of this reaction can also serve as important reference reactions for subsequent astrophysics- as well as fusion energy-relevant experiments that use these detectors.

The gamma branch DT reaction produces gammas into a distributed energy spectrum that is related to the nuclear structure of $^5$He. An example of the spectrum was recently reported in Ref. 24, which calculated a spectrum based on GCD-1 measurements collected with different gas pressures (i.e., different gamma energy thresholds) in combination with R-matrix values for the structure of $^5$He. The spectrum is reproduced in Figure 6.

It should be noted that results reported from accelerator experiments span an entire order of magnitude for the DT gamma-to-neutron branching ratio. This is thought to be because accelerator targets generate a gamma background due to DT neutrons impinging upon target nuclei, as these target nuclei may then enter an excited state and emit gammas upon return to their ground states [18]. ICF facilities offer a unique opportunity to study this reaction without this gamma background and at low center-of-mass (CM) energies which are relevant to BBN and stellar nucleosynthesis but remain difficult to reach in accelerator experiments.

To date, two studies have attempted to determine the DT gamma-to-neutron branching ratio using the GCD's at OMEGA while one study has made the same attempt using the DAD. All of these studies measured DT gammas and DT neutrons simultaneously. Each of the relevant experimental campaigns showed branching ratios that appeared to be constant over the range of ion temperatures (or CM energies) studied in the ICF experiments [16, 18, 19, 32]. No S factors were calculated for this reaction, as the shape of the D(T,$\gamma$)$^5$He S factor would simply take on the shape of the well-known D(T,n)$^4$He S factor with use of Eq. 2. The first ICF-based study of the DT gamma-to-neutron branching ratio used GCD-1 filled with 100 psia $CO_2$, which corresponds to a threshold energy of 6.3 MeV. Two calibration approaches (absolute detector calibration and cross-calibration based on D$^3$He implosions) were used to calculate a gamma-to-neutron branching ratio of $(4.2 \pm 2.0) \times 10^{-5}$ [18, 19]. The 48% error bar on this measurement was largely due to the D$^3$He calibration/cross section. The second study used GCD-3 filled with 400 psia $CO_2$, which corresponds to a threshold energy of 2.6 MeV. The carbon calibration outlined in Section 2 and detailed in Ref. 15 was used to calculate a branching ratio of $(4.56 \pm 0.58) \times 10^{-5}$ [32]. Note the reduced uncertainty due to the use of the carbon calibration, as the C(n,n')$\gamma$ cross section is more well-known than the D($^3$He,$\gamma$)$^5$Li cross section.

A third study attempted to determine the DT gamma-to-neutron branching ratio using the DAD detector, which has a threshold energy of 0.34 MeV. Carbon calibration was performed for the DAD, resulting in a final branching ratio of $(8.42 \pm 2.84) \times 10^{-5}$ [16, 33]. The relatively higher uncertainty on this measurement in comparison to the GCD-3 measurement from

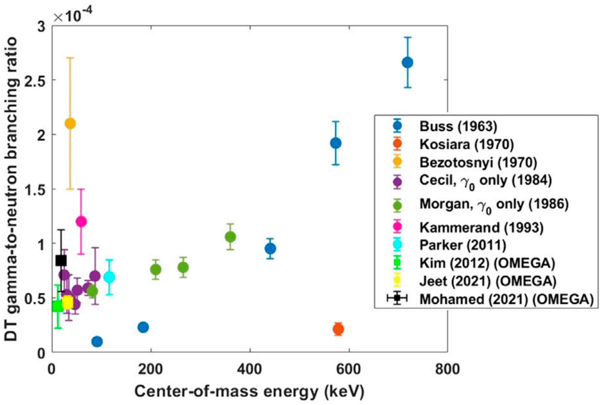

FIGURE 7
Branching ratio from the GCD-1, GCD-3, and DAD measurements on OMEGA shown along with those from accelerator experiments discussed in Refs. 25–32.

Ref. 32 comes mainly from the statistics involved in the carbon calibration as well as uncertainty in the DAD detector response (which was generated using Geant4 simulations).

These measurements are shown in comparison to some accelerator measurements in Figure 7. The DAD measurement from Ref. 16, 33 was a factor of ~2 higher than the GCD measurements from Refs. 18, 19, and 32, but its error bars overlap with the error bars from the GCD-1 value from Refs. 18 or 19. Note that ICF-based measurements necessarily measure the gammas associated with the ground state of $^5$He ($\gamma_0$) as well as the gamma associated with the first excited state of $^5$He ($\gamma_1$). In contrast, some of the accelerator measurements aimed to measure the ground state gamma only. Considering the $\gamma_1$: $\gamma_0$ ratio of 2.1: 1 reported in Ref. 24, the OMEGA measurements can be divided by 3.1 to get an approximate $\gamma_0$ only branching ratio. All three Ω measurements [16, 18, 32] would give a $\gamma_0$ measurement that appears to be consistent with the approximately linear trend in the accelerator data from Refs. 28 and 29. The DAD measurement, however, is the only of the three measurements with a total gamma measurement that seems consistent with the $\gamma_0$ accelerator measurements from Refs. 28 and 29, as the DAD measurement gives a ($\gamma_0$ + $\gamma_1$) value that is larger than the accelerator $\gamma_0$ quantities. In contrast, the total GCD-1 and GCD-3 ($\gamma_0$ + $\gamma_1$) measurements are lower than the $\gamma_0$ only measurements from Refs. 28 and 29.

## B. H(D,$\gamma$)$^3$He ($E_\gamma$ = 5.5 MeV)

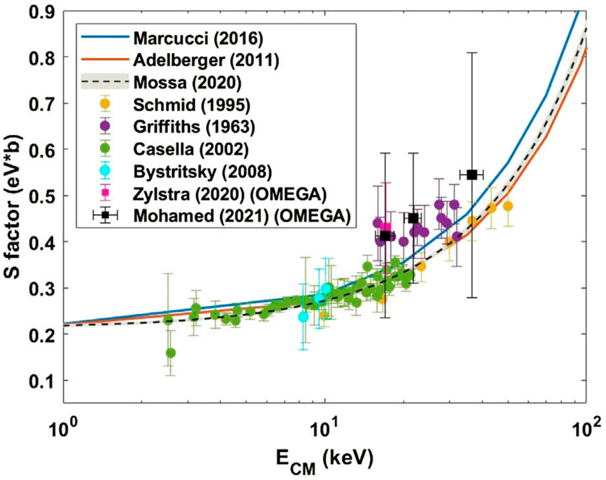

FIGURE 8
Comparison between OMEGA (GCD-3) S-factor measurements for H(D,$\gamma$)$^3$He and accelerator measurements for this reaction. Accelerator results are from Refs. 7, 37–42. The OMEGA results inferred here appear to agree with the accelerator results within error bars, though the OMEGA error bars are generally larger due to detection statistics.

The reaction H(D,$\gamma$)$^3$He is important within the context of BBN as a limiting reaction which consumes deuterium and produces the $^3$He needed to build heavier nuclei. As such, its cross section/S factor is considered to be an important bound on theoretical predictions of the primordial baryon density of the Universe [34–36]. Multiple accelerator experiments [7, 37–42] have produced S-factor measurements for this reaction, though it has been notoriously difficult to study on accelerators due to the low energy, low cross-section gammas it produces. The recent completion of the underground LUNA facility enabled high precision accelerator measurements for this reaction [42, 43]. This reaction is also considered important in the evolution of protostars [7].

Two ICF-based experimental campaigns have studied this reaction. Both campaigns included shots with targets filled with a mixture of $H_2$ and $D_2$ as well as targets filled with $D_2$ only (to measure backgrounds from the reaction D(D,$\gamma$)$^4$He, which produces a 23.9-MeV gamma) and targets filled with $H_2$ only (to measure any contribution from non-nuclear sources such as laser-plasma interactions). Both campaigns used D(D,n)$^3$He as the reference reaction for calculation of the H(D,$\gamma$)$^3$He S factor using Eq. 2. DD neutrons were also used for ion temperature measurements.

The first study used GCD-3 at 400 psia $CO_2$ (2.9 MeV energy threshold) and focused on implosions at ion temperatures of ~ 5 keV ($E_{CM}$ = 16 keV) [21]. The second study [14, 33] used GCD-1 with a fused silica radiator (0.34 MeV energy threshold), GCD-3 with 400 psia $CO_2$ (2.9 MeV energy threshold), and the DAD detector (0.34 MeV energy threshold) simultaneously. The goal of the second study was to span a range of ion temperatures (or CM energies) so as to determine an S factor as a function of CM energy for comparison to accelerator measurements. The implosions involved in this study spanned ion temperatures of 5.0–16.6 keV, corresponding to $E_{CM}$ = 17–37 keV. Of the three detectors used in the second study, only GCD-3 produced viable measurements, as GCD-1 showed considerable background during the $H_2$ shots while the detection statistics on the DAD were too poor to produce a meaningful measurement for this low energy, low cross-section reaction [14, 33]. The GCD-3 measurements from both campaigns were in agreement at ~ 5 keV ion temperature, though the value reported by Ref. 21 had a smaller uncertainty due to a larger number of shots at this ion temperature.

Both GCD-3 measurements used the carbon calibration outlined in Section 2 and detailed in Ref. 15. Both report values that appear to agree with accelerator measurements within their error bars. A comparison is shown in Figure 8. The OMEGA experiments both had larger uncertainties than those associated with accelerator measurements. This is due to a fundamental limitation associated with the implosion experiments involving low cross-section reactions: statistics on the number of particles incident on the detectors and the number of detector events resulting from these interactions are limited and cannot easily be increased at a given ion temperature/CM energy. To some extent, this issue can be addressed in accelerator experiments by increasing their run time, as accelerator experiments generally use time-integrated, energy-resolved measurements (i.e., pulse height detectors).

Approximate agreement between the ICF-based measurements and the accelerator measurements suggests that revision of the $H(D,\gamma)^3He$ cross section is not a viable solution to the cosmological lithium problem. It has been hypothesized that *in situ* stellar production of lithium or physics beyond the standard model may instead be responsible for the cosmological lithium problem, or that use of non-Maxwellian velocity distributions could resolve this issue from a theoretical standpoint [5, 44].

## C. $H(T,\gamma)^4He$ ($E_\gamma$ = 19.8 MeV)

$H(T,\gamma)^4He$ is also a form of hydrogen burning. This reaction is directly relevant to high-performance ICF experiments that seek to achieve ignition and/or determine improved approaches towards reaching ignition, as it can be used in experiments that seek to examine burn histories of these implosions as well as to study mix of ablator material into the central hot spot [2]. The HT reaction only has a gamma branch. There is no corresponding neutron-producing branch, but small amounts of deuterium are present in the tritium part of the target fill, so DT gammas and DT neutrons are also generated in "HT" implosions. The $D(T,n)^4He$ reaction has a well-known S factor and can be used as a reference reaction for calculation of the $H(T,\gamma)^4He$ S factor using Eq. 2. DT neutrons can also be used to infer ion temperatures.

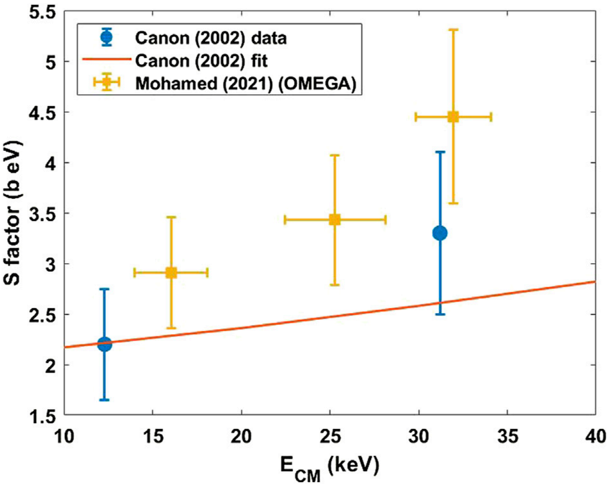

FIGURE 9
Comparison between OMEGA (GCD-1) S factor measurements for $H(T,\gamma)^4He$ and accelerator measurements for this reaction at similar energies. The accelerator data is from Ref. 52, which provides two data points at incident beam energies of 40 and 80 keV (or $E_{CM}$ = 12.3 and 31.2 keV) as well as a fit to these two data points along with data from Refs. 45 and 46. The OMEGA data points appear to agree with the data points from Ref. 52, though they are higher than the fit which included the data at higher CM energies.

Despite its utility in mix experiments, studies such as those outlined in Ref. 2 typically use the HT $\gamma$ for burn history measurements rather than cross-section, S-factor, or yield measurements. Only one recent OMEGA campaign has attempted to study the S factor for this reaction [14, 33]. The goal of this campaign was to span a range of ion temperatures (or CM energies) to determine an S factor as a function of CM energy for comparison with the accelerator data. The implosions involved spanned ion temperatures of 4.4–12.7 keV ($E_{CM}$ = 16–32 keV). Gamma detectors used in this campaign included GCD-1 with 100 psia $CO_2$ (6.3 MeV energy threshold), GCD-3 with 30 psia $CO_2$ (12 MeV energy threshold), and the DAD detector (0.34 MeV energy threshold). The GCD-3 signal included unexpected oscillations which were thought to be associated with the PMT while the DAD signal is believed to have been contaminated with secondary gammas from DT neutrons incident on the target's shell, so only the GCD-1 data was considered to be reliable for the purpose of this measurement [14, 33].

The total gamma signal is known to include both the DT gamma and the HT gamma at similar levels, so a DT gamma background based on the GCD-1 measurements from Ref. 18 was subtracted from the total signal in order to isolate the HT gamma signal. The carbon calibration outlined in Section 2 and detailed

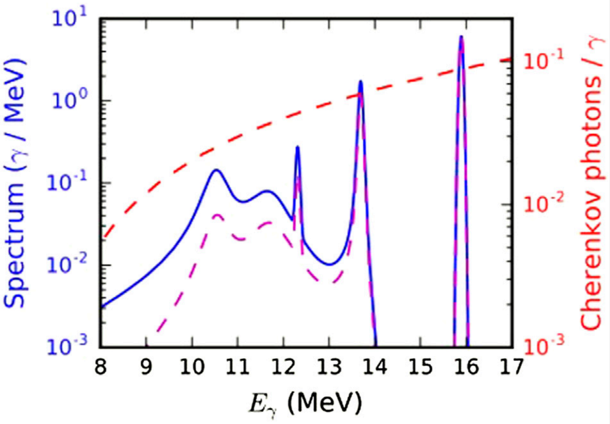

FIGURE 10
Gamma spectrum produced by the reaction $T(^3He,\gamma)^6Li$. The blue line shows the spectrum while the red dotted line shows the GCD response relevant to this experiment. The magenta dotted line shows the sensitivity-normalized spectrum. Plot originally published in Ref. 9 and reproduced with permission of the corresponding author. Copyright 2016 by The American Physical Society.

in Ref. 15 was then used to calculate the HT gamma yield. Of the several accelerator measurements that have investigated this reaction [45–52], only one was conducted at energies comparable to the OMEGA measurement. The data from this experiment [52] appear to agree with the data from the OMEGA experiment within their error bars. A comparison is shown in Figure 9.

## D. $T(^3He,\gamma)^6Li$ (distributed spectrum, $\gamma_0$ = 15.8 MeV)

The reaction $T(^3He,\gamma)^6Li$ is astrophysically relevant within the context of BBN. This reaction is directly related to the $^6Li$ component of the primordial lithium problem, which refers to the factor of ~ 1000 discrepancy between predicted $^6Li$ abundances based on the standard model of BBN and observations from low metallicity stars [3, 4]. The gamma spectrum for this reaction is known to span a range of energies with a spectrum like that shown in Figure 10. Some accelerator measurements for this reaction have been conducted, but not at CM energies relevant to BBN.

There was one OMEGA measurement for $T(^3He,\gamma)^6Li$ which used GCD-3 with 100 psia $CO_2$ (6.3 MeV energy threshold) [9]. Deuterium was also present in the implosion as an impurity in the tritium part of the target fill. Ion temperatures were determined from protons produced by the reaction $D(^3He,p)^4He$. The OMEGA measurement was performed at $E_{CM} = 81$ keV, which is within the range relevant to BBN. Gamma backgrounds were produced by DT and $D^3He$ reactions, and dedicated shots were performed during the campaign to quantify these backgrounds. The reference reaction used to determine the $T(^3He,\gamma)^6Li$ S factor in Eq. 2 was $T(^3He,D)^4He$. CR-39 tracks as well as dipole magnetic spectroscopy were used to detect deuterons from this reaction.

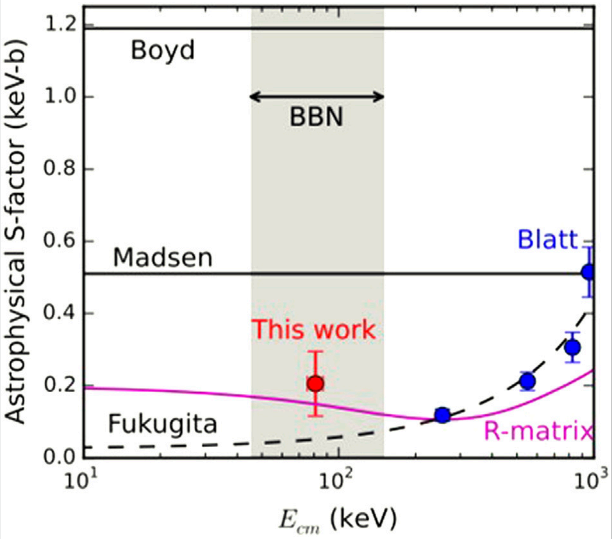

FIGURE 11
Comparison between OMEGA [9] and accelerator measurements [53–56] for the $T(^3He,\gamma)^6Li$ S factor. The OMEGA measurement is the only of these experiments that was performed at an energy directly relevant to BBN. The "R-matrix" line is a fit performed to the data from Ref. 53 when corrected for angular effects [9]. The OMEGA measurement agrees with this fit. Plot originally published in Ref. 9 and reproduced with permission of the corresponding author. Copyright 2016 by The American Physical Society.

Ref. 9 notes that the ICF-based S factor for this reaction was determined over 4π (as is relevant to BBN) while the accelerator data from Ref. 53 was measured as a differential cross section at 90 degrees. Ref. 9 uses an R-matrix calculation based on the 90 degree data from Ref. 53 for comparison. The data point from the ICF experiment agrees with this R-matrix calculation [9]. The relevant comparison is shown is Figure 11. This agreement suggests that a nuclear solution to the lithium problem seems unlikely. It has been hypothesized that *in situ* stellar production of lithium or physics beyond the standard model may instead be responsible for the $^6Li$ problem, or that use of non-Maxwellian velocity distributions could resolve the lithium problem from a theoretical standpoint [5, 44].

## E. Discussion of gamma measurements performed on an ICF experimental platform using existing Cherenkov detectors

Based on the preceding review of the gamma detectors available for nuclear astrophysics measurements at OMEGA and the NIF as well as recent branching ratio and S-factor measurements performed at OMEGA, it is clear that it is possible to make such measurements for gamma branch fusion reactions on an ICF platform. Advantages associated with the use of the ICF platform include the presence of physical conditions such as ion populations, ion temperatures, and electron screening effects that are relevant to astrophysical situations as well as the relative ease of accessing low CM energies that are relevant to BBN and stellar nucleosynthesis. The fact that implosion experiments generate relatively large particle fluxes per unit time and therefore do not have the issue of background from cosmic rays that may arise in accelerator experiments is an additional advantage.

There are also clear complications that arise as a result of the use of ICF experimental platforms to study nuclear reactions *via* gamma detection. As previously mentioned, most implosion experiments will generate nuclear backgrounds in addition to the main reaction that is being examined. For example, an experiment that attempts to study the reaction H(D,$\gamma$)$^3$He will produce gammas from this reaction as well as the reaction D(D,$\gamma$)$^4$He. It is therefore necessary to allot shots with different target fills in order to properly quantify these backgrounds. This is one reason that HED experiments relevant to nuclear astrophysics are performed at OMEGA much more often than the NIF even though the NIF can produce reactions with higher yields: the NIF shot cycle is relatively long compared to the OMEGA shot cycle, so fewer shots are available per campaign and it is therefore difficult to complete a coherent campaign of this nature, which would require many shots to quantify backgrounds or to reach different ion temperatures.

The quality of ICF-based measurements for reactions relevant to nuclear astrophysics depends on the detectors used as well as the reaction in question. Reactions with low cross sections as well as reactions that produce gammas with low energies are generally more challenging to study on an ICF platform. ICF-based experimental campaigns that seek to study these reactions may yield results with larger error bars than equivalent accelerator experiments, as accelerator experiments may simply increase run time in order to improve particle statistics (assuming the facility and the relevant detectors are sufficiently shielded from backgrounds that may be generated by cosmic rays).

The availability of multiple Cherenkov detectors at OMEGA is advantageous, as different configurations of GCD-1 and GCD-3 radiators can be used together and in conjunction with the DAD detector, which has a lower energy threshold but receives less background signal due to its shielding and location. It is known that the DAD may collect data with poor counting statistics for low cross-section reactions, but it is simple to field and can therefore be employed in experimental campaigns without the special preparation that is required to field more complicated diagnostics like the GCD's, which require highly pressurized gas, leak testing, and pointing within the target chamber.

All of these detectors are, however, somewhat complicated to calibrate in comparison to the pulse height detectors used at accelerator facilities. Uncertainties associated with the calibration of current-mode gamma detectors are a major source of uncertainty in S-factor measurements that come from these detectors. This issue could be addressed if another viable material for calibration could be identified. This material would need to produce secondary gammas when impinged upon by DT neutrons and would need to produce these gammas with a cross section that is more well-known than the C(n,n')$\gamma$ cross section in order to constitute improvement in the calibration of the OMEGA gamma detectors.

S factors for BBN-relevant reactions H(D,$\gamma$)$^3$He and T($^3$He,$\gamma$)$^6$Li have been studied at OMEGA [9, 14, 21, 33]. The inferred S factors were in agreement with those from accelerator-based measurements within their error bars, though the error bars from the ICF-based measurements were notably larger than those from the accelerator-based measurements. This agreement for both reactions suggests that a nuclear solution to the lithium problem is not likely. *In situ* stellar production of lithium or physics beyond the standard model may instead be responsible for the cosmological lithium problem [5]. It has also been shown that use of non-Maxwellian velocity distributions could resolve the issue from a theoretical standpoint [44].

## 5 Future work: Potential for a gamma spectrometer

As previously discussed, the gamma detectors available at ICF facilities are temporally-resolved, energy-thresholded current-mode detectors which do not collect direct spectral information. Experiments which seek to make yield, cross-section, or S-factor measurements using these detectors must therefore make some assumptions about the gamma spectrum of interest in order to proceed. With reactions such as H(T,$\gamma$)$^4$He which are known to produce nearly monoenergetic gammas *via* a single reaction branch, it is simple to determine the energy of the incident gammas using kinematic calculations. It is, however, more complicated for reactions such as D(T,$\gamma$)$^5$He or T($^3$He,$\gamma$)$^6$Li, which produce gammas into a broad range of energies. Current best estimates of these gamma spectra are based on R-matrix calculations [9, 24], but at this time, there is no simple way to directly measure these gamma energy spectra.

Development of a true gamma spectrometer for use at ICF facilities would contribute an improved ability to determine cross sections/S factors for such experiments while expanding the ability to study nuclear reactions *via* implosion experiments in general. For example, though the reaction D(T,$\gamma$)$^5$He is interesting due to its diagnostic utility in ICF experiments, the gamma spectrum from this reaction also contains information about the nuclear level structure of the $^5$He nucleus, which is not currently well understood despite the fact that it is expected to have a relatively simple shell structure. In addition to its utility for basic science experiments, the presence of a true gamma spectrometer at OMEGA and/or the NIF would provide expanded diagnostic capabilities for high-performance ICF experiments. Secondary gammas can, for example, be used in areal density and total yield measurements for ignition-relevant experiments.

There are two main difficulties in building a gamma spectrometer for use in ICF experiments: 1) Traditional pulse height gamma spectroscopy cannot be used for implosion experiments due to their short duration, and 2) ICF experiments generally produce neutron fluxes that are several orders of magnitude larger than the gamma flux. A concept for a gamma-to-electron magnetic spectrometer has been proposed for the NIF in the past [57, 58], however, this particular design was developed specifically for the NIF and has not been built due to the intensive resources that would be required. Brainstorming and some preliminary work towards the development of an alternative gamma spectrometer that could operate at OMEGA have been performed within the OMEGA nuclear group. Two potential technologies that could be used for this purpose include an electron-positron pair spectrometer and a single-hit detector [33].

The concept for an electron-positron pair spectrometer requires placement of a foil near the front face of the detector. When gamma rays are incident on the foil, electrons and positrons will be produced *via* pair production and Compton scattering. The energy spectra of these electrons and positrons can be measured using a permanent magnet that is located within the detector to deflect electrons/positrons onto image plates arranged along the sides of the detector. For most of the gamma reactions of astrophysical relevance that can be measured on an ICF platform, such a spectrometer would rely primarily on electrons and positrons from pair production rather than Compton electrons because photons with energies greater than 5 MeV have a pair-production cross section that is greater than the Compton scattering cross section. This design is a derivative of the existing Electron Positron Pair Spectrometer (EPPS) designed by Lawrence Livermore National Laboratory and fielded at the Omega laser facility and the NIF [59] in order to measure electrons and positrons coming directly from a plasma. Some basic design work for the electron-positron gamma spectrometer has already been carried out. Preliminary Monte Carlo simulations have shown that the optimal foil to use to detect the DT gamma is 100 $\mu$m of tungsten in an entrance slit of 2 mm × 4 mm. Assuming a DT gamma-to-neutron branching ratio of $4.2 \times 10^{-5}$ [18, 19, 32] and a W foil located 10 cm from a DT-filled target that produces a neutron yield of $10^{14}$, this configuration would detect ~1300 gamma rays with an energy resolution of ~0.7 MeV. The issue with this method lies primarily in the use of image plates, which have proven to be susceptible to high levels of background from DT neutrons. It is, however, possible that microchannel plates (MCP’s) could be used instead of image plates. MCP’s offer spatial resolution (which is necessary to resolve an energy spectrum by this method) as well as the potential for temporal gating between the gamma and neutron signals.

An alternative to this design is a single-hit detector, which would be somewhat similar to the detector concept [57, 58] proposed for the NIF. Such a detector could easily use temporal discrimination between gamma rays and the neutrons to avoid the issue of the neutron background. Individual $LaBr_3$(Ce) detectors (i.e., $LaBr_3$(Ce) crystals paired with PMT’s) are readily available and are known to have decay times of ~26 ns. They have been used in magnetic confinement experiments and are also used at the NIF in activation measurements, proving that they can withstand high neutron flux environments [60, 61]. The required distance from TCC and the necessary size of $LaBr_3$(Ce) array required to make the desired spectral measurements would need to be further investigated in order to determine whether this would be a viable design.

Overall, much dedicated R&D work would be necessary to build and implement a true gamma spectrometer at OMEGA or the NIF. A gamma spectrometer has, however, been recognized by the OMEGA Laser Users Group as a potentially transformative diagnostic for several years, though little progress has yet been made towards this goal.

## Author contributions

ZM wrote the article, some of which is based upon work that was conducted as part of her doctoral thesis. Review of the references/methods presented herein were vital to her ability to perform similar experiments as part of her thesis work. JK provided support as thesis advisor, assisting in experimental development and review/discussion of the methods and references discussed in the manuscript. YK provided additional editorial advice and suggestions as an expert on diagnostics relevant to this specific topic.

## Conflict of interest

The authors declare that the research was conducted in the absence of any commercial or financial relationships that could be construed as a potential conflict of interest.

The handling editor MG declared a past co-authorship with the author YK, JK.

## Publisher’s note

# References

1. Forrest CJ, Knauer J, Schroeder W, Glebov V, Radha P, Regan S, et al. Nuclear science experiments with a bright neutron source from fusion reactions on the OMEGA laser system. *Nucl Instr Methods Phys Res Section A: Acc Spectrometers Detectors Associated Equipment* (2018) 888:169–76. doi:10.1016/j.nima.2018.01.072

2. Zylstra AB, Herrmann HW, Kim YH, McEvoy AM, Schmitt MJ, Hale G, et al. Simultaneous measurement of the HT and DT fusion burn histories in inertial fusion implosions. *Rev Sci Instrum* (2017) 88:053504. doi:10.1063/1.4983923

3. Anders M. First direct measurement of the $^2H(\alpha, \gamma)^6Li$ cross section at big bang energies and the primordial lithium problem *Phys Rev Lett* (2014) 113: 042501. doi:10.1103/PhysRevLett.113.042501

4. Asplund M, Lambert D, Nissen P, Primas F, Smith V. Lithium isotopic abundances in metal-poor halo stars. *Astrophys J* (2006) 644:229–59. doi:10.1086/503538

5. Fields BD. The primordial lithium problem. *Annu Rev Nucl Part Sci* (2011) 61: 47–68. doi:10.1146/annurev-nucl-102010-130445

6. Cyburt RH, Fields BD, Olive KA, Yeh T. Big bang nucleosynthesis: Present status. *Rev Mod Phys* (2016) 88:015004. doi:10.1103/RevModPhys.88.015004

7. Adelberger EG, Garcia A, Robertson RGH, Snover KA, Balantekin AB, Heeger K, et al. Solar fusion cross sections. II. The pp chain and CNO cycles. *Rev Mod Phys* (2011) 83:195–245. doi:10.1103/revmodphys.83.195

8. Coc A, Petitjean P, Uzan JP, Vangioni E, Descouvemont P, Iliadis C, et al. New reaction rates for improved primordial D/H calculation and the cosmic evolution of deuterium. *Phys Rev D* (2015) 92:123526. doi:10.1103/physrevd.92.123526

9. Zylstra AB. Using inertial fusion implosions to measure the T + $^3$He fusion cross section at nucleosynthesis-relevant energies. *Phys Rev Lett* (2016) 117:035002. doi:10.1103/PhysRevLett.117.035002

10. Berggren RR, Caldwell SE, Lerche RA, Mack JM, Moy KJ, Oertel JA, et al. Gamma-ray-based fusion burn measurements. *Rev Sci Instrum* (2001) 72:873–6. doi:10.1063/1.1321003

11. Herrmann HW, Mack JM, Young CS, Malone RM, Stoeffl W, Horsfield CJ. Cherenkov radiation conversion and collection considerations for a gamma bang time/reaction history diagnostic for the NIF. *Rev Sci Instrum* (2008) 79:10E531. doi:10.1063/1.2979868

12. McEvoy AM, Herrmann HW, Kim Y, Zylstra AB, Young CS, Fatherley VE, et al. Gamma ray measurements at OMEGA with the newest gas Cherenkov detector 'GCD-3'. *J Phys: Conf Ser* (2016) 717:012109. doi:10.1088/1742-6596/717/1/012109

13. Rubery MS, Horsfield CJ, Gales SG, Garbett WJ, LeAtherlAnd A, Young C, et al. First measurements of remaining shell areal density on the OMEGA laser using the Diagnostic for Areal Density (DAD). *Rev Sci Instrum* (2018) 89:083510. doi:10.1063/1.5023400

14. Mohamed ZL. S-factor measurements for $H(D,\gamma)^3He$ and $H(T,\gamma)^4He$ at low center-of-mass energies as measured in high-energy-density plasmas. *submitted to Phys Rev C* (2022).

15. Zylstra AB, Herrmann HW, Kim YH, McEvoy A, Meaney K, Glebov VY, et al. Improved calibration of the OMEGA gas Cherenkov detector. *Rev Sci Instrum* (2019) 90:123504. doi:10.1063/1.5128765

16. Mohamed ZL. DT gamma-to-neutron branching ratio determined using high-energy-density plasmas and a fused silica Cherenkov detector. *submitted to Phys Rev C* (2022).

17. Hermann HW. ICF gamma-ray reaction history diagnostics. *J Phys Conf Ser* (2010) 244:032047. doi:10.1088/1742-6596/244/3/032047

18. Kim Y, Mack JM, Herrmann HW, Young CS, Hale GM, Caldwell S, et al. Determination of the deuterium-tritium branching ratio based on inertial confinement fusion implosions. *Phys Rev C* (2012) 85:061601. doi:10.1103/physrevc.85.061601

19. Kim Y. D-T gamma-to-neutron branching ratio determined from inertial confinement fusion plasmas. *Phys Plasmas* (2012) 19:056313. doi:10.1063/1.4718291

20. Moore AS, Schlossberg DJ, Hartouni EP, Sayre D, Eckart MJ, Hatarik R, et al. A fused silica Cherenkov radiator for high precision time-of-flight measurement of DT γ and neutron spectra (invited). *Rev Sci Instrum* (2018) 89:10I120. doi:10.1063/1.5039322

21. Zylstra AB, Herrmann HW, Kim YH, McEvoy A, Frenje JA, Johnson MG, et al. $^2H(p, \gamma)^3He$ cross section measurement using high-energy-density plasmas. *Phys Rev C* (2020) 101:042802. doi:10.1103/physrevc.101.042802

22. Kim Y, Herrmann HW, Hoffman NM, Schmitt MJ, Kagan G, McEvoy AM, et al. First observation of increased DT yield over prediction due to addition of hydrogen. *Phys Plasmas* (2021) 28:012707. doi:10.1063/5.0030852

23. Gatu Johnson M. Development of an inertial confinement fusion platform to study charged-particle-producing nuclear reactions relevant to nuclear astrophysics. *Phys Plasmas* (2017) 24:041407. doi:10.1063/1.4979186

24. Horsfield CJ, Rubery MS, Mack JM, Herrmann HW, Kim Y, Young CS, et al. First spectral measurement of deuterium-tritium fusion γ rays in inertial fusion experiments. *Phys Rev C* (2021) 104:024610. doi:10.1103/physrevc.104.024610

25. Buss W, Wäffler H, Ziegler B. Radiative capture of deuterons by $H^3$. *Phys Lett* (1963) 4:198–9. doi:10.1016/0031-9163(63)90362-7

26. Kosiara A, Willard H. Gamma ray-neutron branching ratio in the triton-deutron reaction. *Phys Lett B* (1970) 32:99–100. doi:10.1016/0370-2693(70)90596-4

27. Bezotosnyi VM, Zhmailo VA, Surov LM, Shvetsov MS. Cross section of the reaction $T(d,\gamma)^5He$ with emission of 16.7-MeV γ quanta at 25 – 100 keV deuteron energy. *Sov J Nucl Phys* (1970) 10:25–127.

28. Cecil FE, Wilkinson IFJ. Measurement of the ground-state gamma-ray branching ratio of the dt reaction at low energies. *Phys Rev Lett* (1984) 53: 767–70. doi:10.1103/physrevlett.53.767

29. Morgan GL, Lisowski PW, Wender SA, Brown RE, Jarmie N, Wilkerson JF, et al. Measurement of the branching ratio $^3H(d, \gamma)/^3H(d, n)$ using thick tritium gas targets. *Phys Rev C* (1986) 33:1224–7. doi:10.1103/physrevc.33.1224

30. Kammeraad JE, Hall J, Sale KE, Barnes CA, Kellogg SE, Wang TR. Measurement of the cross-section ratio $H(d,\gamma)^5He/^3H(d, \alpha)n$ at 100 keV. *Phys Rev C* (1993) 47:29–35. doi:10.1103/physrevc.47.29

31. Parker CE. *The $^3H(d,\gamma)$ Reaction and the $^3H(d,\gamma)/^3H(d, n)$ Branching Ratio at $E_{CM} \leq 300$ keV.* Ph.D. thesis. Ann Arbor, MI (Proquest): Ohio University (2016).

32. Jeet J, Zylstra AB, Rubery M, Kim Y, Meaney KD, Forrest C, et al. Inertial-confinement fusion-plasma-based cross-calibration of the deuterium-tritium γ-to-neutron branching ratio. *Phys Rev C* (2021) 104:054611. doi:10.1103/physrevc.104.054611

33. Mohamed ZL. *Neutron and gamma time-of-flight measurements in inertial confinement fusion experiments.* Ph.D. thesis. Rochester, NY University of Rochester (2021).

34. Iocco F, Mangano G, Miele G, Pisanti O, Serpico PD. Primordial nucleosynthesis: From precision cosmology to fundamental physics. *Phys Rep* (2009) 472:1–76. doi:10.1016/j.physrep.2009.02.002

35. Di Valentino E, Gustavino C, Lesgourgues J, Mangano G, Melchiorri A, Miele G, et al. Probing nuclear rates with Planck and BICEP2. *Phys Rev D* (2014) 90: 023543. doi:10.1103/physrevd.90.023543

36. Fields BD, Olive KA, Yeh TH, Young C. Big bang nucleosynthesis after Planck. *J Cosmol Astropart Phys* (2020) 010. doi:10.1088/1475-7516/2020/03/0103

37. Griffiths GM, Lal M, Scarfe CD. The reaction $D(p, \gamma)^3He$ below 50 keV. *Can J Phys* (1963) 41:724–36. doi:10.1139/p63-077

38. Marcucci LE, Mangano G, Kievsky A, Viviani M. Implication of the proton-deuteron radiative capture for big bang nucleosynthesis. *Phys Rev Lett* (2016) 116: 102501. doi:10.1103/physrevlett.116.102501

39. Schmid GJ. Effects of non-nucleonic degrees of freedom in the $D(p,\gamma)^3He$ and $p(d,\gamma)^3He$ reactions. *Phys Rev Lett* (1996) 76:3088. doi:10.1103/PhysRevLett.76.3088

40. Casella C, Costantini H, Lemut A, Limata B, Bonetti R, Broggini C, et al. First measurement of the $d(p,\gamma)^3He$ cross section down to the solar Gamow peak. *Nucl Phys A* (2002) 706:203–16. doi:10.1016/s0375-9474(02)00749-2

41. Bystritsky VM, Gerasimov V, Krylov A, Parzhitskii S, Dudkin G, Kaminskii V, et al. Study of the pd reaction in the astrophysical energy region using the Hall accelerator. *Nucl Instr Methods Phys Res Section A: Acc Spectrometers Detectors Associated Equipment* (2008) 595:543–8. doi:10.1016/j.nima.2008.07.152

42. Mossa V, Stockel K, Cavanna F, Ferraro F, Aliotta M, Barile F, et al. The baryon density of the Universe from an improved rate of deuterium burning,. *Nature* (2020) 587:210–3. doi:10.1038/s41586-020-2878-4

43. Mossa V, Stockel K, Cavanna F, Ferraro F, Aliotta M, Barile F, et al. Setup commissioning for an improved measurement of the $D(p,\gamma)^3He$ cross section at Big Bang Nucleosynthesis energies. *Eur Phys J A* (2020) 56:144. doi:10.1140/epja/s10050-020-00149-1

44. Hou SQ, He JJ, Parikh A, Kahl D, Bertulani CA, Kajino T, et al. Non-extensive statistics to the cosmological lithium problem. *Astrophys J* (2017) 834:165. doi:10.3847/1538-4357/834/2/165

45. Hahn KI, Brune CR, Kavanagh RW. $^3H(p,\gamma)^4He$ cross section. *Phys Rev C* (1994) 51:1624–32. doi:10.1103/physrevc.51.1624

46. Perry JE, Bame SJ. $T(p,\gamma)He^4$ reaction*. *Phys Rev* (1955) 99:1368–75. doi:10.1103/physrev.99.1368

47. Calarco JR. Absolute cross section for the reaction $^3$H(p, $\gamma_0$)$^4$He and a review of $^4$He($\gamma$,p$_0$)$^3$H measurements. *Phys Rev C* (1983) 28:483. doi:10.1103/physrevc.28.483

48. Feldman G. $^3$H(p,$\gamma$)$^4$He reaction and the ($\gamma$,p)/($\gamma$,n) ratio in $^4$He. *Phys Rev C* (1990) 42:1167. doi:10.1103/physrevc.42.r1167

49. Bernabei R, Chisholm A, d'Angelo S, De Pascale MP, Picozza P, Schaerf C, et al. Measurement of the $^4$He($\gamma$, p)$^3$H total cross section and charge symmetry. *Phys Rev C* (1988) 38:1990–5. doi:10.1103/physrevc.38.1990

50. Gardner CC, Anderson JD. Gamma yield from the proton bombardment of tritium. *Phys Rev* (1962) 125:626–8. doi:10.1103/physrev.125.626

51. Gemmell DS, Jones GA. The T(p,γ)He$^4$ reaction. *Nucl Phys* (1962) 33:102–9. doi:10.1016/0029-5582(62)90508-4

52. Canon RS. $^3$H(p,$\gamma$)$^4$He reaction below $E_p$ = 80 keV. *Phys Rev C* (2002) 65: 044008. doi:10.1103/physrevc.65.044008

53. Blatt SL, Young AM, Ling SC, Moon KJ, Porterfield CD. Reaction T($^3$He,$\gamma$)$^6$Li in the energy range 0.5-11 MeV. *Phys Rev* (1968) 176:1147–53. doi:10.1103/physrev.176.1147

54. Fukugita M, Kajino T. Contribution of the $^3$He(t,$\gamma$)$^6$Li reaction to $^6$Li production in primordial nucleosynthesis. *Phys Rev D* (1990) 42:4251. doi:10.1103/PhysRevD.42.4251

55. Madsen J. CNO and $^6$Li from big-bang nucleosynthesis—Impact of unmeasured reaction rates. *Phys Rev D* (1990) 41:2472–8. doi:10.1103/physrevd.41.2472

56. Boyd RN, Brune CR, Fuller GM, Smith CJ. New nuclear physics for big bang nucleosynthesis. *Phys Rev D* (2010) 82:105005. doi:10.1103/physrevd.82.105005

57. Kim Y, Herrmann HW, Hilsabeck TJ, Moy K, Stoeffl W, Mack JM, et al. Gamma-to-electron magnetic spectrometer (GEMS): An energy-resolved $\gamma$-ray diagnostic for the National Ignition Facility. *Rev Sci Instrum* (2012) 83:10D311. doi:10.1063/1.4738650

58. Kim Y, Herrmann HW, Jorgenson HJ, Barlow DB, Young CS, Stoeffl W, et al. Conceptual design of the gamma-to-electron magnetic spectrometer for the National Ignition Facility. *Rev Sci Instrum* (2014) 85:11E122. doi:10.1063/1.4892900

59. Chen H, Link AJ, van Maren R, Patel PK, Shepherd R, Wilks SC, et al. High performance compact magnetic spectrometers for energetic ion and electron measurement in ultraintense short pulse laser solid interactions. *Rev Sci Instrum* (2008) 79:10E533. doi:10.1063/1.2953679

60. Giacomelli L, Rigamonti D, Nocente M, Rebai M, Tardocchi M, Cecconello M, et al. Conceptual studies of gamma ray diagnostics for DEMO control. *Fusion Eng Des* (2018) 136:1494–8. doi:10.1016/j.fusengdes.2018.05.041

61. Root J. Development of the real-time neutron activation diagnostic system for NIF. *Target diagnostics physics and engineering for inertial confinement fusion VI* (2017) 10390:103990J. doi:10.1117/12.2274343

frontiers | Frontiers in Physics

TYPE Original Research
PUBLISHED 05 January 2023
DOI 10.3389/fphy.2022.1057603

OPEN ACCESS

EDITED BY
Giuseppe Verde,
Universities and Research, Italy

REVIEWED BY
Marco La Cognata,
Laboratori Nazionali del Sud (INFN), Italy
Antonio Caciolli,
University of Padua, Italy

*CORRESPONDENCE
Daniel T. Casey,
✉ casey21@llnl.gov

SPECIALTY SECTION
This article was submitted to Nuclear Physics, a section of the journal Frontiers in Physics

RECEIVED 29 September 2022
ACCEPTED 05 December 2022
PUBLISHED 05 January 2023

CITATION
Casey DT, Weber CR, Zylstra AB, Cerjan CJ, Hartouni E, Hohenberger M, Divol L, Dearborn DS, Kabadi N, Lahmann B, Gatu Johnson M and Frenje JA (2023), Towards the first plasma-electron screening experiment. *Front. Phys.* 10:1057603.
doi: 10.3389/fphy.2022.1057603

# Towards the first plasma-electron screening experiment

Daniel T. Casey[1]*, Chris R. Weber[1], Alex B. Zylstra[1], Charlie J. Cerjan[1], Ed Hartouni[1], Matthias Hohenberger[1], Laurent Divol[1], David S. Dearborn[1], Neel Kabadi[2], Brandon Lahmann[3], Maria Gatu Johnson[3] and Johan A. Frenje[3]

[1]Lawrence Livermore National Laboratory (DOE), Livermore, CA, United States, [2]Laboratory for Laser Energetics University of Rochester, Rochester, NY, United States, [3]Massachusetts Institute of Technology, Cambridge, MA, United States

The enhancement of fusion reaction rates in a thermonuclear plasma by electron screening of the Coulomb barrier is an important plasma-nuclear effect that is present in stellar models but has not been experimentally observed. Experiments using inertial confinement fusion (ICF) implosions may provide a unique opportunity to observe this important plasma-nuclear effect. Herein, we show that experiments at the National Ignition Facility (NIF) have reached the relevant physical regime, with respect to the density and temperature conditions, but the estimated impacts of plasma screening on nuclear reaction rates are currently too small and need to be increased to lower the expected measurement uncertainty. Detailed radiation hydrodynamics simulations show that practical target changes, like adding readily available high-Z gases, and significantly slowing the inflight implosion velocity, while maintaining inflight kinetic energy, might be able to push these conditions to those where plasma screening effects may be measurable. We also perform synthetic data exercises to help understand where the anticipated experimental uncertainties will become important. But challenges remain, such as the detectability of the reaction products, non-thermal plasma effects, species separation, and impacts of spatial and temporal gradients. This work lays the foundation for future efforts to develop an important platform capable of the first plasma electron screening observation.

KEYWORDS

**astrophysics, nuclear physics, plasma physcis, high-energy density astrophysics, inertial confinement fusion (ICF)**

## 1 Introduction

For decades, numerous research groups have identified plasma-electron screening as an important physical process worth pursuing in high-energy-density (HED) experiments. For example, the National Research Council [1] describes a “raging debate” surrounding questions related to plasma screening models and that HED

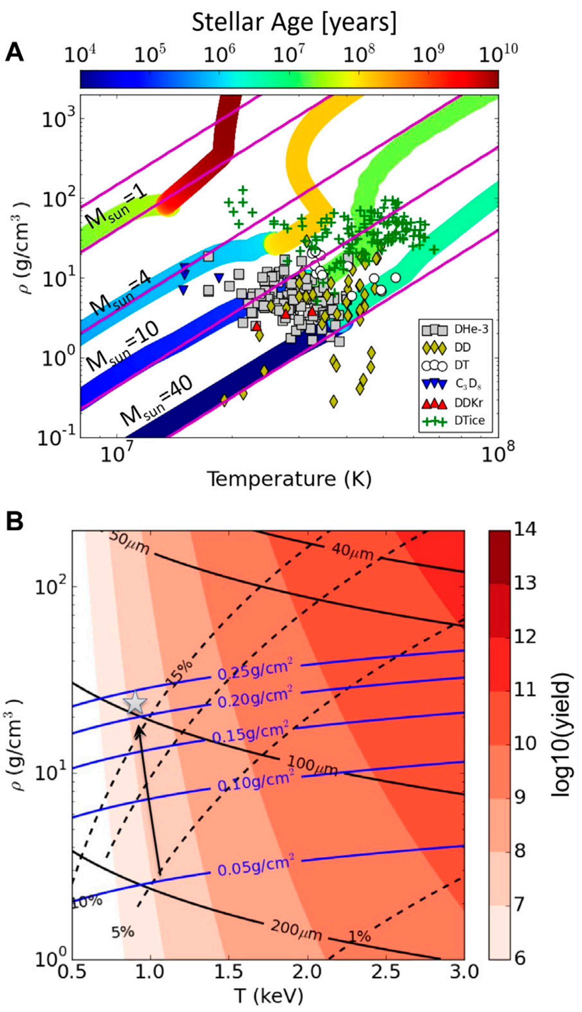

FIGURE 1
**(A)** Stellar conditions computed for the evolution of stars with 1, 4, 10, and 40 solar mass compared with NIF experiments. **(B)** Design space considering various requirements of a potential screening experiment. The arrow illustrates how current experiments need to be modified to reach an optimum in design space (the star) that balances various design constraints.

experiments may be well suited to help. In fact, ideas emerge periodically from the literature challenging the established models [2–7], but the debate is hampered by the complete lack of experimental data. This situation is exacerbated by the "electron screening puzzle" caused by discrepancies observed in terrestrial laboratory target experiments [8–15] when compared to screening theory [5, 6]. This makes measurements made directly in the plasma environments of stellar interiors particularly important so that stellar plasma screening models can be tested against data.

The screening process becomes important when nuclei undergo a fusion reaction as their kinetic energy overcomes the repulsive Coulomb force and exploits favorable binding energy. In many HED environments where these reactions are occurring, such as in stellar cores or inertial confinement fusion implosions, the nuclei are embedded in a plasma. The background electrons in this plasma can lower the Coulomb barrier, enhancing the fusion reactivity.

Plasma screening of nuclear reactions occurs when ions within the plasma interact with a Coulomb potential energy of $U(r) = \frac{Z_1 e^2}{r}$. Due to this potential, electrons will cluster around the ion and reduce the potential by a factor of $U_{screen} = \frac{Z_1 e^2}{\lambda_D}$, where $\lambda_D$ is the Debye length, $\lambda_D^2 = \frac{\varepsilon_0\, k_B T}{n\, e^2}$. This results in an enhancement (appropriate in the weak screening limit) of the cross section of [2, 7, 16]

$$\frac{\sigma_{screened}(E)}{\sigma(E)} \approx \exp\left(Z_1 Z_2 \tilde{Z} \Lambda_0\right)$$
$$\approx \exp\left(\frac{Z_1 Z_2 e^2}{4\pi\varepsilon_0 T \lambda_D}\right)$$

where $\Lambda_0$ is the charge-free plasma parameter, $(4\pi)^{\frac{1}{2}} e^3 n^{\frac{1}{2}} / (kT)^{3/2}$.

A similar screening effect occurs in accelerators that study nuclear reactions. In accelerator experiments, the bound electrons of the target screen the target nuclei and enhance the reaction rate. In this bound-electron screening scenario, the targets are not sufficiently hot to fully ionize the target nuclei. This effect, differing from plasma screening, must be removed to compute the bare nuclear cross section. This effect is significant for low center-of-mass energy cross-sections and has in some cases been observed to be ~1.7–1.8 times larger than expected [10, 11, 17].

Despite widespread interest, the realization of a nuclear plasma screening experiment has been elusive because of several daunting challenges. First, extreme density and temperature conditions must be produced and diagnosed. Second, precise nuclear cross-section measurements must be made where these conditions are produced, implying the presence of strong density and temperature gradients. Finally, as the effect on fusion rates is often weak in the regimes that can be reproduced in the laboratory, care must be exercised to develop a test where the magnitude of the measurement is expected to exceed the experimental uncertainties. Significant progress has recently made resolving the first two of these challenges by using gas-filled indirect-drive experiments at the NIF [18]. Likewise, the $^3$He + T gamma-branch cross-section was obtained [19] and the emitted $^3$He + T and $^3$He+$^3$He reaction product spectra have been recovered from ICF experiments at OMEGA [20]. This demonstrates that nuclear physics and cross-section experiments can be conducted in the complex environments of ICF implosions, while also carefully diagnosing the plasma using nuclear diagnostic and neutron and x-ray imaging. Here, we seek to partly address the third challenge by assessing whether these ICF implosions can produce conditions where this screening effect is expected to be large enough to be measured.

This paper is organized as follows, Section 1 introduces the problem, Section 2 discusses the approach to measuring plasma screening, Section 3 overviews detailed design considerations and offers a potential experimental design solution, and Section IV concludes and summarizes.

## 2 Approach to measuring plasma screening

The generation of thermonuclear plasmas at the National Ignition Facility (NIF) may enable an observation of plasma screening of nuclear reactions. Inertial Confinement Fusion (ICF) experiments at NIF use 192 laser beams, with a maximum 1.9 MJ of energy delivered, to irradiate the inside of a gold or uranium cylindrical enclosure (“hohlraum”). This creates an x-ray environment that ablatively implodes a spherical capsule. When the capsule compresses radially by a factor of 20–40, the central hot-spot typically reaches temperatures of 2–6 keV and densities of 1–100 g/cm$^3$.

Figure 1A shows the stellar-core density and temperature trajectories of relevant stars with metallicity of Z = 0.02 and with 1, 4, 10, and 40 solar mass (where 1 solar mass or $M_{sun}$ = 1 corresponds to the Sun’s mass) calculated with a 1D stellar evolution code [21]. These stars spend the majority of their time in the main hydrogen burning phase of their lifetime, as indicated by the largest jump in the corresponding color scale that illustrates the age of the star in years. As the stars begin to extinguish the hydrogen in their core, they contract and heat to the point where helium can begin to burn. Likewise, as the star evolves, hydrogen in regions outside the depleted core (shell regions) can achieve the conditions that can sustain burn.

Figure 1A also compares these stellar conditions to ICF implosions by plotting inferences of density and temperature from a wide range of NIF experiments. The experimental data from the NIF (points) are plotted in terms of the burn-averaged temperature, as observed from the width of the neutron spectrum in time-of-flight measurements [22–24], and the burn-averaged density, as inferred from the yield, hot-spot size, and burn-width [25]. Each NIF experiment features a gas (on the order of 10 mg/cm$^3$ fill density) or an ice-layer filled capsule (on the order of ~100 μm thick) made of high-density carbon, plastic, or beryllium. The green “+” symbols show implosions that have a cryogenically frozen DT ice layer inside the shell. The cryogenic layer allows the implosion to achieve higher compression and larger densities. We are more interested in the other points which are gas-filled capsules (symcaps) as they provide more flexibility in the gas composition and because the ratio method requires multiple reactants that is enabled by mixed species. Mixed species are especially challenging to field in solid layers because of differences in species freezing temperatures. Each solid symbol represents a different gas-fill class (squares utilize D$^3$He gas, diamonds pure D gas, circles DT gas, downward triangles deuterated propane, and upward triangles Kr doped D). The comparison between the NIF data and the stellar calculations shows that implosion conditions on NIF are very similar to that of stars during most of the stellar lifetime.

The $^3$He + D mixture has some promising features, including two branches, a gamma ($^3\text{He} + \text{D} \rightarrow {}^5\text{Li} + \gamma$) and proton ($^3\text{He} + \text{D} \rightarrow {}^4\text{He} + \text{p}$) branch and the presence of deuterium enables the observation of neutrons from the $\text{D} + \text{D} \rightarrow {}^3\text{He} + \text{n}$ (note we expect the proton branch is not be measurable because of high-plasma densities) reaction within the same experiment. These features will be considered in greater detail later in the manuscript. In following sections, we will detail the feasibility of fielding D-$^3$He filled capsules, but a couple of other interesting cases stand out here. The red points show the effect of the addition of krypton gas (0.01–0.03 atomic percent), which cools the implosion temperature and increases the effective Z of the background plasma. A similar effect is seen in the C3D8 (deuterated propane) implosions, which have cooler temperatures than the other cases. This effect pushes the screening enhancement up to 3%.

A successful plasma screening experiment requires the following: 1) the expected screening enhancement is larger than fusion product yield (proton, neutron, or gamma) measurement uncertainties, 2) the total yield (proton, neutron, or gamma) is at a measurable level, and 3) if measuring protons, the areal density must be low enough that they will escape and reach the proton detector. At the NIF, wedge-range-filter proton detectors are routinely employed to detect protons between the energies of ~6–15 MeV [26, 27]. A modified step-range filter detector [28] is also being developed to extend the measurement to lower energies (~1 MeV), and thus enabling higher ρR measurements.

To find conditions in density-temperature space where a plausible screening measurement could occur, consider an inertially confined sphere of plasma with a density $\rho$, temperature $T$, and radius r. The total yield between two reactants 1 + 2 is $Y_{12} = \int \frac{f_1 f_2}{1+\delta_{12}} \frac{\rho(\vec{r},t)^2}{\bar{m}^2} \sigma v_{12}\, d\vec{r}\, dt$, where $f_1$ and $f_2$ are the atomic fractions reactants 1 and 2, respectively, $\bar{m}$ is the average reactant mass, and $\sigma v_{12}$ is the reactivity. This sphere will disassemble in a timescale $\tau \sim r/c_s$, where $c_s$ is the speed of sound. Using this disassembly time as the burn duration, we can estimate the yield, the areal density ($\rho r$), and screening enhancement, shown in Figure 1B. The screening enhancement increases as one travels vertically along a contour of constant yield. For a measurable proton signature, the $\rho R$ must be kept below ~0.2–0.25 g/cm$^2$. For a yield of $10^7$, this limits the maximum screening amount to ~15% enhancement. The arrow in Figure 1B notionally represents the direction that current experiments need to be pushed in order to reach the density and temperature where enough signal will escape the implosion and where the screening impact is calculated to be non-neglegable (>10%). The star shows our

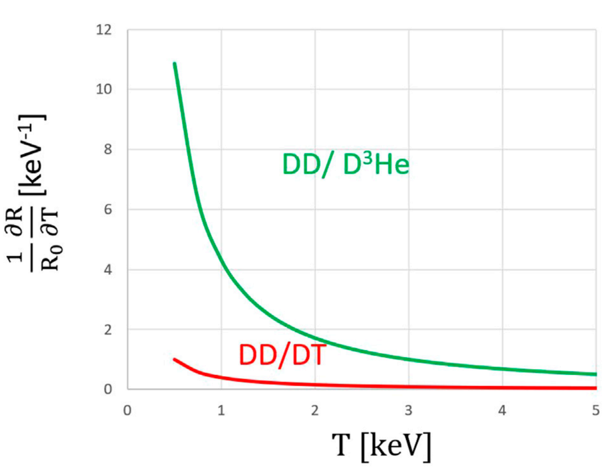

**FIGURE 2**
Plot of the temperature dependance of the relative reactant reactivities ($R = \sigma v_{12}/\sigma v_{11}$) for DD and D3He.

plasma screening experiment design goal. It is also worth noting that increasing the number of plasma electrons by adding a high Z dopant to the gas can also increase the screening at a given density and temperature (an effect not accounted for in Figure 1B).

### A. Observation Using the Ratio Method

To observe the impact of screening, we propose to observe the relative ratio of fusion products from D$^3$He (protons or gammas) and DD (neutrons) reactions emitted in the same ICF implosion. Then, following the same procedure developed in [18, 29, 30], we plan to use this to infer the relative reactivities (R is the D3He/DD reactivity ratio $R = \sigma v_{12}/\sigma v_{11}$) in the presence of plasma-electron screening. The procedure developed in [18] should be modified with the inclusion of an additional term for very low temperatures where a screening measurement would likely operate. This term brings in the effect of temporal and spatial gradients from the temperature dependence of R in the range of interest, unlike the DT/DD reactivity in the prior study. The result is: $\frac{Y_{\mathrm{DD}}}{Y_{\mathrm{D3He}}} = \frac{1}{2}\frac{f_D}{f_{3\mathrm{He}}} R_0 \left[1 + \frac{1}{R_0}\frac{\partial R}{\partial T}\left[T_{\mathrm{D3He}} - T_{\mathrm{DD}}\right]\right]$,

And that

$$T_{\mathrm{D3He}} - T_{\mathrm{DD}} = \frac{1}{2}\left[\frac{1}{R_0}\frac{\partial R}{\partial T}\right]^{-1}\left[1 - \sqrt{1 - \left(2\frac{1}{R_0}\frac{\partial R}{\partial T}\sigma_{T-\mathrm{D3He}}\right)^2}\right]$$

where $\sigma_T$ is the width of the burning temperature distribution, and the terms $R_0$ and $\frac{\partial R}{\partial T}$ are evaluated at $T_{\mathrm{DD}}$. This implies that if the quantity $T_{\mathrm{D3He}} - T_{\mathrm{DD}}$ can be measured, the impacts of gradients can be directly accounted for. However, the second equation may become important since $T_{\mathrm{D3He}}$ may prove difficult to measure but $T_{\mathrm{D3He}} - T_{\mathrm{DD}}$ could be inferred if $\sigma_{T-\mathrm{D3He}}$ can be determined from moments of the DD neutron spectrum [31] or estimated from models of the platform.

If the S-factor is non-resonant within the region of the reacting nuclei, the term $\frac{1}{R_0}\frac{\partial R}{\partial T}$ can be estimated simply assuming barrier penetrability and geometric factors dominate the energy dependance over the burn. The result is: $\frac{1}{R_0}\frac{\partial R}{\partial T} = \frac{K}{9}\left[\frac{4}{T^{7/3}} + \frac{K}{T^{8/3}}\right]$, where $K = \frac{-3\,(\pi\,\alpha_f)^{2/3}\,(m_p c^2)^{1/3}}{2^{1/3}}\left[\left(\frac{Z_1{}^4\,A_1}{2}\right)^{1/3} - \left(\frac{(Z_1 Z_2)^2\,A_1 A_2}{A_1 + A_2}\right)^{1/3}\right]$. Here, the subscripts 1 and 2 label each reactant, $Z_1$ and $Z_2$ are the atomic numbers, $A_1$ and $A_2$ are the atomics masses, $T$ is the burn averaged temperature of reaction between the identical reactants 1 + 1 ($T_{\mathrm{DD}}$ in the example above), $\alpha_f$ is the fine structure constant, and $m_p c^2$ is the rest mass energy of the proton. This expression is especially useful, because it enables an estimate of how the relative energy dependance of the cross-sections burn-weight with the reacting ion energy distributions without needing to know the absolute cross-sections themselves. $\frac{1}{R_0}\frac{\partial R}{\partial T}$ is shown in the region of interest in Figure 2 below.

### B. Estimating the Impact of Gradients on the Ratio Method

To evaluate how spatial and temporal profiles impact burn weighted quantities like yield and temperature, a simple hotspot model developed by Betti [32] can be used. Figure 3 shows the results of reactant distributions in space at peak compression (a and c) and evolutions in time (b and d) for two example implosions. One example is representative of the conditions required for a screening measurement (Figures 3A, B) with burn averaged temperatures of $T_{\mathrm{D3He}} = 1.7\,keV$, $T_{\mathrm{DD}} = 1.5\,keV$, a DD yield $Y_{\mathrm{DD}} = 1.1 \times 10^{11}$, and a D$^3$He yield of $Y_{\mathrm{D3He}} = 4.0 \times 10^8$. The other example is more typical of experiments that are routinely conducted (Figures 3C, D) $T_{\mathrm{D3He}} = 3.9\,keV$, $T_{\mathrm{DD}} = 3.3\,keV$, a DD yield $Y_{\mathrm{DD}} = 9.0 \times 10^{11}$, and a D$^3$He yield of $Y_{\mathrm{D3He}} = 4.7 \times 10^{10}$. This sort of synthetic data exercise can enable tests of the equations presented earlier and provides at least some indication on whether the presence of temperature and density gradients are an issue.

Figure 4A shows the results of comparing the analytic equation for $T_{\mathrm{D3He}} - T_{\mathrm{DD}}$ *versus* a numeric calculation with the hotspot model. The results show at five different representative temperatures the analytic equation works very well if the reactant distribution width $\sigma_{T-\mathrm{D3He}}$ is known. However, $\sigma_{T-\mathrm{D3He}}$ is not yet directly measurable and so it may need to be inferred or estimated from calculations to help constrain the role of gradients. Figure 4B shows the results of comparing $T_{\mathrm{DT}} - T_{\mathrm{DD}}$ *versus* actual experimental data from a variety of implosion platforms including gas filled HDT symcap implosions [33, 34], gas filled indirect drive exploding pusher implosions [35], and layered DT experiments [36, 37]. Here, the $\sigma_{T-\mathrm{DT}}$ was calculated from 1D radiation hydrodynamic simulations using the code HYDRA [38] for two representative cases, an indirect drive exploding pusher [35] and a DT filled symcap [39]. The curve with predicted $\sigma_{T-\mathrm{DT}}$ (dotted black) appears to be significantly less than the data, an

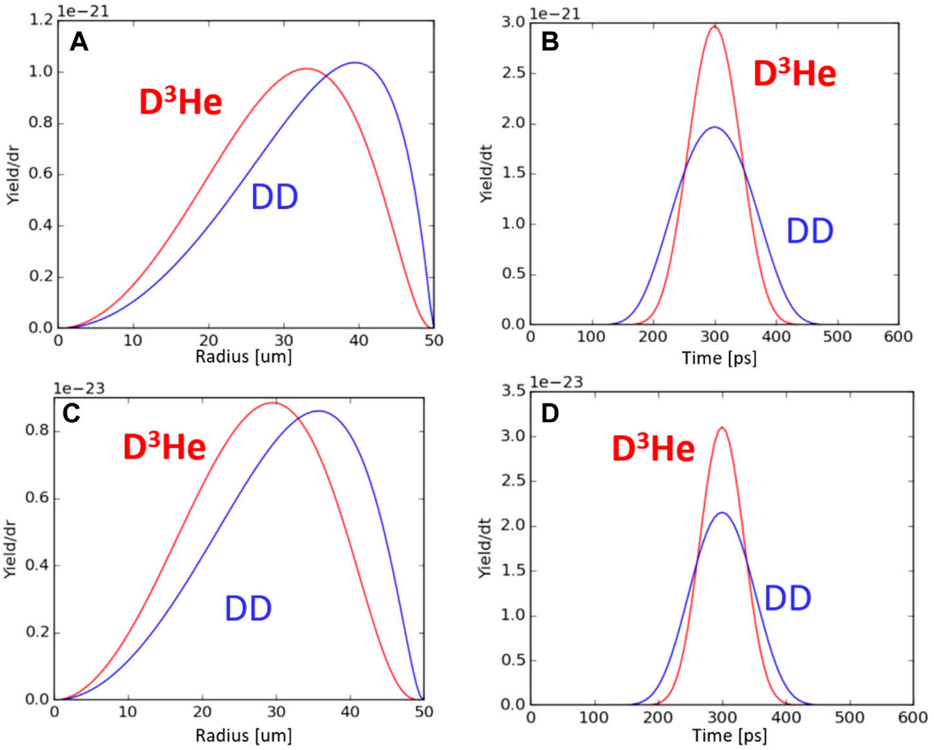

FIGURE 3
DD and D$^3$He reactant distribution in space **(A,C)** and time **(B,D)** using a numeric hotspot model to estimate the impact of temporal and spatial gradients on burn-weighted quantities for two different example implosions.

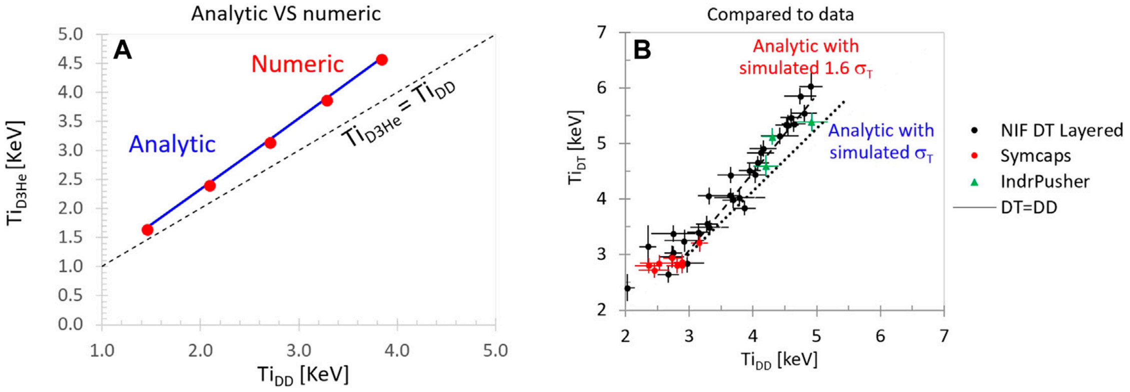

FIGURE 4
**(A)** Comparison of $T_{D3He} - T_{DD}$ estimated using the analytic calculation of vs. numeric integration assuming a Betti 1D hotspot profile [32]. **(B)** Comparison of the analytic $T_{DT} - T_{DD}$ assuming $\sigma_T$ simulated by hydra vs. measured data and analytic curve with $\sigma_T$ increased by 1.6x.

observation in line with those of Gatu-Johnson [36]. However, if $\sigma_{T-\mathrm{DT}}$ is increased by a factor of 1.6 (dashed black), then a good match to the measured trend is reproduced. This indicates that the gradients are more important in the experiments than the 1D simulations would suggest. The exact reasons for this are unclear but it could be due to the enhancement of $\sigma_{T-\mathrm{DT}}$ from 2D and 3D effects not captured by 1D simulations and so high resolution 2D and 3D simulations are required. This also strongly motivates the need for specific experiments to determine $\sigma_T$ in a future plasma screening experiment where $T_{\mathrm{D3He}}$ cannot be directly. For

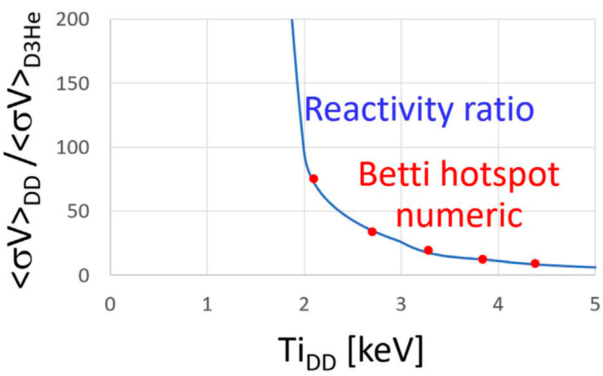

FIGURE 5
Comparison of the reaction ratio for DD and D3He vs. the extracted reactivity ratio using a synthetic data set calculated using a Betti 1D hotspot profile [32].

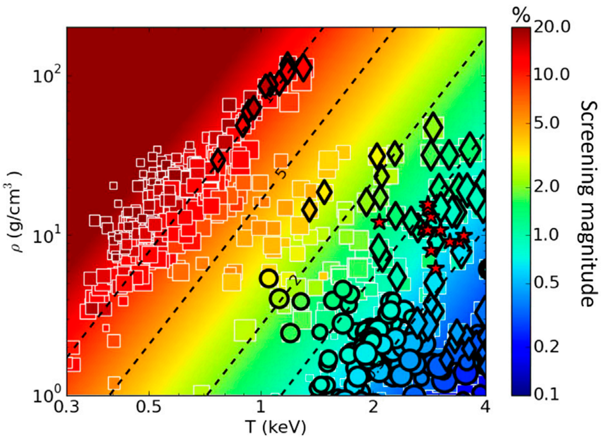

FIGURE 6
Large collection of HYDRA simulations of capsule implosions. The size of each marker is proportional to the simulated $D^3He$ yield. Several designs show significant screening and the most promising are outlined in black.

example, adding trace tritium in a predominantly $D^3He$ gas fill may allow the measurement of the $T_{DT}$ and $T_{DD}$ in a three-component plasma providing a constraint on the unmeasured $T_{D3He}$.

As a check on how the formula for extracting the reactivity ratio will work with these predicted gradients, the ENDF evaluated cross sections were input [40] with a 1D Betti [32] hotspot profile from which the yields and temperatures were calculated and used to recover the reactivity input in the calculation. The results are shown in Figure 5 and indicate that in the presence of this level of temperature variation, the extracted reactivity ratio is recovered.

## 3 Detailed experimental design considerations

To help understand the design space for a screening experiment, Figure 6 shows the results of an ensemble of 1D HYDRA simulations. These start with existing experimental design features and then perturb in directions to increase the calculated enhancement of the reaction rate from plasma screening, which is shown as the background color scale. The size of each individual point is proportional to the simulated $D^3He$ yield. Markers with solid outlines represent yield and ρR combinations that are promising for a screening experiment. The star points are the experimental results from gas-filled implosions, shown previously in Figure 1A.

To observe screening in an ICF experiment, two principal design paths are being actively explored. The first would use $D^3He$ protons as the primary measurement that would require the total areal density to not exceed the ~15 MeV proton range (~0.25 g/cm$^2$) to be detectable with WRF or step range filters [27, 28] placed near the implosion. Existing data in gas filled implosions was examined to assess the ability to measure $D^3He$ protons from implosions with moderately high compression (or areal density) and then determine the reactivity $<\sigma v>_{D3He}$ in density and temperature conditions where screening is expected to be weak. This work initially encountered significant detector analysis challenges with low energy protons (~7 MeV) and work is ongoing to attempt to resolve those issues [41]. The points with dark outlined circles are implosions that have proton yields high enough for a WRF measurement (>$10^5$) and ρRs low enough for the protons to be detectable (<0.2 g/cm$^2$).

An alternative design path would be to maximize the yield at high hotspot density for measurements of the $D^3He$ gamma ray (branching ratio ~ 1e-4) [42], since gammas and neutrons can escape high areal density implosions but carry with it increased uncertainty due to uncertainties in the gamma branching ratio [42] and reduced absolute signal levels. Therefore, this measurement would require a high solid angle Cherenkov detector [43, 44]. Since these detectors have high systematic uncertainties, we would measure the $D^3He$/DD yield ratio at both screening-relevant conditions and in a low-density plasma (exploding pusher) to eliminate systematics. HYDRA simulations explored the potential parameter space and have found several interesting designs that look promising in each of these design directions. In Figure 6, the diamonds with dark outlines represent designs with $D^3He$ yields that are potentially high enough (>$10^9$) for a gamma branch measurement.

The results in Figure 6 show that estimated screening corrections greater than 10% can be achieved, but most of these simulated designs would be significantly challenging to measure because of high ρR. Of these, some designs show potential (marked as black-outlined points). In the next section, we delve into one of the most promising black-outlined diamond points, to understand what features make this an interesting potential design to observe plasma screening.

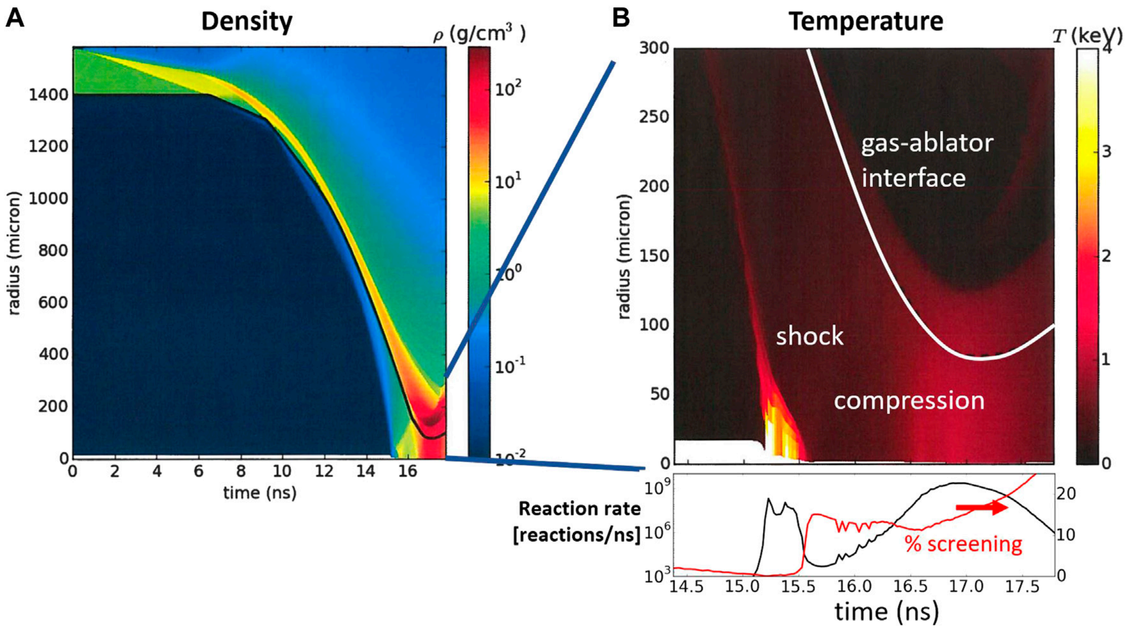

FIGURE 7
**(A)** HYDRA simulation of radius vs. time for an example screening experiment design candidate. The hotspot density reaches high conditions ~100 g/cm$^3$ **(B)** Zoom in temperature dynamics showing a brief shock flash and extended compression phase. Also shown are the reaction rate and screening magnitude of this design.

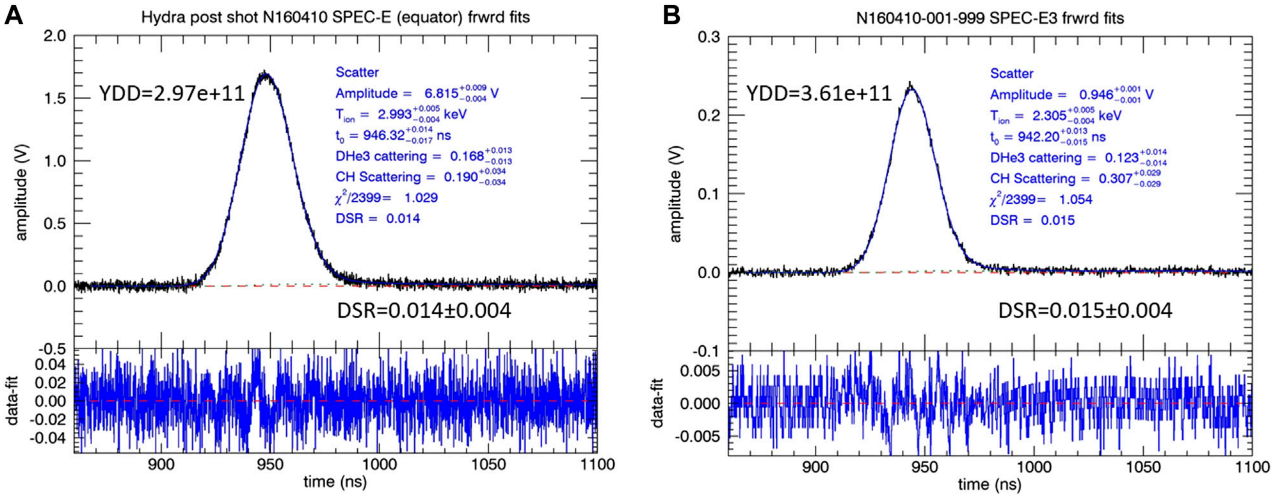

FIGURE 8
The result of a forward fit model to, **(A)** the data from shot N160410−001 and **(B)** of the synthetic neutron time-of-flight spectrum generated in post-shot Hydra simulation. Included in the forward fit model are the effects of neutron scattering from the CH ablator shell and the compressed D$^3$He fuel. The "down scatter ratio," DSR, is fraction of yield for neutrons of energy 1.9–2.2 MeV divided by the yield from 2.2 to 2.7 MeV.

### A. The "Slow-Cooker" Radiative Cooling Design Proposal

One especially interesting HYDRA simulation in Figure 6 is explored in more detail in Figure 7. This design uses a large 1400 μm inner radius capsule that is 200 μm thick, and initially filled with a D$^3$He mixture with added Kr. The large capsule ensures that high areal density will remain to produce a prominent compression phase. Figure 7B shows that after the shock flash, the Kr mixed in with the gas cools the hot spot and so it reaches an iso-thermal state near 1 keV, lasting for almost 1 ns For perspective, typical NIF implosions are confined for about a 10th of a nanosecond. This interesting set of implosion dynamics is established as the temperature and density conditions are in a radiation dominated energy loss regime, rather than the more typical thermal conduction dominated regimes of most hotspot ICF designs. This design is called the "slow-cooker," because the conditions are advantageous for increasing the burn by maximizing the plasma confinement, while also favoring the conditions for finite screening of reacting nuclei. Furthermore, the radiation cooling dominated regime may also result in reduced spatial temperature gradients because the hotspot becomes nearly iso-thermal. This radiation dominated isothermal system is interesting enough to warrant study just to understand this radiation dominated physics regime for its own sake, but also to produce conditions where screening becomes non-negligible, as shown in the subplot of the reaction rate and time dependent screening magnitude Figure 7.

B. Estimating the Uncertainty of the Yield and Ti at Low Yield

The design space of interest for observing screening is expected to produce neutron yields from DD fusion of order $10^7$ to $10^8$ neutrons. This low yield also presents a challenge to the neutron time-of-flight spectrometry that will be used to measure the yield and ion temperature of the implosions. To help enable measurements at these challenging yields, the current analysis process [22] was modified to include neutron elastic scattering from both the $D^3He$ and the ablator shell, to account for scattering effects on the low-energy tail. This modified analysis was then performed on the higher yield shot data from shot N160410-001-999 [note that NIF experiments have the following naming convention N (Year) (Month) (day)-(Shot index of that day)-999, where-999 indicates a full system shot], and on the simulated HYDRA post-shot neutron spectrum. The post-shot spectrum was transformed into a synthetic neutron time-of-flight including the various features of the neutron transport, detection, and digitization. This time-of-flight data was then analyzed and compared to the shot data. Figure 8 shows the results of this process. This analysis will allow additional simulation generated neutron spectra to be generated and analyzed to investigate the statistical significance of both yield and ion temperature.

## 4 Conclusion and next steps

Plasma electron screening is an important fundamental process in the thermonuclear burn of astrophysical objects, like stars, but observing it in laboratory plasma experiments is a significant challenge. In this work, we show that ICF implosions have already reached the relevant conditions for stellar burn but that the magnitude of the plasma screening effect was too weak to directly measure in those experiments. However, there are clear design directions to increase the magnitude of the plasma screening effect by utilizing higher-Z reactions, higher-Z plasmas, reducing the plasma ion temperature, and increasing the plasma density. The ratio method is a powerful approach to infer the thermonuclear S-fact in the presence of strong temperature and density gradients. We show a simple treatment that includes a correction to the ratio method for these gradients that is needed at the very low temperatures for a screening measurement. Furthermore, to develop a credible experimental design, an ensemble of HYDRA simulations was run to increase the calculated level of plasma electron screening to levels >10%. A promising resultant design, called the "slow-cooker," features a very large (1400 μm inner diameter) and thick ablator (200 μm) filled with a mixture of $Kr/D/^3He$. The slow-cooker enters the radiation dominated implosion regime, resulting in a relatively cold (1 keV) and dense (100 g/cm$^3$) $Kr/D/^3He$ plasma that is confined for nearly 1 ns. These conditions are all favorable for plasma electron screening and are predicted to increase the $D+^3He$ reaction rate relative to D + D to levels that may be measurable on the NIF.

The present work assessed the issues with respect to a plasma screening measurement and identifies some credible solutions to long standing challenges. The next step is to test the null hypothesis of implosions where screening is expected to be negligible, an effort that is currently underway in the NIF discovery science program [45]. The physics of the radiation dominated "slow-cooker" implosion should also be explored and tested to see if the required conditions are achieved and assess whether the reaction products will be measurable. While substantial challenges remain, we have shown that experiments on NIF show promise and may enable the first observation of plasma screening of nuclear reactions, addressing one of the fundamental questions of high-energy-density physics. This work is performed under the auspices of the U.S. Department of Energy by LLNS, LLC, under contract no. DE-AC52-07NA27344.

## Data availability statement

The raw data supporting the conclusions of this article will be made available by the authors, without undue reservation.

## Author contributions

DC lead author and screening project PI. CW capsule design and HYDRA simulations. AZ experiment analysis and screening DS project PI. CC capsule design expert. EH nuclear and time-of-flight detector analysis. MH experiment and analysis. LD HYDRA simulations. DD stellar system simulations. NK experiment and particle detector analysis. BL particle detector analysis. MGJ nuclear and particle detector analysis. JF nuclear and particle detector analysis.

## Funding

This work is performed under the auspices of the U.S. Department of Energy by LLNS, LLC, under contract no. DE-AC52-07NA27344.

## Conflict of interest

## Publisher's note

## References

1. National Research Council. *Frontiers in high energy density physics: The X-games of contemporary science*. Washington, D.C: The National Academies Press (2003).

2. Bahcall JN, Brown LS, Gruzinov A, Sawyer RF. The Salpeter plasma correction for solar fusion reactions. *A. A* (2002) 383:291–5. doi:10.1051/0004-6361:20011715

3. Shaviv NJ, Shaviv G. Obtaining the electrostatic screening from first principles. *Nucl Phys A* (2003) 719:C43–C51. doi:10.1016/S0375-9474(03)00956-4

4. Däppen W, Mussack K. Dynamic screening in solar and stellar nuclear reactions. *Contrib Plasma Phys* (2012) 52:149–52. doi:10.1002/ctpp.201100099

5. Spitaleri C, Bertulani CA, Fortunato L, Vitturi A. The electron screening puzzle and nuclear clustering. *Phys Lett B* (2016) 755:275–8. doi:10.1016/j.physletb.2016.02.019

6. Bertulani CA, Spitaleri C. Nuclear clustering and the electron screening puzzle. *EPJ Web Conf* (2017) 165:02002. doi:10.1051/epjconf/201716502002

7. Dzitko H, Turck-Chieze S, Delbourgo-Salvador P, Lagrange C. The screened nuclear reaction rates and the solar neutrino puzzle. *ApJ* (1995) 447:428. doi:10.1086/175887

8. Adelberger EG, Austin SM, Bahcall JN, Balantekin AB, Bogaert G, Brown LS, et al. Solar fusion cross sections. *Rev Mod Phys* (1998) 70:1265–91. doi:10.1103/revmodphys.70.1265

9. Adelberger EG, Balantekin AB, Bemmerer D, Bertulani CA, Chen JW, Costantini H, et al. (2010). *Solar fusion cross sections II: The pp chain and CNO cycles.*

10. Aliotta M, Raiola F, Gyurky G, Formicola A, Bonetti R, Broggini C, et al. Electron screening effect in the reactions 3He(d, p)4He and d(3He, p)4He. *Nucl Phys A* (2001) 690:790–800. doi:10.1016/s0375-9474(01)00366-9

11. Aliotta M, Langanke K. Screening effects in stars and in the laboratory. *Front Phys* (2022) 10. doi:10.3389/fphy.2022.942726

12. Raiola F, Migliardi P, Gang L, Bonomo C, Gyurky G, Bonetti R, et al. Electron screening in d(d, p)t for deuterated metals and the periodic tablep)t for deuterated metals and the periodic table. *Phys Lett B* (2002) 547:193–9. doi:10.1016/S0370-2693(02)02774-0

13. Cognata ML, Spitaleri C, Tumino S, Typel S, Cherubini S, Lamia L Bare-nucleus astrophysical factor of the (3)He(d, p)(4)He reaction via the ``Trojan horse'' method. *Phys Rev C* (2005) 72(6):065802. doi:10.1103/PhysRevC.72.065802

14. Czerski K, Huke A, Biller A, Heide P, Hoeft M, Ruprecht G. Enhancement of the electron screening effect for d + d fusion reactions in metallic environments. *Europhys Lett* (2001) 54:449–55. doi:10.1209/epl/i2001-00265-7

15. Kasagi J, Yuki H, Baba T, Noda T, Ohtsuki T, G. Lipson A. Strongly enhanced DD fusion reaction in metals observed for keV D+ bombardment. *J Phys Soc Jpn* (2002) 71:2881–5. doi:10.1143/JPSJ.71.2881

16. Salpeter E. Electron screening and thermonuclear reactions. *Aust J Phys* (1954) 7:373–88. doi:10.1071/PH540373

17. Schröder U, Engstler S, Krauss A, Neldner K, Rolfs C, Somorjai E, et al. Search for electron screening of nuclear reactions at sub-coulomb energies. *Nucl Instr Methods Phys Res Section B: Beam Interactions Mater Atoms* (1989) 40-41:466–9. doi:10.1016/0168-583x(89)91022-7

18. Casey DT, Sayre DB, Brune CR, Smalyuk VA, Weber CR, Tipton RE, et al. Thermonuclear reactions probed at stellar-core conditions with laser-based inertial-confinement fusion. *Nat Phys* (2017) 13:1227–31. doi:10.1038/nphys4220

19. Zylstra AB, Herrman HW, Johnson MG, Kim YH, Frenje JA, Hale G, et al. Using inertial fusion implosions to measure the $\mathrm{T}+^{3}\mathrm{He}$ fusion cross section at nucleosynthesis-relevant energies. *Phys Rev Lett* (2016) 117(3):035002.

20. Zylstra AB, Frenje JA, Gatu Johnson M, Hale GM, Brune CR, Bacher A, et al. Proton spectra from 3He+T and 3He+3He fusion at low center-of-mass energy, with potential implications for solar fusion cross sections. *Phys Rev Lett* (2017) 119(22):222701. doi:10.1103/PhysRevLett.119.222701

21. Dearborn DSP, Lattanzio JC, Eggleton PP. Three-dimensional numerical experimentation on the core helium flash of low-mass red giants. *ApJ* (2006) 639:405–15. doi:10.1086/499263

22. Hatarik R, Sayre DB, Caggiano JA, Phillips T, Eckart MJ, Bond EJ, et al. Analysis of the neutron time-of-flight spectra from inertial confinement fusion experiments. *J Appl Phys* (2015) 118:184502. doi:10.1063/1.4935455

23. Moore AS, Schlossberg DJ, Hartouni EP, Sayre D, Eckart MJ, Hatarik R, et al. A fused silica Cherenkov radiator for high precision time-of-flight measurement of DT γ and neutron spectra (invited). *Rev Scientific Instr* (2018) 89:10I120. doi:10.1063/1.5039322

24. Glebov VY, Sangster TC, Stoeckl C, Knauer JP, Theobald W, Marshall KL, et al. The National Ignition Facility neutron time-of-flight system and its initial performance (invited). *Rev Scientific Instr* (2010) 81:10D325–326. doi:10.1063/1.3492351

25. Cerjan C, Springer PT, Sepke SM. Integrated diagnostic analysis of inertial confinement fusion capsule performance. *Phys Plasmas (1994-present)* (2013) 20:056319. doi:10.1063/1.4802196

26. Zylstra AB, Frenje JA, Seguin FH, Rosenberg MJ, Rinderknecht HG, Johnson MG, et al. Charged-particle spectroscopy for diagnosing shock rho R and strength in NIF implosions. *Rev Scientific Instr* (2012) 83:10D901. doi:10.1063/1.4729672

27. Seguin FH, Frenje JA, Li CK, Hicks DG, Kurebayashi S, Rygg JR, et al. Spectrometry of charged particles from inertial-confinement-fusion plasmas. *Rev Scientific Instr* (2003) 74:975–95. doi:10.1063/1.1518141

28. Lahmann B, Johnson MG, Frenje JA, Birkel AJ, Adrian PJ, Kabadi N, et al. Extension of charged-particle spectrometer capabilities for diagnosing implosions on OMEGA, Z, and the NIF. *Rev Scientific Instr* (2021) 92:083506. doi:10.1063/5.0062584

29. Kabadi NV, Adrian PJ, Bose A, Casey DT, Frenje JA, Gatu Johnson M, et al. A second order yield-temperature relation for accurate inference of burn-averaged quantities in multi-species plasmas. *Phys Plasmas* (2021) 28:022701. doi:10.1063/5.0032139

30. Zylstra AB, Herrmann HW, Kim YH, McEvoy A, Frenje JA, Johnson MG, $^{2}$H(p,γ)$^{3}$He cross section measurement using high-energy-density plasmas. *Phys Rev C* (2020) 101(4):042802. doi:10.1103/PhysRevC.101.042802

31. Munro DH. Interpreting inertial fusion neutron spectra. *Nucl Fusion* (2016) 56:036001. doi:10.1088/0029-5515/56/3/036001

32. Betti R, Umansky M, Lobatchev V, Goncharov VN, McCrory RL. Hot-spot dynamics and deceleration-phase Rayleigh? Taylor instability of imploding inertial confinement fusion capsules. *Phys Plasmas* (2001) 8:5257–67. AIP. doi:10.1063/1.1412006

33. Casey DT, Smalyuk VA, Tipton RE, Pino JE, Grim GP, Remington BA, et al. Development of the CD Symcap platform to study gas-shell mix in implosions at the National Ignition Facility. *Phys Plasmas* (2014) 21:092705. doi:10.1063/1.4894215

34. Khan SF, MacLaren SA, Salmonson JD, Ma T, Kyrala GA, Pino JE, et al. Symmetry tuning of a near one-dimensional 2-shock platform for code validation at the National Ignition Facility. *Phys Plasmas* (2016) 23:042708. doi:10.1063/1.4947223

35. Le Pape S, Divol L, Berzak Hopkins L, Mackinnon A, Meezan N, Casey D, et al. Observation of a reflected shock in an indirectly driven spherical implosion at the national ignition facility. *Phys Rev Lett* (2014) 112:225002. doi:10.1103/physrevlett.112.225002

36. Gatu Johnson M, Knauer JP, Cerjan CJ, Eckart MJ, Grim GP, Hartouni EP, et al. Indications of flow near maximum compression in layered deuterium-tritium implosions at the National Ignition Facility. *Phys Rev E* (2016) 94:021202. doi:10.1103/physreve.94.021202

37. Edwards MJ, Lindl JD, Spears BK, Weber SV, Atherton LJ, Bleuel DL, et al. The experimental plan for cryogenic layered target implosions on the National Ignition Facility?The inertial confinement approach to fusion. *Phys Plasmas* (2011) 18(5):051003.

38. Marinak MM, Kerbel GD, Gentile NA, Jones O, Munro D, Pollaine S, et al. Three-dimensional HYDRA simulations of national ignition facility targets. *Phys Plasmas* (2001) 8:2275–80. doi:10.1063/1.1356740

39. Schlossberg DJ, Grim G, Casey D, Moore A, Nora R, Bachmann B, et al. Observation of hydrodynamic flows in imploding fusion plasmas on the national ignition facility. *Phys Rev Lett* (2021) 127:125001. doi:10.1103/PhysRevLett.127.125001

40. Chadwick MB, Oblozinsky P, Herman M, Greene N, McKnight R, Smith D, et al. ENDF/B-VII.0: Next generation evaluated nuclear data library for nuclear science and technology. *Nucl Data Sheets* (2006) 107:2931–3060. doi:10.1016/j.nds.2006.11.001

41. Kabadi N. Ph.D. dissertation. MIT (2022).

42. Kim Y, Mack JM, Herrmann HW, Young CS, Hale GM, Caldwell S, et al. D-T gamma-to-neutron branching ratio determined from inertial confinement fusion plasmas. *Phys Plasmas* (2012) 19:056313. doi:10.1063/1.4718291

43. McEvoy AM, Herrmann HW, Kim Y, Zylstra AB, Young CS, Fatherley VE, et al. Gamma ray measurements at OMEGA with the newest gas Cherenkov detector “GCD-3”. *J Phys : Conf Ser* (2016) 717:012109. doi:10.1088/1742-6596/717/1/012109

44. Jeet J, Zylstra AB, Rekow V, Hardy CM, Pelepchan N, Eckart M, et al. The Vacuum Cherenkov Detector (VCD) for γ-ray measurements in inertial confinement fusion experiments. *Rev Sci Instrum* (2022) 93(10):103543.

45. Zylstra A. *Personal communication.*

frontiers | Frontiers in Physics

TYPE Original Research
PUBLISHED 09 January 2023
DOI 10.3389/fphy.2022.964696

EDITED BY
Mark Paris,
Los Alamos National Laboratory (DOE),
United States

REVIEWED BY
Arnaud Le Fèvre,
Helmholtz Association of German
Research Centres (HZ), Germany
Dario Lattuada,
Kore University of Enna, Italy

*CORRESPONDENCE
O. Z. Labun,
ozlabun@utexas.edu

SPECIALTY SECTION
This article was submitted to Nuclear Physics, a section of the journal Frontiers in Physics

RECEIVED 08 June 2022
ACCEPTED 15 December 2022
PUBLISHED 09 January 2023

CITATION
Jiao X, Curry CB, Gauthier M, Chou H-GJ, Fiuza F, Kim JB, Phan DD, McCary E, Galtier EC, Dyer GM, Ofori-Okai BK, Labun L, Labun OZ, Schoenwaelder C, Roycroft R, Tiwari G, Glenn GD, Treffert F, Glenzer SH and Hegelich BM (2023), High deuteron and neutron yields from the interaction of a petawatt laser with a cryogenic deuterium jet.
*Front. Phys.* 10:964696.
doi: 10.3389/fphy.2022.964696

# High deuteron and neutron yields from the interaction of a petawatt laser with a cryogenic deuterium jet

X. Jiao[1], C. B. Curry[2,3], M. Gauthier[2], H.-G. J. Chou[2,4], F. Fiuza[2], J. B. Kim[2], D. D. Phan[1], E. McCary[1], E. C. Galtier[2], G. M. Dyer[2], B. K. Ofori-Okai[2], L. Labun[1], O. Z. Labun[1]*, C. Schoenwaelder[2,5], R. Roycroft[1], G. Tiwari[1], G. D. Glenn[2,6], F. Treffert[2,7], S. H. Glenzer[2] and B. M. Hegelich[1,8]

[1]Center for High Energy Density Science, University of Texas at Austin, Austin, TX, United States, [2]SLAC National Accelerator Laboratory, Menlo Park, CA, United States, [3]Department of Electrical and Computer Engineering, University of Alberta, Edmonton, AB, Canada, [4]Physics Department, Stanford University, Stanford, CA, United States, [5]Friedrich-Alexander-Universität Erlangen-Nürnberg, Erlangen Centre for Astroparticle Physics, Erlangen, Germany, [6]Applied Physics Department, Stanford University, Stanford, CA, United States, [7]Institute for Nuclear Physics, Technical University Darmstadt, Darmstadt, Germany, [8]CoReLS, Institute for Basic Science (IBS), Gwangju, South Korea

A compact high-flux, short-pulse neutron source would have applications from nuclear astrophysics to cancer therapy. Laser-driven neutron sources can achieve fluxes much higher than spallation and reactor neutron sources by reducing the volume and time in which the neutron-producing reactions occur by orders of magnitude. We report progress towards an efficient laser-driven neutron source in experiments with a cryogenic deuterium jet on the Texas Petawatt laser. Neutrons were produced both by laser-accelerated multi-MeV deuterons colliding with Be and mixed metallic catchers and by $d\ (d,n)^3$He fusion reactions within the jet. We observed deuteron yields of $10^{13}$/shot in quasi-Maxwellian distributions carrying ~ 8 – 10% of the input laser energy. We obtained neutron yields greater than $10^{10}$/shot and found indications of a deuteron-deuteron fusion neutron source with high peak flux ($>10^{22}$ cm$^{-2}$ s$^{-1}$). The estimated fusion neutron yield in our experiment is one order of magnitude higher than any previous laser-induced *dd* fusion reaction. Though many technical challenges will have to be overcome to convert this proof-of-principle experiment into a consistent ultra-high flux neutron source, the neutron fluxes achieved here suggest laser-driven neutron sources can support laboratory study of the rapid neutron-capture process, which is otherwise thought to occur only in astrophysical sites such as core-collapse supernova, and binary neutron star mergers.

KEYWORDS

**laser-driven neutron source, high-flux neutron source, rapid neutron capture process, laboratory astro-nuclear physics experiment, laser-driven fusion, laser-driven ion source**

## 1 Introduction

The synthesis of approximately half of the atomic nuclei heavier than iron is theorized to occur *via* the rapid neutron-capture process (r-process) in astrophysical environments of extreme temperature and density. While such temperature and density are unlikely to be recreated in the lab, a broadly-recognized goal is to develop experiments to study the nuclear scattering and excitation dynamics of multi-neutron capture, which is estimated to require neutron fluxes greater than $10^{22}\,\mathrm{cm}^{-2}\,\mathrm{s}^{-1}$ [1]. Beyond nuclear astrophysics, fast neutrons produced in a compact, ultra-short pulse source, would have wide ranging applications including high energy density physics [2], materials science [3], and medical research [4]. For this reason, high-flux neutron sources remain an important subject of research and development. Laser-driven neutron sources in particular are a promising approach [5], having already achieved much higher peak neutron fluxes than fission reactors ($\sim 10^{15}/\mathrm{cm}^2/\mathrm{s}$) or spallation ($\sim 10^{17}/\mathrm{cm}^2/\mathrm{s}$) sources in laboratory experiments, potentially in a more compact facility [6].

The highest neutron yields achieved by laser-driven sources are from inertial confinement fusion (ICF) [7] experiments. The most successful shots at the National Ignition Facility (NIF) produced $> 10^{15}$ neutrons in less than a nanosecond [8] suggesting that neutron fluxes greater than $10^{24}/\mathrm{cm}^2/\mathrm{s}$ are achieved just outside the cm-long hohlraum. However, ICF user facilities like OMEGA [9] or the NIF [10] are too large to be available for smaller-scale nuclear physics studies with neutrons for the foreseeable future.

The advent of ultrahigh intensity lasers thanks to chirped pulse amplification [11] has enabled the production of neutrons in a much more compact arrangement [3, 12–24]. Several schemes have been tested on laser systems ranging in scale from millijoules [22] to kilojoules [3]. Among them, the most promising method is the ion-driven neutron source approach [20] because of its comparatively high efficiency and neutron yield. Experiments have demonstrated a directional peak yield of up to $1 \times 10^{10}$ n/sr/shot [19]. The scheme is usually employed in "pitcher-catcher" configuration, where the laser interacts with a thin ( ~μm) pitcher target to accelerate ions, typically protons or preferably deuterons. These ions then interact with a cm-scale, low-Z "catcher" target, beryllium-9 [18], lithium-7 [25] or deuterated plastic [23], undergoing nuclear reactions and producing neutrons in the process. Using break-out afterburner acceleration in the relativistic transparency regime [19], this method could achieve an overall laser-to-neutron energy conversion efficiency of $\sim 6 \times 10^8$ n/J compared to $\sim 4 \times 10^8$ n/J for TNSA acceleration driven laser-neutron generation, $\sim 4 \times 10^6$ n/J for laser-electron driven neutron source [24], and only $\sim 10^5$ n/J for laser-cluster fusion neutron source [17].

We report on a novel approach to laser-driven neutron generation. For the first time in a petawatt laser facility, cryogenic deuterium jet targets were used to efficiently generate neutrons. These targets offer several advantages over the deuterated plastic foils used in previous experiments [16, 18, 19, 26], including near-critical electron density allowing access to the relativistic transparency regime and potential for high repetition rate target preparation [27]. The thin, above critical density target results in efficient ion acceleration ($\sim 10\%$ of laser energy transferred to ions), and the higher yield ($\sim 10^{13}$/shot) and energy deuteron beam produces a higher yield of neutrons in the pitcher-catcher configuration. We find higher neutron yields detected in the bubble detectors than can be explained by deuteron-converter interactions. E other sources and simulating the laser-plasma interaction, we consider the most plausible explanation is that, in addition to being efficiently accelerated out of the target, deuterons in the target are volumetrically heated and produce a significant number of neutrons by the $d\ (d,n)^3\mathrm{He}$ reaction. The deduced fusion neutron yield is consistent with simulation estimates and, considering the small source size ( $\lesssim 100\,\mu\mathrm{m}$), suggests a route to the ultra-high fluxes required for r-process studies.

## 2 Experimental setup

The experiment was carried out at the Texas Petawatt laser [28] facility at the University of Texas at Austin. The experimental setup is depicted in Figure 1. The 1057 nm Nd: Glass laser delivered 90–140 J, 140 fs laser pulses to irradiate the deuterium jet targets. Using an *f*/3 off-axis parabolic mirror, the laser beam was focused to a spot size of 6 μm full-width half-maximum (FWHM) to an average encircled laser intensity of $> 10^{21}\ \mathrm{W/cm}^2$. A plasma mirror was installed 5 cm before the target to remove pre-pulses and steepen the rising edge of the main pulse (see temporal profile in Appendix A), reaching a contrast ratio of $> 10^5$ at 10 ps before the arrival of the main beam. The plasma mirror reflectivity was estimated to be approximately 80%.

The deuterium jet was made by a cryogenic microjet system developed at SLAC [29, 30]. Deuterium gas is liquified and held at 19–21K in a copper source assembly cooled by a continuous-flow helium cryostat. The liquid deuterium enters the chamber through a 2 × 40 μm rectangular aperture and rapidly solidifies a few 100 μm from the nozzle by evaporative cooling. The resulting cryogenic deuterium jet is a relatively flat planar sheet of width 15 μm between two 5 μm diameter cylindrical columns, as illustrated in Figure 1A, running at a speed of 50–100 m/s into vacuum [31]. At this temperature, the density of the deuterium is expected to be $n_d \simeq 6 \times 10^{22}\,\mathrm{cm}^{-3}$. The jet-laser overlap was monitored and adjusted using two orthogonal probe imaging systems.

Either a radiochromic film (RCF) stack or a Be converter was placed downstream of the laser forward direction. The RCF stack consisted of alternating layers of aluminum foil, copper sheets and calibrated RCF films [32] of different thicknesses to measure

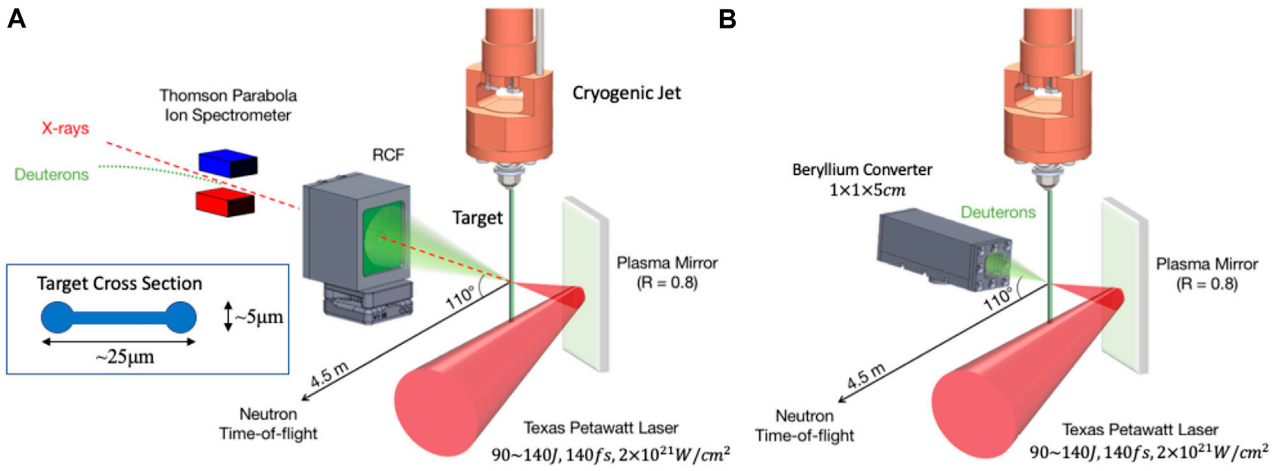

FIGURE 1
**(A)** Experiment setup with RCF stack. Inset: cross section of the deuterium ice targets. **(B)** Experiment setup with beryllium converter.

the deuteron beam divergence profile and rough spectrum. The precise composition of the stack is given in Appendix B. The 2.7 × 2.3 $cm^2$ RCF stack was centered on the laser axis 4.5 cm behind the target. It had a centered 5 mm diameter hole providing line of sight for a Thomson parabola spectrometer (TPS). The TPS was analyzed in conjunction with the RCF stack to provide an absolutely calibrated, high resolution measurement of the deuteron beam energy spectrum. A second TPS and an electron spectrometer were respectively located 30° and 36° counter clockwise from the laser axis. The high voltage setting on the TPS was not turned on during the measurements since the irradiated target introduces a significant load on the vacuum system resulting in pressures which cause electrical arcing in the TPS thereby corrupting the signal recorded on the imaging plate. However, a previous experiment which utilized differential pumping to separate the TPS from the vacuum chamber, demonstrated that other ion species are negligible compared to the main source because of the high purity of the deuterium gas ($D_2$, 99.6% + HD, 0.4%) used to create the cryogenic deuterium jet target [33].

In addition to measuring the energy-resolved spatial distribution of the deuteron beam, the RCF stack also acts as a neutron converter where laser-accelerated deuterons produce neutrons *via* breakup reactions. We also investigated enhancing neutron production by installing a 1 × 1 × 5 $cm^3$ Be converter centered on the laser axis at a distance of 2.7 cm. Due to its light atomic weight and high (d,n) reaction cross section, the Be converter is expected to produce a higher neutron yield than the RCF stack. The beryllium converter was housed in an aluminum casing with a 100 μm thick aluminum window on the side facing the laser-plasma interaction. This shields the beryllium from the transmitted laser pulse, while still allowing the majority of MeV-energy deuterons to pass through.

A neutron time of flight (n-TOF) detector was used to measure the neutron energy spectrum 4.5 m away from the target chamber center (TCC) and 110° away from the laser propagation direction, which was the only available line-of-sight given the radiation shielding. The n-TOF consists of a fast plastic scintillator (EJ-200), a photomultiplier (XP2020) and a fast-digital oscilloscope (TDS5104). The strong x-ray signal from the laser target interaction was shielded by a 32.5 mm thick Cu plate to reduce the decay signal width (FWHM) to below 25 ns. The thickness is chosen to ensure the neutron signal remains greater than the x-ray-generated background, which thereby served as a time reference for the neutron energy analysis. The response function of the scintillator was measured beforehand and the width (FWHM) was found to be around 10 ns per volt. For our setup, this would introduce a 10% uncertainty in the energy measurement and it affects the low energy range less than the high energy range. Ten bubble detectors [34] were positioned in the laser plane at various angles around the target chamber (−177° – 90° from target normal, to measure the fast neutron flux at the detector position. The bubble detectors' sensitivities varied between 2–2.5 bubbles/mrem. Distances of the bubble detectors were measured using the front of the Be converter or the front of the RCF stack as a reference point as our analysis, presented in the following sections, suggests this is the primary source of neutrons.

## 3 Results

A typical deuteron energy spectrum measured at 0 and 30° from the laser forward direction, as well as the reconstructed average spectrum from the dose recorded on each RCF film are

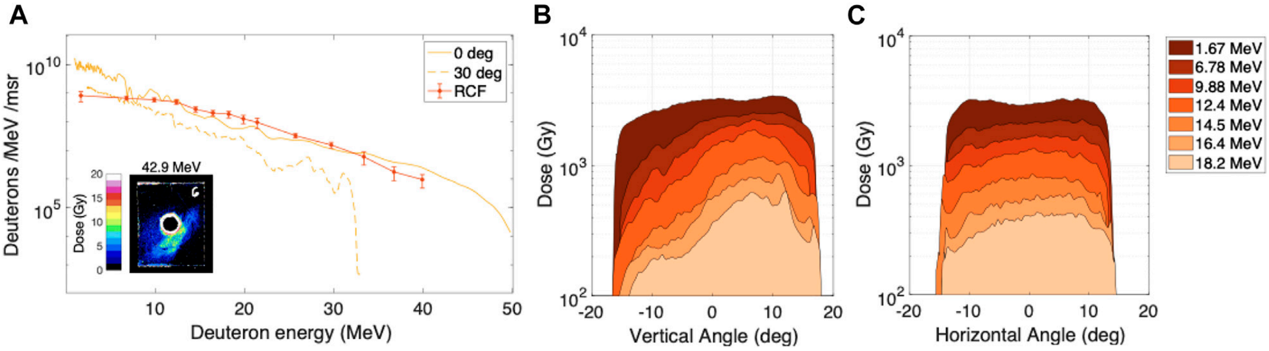

FIGURE 2
Deuteron beam characteristics for shot 11,557: **(A)** Deuteron spectrum, measured in the laser forward direction through a 5 mm diameter hole in RCF stack centered on the laser plasma acceleration with a TPS. Inset: Deuteron spatial profile on last RCF film which corresponds to 42.9 MeV **(B, C)** Average deuteron emission distribution in the vertical and horizontal direction from the first 7 HD-V2 layers of the RCF stack.

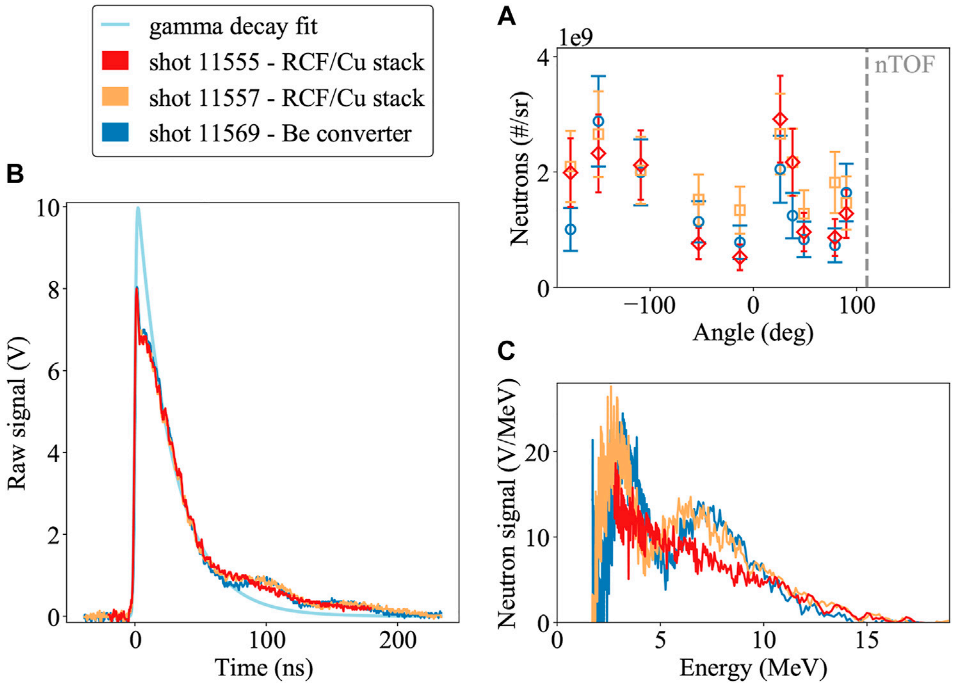

FIGURE 3
**(A)** Number of neutrons detected in each bubble detector, as a function of their angles with respect to the laser-forward direction. Fluxes are given assuming a source at the front surface of converter or RCF stack. Total neutron yield is $2.0 \times 10^{10}$ assuming an isotropic source in $4\pi$. **(B)** The neutron TOF signals with gamma decay fit for shot 11,557 (light blue) overlaid. **(C)** The neutron spectrum in V/MeV as a function of detected neutron energy after the gamma background is subtracted.

shown in Figure 2A. Note that the absolute flux was calculated using the energy-dependent image plate calibration from [35] in conjunction with doses extracted from the RCF films in the laser forward direction. The deuteron spectrum follows a semi-Maxwellian distribution, indicative of a TNSA-dominated regime [31], with a cut-off energy of 50 MeV (shot 11,557) at 0 deg. Consistent with a previous study using planar cryogenic hydrogen jets [31], the deuteron beam is comprised of two main components which are attributed to the planar central region and cylindrical rims of the cryogenic jet. The former produces a conical beam with a half-angle decreasing from approximately 20° at the lowest energies to less than 10° near the cut-off energy (Figure 2B). The latter produces a near azimuthally symmetric deuteron emission with similar confinement along the jet axis as illustrated in Figure 2C.

The neutron yield was measured using the bubble detector array and the neutron spectrum measured using the n-TOF detector for 3 consecutive shots. For shots 11,555 and 11,557, deuterons were impinging on the RCF stack as shown in Figure 1A, while for shot 11,569, the Be converter was implemented in the setup replacing the RCF, see (b).

Absolute neutron numbers at the location of the bubble detectors were calculated by converting bubble counts to dose in mrem using the manufacturer provided sensitivity of the individual detectors. Dosages (mrem) were then converted to neutron flux (n/sr) using the conversion relation provided in [18] and the distances of the detectors to the RCF or converter. Figure 3A shows the calculated neutron flux as a function of angle with respect to laser forward direction for the three recorded shots. The error bars shown in the plot are a combination of the statistical error of the measurement ($\sqrt{N}/N$) and the response fluctuation of the bubble detector across its sensitivity range. This response dependent error (19%) is determined by calculating the standard deviation of the response measurement conducted by [18] across an energy ranging from 0.3 to 32 MeV. Calculated fluxes across the three shots ranged from ($5.2 \times 10^8$–$2.9 \times 10^9$) n/sr. As seen in Figure 3A the neutron fluence distribution is predominantly isotropic with two broadened peaks visible at −150 and 30°. Monte Carlo simulations described in the next section show that the peak at 30° is due to the forward-directed conical-beam component of the deuteron distribution described above. Averaging over the detected neutron flux for all shots and integrating over $4\pi$, in the same way as previously published works, we obtain a total neutron yield of ~ $2 \times 10^{10}$ n/shot. Note that due to the lack of neutron flux measurements outside of the laser propagation plane, this number can be viewed as the ideal case and as an upper bound to the actual on-shot neutron yield. Future measurements will give more insight into the neutron flux distribution outside the laser plane. Even though the flux we calculate is based on the important assumption of isotropy in $4\pi$, the estimate still agrees within error bars with Monte Carlo simulation described below.

Figure 3B shows the raw neutron traces acquired by the n-TOF detector for all three shots (11,555, 11,557 and 11,569). The spectra were extracted first by subtracting the signals corresponding to the x-rays from the overall time of flight signals, which is accomplished by fitting the X-ray peak with a skewed Gaussian model

$$f(x) = A\, e^{\alpha\left(\mu - x + \frac{\alpha\sigma^2}{2}\right)}\left[1 - \operatorname{erf}\left(\frac{\mu - x + \alpha\sigma^2}{\sqrt{2}\,\sigma}\right)\right] \qquad (1)$$

with the center of the peak $\mu$, the standard deviation $\sigma$, the amplitude $A$, the fit factor $\alpha$ and the error function erf. As an example the gamma peak decay fit for shot 11,557 is displayed in Figure 3B as the light blue curve. We fit the decay line after the first 16 ns to avoid the interference of the fast decay process, corresponding to the very sharp peaks at time zero. Then the neutron signal was converted from the time domain to energy domain ($\mathrm{d}V/\mathrm{d}t \rightarrow \mathrm{d}V/\mathrm{d}E$) by setting a 10% threshold on the X-ray peak to determine the laser-target interaction time. Figure 3C shows the three different spectra as a function of energy in MeV and the neutron signal in terms of V/MeV. By allowing systematic uncertainties in the x-ray signal subtraction, we estimated the error on the neutron spectrum to be less than 10%.

In shot 11,555, the spectrum is monotonically decreasing with an endpoint energy $E_n \simeq 15$ MeV, consistent with simulations of deuteron break-up on Be, Al in the chamber walls and other experimental apparatus. In shots 11,557 and 11,569, we identify two distinct peaks, one around 2.7 MeV for 11,557 and 3.2 MeV for 11,569, the other broader and peaked around 6 MeV, suggesting two populations of neutrons with different origins.

# 4 Discussion

## 4.1 Neutron source modeling

The high yield of fast deuterons enables several channels for neutron production. Deuterons produce neutrons colliding with nuclei in the intended catcher or with experimental apparatus, mostly due to break-up of the deuteron. Deuterons can also fuse to produce neutrons *via* the $d\,(d,n)^3$He reaction. Deuteron break-up can occur anywhere in the target chamber, from the catcher near the center to the chamber walls near to the bubble detectors, whereas $d\,(d,n)^3$He reactions are only likely to occur within the deuterium plasma. These source distributions are very different but cannot be distinguished with the layout of detectors in the experiment, and we must therefore rely on Monte Carlo simulations to predict and interpret the neutron signal in each detector.

First, to estimate the yield from deuteron collisions with the Be converter, the RCF stack or other experimental apparatus, we constructed a simplified GEANT4 [36] model of the target chamber, including the aluminium walls and optical breadboard. The simulation includes seven bubble detectors placed at the angular positions −177°, − 150°, − 109°, − 53°, − 12°, 26°, 90°, with respect to the laser forward direction, and one TOF at 110°, mimicking the neutron diagnostics in the actual experimental setup. The deuteron source is modelled by the combination of two components as described earlier in the Results section: (1) a conical component with a 20° half-angle

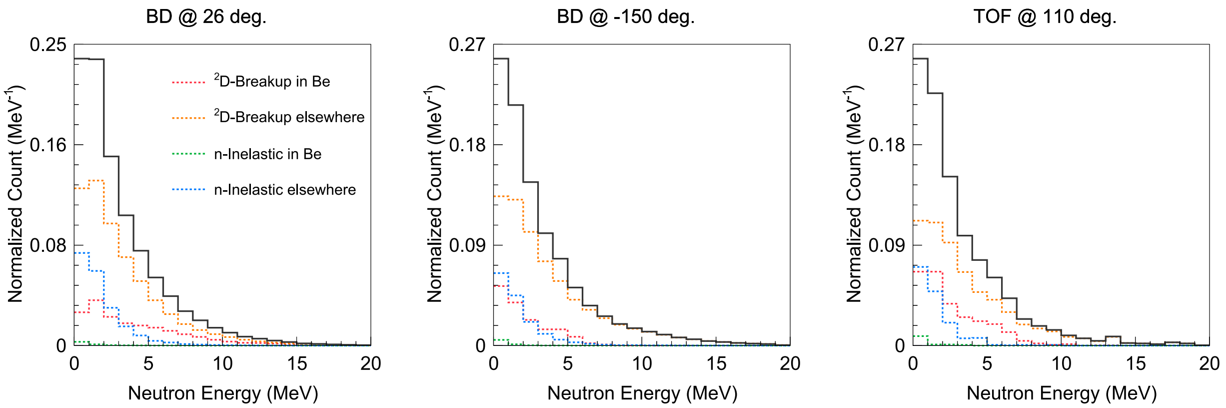

FIGURE 4
Non-fusion neutron spectrum from GEANT4 simulation obtained in the bubble detectors at 26°, −150° and the n-TOF at 110° with respect to the laser-forward direction are shown. The spectrum is broken down by the processes that created the neutrons: deuteron break-up on Be converter (red) or elsewhere in the chamber (orange), and neutron inelastic scattering in Be converter (green) or elsewhere (blue).

cone of emission guided by the measured spatial distribution on the RCF stack with the energy spectrum from the TPS at 0°; and (2) an azimuthally symmetric ring that extends ± 20° above and below the plane perpendicular to the jet axis with the deuteron energy spectrum measured by the TPS at 30°. The numbers of deuterons in each component are set equal, to stay consistent with the observation that the average flux seen by the TPS at 0° is about one order of magnitude larger than that at 30°. Due to the semi-Maxwellian energy distribution and accounting for changes in reaction cross-sections as a function of deuteron energy, neutrons are predominantly produced by the deuterons from the lower energy part of the spectrum ( < 20 MeV). We may therefore neglect the variability in the beam divergence as a function of energy without loss of accuracy. The virtual detectors in the simulation retain information (type and event location) about the parent process that produced a detected neutron, along side with its kinematic variables (energy and momentum). This level of detail allows us to resolve different origins of non-fusion neutrons. To compare the GEANT4 Monte Carlo results with the experimental data, the simulation results are scaled to the actual deuteron numbers, which are measured in the Thomson parabola spectrometers and the RCF stack (if available for the shot).

GEANT4 contains a built-in model for nuclide break-up based on the Fermi model, which assumes the nuclide begins near mass shell. Consequently, this break-up model inevitably produces an exponential neutron spectrum, because it has no information about the threshold or cause of the nucleus' excitation. Varying the input parameters for the break-up model does not change this spectral shape as shown in Figure 4. For this reason, neutrons emitted from the RCF stack and the Be converter exhibit almost the same exponential decay spectral profile with energies up to 16 MeV. However, GEANT4's break-up model is generic and not tied to data; a back-of-the-envelope calculation suggests it overestimates the neutron yield considering the available cross section data for d-Be [37] and d-Al [38] collisions. Since these cross section data and models cover only a limited range of deuteron energies, we minimally extended the cross section data so that the thick target yields reproduced experimental data for a monoenergetic deuteron beam incident on Be [39] and Al targets [40, 41]. Uncertainty in these cross section data is primarily from the sparseness of data at higher deuteron energy $E_d \gtrsim 10$ MeV, and the resulting uncertainty in the neutron yields given the deuteron spectra in Figure 2 is less than 1%. The GEANT4 simulation results for the number of neutrons arriving at each bubble detector are corrected with these experimentally-validated cross sections. In addition to deuteron break-up as a primary source, neutrons can inelastically scatter in the same medium and produce additional, secondary neutrons. Neutron re-scattering contributes a non-negligible 10%–15% enhancement of the neutron yield shown in Figure 5.

The neutron numbers estimated from the bubble detectors data are compared against those predicted from the GEANT4 simulation in Table 1. Whether Be catcher or RCF stack was in place, deuteron scattering in the Al experimental apparatus contributes the largest share of neutrons in the bubble detectors. In shot 11,569 with Be, the apparatus is the source of roughly 3 times as many neutrons as the catcher. Given the relative number of deuterons striking the apparatus versus the catcher and the relative probability of neutron production in Al versus Be, we deduce that the geometric enhancement from the bubble detector being immediately adjacent to the chamber wall is roughly a factor of 3. This agrees with a simple analytic model of the geometric enhancement. For shots 11,555 and 11,557, the neutron production probability in the RCF stack is estimated two

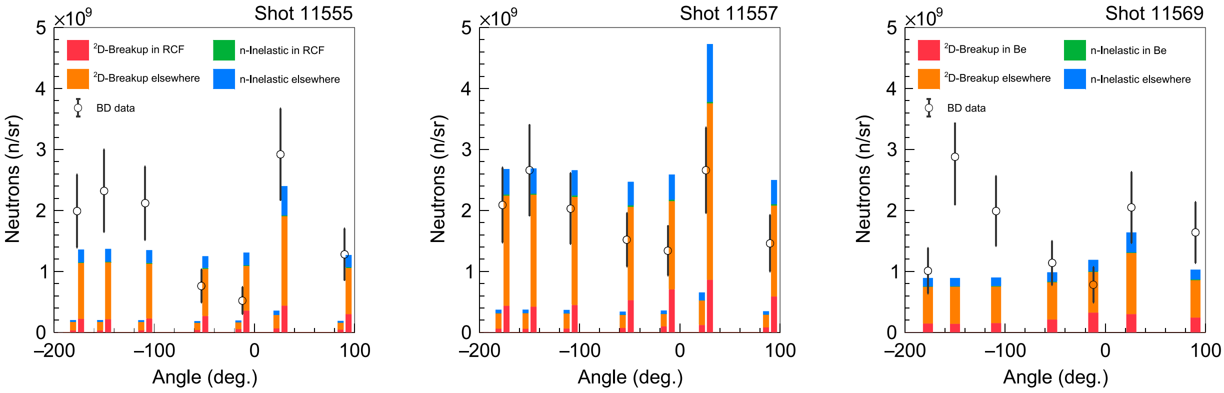

FIGURE 5
Comparison between the non-fusion neutron contribution from Geant4 simulation and the bubble detector measurements. Fluxes are given assuming a source at the front surface of converter, which coincides with the center of the target chamber to well-within the error.

**TABLE 1 The measured neutron yield is determined by averaging the yields in the bubble detectors and assuming the same apparent flux holds isotropically. This procedure compares favorably with the GEANT4 simulation in the second row.**

| Neutron yield | Shot 11,555 | Shot 11,557 | Shot 11,569 |
|---|---|---|---|
| Measured ($\times 10^{10}$) | 2.14 ± 0.90 | 2.47 ± 0.97 | 2.06 ± 0.84 |
| GEANT4 ($\times 10^{10}$) | 0.28–1.85 | 0.51–3.65 | 1.35 |

ways: optimistically the neutron production probability is as high as Be and more pessimistically the neutron production probability is similar to Al, represented respectively by the taller and shorter colored bars in Figure 5. In reality, the RCF stack is layered construction of polymer and Cu; both materials have deuteron break-up cross sections greater than Al but less than Be [38]. Thus, the two estimates are upper and lower bounds on the neutron yield from the RCF stack. In shots 11,555 and 11,569, deuteron scattering in the catcher and apparatus is comparable in order of magnitude but systematically lower than the total measured neutron yield. In shot 11,557, the simulation results suggest that deuteron scattering in the apparatus suffices to explain the measured neutron yield.

The TOF spectra can provide further evidence to identify the likely origins for the neutrons. The GEANT4-predicted spectrum is consistent with the spectrum in shot 11,555, suggesting the majority of neutrons in that shot were derived from deuteron scattering in the apparatus. This evidence is consistent with the analysis of the bubble detector yields in Figure 5.

Interpreting the spectra in shots 11,557 and 11,569 is more difficult. A thermal d (d,n)$^3$He fusion spectrum fit [42] to the lower energy peak in 11,557 would suggest deuterons in the target achieved a Maxwellian distribution with $T \gtrsim 200$ keV. A similar fit is not consistent with the 11,569 spectrum due to the shift of the peak to 3.2 MeV. Moreover a fusion interpretation of the lower-energy peak in shots 11,557 and 11,569 is difficult to sustain in view of time, volume and energy constraints. Then to explain the second peak, we would need to identify an independent source of neutrons producing similar flux with a Gaussian spectrum centered near ≃ 6 MeV.

While the two-peak structure of the spectra in shots 11,557 and 11,569 defies easy explanation, the endpoint of the spectrum in all 3 shots, ≃ 15 MeV, agrees with the GEANT4 simulation. This suggests that the detector responded to a neutron pulse similar to that predicted, but the waveform may have been distorted. The same detector was subsequently used in other laser-plasma experiments without presenting a similar signal, and the waveform is not recognized as caused by known detector errors or miscalibration.

## 4.2 In-target fusion hypothesis

Figure 5 shows the bubble detector neutron counts and the background computed from available cross-section data and Monte Carlo simulation described above. On two out of the three shots, we find a small but significant difference between the predicted neutron yield from break-up and the measured neutron yield. Having accounted for the most significant sources of neutrons from non-fusion reactions, we identify the remainder with *dd* fusion (d (d,n)$^3$He) reactions in the target. Averaging the difference between the observed neutron number and the simulation and assuming isotropic emission from the plasma, we estimate that ≃ $1.2 \times 10^9$ neutrons were produced by *dd* fusion. The most significant uncertainties in this estimate are due to incomplete information on the deuteron beam, which we

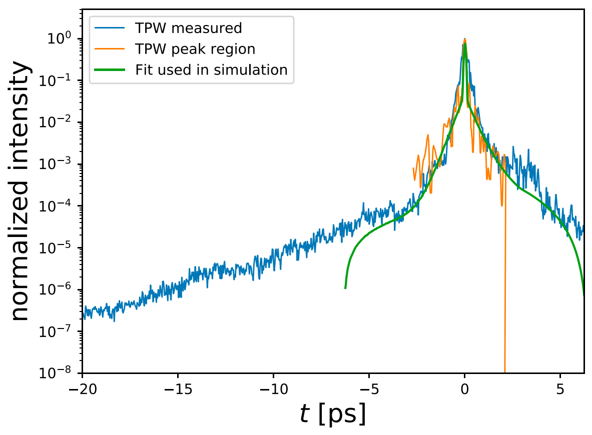

FIGURE 6
Temporal intensity profile of the Texas Petawatt laser pulse, without plasma mirror.

have modeled from the RCF and TP spectra and comparison with past experiments. In particular, the two-component model of the deuteron beam implies that $\gtrsim$ 8% of the on-target laser energy is transferred to the deuterons. With shot-to-shot fluctuations in the laser energy and plasma mirror reflectivity accounted for, shot 11,557 showed the highest energy transfer $\gtrsim$ 10%, shot 11,555 showed the lowest energy transfer, in the range 8%–9%, and shot 11,569 showed ~ 10%. In shot 11,569, a spectrum is only available from the 30-degree TP but the neutron yield suggests that the forward-directed component of accelerated deuterons was similar or higher than 11,555 and 11,557. Energy conversion ≥10% into ions has been achieved before, but required a complicated multi-pulse scheme [43], suggesting our model of the deuteron beam may err high in deuteron number compared to the experiment. It would follow that the GEANT4 simulations err high on the predicted neutron yield and the derived fusion neutron yield is low.

In order to investigate the deuteron heating associated with the intense laser-plasma interaction and the possibility of high neutron yield from *dd* fusion in our experimental setup, we have performed two-dimensional (2D) particle-in-cell (PIC) simulations with the OSIRIS code [44, 45]. We model the interaction of a laser with 88 J, peak $a_0$ = 24, 8.5 μm spot size, and pulse duration of 135 fs with a deuterium slab jet of density 48 $n_c$ and thickness of 2 μm. We model the laser pre-pulse from 6 ps before the main pulse by fitting the temporal profile of the Texas Petawatt laser (see Figure 6) and including this pre-pulse profile in the simulation. In our simulations the laser (with frequency $\omega_0$) is launched along the $z$ direction from the left boundary. The electron-deuteron target plasma is simulated with 36 particles per cell per species, and the total simulation domain of ≃ 1400 μm × 700 μm is resolved with a spatial resolution (cell size) of 0.25 $c/\omega_0$. The time step is chosen according to the Courant–Friedrichs–Lewy condition. Open (absorbing) boundary conditions for both particles and fields are used in both the longitudinal and transverse directions. We have tested different resolutions and numbers of particles per cell to ensure convergence of the results and have used a third order particle interpolation scheme for improved numerical accuracy.

We observe that the laser pre-pulse starts expanding the central region of the target before the main pulse arrives. The main pulse then interacts with the pre-expanded target, strongly heating the electrons, and accelerating the deuterons. The laser eventually breaks through the target *via* relativistic transparency, further accelerating the deuterons [46, 47]. Figure 7 summarizes the main results in terms of deuteron heating and neutron production from *dd* fusion reactions. The neutron reaction rates were obtained by integrating the *dd* fusion cross-sections [48] from the local deuteron distribution functions in the simulations. In panel (a) we see the spatial distribution of the *dd* neutron rate 6 ps after the arrival of the main pulse. While deuterons are significantly heated in the central region, the neutron yield there is moderate due to the lower plasma density. We find that most of the neutron generation occurs just outside this central region, in two hot spots, where the density is still comparable to the initial target density but deuterons have been heated to $T_d \sim$ 10 keV (panel b). Moreover, we find that in this region, the deuteron distribution has significant non-thermal tails above 25 keV increasing the neutron production rate as seen in panel (b). We observe that most of the neutron generation occurs within the first 4 ps after the interaction of the main pulse. By assuming cylindrical symmetry around the laser axis we calculate a total neutron yield from *dd* fusion reactions of $4 \times 10^9$. However, it is important to note that in the actual 3D configuration of the experiment the target size should be limited in the transverse direction not captured by 2D simulations, which should decrease the total yield. While 3D PIC simulations will be needed to produce a more precise calculation of the total neutron yield, our simulation results indicate the possibility of producing order $10^9$ *dd* fusion neutrons consistent with the experimental analysis discussed above.

With $10^9$ neutrons produced over ~ 10 ps, the surface neutron flux on a 100 μm-radius sphere around the deuterium plasma is estimated ≃ $8 \times 10^{22}$ n/cm$^2$/s, which is almost $10^6$ times higher than the neutron flux from the ion-driven method [26] due to its smaller source size and shorter pulse duration. In the ion-driven method, the neutron pulse duration is determined by the flight time of ion passing through the reaction region, which is usually in ns level, as opposed to tens of ps over which the reaction rate is significant.

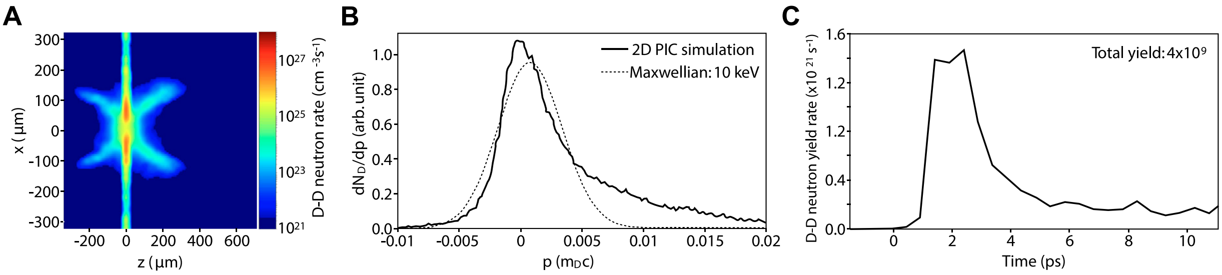

FIGURE 7
Neutron generation from *dd* fusion reactions obtained in a 2D PIC simulation of the interaction of the Texas Petawatt laser with a deuterium target. **(A)** *dd* fusion neutron rate 6 ps after the main pulse arrival. **(B)** Local deuteron momentum distribution in the region of the highest neutron rate indicating development of significant energetic tails above 25 keV. **(C)** Temporal evolution of the *dd* fusion neutron yield rate shows the majority of neutron generation within 4 ps of main pulse arrival. By assuming cylindrical symmetry around the laser axis, we estimate a total neutron yield of $4 \times 10^9$.

# 5 Conclusion

Combining a thin, several micron-scale cryogenic deuterium target with a petawatt-class laser, we obtained a total deuteron yield of $10^{13}$/shot with efficient $\sim 8-10\%$ energy transfer from the laser. This high deuteron yield supported a high neutron yield $\gtrsim 10^{10}$ and efficiency of $10^8$ neutrons/J, comparable to previously published highest neutron yields from laser-driven sources. With $10^{10}$ neutrons produced by the forward-directed beam in the beryllium catcher, fluences $> 10^9/\text{cm}^2$ would have been achieved, primarily in the beam direction in the catcher. Accounting for the nanosecond delay between faster and slower deuterons in the beam, we infer that fluxes exceeding $10^{18}/\text{cm}^2/\text{s}$ were obtained at the catcher. If the catcher could be placed closer to the ion source, millimeters away instead of centimeters, this flux could be enhanced by at least an order of magnitude, if not more. Deuteron break-up on Be and Al experimental apparatus explains a majority but not all the observed neutron yield. Identifying the remaining neutrons as derived from $d(d,n)^3\text{He}$ fusion reactions in the laser-irradiated deuterium jet, we infer a fusion neutron yield ($10^7$ n/J) and high peak flux ($> 10^{22}$ n/cm²/s) near the plasma. As a consequence of the much higher neutron contribution from break-up, a signal of fusion was not clearly identifiable in the neutron spectrum. The double peak feature in two observed neutron spectra is currently not fully understood. In future experiments, multiple neutron time-of-flight detectors should be employed to allow coincidence-based background rejection to determine if the second, higher energy peak is due to a physical neutron signal or not. In case this peak represents a real signal, a multiple detector setup also enables extraction of additional information about the location of the source of the signal.

The neutron flux inferred to originate from in-target fusion is almost a million times higher than the laser-ion driven method ($10^{17}$ n/cm²/s) [26] as well as conventional neutron source like spallation sources ($10^{17}$ n/cm²/s) and fission reactors ($10^{15}$ n/cm²/s) [6]. Additional experiments with improved diagnostics (multiple TOF spectrometers and yield measurements out of plane) are necessary to confirm both the yield and $d(d,n)^3\text{He}$ nature of the source. We anticipate that a thicker target could suppress high energy deuteron emission without significantly reducing the neutron yield. If harnessed and controlled in the right setup, this high peak flux can enable experiments up to now infeasible, for example, the study of the nuclear cross sections and excitation dynamics essential to the r-process [49], responsible for the creation of heavy elements. The key requirement for this research is an extremely high flux of neutrons to allow successive neutron absorption at a rate faster than the decay time. A laser-driven neutron source such as described here introduces additional technical challenges to designing a multi-neutron capture experiment, not least because of the high energy particle and radiation background from the nearby laser-plasma interaction. Future work can stabilize this mechanism as a neutron source and improve the design to begin addressing these challenges. A future multi-beam facility could irradiate a target of interest using two or more laser-driven fusion neutron sources with ultrahigh neutron flux in precision intervals down to ps. This method has potential to significantly increase the peak neutron flux with the next-generation lasers such as 10 PW Extreme Light Infrastructure [50] and multi-PW Apollon laser [51].

# Data availability statement

The raw data supporting the conclusions of this article will be made available by the authors, without undue reservation.

# Author contributions

XJ led and conducted the experiment and prepared the manuscript. CC, MG, JK, EM, EG, GD, BO-O, CS, RR, GT, GG, FT, and SG prepared the target and helped with the experiment. HC and FF conducted PIC simulations. LL, XJ, MG. DP, and EM analyzed data. OL contributed to the theory analysis and the manuscript preparation. BH organized the collaboration and contributed to the manuscript contribution.

## Funding

Work performed under the auspices of the University of Texas at Austin. This work was supported by the Air Force Office of Scientific Research (FA9550-14-1-0045). High performance computing resources were provided by the Texas Advanced Computing Center and OSIRIS simulations were performed on Cori (NERSC) through ERCAP and ALCC compuational grants. This work used the Extreme Science and Engineering Discovery Environment (XSEDE), which is supported by National Science Foundation grant number ACI-1548562. Development of the cryogenic deuterium jet was supported by the U.S. DOE Office of Science, Fusion Energy Sciences under FWP No. 100182. GG acknowledges support from the U.S. DOE NNSA SSGF program under DE-NA0003960. This material is based upon work supported in part by the National Science Foundation under Grant No. 1632708.

## Acknowledgments

We would like to thank the Texas Petawatt laser facility staff for their brilliant and unwavering support.

## Conflict of interest

The authors declare that the research was conducted in the absence of any commercial or financial relationships that could be construed as a potential conflict of interest.

## Publisher's note

## References

1. Wallerstein G, Iben I, Parker P, Boesgaard AM, Hale GM, Champagne AE, et al. Synthesis of the elements in stars: Forty years of progress. *Rev Mod Phys* (1997) 69: 995–1084. doi:10.1103/revmodphys.69.995

2. Yuan V, Bowman JD, Funk D, Morgan G, Rabie R, Ragan C, et al. Shock temperature measurement using neutron resonance spectroscopy. *Phys Rev Lett* (2005) 94:125504. doi:10.1103/physrevlett.94.125504

3. Higginson D, McNaney J, Swift D, Bartal T, Hey D, Kodama R, et al. Laser generated neutron source for neutron resonance spectroscopy. *Phys Plasmas* (2010) 17:100701. doi:10.1063/1.3484218

4. Barth RF, Coderre JA, Vicente MGH, Blue TE. Boron neutron capture therapy of cancer: Current status and future prospects. *Clin Cancer Res* (2005) 11: 3987–4002. doi:10.1158/1078-0432.ccr-05-0035

5. Hill P, Wu Y. Exploring laser-driven neutron sources for neutron capture cascades and the production of neutron-rich isotopes. *Phys Rev C* (2021) 103: 014602. doi:10.1103/physrevc.103.014602

6. Taylor A, Dunne M, Bennington S, Ansell S, Gardner I, Norreys P, et al. A route to the brightest possible neutron source? *Science* (2007) 315:1092–5. doi:10.1126/science.1127185

7. Glenzer S, MacGowan B, Michel P, Meezan N, Suter L, Dixit S, et al. Symmetric inertial confinement fusion implosions at ultra-high laser energies. *Science* (2010) 327:1228–31. doi:10.1126/science.1185634

8. Le Pape S, Berzak Hopkins LF, Divol L, Pak A, Dewald EL, Bhandarkar S, et al. Fusion energy output greater than the kinetic energy of an imploding shell at the national ignition facility. *Phys Rev Lett* (2018) 120:245003. doi:10.1103/physrevlett.120.245003

9. Boehly T, Brown D, Craxton R, Keck R, Knauer J, Kelly J, et al. Initial performance results of the OMEGA laser system. *Opt Commun* (1997) 133: 495–506. doi:10.1016/s0030-4018(96)00325-2

10. Spaeth ML, Manes K, Kalantar D, Miller P, Heebner J, Bliss E, et al. Description of the NIF laser. *Fusion Sci Technol* (2016) 69:25–145. doi:10.13182/fst15-144

11. Mourou DG, Mourou G. Compression of amplified chirped optical pulses. *Opt Commun* (1985) 55:447–9. doi:10.1016/0030-4018(85)90151-8

12. Norreys P, Fews A, Beg F, Bell A, Dangor A, Lee P, et al. Neutron production from picosecond laser irradiation of deuterated targets at intensities of. *Plasma Phys Control Fusion* (1998) 40:175–82. doi:10.1088/0741-3335/40/2/001

13. Zweiback J, Smith R, Cowan T, Hays G, Wharton K, Yanovsky V, et al. Nuclear fusion driven by coulomb explosions of large deuterium clusters. *Phys Rev Lett* (2000) 84:2634–7. doi:10.1103/physrevlett.84.2634

14. Karsch S, Düsterer S, Schwoerer H, Ewald F, Habs D, Hegelich M, et al. *Phys Rev Lett* (2003) 91:015001. doi:10.1103/physrevlett.91.015001

15. Buersgens F, Madison K, Symes D, Hartke R, Osterhoff J, Grigsby W, et al. *Phys Rev E* (2006) 74:016403. doi:10.1103/physreve.74.016403

16. Willingale L, Petrov G, Maksimchuk A, Davis J, Freeman R, Joglekar A, et al. Comparison of bulk and pitcher-catcher targets for laser-driven neutron production. *Phys Plasmas* (2011) 18:083106. doi:10.1063/1.3624769

17. Bang W, Barbui M, Bonasera A, Dyer G, Quevedo H, Hagel K, et al. Temperature measurements of fusion plasmas produced by petawatt-laser-irradiated $D_2 - {}^3$He or $CD_4 - {}^3$He clustering gases. *Phys Rev Lett* (2013) 111: 055002. doi:10.1103/PhysRevLett.111.055002

18. Jung D, Falk K, Guler N, Deppert O, Devlin M, Favalli A, et al. Characterization of a novel, short pulse laser-driven neutron source. *Phys Plasmas* (2013) 20:056706. doi:10.1063/1.4804640

19. Roth M, Jung D, Falk K, Guler N, Deppert O, Devlin M, et al. *Phys Rev Lett* (2013) 110:044802. doi:10.1103/physrevlett.110.044802

20. Storm M, Jiang S, Wertepny D, Orban C, Morrison J, Willis C, et al. Fast neutron production from lithium converters and laser driven protons. *Phys Plasmas* (2013) 20:053106. doi:10.1063/1.4803648

21. Pomerantz I, McCary E, Meadows AR, Arefiev A, Bernstein AC, Chester C, et al. Ultrashort pulsed neutron source. *Phys Rev Lett* (2014) 113:184801. doi:10.1103/physrevlett.113.184801

22. Hah J, Petrov G, Nees J, He Z-H, Hammig M, Krushelnick K, et al. High repetition-rate neutron generation by several-mJ, 35 fs pulses interacting with free-flowing D2O. *Appl Phys Lett* (2016) 109:144102. doi:10.1063/1.4963819

23. Kar S, Green A, Ahmed H, Alejo A, Robinson A, Cerchez M, et al. Beamed neutron emission driven by laser accelerated light ions. *New J Phys* (2016) 18: 053002. doi:10.1088/1367-2630/18/5/053002

24. Jiao X, Shaw J, Wang T, Wang X, Tsai H, Poth P, et al. A tabletop, ultrashort pulse photoneutron source driven by electrons from laser wakefield acceleration. *Matter Radiat Extremes* (2017) 2:296–302. doi:10.1016/j.mre.2017.10.003

25. Higginson D, McNaney J, Swift D, Petrov G, Davis J, Frenje J, et al. Production of neutrons up to 18 MeV in high-intensity, short-pulse laser matter interactions. *Phys Plasmas* (2011) 18:100703. doi:10.1063/1.3654040

26. Guler N, Volegov P, Favalli A, Merrill FE, Falk K, Jung D, et al. Neutron imaging with the short-pulse laser driven neutron source at the Trident laser facility. *J Appl Phys* (2016) 120:154901. doi:10.1063/1.4964248

27. Gauthier M, Curry C, Göde S, Brack F-E, Kim J, MacDonald M, et al. High repetition rate, multi-MeV proton source from cryogenic hydrogen jets. *Appl Phys Lett* (2017) 111:114102. doi:10.1063/1.4990487

28. Gaul EW, Martinez M, Blakeney J, Jochmann A, Ringuette M, Hammond D, et al. Demonstration of a 11 petawatt laser based on a hybrid optical parametric chirped pulse amplification/mixed Nd:glass amplifier. *Appl Opt* (2010) 49:1676. doi:10.1364/ao.49.001676

29. Kim J, Göde S, Glenzer S. Development of a cryogenic hydrogen microjet for high-intensity, high-repetition rate experiments. *Rev Sci Instrum* (2016) 87:11E328. doi:10.1063/1.4961089

30. Curry CB, Schoenwaelder C, Goede S, Kim JB, Rehwald M, Treffert F, et al. Cryogenic liquid jets for high repetition rate Discovery science. *J Visualized Experiments* (2020) 159:e61130. doi:10.3791/61130

31. Obst L, Göde S, Rehwald M, Brack F-E, Branco J, Bock S, et al. *Scientific Rep* (2017) 7:1. doi:10.1038/s41598-017-10589-3

32. Curry C, Dunning C, Gauthier M, Chou H-G, Fiuza F, Glenn G, et al. Optimization of radiochromic film stacks to diagnose high-flux laser-accelerated proton beams. *Rev Scientific Instr* (2020) 91:093303. doi:10.1063/5.0020568

33. Gauthier M, Kim J, Curry C, Aurand B, Gamboa E, Göde S, et al. High-intensity laser-accelerated ion beam produced from cryogenic micro-jet target. *Rev Sci Instrum* (2016) 87:11D827. doi:10.1063/1.4961270

34. Ing H, Noulty R, McLean T. Bubble detectors-A maturing technology. *Radiat measurements* (1997) 27:1–11. doi:10.1016/s1350-4487(96)00156-4

35. Alejo A, Kar S, Ahmed H, Krygier A, Doria D, Clarke R, et al. Characterisation of deuterium spectra from laser driven multi-species sources by employing differentially filtered image plate detectors in Thomson spectrometers. *Rev Scientific Instr* (2014) 85:093303. doi:10.1063/1.4893780

36. Allison J, Amako K, Apostolakis J, Araujo H, Arce Dubois PA, Asai M, et al. Geant4 developments and applications. *IEEE Trans Nucl Sci* (2006) 53:270–8. doi:10.1109/tns.2006.869826

37. Abramovich S, Generalov L, Zvenigorodskij A. Izvestiya akademii nauk. Rossijskaya akademiya nauk. *Seriya Fizicheskaya* (1999) 63:76.

38. Bém P, Šimečková E, Honusek M, Fischer U, Simakov S, Forrest R, et al. Low and medium energy deuteron-induced reactions on Al27. *Phys Rev C* (2009) 79: 044610. doi:10.1103/physrevc.79.044610

39. Ménard S, Mirea M, Clapier F, Pauwels N, Proust J, Donzaud C, et al. Fast neutron forward distributions from C, Be, and U thick targets bombarded by deuterons. *Phys Rev Spec Topics-Accelerators Beams* (1999) 2:033501. doi:10.1103/physrevstab.2.033501

40. Pampus J, Bisplinghoff J, Ernst J, Mayer-Kuckuk T, Rama Rao JR, Baur G, et al. Inclusive proton spectra from deuteron break-up: Theory and experiment. *Nucl Phys A* (1978) 311:141–60. doi:10.1016/0375-9474(78)90506-7

41. Matsuoka N, Kondo M, Shimizu A, Saito T, Nagamachi S, Sakaguchi H, et al. Deuteron break-up in the fields of nuclei at 56 MeV. *Nucl Phys A* (1980) 345:1–12. doi:10.1016/0375-9474(80)90409-1

42. Chittenden BJ, Chittenden J. The production spectrum in fusion plasmas. *Plasma Phys Control Fusion* (2011) 53:045002. doi:10.1088/0741-3335/53/4/045002

43. Brenner CM, Robinson A, Markey K, Scott R, Gray R, Rosinski M, et al. High energy conversion efficiency in laser-proton acceleration by controlling laser-energy deposition onto thin foil targets. *Appl Phys Lett* (2014) 104:081123. doi:10.1063/1.4865812

44. Fonseca RA, Silva LO, Tsung FS, Decyk VK, Lu W, Ren C, et al. Osiris: A three-dimensional, fully relativistic particle in cell code for modeling plasma based accelerators. In: PMA Sloot, AG Hoekstra, CJK Tan, JJ Dongarra, editors. *Computational science — ICCS 2002: International conference amsterdam, The Netherlands, april 21–24, 2002 proceedings, Part III*. Berlin, Heidelberg: Springer Berlin Heidelberg (2002). p. 342–51. doi:10.1007/3-540-47789-6_36

45. Fonseca RA, Martins SF, Silva LO, Tonge JW, Tsung FS, Mori WB. One-to-one direct modeling of experiments and astrophysical scenarios: Pushing the envelope on kinetic plasma simulations. *Plasma Phys Controlled Fusion* (2008) 50:9. doi:10.1088/0741-3335/50/12/124034

46. Yin L, Albright B, Bowers K, Jung D, Fernández J, Hegelich B. Three-dimensional dynamics of breakout afterburner ion acceleration using high-contrast short-pulse laser and nanoscale targets. *Phys Rev Lett* (2011) 107:045003. doi:10.1103/physrevlett.107.045003

47. Mishra R, Fiuza F, Glenzer S. Enhanced ion acceleration in transition from opaque to transparent plasmas. *New J Phys* (2018) 20:043047. doi:10.1088/1367-2630/aab8db

48. Bosch HS, Hale GM. Improved formulas for fusion cross-sections and thermal reactivities. *Nucl Fusion* (1992) 32:611–31. doi:10.1088/0029-5515/32/4/i07

49. Bartlett A, Görres J, Mathews GJ, Otsuki K, Wiescher M, Frekers D, et al. Two-neutron capture reactions and the *r* process. *Phys Rev C* (2006) 74:015802. doi:10.1103/physrevc.74.015802

50. Gales S, Tanaka K, Balabanski D, Negoita F, Stutman D, Tesileanu O, et al. The extreme light infrastructure-nuclear physics (ELI-NP) facility: New horizons in physics with 10 PW ultra-intense lasers and 20 MeV brilliant gamma beams. *Rep Prog Phys* (2018) 81:094301. doi:10.1088/1361-6633/aacfe8

51. Papadopoulos D, Zou J, Le Blanc C, Chériaux G, Georges P, Druon F, et al. The Apollon 10 PW laser: Experimental and theoretical investigation of the temporal characteristics. *High Power Laser Sci Eng* (2016) 4:e34. doi:10.1017/hpl.2016.34

## Appendix A: Laser temporal profile

The Texas Petawatt laser temporal profile is measured without a plasma mirror. Figure 6 shows a coarse scan (blue) revealing a long prepulse extending $> 20$ ps before the peak. The fine scan (orange) around the peak determines the intensity FWHM pulse duration of 135 fs. A plasma mirror enhances the contrast by approximately the ratio between the mirror reflectivity before being triggering and the mirror reflectivity after triggered. The reflectivity before triggering is determined by the coating's reflectivity averaged over angle of incidence and spectral bandwidth of the laser. This ratio leads to an expected contrast enhancement of ~ 200.

For the expected peak intensity of the laser we estimate that the plasma mirror would trigger about 6 ps before the peak. Therefore, we model (green line) the effect of the plasma mirror by rapidly suppressing the laser field strength 6 ps before the peak, which also provides a well-defined starting point for evolution in the simulation.

## Appendix B: RCF formula

From front to back: 13 μm Al + HDv2 + 8×(100 μm Al + HDv2) + 6×(150 μm Cu + MDv3) + 16×(500 μm Cu + EBT3) + 5×(1 mm Cu + EBT3). HDv2 is Mylar, thickness 105 μm, MDv3 is Mylar, thickness: 260 μm, and EBT3 is Mylar, thickness 280 μm.

# Frontiers in
# Physics

**Investigates complex questions in physics to understand the nature of the physical world**

Addresses the biggest questions in physics, from macro to micro, and from theoretical to experimental and applied physics.

## Discover the latest Research Topics

See more →

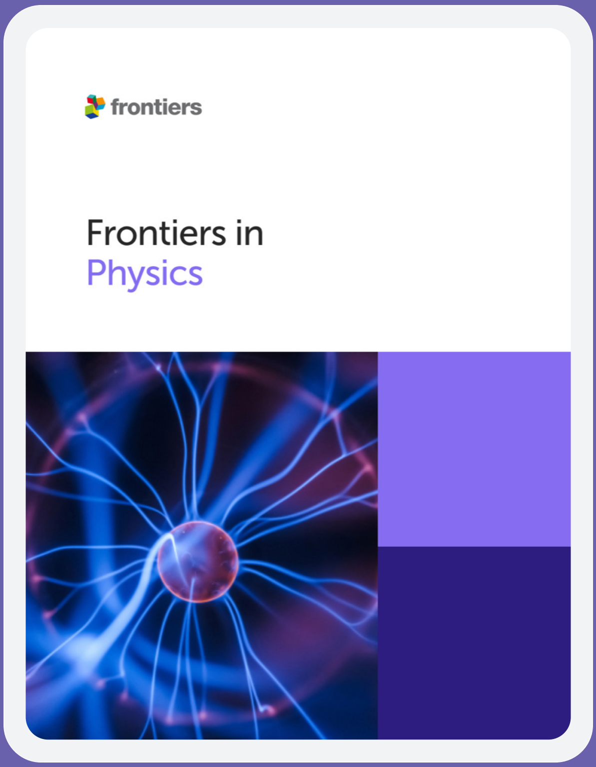

frontiers

Frontiers in
Physics

**Frontiers**

Avenue du Tribunal-Fédéral 34
1005 Lausanne, Switzerland
frontiersin.org

**Contact us**

+41 (0)21 510 17 00
frontiersin.org/about/contact